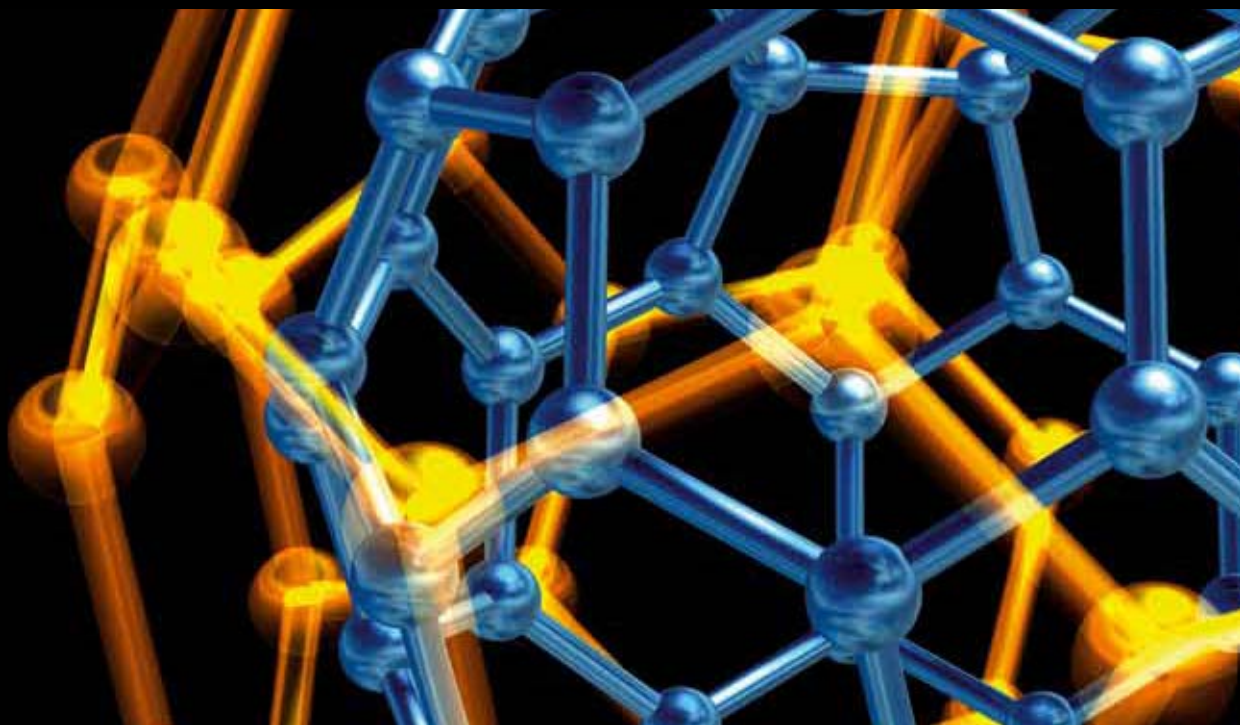


# NANOCOMPOSITES

GUEST EDITORS: GUIFU ZOU, HONGMEI LUO, BAOQUAN SUN, MENKA JAIN,  
AND HUIHENG PENG



---



# **Nanocomposites**

Journal of Nanotechnology

---

## **Nanocomposites**

Guest Editors: Guifu Zou, Hongmei Luo, Baoquan Sun,  
Menka Jain, and Huisheng Peng



---

Copyright © 2011 Hindawi Publishing Corporation. All rights reserved.

This is a special issue published in "Journal of Nanotechnology." All articles are open access articles distributed under the Creative Commons Attribution License, which permits unrestricted use, distribution, and reproduction in any medium, provided the original work is properly cited.

## Editorial Board

Simon Joseph Antony, UK  
Y. Bando, Japan  
B. Bhushan, USA  
Felix A. Buot, USA  
Carlos R. Cabrera, Puerto Rico  
John A. Capobianco, Canada  
Franco Cerrina, USA  
Gan Moog Chow, Singapore  
Jeffery L. Coffey, USA  
Dmitriy A. Dikin, USA  
Dimitris Drikakis, UK  
H. D. Espinosa, USA  
John S. Foord, UK  
E. Goldys, Australia  
Lambertus Hesselink, USA  
Joseph Irudayaraj, USA

Niraj K. Jha, USA  
Miguel Jose-Yacamán, USA  
Valery Khabashesku, USA  
Yoke Khin Yap, USA  
Sakhrat Khizroev, USA  
Andrei Kolmakov, USA  
Charles M. Lieber, USA  
Charles M. Lukehart, USA  
A. H. Makhlof, Germany  
Constantinos Mavroidis, USA  
Vincent Meunier, USA  
Paolo Milani, Italy  
Oded Millo, Israel  
M. Grant Norton, USA  
R. Lee Penn, USA  
S. N. Piramanayagam, Singapore

A. M. Rao, USA  
Paresh Chandra Ray, USA  
Benjaram M. Reddy, India  
Federico Rosei, Canada  
Mehmet Sarikaya, USA  
Jorge M. Seminario, USA  
V. Shalaev, USA  
Mahi R. Singh, Canada  
Bobby G. Sumpter, USA  
Xiao Wei Sun, Singapore  
Weihong Tan, USA  
O. K. Tan, Singapore  
Thomas Thundat, USA  
Boris I. Yakobson, USA  
Nan Yao, USA  
Chuan Jian Zhong, USA

# Contents

**Nanocomposites**, Guifu Zou, Hongmei Luo, Baoquan Sun, Menka Jain, and Huisheng Peng  
Volume 2011, Article ID 367938, 2 pages

**Effects of Au Nanoparticle Addition to Hole Transfer Layer in Organic Photovoltaic Cells Based on Phthalocyanines and Fullerene**, Akihiko Nagata, Takeo Oku, Tsuyoshi Akiyama, Atsushi Suzuki, Yasuhiro Yamasaki, and Tomohiro Mori  
Volume 2011, Article ID 869596, 6 pages

**Photocatalytic Properties of Tin Oxide and Antimony-Doped Tin Oxide Nanoparticles**, J. C. M. Brokken-Zijp, O. L. J. van Asselen, W. E. Kleinjan, R. van de Belt, and G. de With  
Volume 2011, Article ID 106254, 15 pages

**Photodegradation of Chloridazon Using Coreshell Magnetic Nanocomposites**, Dina Mamdouh Fouad and Mona Bakr Mohamed  
Volume 2011, Article ID 416060, 7 pages

**Structure and Optical Properties of Doped SiO<sub>2</sub> Mesoporous Glasses**, G. Hernández-Padrón, M. Hernández-Ortiz, H. A. Durán-Muñoz, M. García-Garduño, and V. M. Castaño  
Volume 2011, Article ID 361347, 8 pages

**Light-Emitting Polymer Nanocomposites**, Kyle Gipson, Brett Ellerbrock, Kathryn Stevens, Phil Brown, and John Ballato  
Volume 2011, Article ID 386503, 8 pages

**A Novel Route for Development of Bulk Al/SiC Metal Matrix Nanocomposites**, Payodhar Padhi and Sachikanta Kar  
Volume 2011, Article ID 413512, 5 pages

**Process Modeling of Deagglomeration of Ceramic Nanoparticles in Liquid Metal during Synthesis of Nanocomposites**, Payodhar Padhi, Biranchi Narayan Dash, and Sachi Kanta Kar  
Volume 2011, Article ID 734013, 4 pages

**Structure and Properties of Multiwall Carbon Nanotubes/Polystyrene Composites Prepared via Coagulation Precipitation Technique**, I. N. Mazov, V. L. Kuznetsov, D. V. Krasnikov, N. A. Rudina, A. I. Romanenko, O. B. Anikeeva, V. I. Suslyaev, E. Yu. Korovin, and V. A. Zhuravlev  
Volume 2011, Article ID 648324, 7 pages

**Self-Organization of ZnO Nanoparticles on UV-Curable Acrylate Nanocomposites**, J. A. Burunkova, I. Yu. Denisyuk, and S. A. Semina  
Volume 2011, Article ID 951036, 6 pages

**Carbon-Based Fibrous EDLC Capacitors and Supercapacitors**, C. Lekakou, O. Moudam, F. Markoulidis, T. Andrews, J. F. Watts, and G. T. Reed  
Volume 2011, Article ID 409382, 8 pages

**Microwave-Assisted Preparation of Biodegradable Water Absorbent Polyacrylonitrile/Montmorillonite Clay Nanocomposite**, Prafulla K. Sahoo, Trinath Biswal, and Ramakanta Samal  
Volume 2011, Article ID 143973, 11 pages



---

**Enhancing the Mechanical Properties of Cross-Linked Rubber-Toughened Nanocomposites via Electron Beam Irradiation**, N. A. Jamal, H. Anuar, and A. R. Shamsul Bahri

Volume 2011, Article ID 769428, 8 pages

**The Influence of EB-Irradiated Treatment on Enhancing Barrier Property and Crystallization Behavior of Rubber-Toughened Nanocomposites**, N. A. Jamal, H. Anuar, and A. R. Shamsul Bahri

Volume 2011, Article ID 683725, 8 pages

**A New Ultra Fast Conduction Mechanism in Insulating Polymer Nanocomposites**, M. Xu, G. C. Montanari, D. Fabiani, L. A. Dissado, and A. Krivda

Volume 2011, Article ID 985801, 11 pages

## Editorial

# Nanocomposites

**Guifu Zou,<sup>1,2</sup> Hongmei Luo,<sup>3</sup> Baoquan Sun,<sup>4</sup> Menka Jain,<sup>5</sup> and Huisheng Peng<sup>6</sup>**

<sup>1</sup> School of Energy, Soochow University, Suzhou 215000, China

<sup>2</sup> Center for Integrated Nanotechnologies, Los Alamos National Laboratory, MS: K763, Los Alamos, NM 87544, USA

<sup>3</sup> Department of Chemical Engineering, New Mexico State University, Las Cruces, NM 88001, USA

<sup>4</sup> Center for Soft Matter, Soochow University, Suzhou 215015, China

<sup>5</sup> Department of Physics, University of Connecticut, Storrs, CT 06269, USA

<sup>6</sup> Macromolecular Science Department, Fudan University, Shanghai 200433, China

Correspondence should be addressed to Guifu Zou, zoulanl@gmail.com

Received 1 March 2012; Accepted 1 March 2012

Copyright © 2011 Guifu Zou et al. This is an open access article distributed under the Creative Commons Attribution License, which permits unrestricted use, distribution, and reproduction in any medium, provided the original work is properly cited.

Nanocomposites have shown unique advantages in achieving properties to find tremendous potential applications in science and technology. Due to their diverse structures, nanocomposites exhibit a wide variety of tunable properties to realize the prominent and desirable performances in mechanical, electrical, thermal, optical, electrochemical, and catalytic fields. The properties of nanocomposite materials depend not only on the properties of the building components, but also on their morphologies and interfacial characteristics. There is also the possibility of producing improved multifunctionalities and/or new properties due to the coupling between the two components, which may not be found for each component at a pure state. In this special issue on nanocomposites, we have already received the relevant nanocomposites' work of broad field from worldwide scientists. The published works are briefly addressed as follows.

The first paper of this issue is by Japanese research group about phthalocyanines/fullerene organic photovoltaic cells. Effects of Au nanoparticle addition to a hole transfer layer were investigated, and power conversion efficiencies of the photovoltaic cells were improved after blending the Au nanoparticle into PEDOT:PSS. The second paper by Netherlandish scientists reports that N-doped SnO<sub>2</sub> nanoparticles photocatalyze directly the polymerization of the C=C bonds of (meth)acrylates under visible light illumination. The Egyptian professors in the third paper show a new chemically synthesized magnetic nanoparticle of Fe<sub>3</sub>O<sub>4</sub> and core-shell Fe<sub>3</sub>O<sub>4</sub>@Au. A comparative study between the photocatalytic

activity between Fe<sub>3</sub>O<sub>4</sub> and core-shell Au-Fe<sub>3</sub>O<sub>4</sub> nanoparticles has been exploring the effect of UV and sun light on the photodegradation of chloridazon. The fourth paper presents the Mexican scientist work regarding the syntheses of monolithic mesoporous silica glasses. The presence of Cu<sup>2+</sup> and Fe<sup>3+</sup> cations during the synthesis of sol-gel precursors leads to different morphologies and pore sizes. Meanwhile, the relationship of materials structure and properties has been analyzed.

The USA research group in the fifth paper states that inorganic nanoparticles doped with optically active rare-earth ions and coated with organic ligands were synthesized in order to create fluorescent polymethyl methacrylate nanocomposites. The sixth and seventh papers from the Indian group present development of deagglomeration and uniform dispersion of nanoparticles in nanocomposites. Russian research groups address coagulation technique applied for preparation of multiwall carbon nanotube (MWNT-) containing polystyrene composite materials with different MWNT loading (0.5–10 wt.%) and synthesis and investigation of nanoparticles role in structuring of homogenous nanocomposite based on ZnO nanoparticles in UV-curable monomers mixture in papers eight and nine, respectively.

The British professors in the tenth paper investigate electrochemical double-layer capacitors including two alternative types of carbon-based fibrous electrodes, a carbon fibre woven fabric (CWF) and a multiwall carbon nanotube (CNT) electrode, as well as hybrid CWF-CNT electrodes.

Another Indian group in the eleventh state that polyacrylonitrile (PAN)/montmorillonite (MMT) clay nanocomposite was prepared in a microwave oven. They used a transition metal Co(III) complex taking ammonium persulfate as initiator with a motive of converting hydrophobic PAN into hydrophilic nanocomposite material by the inclusion of MMT to the virgin polymer. The Malaysian researchers present the nanocomposites systems. It is firstly prepared via intercalation technique with different organophilic montmorillonite in the twelfth. Meanwhile, they also report the crystallization and oxygen barrier properties of high density-polyethylene (HDPE)/ethylene propylene diene monomer (EPDM) matrix and HDPE/EPDM modified by electron beam irradiation technique in the thirteenth paper. The final paper by Chinese scientist reports a new ultrafast conduction mechanism in insulating polymer nanocomposites. A brand new phenomenon, namely, electrical conduction via solution-like ultrafast space charge pulses, is shown for the first time to occur in insulating polymer nanocomposites and its characteristics correlated with the electromechanical properties of nanostructured materials.

*Guifu Zou  
Hongmei Luo  
Baoquan Sun  
Menka Jain  
Huisheng Peng*

## Research Article

# Effects of Au Nanoparticle Addition to Hole Transfer Layer in Organic Photovoltaic Cells Based on Phthalocyanines and Fullerene

Akihiko Nagata,<sup>1</sup> Takeo Oku,<sup>1</sup> Tsuyoshi Akiyama,<sup>1</sup> Atsushi Suzuki,<sup>1</sup>  
Yasuhiro Yamasaki,<sup>2</sup> and Tomohiro Mori<sup>2</sup>

<sup>1</sup>Department of Materials Science, School of Engineering, The University of Shiga Prefecture, 2500 Hassaka, Hikone, Shiga 522-8533, Japan

<sup>2</sup>Department of New Business, Orient Chemical Industries Co., Ltd., 8-1 Sanra-Higashi-machi, Neyagawa, Osaka 572-8581, Japan

Correspondence should be addressed to Takeo Oku, oku@mat.usp.ac.jp

Received 14 February 2011; Revised 12 August 2011; Accepted 7 September 2011

Academic Editor: Guifu Zou

Copyright © 2011 Akihiko Nagata et al. This is an open access article distributed under the Creative Commons Attribution License, which permits unrestricted use, distribution, and reproduction in any medium, provided the original work is properly cited.

Phthalocyanines/fullerene organic photovoltaic cells were fabricated and characterized. Effects of Au nanoparticle addition to a hole transfer layer were also investigated, and power conversion efficiencies of the photovoltaic cells were improved after blending the Au nanoparticle into PEDOT:PSS. Nanostructures of the Au nanoparticles were investigated by transmission electron microscopy and X-ray diffraction. Energy levels of molecules were calculated by molecular orbital calculations, and the nanostructures and electronic property were discussed.

## 1. Introduction

In noble metal particles such as gold or silver from tens of nanometer to several nanometers, the vibrational frequency of localized surface plasmon resonates with a photoelectric field of the wavelength of the visible region [1–4]. When visible light is irradiated to noble metal nanoparticles or nanostructures, light is converted into surface plasmon and the localized electric field generated in the vicinity of surface of nanoparticles or nanostructures. The plasmon electric field is excited dye molecules as well as light, and interesting phenomena and various applications have been reported [5–8]. In addition, the group velocity of light decreases in such nanospace and the photoabsorption efficiency of dye arranged in the nanospace would be reinforced. Therefore, clarifications and applications of the reinforcement mechanism are interesting research objects.

Phthalocyanines have been widely studied as attractive materials for photovoltaic, electrochemical, gas-sensing, and data-storage devices [9, 10]. Phthalocyanine molecules have planar unit and electronic conductivity because of the  $\pi$

electron system and have p-type semiconductor behavior [11]. Therefore, they have been investigated as thin film organic photovoltaic cells, which are expected as next-generation photovoltaic cells because of advantages of easy manufacture process, low production cost, and flexibility [12–14]. The photovoltaic devices consisting of noble metal nanostructures or nanoparticles with the localized electric field have been reported [15, 16]. However, there are few studies on organic photovoltaic cells with noble metal nanostructures or nanoparticles.

The purpose of the present work is to fabricate and characterize organic photovoltaic cells based on phthalocyanines and fullerene ( $C_{60}$ ). In the present work,  $C_{60}$  was used as n-type semiconductor, and copper naphthalocyanine (CuNc) and subphthalocyanine (SubPc) were used as p-type semiconductors, respectively. In addition, effects of Au nanoparticle (AuNP) addition to a hole transfer layer were investigated. For metal nanoparticles such as Au and Ag, strongly enhanced electric fields are locally generated in their nanospaces by irradiation of light. This phenomenon is due to localized surface plasmon resonance (LSPR), which is

expected to enhance light harvesting of the organic solar cells [15–19]. Photovoltaic devices were fabricated, and nanostructures, electronic property, and optical absorption were investigated.

## 2. Experimental Procedures

Aqueous stock solution of  $\text{HAuCl}_4$  ( $2.5 \times 10^{-4}$  M) was prepared and refluxed. After reflux for 40 min, 1 wt.% sodium citrate of 1.4 mL was added to reaction mixture. After reflux for 60 min, it was cooled under the air atmosphere. The fabricated AuNP solution was concentrated by the centrifugation. To prepare the composite buffer layer, the concentrated AuNP solution was blended into the polyethylenedioxythiophene doped with polystyrene sulfonic acid (PEDOT:PSS, Sigma-Aldrich Corp.) solution. The volume ratio of AuNP solution was 20%.

A buffer layer of PEDOT:PSS with AuNPs was spin coated on precleaned indium tin oxide (ITO) glass plates (Geomatec Co. Ltd.,  $\sim 10 \Omega/\square$ ). After annealing at  $100^\circ\text{C}$  for 10 min in  $\text{N}_2$  atmosphere, p-type photoactive layers were prepared on a PEDOT layer. Copper (II) 2,3-naphthalocyanine (CuNc, Sigma-Aldrich Corp., 85%) layers were deposited by a spin coating method, and subphthalocyanine (SubPc, Orient Chemical Industries Co., Ltd.) layers were deposited by evaporation, respectively. After depositing p-type photoactive layers,  $\text{C}_{60}$  thin films were deposited using  $\text{C}_{60}$  powder (Material Technologies Research Ltd., 99.98%) by a vacuum deposition method. Aluminum (Al) metal contacts with a thickness of 100 nm were evaporated as a top electrode. A schematic diagram of the present photovoltaic cells is shown in Figure 1.

The current density-voltage ( $J$ - $V$ ) characteristics (Hokuto Denko Co. Ltd., HSV-110) of the photovoltaic cells were measured both in the dark and under illumination at  $100 \text{ mW cm}^{-2}$  by using an AM 1.5 solar simulator (San-ei Electric Co. Ltd., XES-301S). The photovoltaic cells were illuminated through the side of the ITO substrates, and the illuminated area is  $0.16 \text{ cm}^2$ . Incident photon to current conversion efficiency (IPCE) was measured by using hypermonolight (Bunkoukeiki Co. Ltd., SM-25) and potentiostat (Huso Ltd., HECS 318C). The photovoltaic cells were irradiated by monochromated Xe lamp from the ITO side. Absorption spectra were measured by means of UV-visible spectroscopy (JASCO, V-670), and the wavelength region is in the range of 300 nm~800 nm. Microstructures of AuNPs were analyzed using X-ray diffractometer (Philips X'Pert-MPD System) with  $\text{CuK}\alpha$  radiation operating at 40 kV and 40 mA. Transmission electron microscope (TEM) observation was carried out by a 200 kV TEM (Hitachi, H-8100).

The isolated molecular structures were optimized by *ab initio* molecular orbital calculations using Gaussian 03. Conditions in the present calculation were as follows: calculation type (SP), calculation method (B3LYP), and basis set (LANL2DZ). Electronic structures such as energy gaps between highest occupied molecular orbital (HOMO) and lowest unoccupied molecular orbital (LUMO), and electron densities were investigated.

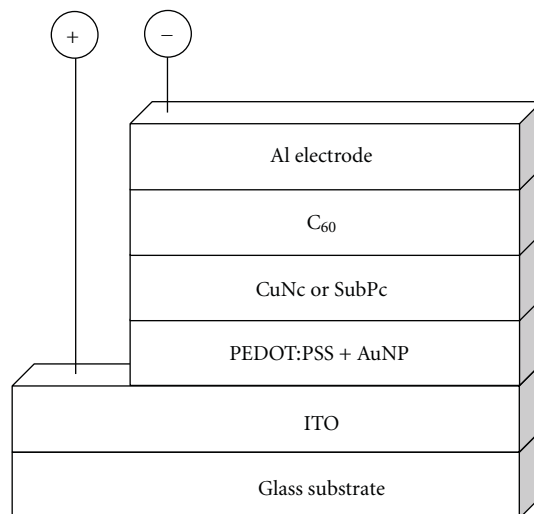


FIGURE 1: Schematic diagram of the present photovoltaic cells.

## 3. Results and Discussion

A TEM image and an electron diffraction pattern of AuNP are shown in Figures 2(a) and 2(b), respectively. AuNPs have an fcc structure with a lattice parameter of  $a = 0.40786 \text{ nm}$ . In the TEM image of Figure 2(a), AuNPs have a spherical shape and grain sizes of AuNPs were in the range of 40~60 nm. An X-ray diffraction pattern of the AuNPs sample prepared by the present reduction method is shown in Figure 3. From a 111 diffraction peak, a grain size was calculated by using Debye-Scherrer formula:  $D = 0.9\lambda/\beta \cos \theta$ , where  $\lambda$ ,  $\beta$ , and  $\theta$  represent the wavelength of X-ray source, the full width at half maximum (FWHM), and the Bragg angle, respectively. An average particle size is calculated to be 42 nm, which agrees well with the observed TEM data as shown in Figure 2(a).

Figure 4 shows absorption spectra of AuNP solution and AuNPs in PEDOT:PSS deposited by a spin coating method on glass substrates. In Figure 4, absorption peaks were confirmed to be 536 and 578 nm, respectively, which were originated from plasmon absorption.

Optical absorption spectra of CuNc/ $\text{C}_{60}$  and SubPc/ $\text{C}_{60}$  thin film on glass substrate are shown in Figures 5(a) and 5(b), respectively. In Figure 5(a), absorption peaks at 350 nm and 450 nm are due to  $\text{C}_{60}$  and other peaks are due to CuNc. In Figure 5(b), an absorption peak at 580 nm is due to SubPc. The present CuNc/ $\text{C}_{60}$  and SubPc/ $\text{C}_{60}$  heterojunction structures with AuNPs provided absorbance increase for the wavelength from 500 nm to 700 nm.

Measured  $J$ - $V$  characteristics of CuNc/ $\text{C}_{60}$  and SubPc/ $\text{C}_{60}$  photovoltaic cells with or without AuNP under illumination are shown in Figure 6. The present structures show characteristic curve for open-circuit voltage and short-circuit current. Measured parameters of the present photovoltaic cells are summarized in Table 1. In Table 1, CuNc/ $\text{C}_{60}$  and SubPc/ $\text{C}_{60}$  heterojunction structures with AuNPs provided higher short-circuit current compared to those of CuNc/ $\text{C}_{60}$  and SubPc/ $\text{C}_{60}$  structures without AuNP. The SubPc/ $\text{C}_{60}$

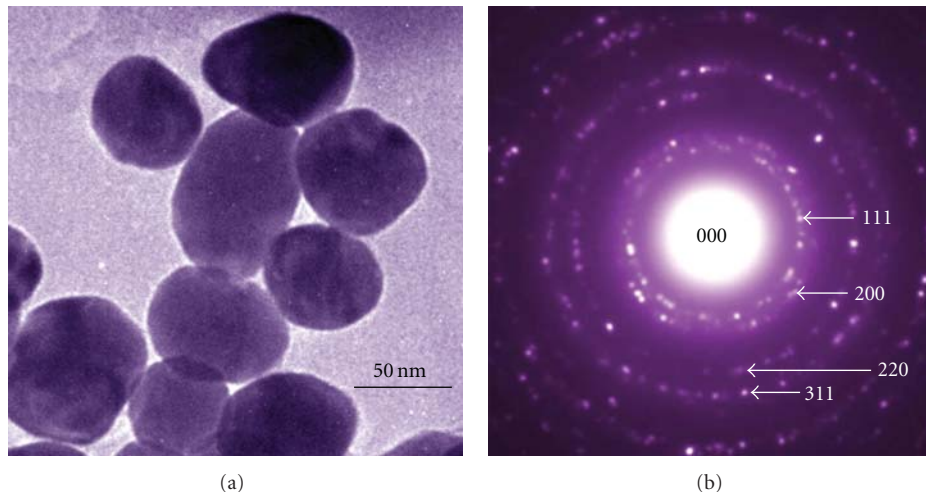


FIGURE 2: (a) TEM image and (b) electron diffraction pattern of AuNPs.

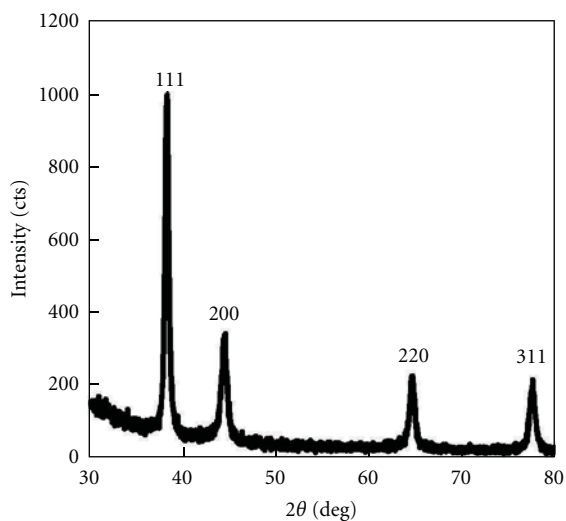


FIGURE 3: X-ray diffraction pattern of AuNPs.

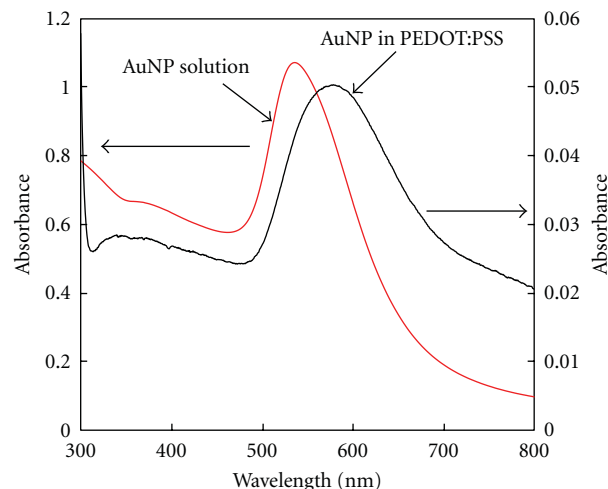


FIGURE 4: Absorption spectra of AuNP solution and AuNP in PEDOT:PSS.

heterojunction structure with AuNPs provided short-circuit current ( $J_{sc}$ ) of  $0.44 \text{ mA cm}^{-2}$ , open-circuit voltage ( $V_{oc}$ ) of 0.55 V, fill factor (FF) of 0.28, and power conversion efficiency ( $\eta$ ) of 0.068%, respectively.

Figure 7 shows the incident photon to current conversion efficiency (IPCE) spectra of SubPc/ $C_{60}$  photovoltaic cells with or without AuNP. The photovoltaic cells with AuNPs demonstrated the high IPCE spectrum in the range of 500–600 nm, which corresponded well with the absorption peak of AuNPs as observed in Figure 4.

Electronic structures, HOMOs, LUMOs, and energy gaps of CuNc and SubPc are shown in Figure 8. HOMO and LUMO of CuNc were calculated to be  $-3.13 \text{ eV}$  and  $-5.01 \text{ eV}$ , respectively, on the basis of molecular orbital calculation. HOMO and LUMO of SubPc were calculated to be  $-3.02 \text{ eV}$  and  $-5.74 \text{ eV}$ , respectively.

An energy level diagram of the present photovoltaic cells is summarized as shown in Figure 9. Previously reported values were also used for the energy levels [20–22]. The carrier transport mechanism is considered as follows. When light is incident from the ITO substrate, light-absorption excitation occurs at the Pcs/ $C_{60}$  interface and electrons and holes are produced by charge separation. Then, the electrons transport through  $C_{60}$  toward the Al electrode, and the holes transport through PEDOT:PSS to the ITO substrate. Since it has been reported that  $V_{oc}$  is nearly proportional to the difference between HOMO of electronic donor (Pcs) and LUMO of electronic acceptor ( $C_{60}$ ) [23], the difference of  $V_{oc}$  would be considered to be the combination of Pcs and  $C_{60}$ .

In the present work, organic photovoltaic cells with AuNPs based on phthalocyanines and  $C_{60}$  were fabricated and characterized. Performance of the present photovoltaic

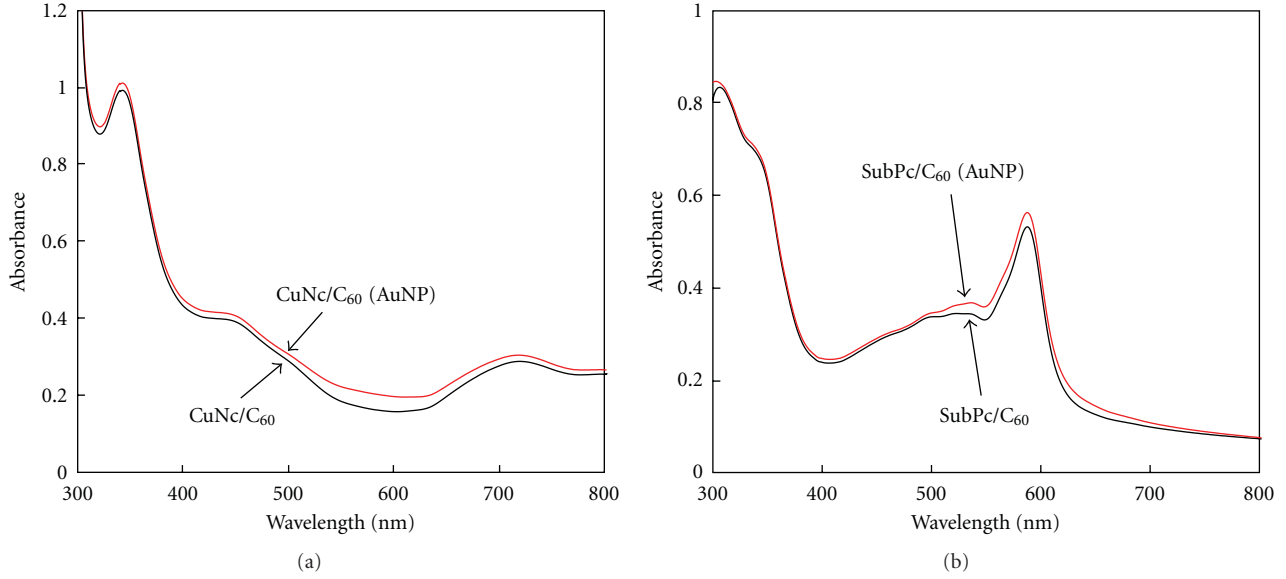


FIGURE 5: Absorption spectra of (a) CuNc/C<sub>60</sub> and (b) SubPc/C<sub>60</sub> films.

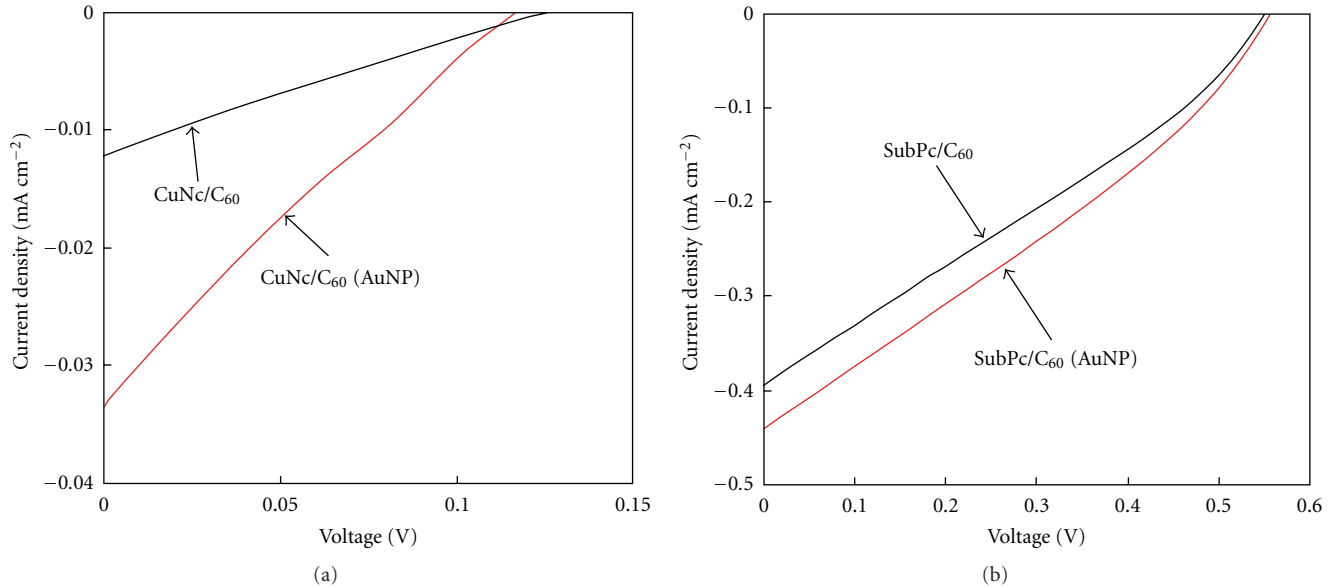


FIGURE 6: Measured  $J$ - $V$  characteristic of (a) CuNc/C<sub>60</sub> and (b) SubPc/C<sub>60</sub> photovoltaic cells with or without AuNP.

TABLE 1: Experimental parameters of the present photovoltaic cells.

Sample	$J_{sc}/\text{mA cm}^{-2}$	$V_{oc}/\text{V}$	FF	$\eta/\%$
CuNc	0.012	0.13	0.25	$3.7 \times 10^{-4}$
CuNc (AuNP)	0.034	0.12	0.24	$9.8 \times 10^{-4}$
SubPc	0.39	0.55	0.27	0.058
SubPc (AuNP)	0.44	0.55	0.28	0.068

cells would be dependent on grain sizes of AuNPs and film thickness of PEDOT:PSS, and control of the grain sizes and film thickness should be investigated further.

## 4. Conclusions

Organic photovoltaic cells were fabricated by using C<sub>60</sub> as n-type semiconductor, and CuNc and SubPc as p-type semiconductors, respectively.  $J$ - $V$  characteristics were investigated under illumination to confirm the photovoltaic cell performance. CuNc/C<sub>60</sub> heterojunction structure with AuNPs provided photoabsorption in the range of 500 to 700 nm and provided  $\eta$  of  $9.8 \times 10^{-4}\%$ , FF of 0.24,  $J_{sc}$  of  $0.034 \text{ mA cm}^{-2}$ , and  $V_{oc}$  of 0.12 V. The device was based on the SubPc/C<sub>60</sub> heterojunction structure with AuNPs provided  $\eta$  of 0.068%, FF of 0.28,  $J_{sc}$  of  $0.44 \text{ mA cm}^{-2}$ , and  $V_{oc}$  of 0.55 V. Nanostructures of AuNPs were investigated

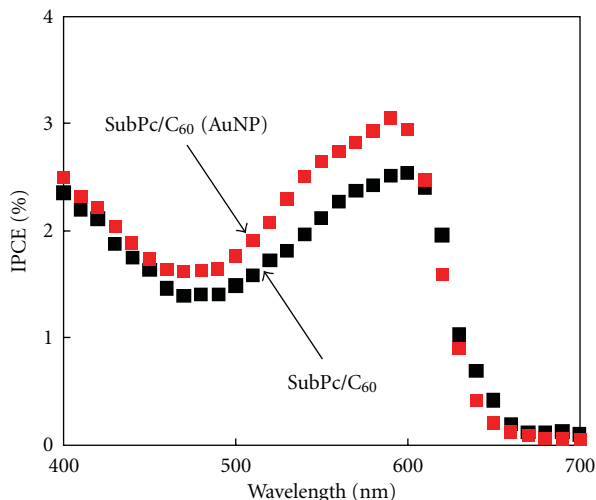


FIGURE 7: IPCE of SubPc/C<sub>60</sub> photovoltaic cells with or without AuNP.

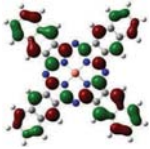
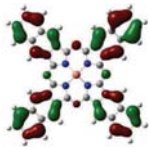
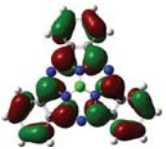
	CuNc	SubPc
Electronic structure (LUMO)		
LUMO	-3.13 eV	-3.02 eV
Electronic structure (HOMO)		
HOMO	-5.01 eV	-5.74 eV
Energy gap	1.88 eV	2.72 eV

FIGURE 8: Calculated electronic structures, HOMOs, LUMOs, and energy gaps of CuNc and SubPc.

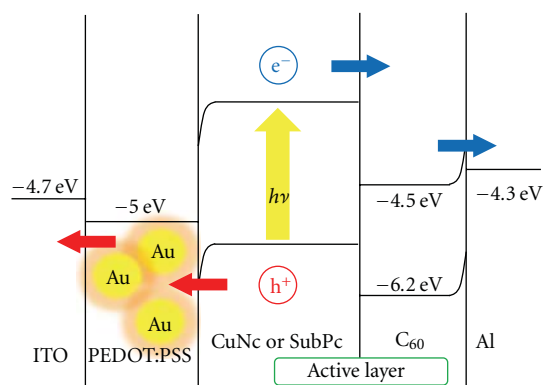


FIGURE 9: Energy level diagram of the present photovoltaic cells.

by TEM and X-ray diffraction, and the grain sizes of the AuNPs were determined to be 40~60 nm. Energy levels of the molecules were calculated by molecular orbital calculations.

## References

- [1] M. Moskovits, "Surface-enhanced spectroscopy," *Reviews of Modern Physics*, vol. 57, no. 3, pp. 783–826, 1985.
- [2] K. Kneipp, Y. Wang, H. Kneipp et al., "Single molecule detection using surface-enhanced Raman scattering (SERS)," *Physical Review Letters*, vol. 78, no. 9, pp. 1667–1670, 1997.
- [3] S. Nie and S. R. Emory, "Probing single molecules and single nanoparticles by surface-enhanced Raman scattering," *Science*, vol. 275, no. 5303, pp. 1102–1106, 1997.
- [4] D. M. Schaadt, B. Feng, and E. T. Yu, "Enhanced semiconductor optical absorption via surface plasmon excitation in metal nanoparticles," *Applied Physics Letters*, vol. 86, no. 6, Article ID 063106, 3 pages, 2005.
- [5] W. L. Barnes, A. Dereux, and T. W. Ebbesen, "Surface plasmon subwavelength optics," *Nature*, vol. 424, no. 6950, pp. 824–830, 2003.
- [6] J. J. Mock, M. Barbic, D. R. Smith, D. A. Schultz, and S. Schultz, "Shape effects in plasmon resonance of individual colloidal silver nanoparticles," *Journal of Chemical Physics*, vol. 116, no. 15, pp. 6755–6759, 2002.
- [7] P. Royer, J. P. Goudonnet, R. J. Warmack, and T. L. Ferrell, "Substrate effects on surface-plasmon spectra in metal-island films," *Physical Review B*, vol. 35, no. 8, pp. 3753–3759, 1987.
- [8] G. Xu, M. Tazawa, P. Jin, S. Nakao, and K. Yoshimura, "Wavelength tuning of surface plasmon resonance using dielectric layers on silver island films," *Applied Physics Letters*, vol. 82, no. 22, pp. 3811–3813, 2003.
- [9] F. I. Bohrer, A. Sharoni, C. Colesniuc et al., "Gas sensing mechanism in chemiresistive cobalt and metal-free phthalocyanine thin films," *Journal of the American Chemical Society*, vol. 129, no. 17, pp. 5640–5646, 2007.
- [10] H. S. Majumdar, A. Bandyopadhyay, and A. J. Pal, "Data-storage devices based on layer-by-layer self-assembled films of a phthalocyanine derivative," *Organic Electronics*, vol. 4, no. 1, pp. 39–44, 2003.
- [11] H. S. Soliman, A. M. A. El-Barry, N. M. Khosifan, and M. M. El Nahass, "Structural and electrical properties of thermally evaporated cobalt phthalocyanine (CoPc) thin films," *EPJ Applied Physics*, vol. 37, no. 1, pp. 1–9, 2007.
- [12] W. Ma, C. Yang, X. Gong, K. Lee, and A. J. Heeger, "Thermally stable, efficient polymer solar cells with nanoscale control of the interpenetrating network morphology," *Advanced Functional Materials*, vol. 15, no. 10, pp. 1617–1622, 2005.
- [13] M. Granström, K. Petritsch, A. C. Arias, A. Lux, M. R. Andersson, and R. H. Friend, "Laminated fabrication of polymeric photovoltaic diodes," *Nature*, vol. 395, no. 6699, pp. 257–260, 1998.
- [14] M. Glatthaar, M. Riede, N. Keegan et al., "Efficiency limiting factors of organic bulk heterojunction solar cells identified by electrical impedance spectroscopy," *Solar Energy Materials and Solar Cells*, vol. 91, no. 5, pp. 390–393, 2007.
- [15] X. Chen, C. Zhao, L. Rothberg, and M. K. Ng, "Plasmon enhancement of bulk heterojunction organic photovoltaic devices by electrode modification," *Applied Physics Letters*, vol. 93, no. 12, Article ID 123302, 3 pages, 2008.
- [16] F.-C. Chen, J.-L. Wu, C.-L. Lee, Y. Hong, C.-H. Kuo, and M. H. Huang, "Plasmonic-enhanced polymer photovoltaic

- devices incorporating solution-processable metal nanoparticles,” *Applied Physics Letters*, vol. 95, no. 1, Article ID 013305, 2009.
- [17] T. Akiyama, K. Aiba, K. Hoashi, M. Wang, K. Sugawa, and S. Yamada, “Enormous enhancement in photocurrent generation using electrochemically fabricated gold nanostructures,” *Chemical Communications*, vol. 46, no. 2, pp. 306–308, 2010.
- [18] W. J. Yoon, K. Y. Jung, J. Liu et al., “Plasmon-enhanced optical absorption and photocurrent in organic bulk heterojunction photovoltaic devices using self-assembled layer of silver nanoparticles,” *Solar Energy Materials and Solar Cells*, vol. 94, no. 2, pp. 128–132, 2010.
- [19] A. J. Morfa, K. L. Rowlen, T. H. Reilly III, M. J. Romero, and J. van de Lagemaat, “Plasmon-enhanced solar energy conversion in organic bulk heterojunction photovoltaics,” *Applied Physics Letters*, vol. 92, no. 1, Article ID 013504, 3 pages, 2008.
- [20] T. Oku, A. Takeda, A. Nagata, T. Noma, A. Suzuki, and K. Kikuchi, “Fabrication and characterization of fullerene-based bulk heterojunction solar cells with porphyrin,  $\text{CuInS}_2$ , diamond and exciton-diffusion blocking layer,” *Energies*, vol. 3, no. 4, pp. 671–685, 2010.
- [21] T. Oku, T. Noma, A. Suzuki, K. Kikuchi, and S. Kikuchi, “Fabrication and characterization of fullerene/porphyrin bulk heterojunction solar cells,” *Journal of Physics and Chemistry of Solids*, vol. 71, no. 4, pp. 551–555, 2010.
- [22] A. Nagata, T. Oku, K. Kikuchi, A. Suzuki, Y. Yamasaki, and E. Osawa, “Fabrication, nanostructures and electronic properties of nanodiamond-based solar cells,” *Progress in Natural Science*, vol. 20, pp. 38–43, 2010.
- [23] M. A. Green, K. Emery, D. L. King, Y. Hishikawa, and W. Warta, “Solar cell efficiency tables (version 28),” *Progress in Photovoltaics: Research and Applications*, vol. 14, no. 5, pp. 455–461, 2006.

## Research Article

# Photocatalytic Properties of Tin Oxide and Antimony-Doped Tin Oxide Nanoparticles

J. C. M. Brokken-Zijp,<sup>1</sup> O. L. J. van Asselen,<sup>2</sup> W. E. Kleinjan,<sup>1</sup> R. van de Belt,<sup>3</sup> and G. de With<sup>1</sup>

<sup>1</sup>Laboratory of Materials and Interface Chemistry, Eindhoven University of Technology, P.O. Box 513, 5600 MB Eindhoven, The Netherlands

<sup>2</sup>Laboratory of Polymer Technology, Eindhoven University of Technology, P.O. Box 513, 5600 MB Eindhoven, The Netherlands

<sup>3</sup>Research and Development Kriya Materials Group, Kriya Materials B. V., P.O. Box 18, 6160 MD Geleen, The Netherlands

Correspondence should be addressed to J. C. M. Brokken-Zijp, j.brokken@tue.nl

Received 8 March 2011; Accepted 12 April 2011

Academic Editor: Huisheng Peng

Copyright © 2011 J. C. M. Brokken-Zijp et al. This is an open access article distributed under the Creative Commons Attribution License, which permits unrestricted use, distribution, and reproduction in any medium, provided the original work is properly cited.

For the first time it is shown that N-doped SnO<sub>2</sub> nanoparticles photocatalyze directly the polymerization of the C=C bonds of (meth)acrylates under visible light illumination. These radical polymerizations also occur when these particles are doped with Sb and when the surfaces of these particles are grafted with methacrylate (MPS) groups. During irradiation with visible or UV light the position and/or intensity of the plasmon band absorption of these nanoparticles are always changed, suggesting that the polymerization starts by the transfer of an electron from the conduction band of the particle to the (meth)acrylate C=C bond. By using illumination wavelengths with a very narrow band width we determined the influence of the incident wavelength of light, the Sb- and N-doping, and the methacrylate (MPS) surface grafting on the quantum efficiencies for the initiating radical formation ( $\Phi$ ) and on the polymer and particle network formation. The results are explained by describing the effects of Sb-doping, N-doping, and/or methacrylate surface grafting on the band gaps, energy level distributions, and surface group reactivities of these nanoparticles. N-doped (MPS grafted) SnO<sub>2</sub> (Sb  $\geq$  0%) nanoparticles are new attractive photocatalysts under visible as well as UV illumination.

## 1. Introduction

The photochemistry of semiconductor nanoparticles and nanoparticulate materials is a fast growing area, both in terms of research and commercial activity [1]. These materials are used, for instance, in the treatment of pollutants, for photosterilisation, for photo-induced superhydrophilicity in solar energy to electrical power conversion and photochemical water splitting systems. Also semiconductive nanoparticles/nanostructures can act as a photocatalyst in (meth)acrylate polymerization [2–4]. Most of these applications require a large conversion efficiency under visible (solar) light illumination, but for many of these materials this efficiency is absent, because they absorb only a small fraction of the UV part of the solar spectrum. To enhance the absorption of radiation at higher wavelengths, the influence of doping of these materials is being studied, and considerable

improvements in, for instance, the photocatalytic activity of TiO<sub>2</sub> for visible light have been reported when these materials were doped with metal ions or nitrogen [1, 5–10]. Also the incorporation of narrow-band-gap semiconductors or the formation of heterostructures using wide-band-gap semiconductors, such as ZnO<sub>2</sub>-SnO<sub>2</sub>, are promising [11]. However, there is still a strong need for new nanomaterials with a large photocatalytic conversion efficiency for visible (solar) light.

Recently, we showed that SnO<sub>2</sub> and Sb-doped SnO<sub>2</sub> nanoparticles without the presence of any other photoinitiator can act as photocatalysts for the radical polymerization of (meth)acrylate C=C double bonds during illumination with radiation of  $315 \pm 5$  nm [12]. The attractiveness of SnO<sub>2</sub> and Sb-doped SnO<sub>2</sub> materials for these and other photocatalytic applications would be enlarged when they could also act as photocatalysts for UV/vis radiation well above 340 nm, that

is, using light quanta of which the energy is too small to bridge the band gap of these particles.

Below we report the results of a study on the photocatalytic properties of highly crystalline Sb-doped and/or N-doped SnO<sub>2</sub> nanoparticles using radiation of 365, 408, 545, or 650 nm. This study shows that without the presence of any other photoinitiator these nanoparticles act as photocatalysts for the radical polymerization of C=C bonds of (meth)acrylates even when radiation of 650 nm is used. It will be shown also that the rate of this polymerization and the quantum yield for the formation of the initiating radical depend on the wavelengths of irradiation used, the amount of surface grafting of the nanoparticles with methacrylate groups, and the level of Sb-doping of these particles. The results found will be related to the bulk and surface compositions and properties of these nanoparticles.

Further on we will, for convenience, refer to SnO<sub>2</sub> and Sb-doped SnO<sub>2</sub> nanoparticles as Sn:SbO<sub>2</sub> (0 ≤ Sb ≤ 13%) nanoparticles although sometimes this abbreviation is used only for Sb-doped SnO<sub>2</sub> particles.

## 2. Experimental

**2.1. Chemicals and Materials Used.** Polyethyleneglycol diacrylate monomer (PEGDA,  $M_w = 575$  g/mol) was purchased from Aldrich, 3-methacryloxypropyltrimethoxysilane (MPS) from ABCR, and methanol (>99.8%) from Merck (Scheme 1). Aqueous dispersions of Sb:SnO<sub>2</sub> nanoparticles (≈10 wt%) with different Sb-doping levels from Sb/(Sb + Sn) = 0 to 13.0 at.% (after this described as % Sb) were obtained from Kriya Materials B.V. (Geleen, The Netherlands). The most important data for these spherical particles are shown in Table 1 and Figure 9 [13].

The surface of these Sb:SnO<sub>2</sub> nanoparticles was, in general, modified before use by grafting them with variable amounts of the silane coupling agent 3-methacryloxypropyl trimethoxysilane (MPS) (Schemes 2 and 3) [2, 12, 14]. Sb-doping, N-doping, and NH<sub>3</sub> surface groups hardly influenced the amount of grafted MPS and MPS oligomers formed [12, 13].

**2.2. Preparation of the Starting Dispersions and Formulations.** The MPS-Sb:SnO<sub>2</sub>/PEGDA 575 starting mixtures were prepared from the corresponding dispersions of the (MPS-grafted) Sb:SnO<sub>2</sub> nanoparticles by mixing them with PEGDA 575 and methanol. In both dispersions the nanoparticles were only well dispersed, when the surfaces of these particles were grafted with MPS [12, 13]. The Sb:SnO<sub>2</sub> particle content was always 10 vol. %, based on the total amount of PEGDA, Sb:SnO<sub>2</sub>, and MPS present. The MPS/Sb:SnO<sub>2</sub> weight ratio of the mixtures after grafting is different from the initial ratio used in the grafting reaction. For convenience, we use in this paper often the MPS/Sb:SnO<sub>2</sub> weight ratio before grafting, but the 10 vol.% particle concentration in the starting dispersion/formulation is based on the corrected MPS/Sb:SnO<sub>2</sub> weight ratio after grafting [12].

**2.3. Measurement of the Polymerization Rate.** Real-time FT-IR measurements were performed using a Biorad Excalibur FT-IR spectrometer, equipped with an MCT detector. The spectra were recorded between 650 and 4000 cm<sup>-1</sup> using different time intervals between 0.3–30 s and the kinetic mode of the WinIR-pro software package. An Oriel Spectral Luminator connected to a light guide was used for the illumination of the formulations with wavelengths of 315, 365, 410, 545, or 650 ± 5 nm. The corresponding incident light intensities used are shown in Table 2.

Grafted MPS, MPS oligomer, and PEGDA 575 contain (meth)acrylate C=C bonds. Before the measurements started the (MPS)-Sb:SnO<sub>2</sub>/PEGDA 575 dispersion was placed on the diamond crystal of the Golden Gate ATR accessory of our IR apparatus and the solvents were evaporated under a dry N<sub>2</sub> flow [12]. After solvent evaporation the layer thickness was adjusted to about 1 μm. The electronic shutter of the lamp was opened at  $t = 0$ , and the initial and maximum rates of polymerization of the (meth)acrylate C=C bonds ( $R_{\text{ini}}^{\lambda}$ ,  $R_{\text{max}}^{\lambda}$ ) were determined by measuring the initial, respectively, maximum changes in the absorption of the peaks at 1408, 1620, and 1637 cm<sup>-1</sup> over a certain time period (C=C bond absorptions of grafted MPS, MPS oligomer, and/or PEGDA 575). For the determination of the maximum slope of a specific starting formulation at least five different data points were measured. During the whole measurement the shutter of the lamp was left open and the dry nitrogen flow was kept on. The results obtained at 1408 and 1620 cm<sup>-1</sup> appeared to be very similar. Hence, only the results measured at 1620 and 1637 cm<sup>-1</sup> are shown below.

The measured decreases in absorptions of the C=C bonds over time during irradiation were plotted either as an absolute decrease in concentration over time ( $R_{\text{ini}}^{\lambda}$ ,  $R_{\text{max}}^{\lambda}$ ; (1a), (1c)) or as a relative decrease in concentration over time ( $R_{\text{ini}}^{\lambda m}$ ,  $R_{\text{max}}^{\lambda m}$ ; (1b), (1d)). Equations (1b), (1d) were used when reaction rates were compared of starting formulations, which contained different amounts of MPS C=C bonds. The concentrations of the C=C double bonds [mol m<sup>-3</sup>] at time  $t$  and time  $t = 0$  are, respectively,  $(c_{\text{C=C}})_t$  and  $(c_{\text{C=C}})_{t=0}$ . The standard deviation,  $\sqrt{(\sum (x-x_{\text{av}})^2)/(n-1)}$ , of  $R$  was taken as error margin:

$$R_{\text{ini}}^{\lambda} = \{c_{(\text{C=C})t=0} - c_{(\text{C=C})t}\} t^{-1}, \quad (1a)$$

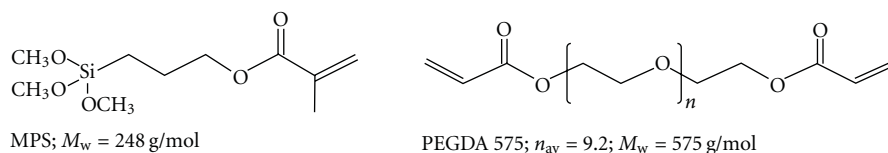
$$R_{\text{ini}}^{\lambda m} = \{c_{(\text{C=C})t=0} - c_{(\text{C=C})t}\} \{c_{(\text{C=C})t=0}\}^{-1} t^{-1}, \quad (1b)$$

$$R_{\text{max}}^{\lambda} = \{c_{(\text{C=C})t1} - c_{(\text{C=C})t2}\} \{t_2 - t_1\}^{-1}, \quad (1c)$$

$$R_{\text{max}}^{\lambda m} = \{c_{(\text{C=C})t1} - c_{(\text{C=C})t2}\} \{c_{(\text{C=C})t=0}\}^{-1} \{t_2 - t_1\}^{-1}. \quad (1d)$$

Each experiment was repeated at least three times. In general, an S-shaped plot was found when the change in C=C bond concentration was plotted against  $t$  and always the  $R_{\text{ini}}^{\lambda}$  (mol m<sup>-3</sup> s<sup>-1</sup>) <  $R_{\text{max}}^{\lambda}$  (mol m<sup>-3</sup> s<sup>-1</sup>) and the  $R_{\text{ini}}^{\lambda m}$  (s<sup>-1</sup>) <  $R_{\text{max}}^{\lambda m}$  (s<sup>-1</sup>). When no S-shaped plot was found the value for  $R_{\text{ini}}^{\lambda}$ ,  $R_{\text{ini}}^{\lambda m}$  was always the largest  $R$  value.

When these experiments were performed in the presence of air, O<sub>2</sub> became a radical scavenger and the C=C polymerization rate slowed down during irradiation.



SCHEME 1: Molecular formula of 3-metacryloxypropyltrimethoxysilane (MPS) and polyethyleneglycol diacrylate (PEGDA 575).

TABLE 1: Properties of the Sb : SnO<sub>2</sub> particles used [13].

Sb/(Sn + Sb) mol % <sup>(a)</sup>	Sb(III)/[Sb(III)+Sb(V)] mol %	$d$ /nm BET <sup>(c)</sup>	$d$ /nm XRD <sup>(d)</sup>	N <sup>(b)</sup> bulk wt. %	N <sup>(b)</sup> surface wt. %	$a$ unit cell Å	$c$ unit cell Å
0	0	8.2	7.3	0.088	0.046	4.7416	3.1808
2.0	0	7.9	6.9	0.068	0.136	4.7432	3.1790
7.0	0 <sup>(e)</sup>	7.1	6.5	0.094	0.188	4.7509	3.1786
13.0	7.6	6.6	6.9 <sup>(f)</sup>	0.200	0.202	4.7435	3.1737

(a) Apart from Sb 0% all the Sb : SnO<sub>2</sub> particles are blue powders.

(b) Present in the bulk and at the surface; at the surface as NH<sub>3</sub> groups.

(c) The diameter is calculated assuming that the particles were spherical, non-porous with a density of 6.99 g/cm<sup>3</sup>.

(d) The particles are (almost) crystalline. The crystallite sizes were calculated from the broadening of the XRD peaks.

(e) No Sb(III) was detected with XPS; IR data suggest that a very small amount of Sb(III)-OH surface groups is present.

(f) Measured with TEM:  $d = 6.3 \pm 1.1$  nm.

TABLE 2: Incident light intensities  $I_0$  at different wavelengths.<sup>a</sup>

$\lambda$ [nm]	315 ± 5	365 ± 5	410 ± 5	545 ± 5	650 ± 5
$I_0$ [mW cm <sup>-2</sup> ]	0.5	1.0	1.0	1.1	0.12

<sup>a</sup> Determined with an Oriel 70260 Radiant Power Meter.

**2.4. Measurement of the Light Absorption Spectra of the Sb : SnO<sub>2</sub> Dispersions and XPS Measurements.** The light absorption spectra of aqueous Sb : SnO<sub>2</sub> nanoparticle dispersions, in which the Sb : SnO<sub>2</sub> particles were well dispersed, [15] were recorded with a Shimadzu UV 3102 PC Scanning Spectrophotometer, using a rectangular quartz cuvette with a diameter of 1 cm. X-ray photoelectron spectroscopy spectra (XPS) were measured as described before [13].

### 3. Results and Discussion

**3.1. Influence of the Wavelength of the Incident Radiation on the Photocatalyzed C=C Polymerization.** In an earlier paper the radical polymerization of PEGDA 575 under the influence of 315 ± 5 nm irradiation photocatalyzed by MPS-Sb : SnO<sub>2</sub> (Sb ≥ 0) nanoparticles was described [12] and the observed photocatalysis was explained as follows: by absorption of light quanta of 315 nm the electrons in the valence band of the Sb : SnO<sub>2</sub> nanoparticles are excited directly into the conduction band. The activated electron in the conduction band and the hole in the valence band react in the presence of a C=C bond and a hydrogen donor under formation of a (meth)acryl radical (YH·). This radical initiates the polymerization of the (meth)acryl C=C groups (Scheme 4).

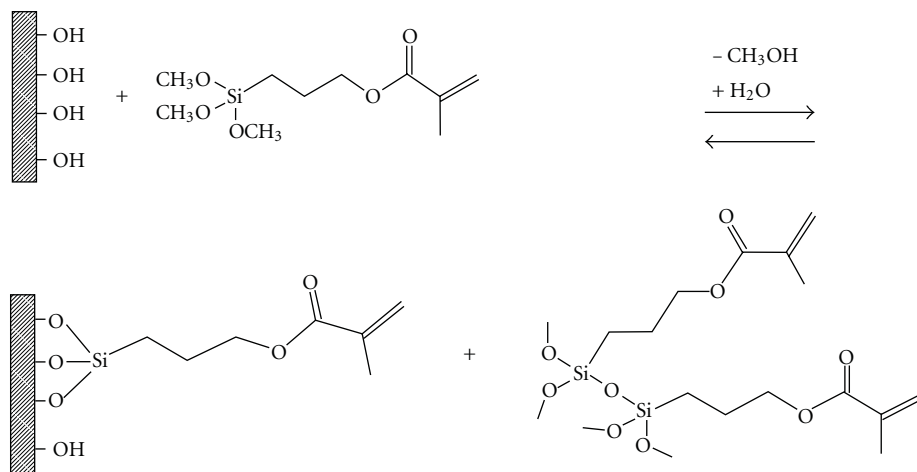
Sb : SnO<sub>2</sub> (Sb = 0%) particles/films have a band gap of 3.6 eV–3.8 eV, which corresponds with light quanta of

320–340 nm [16, 17]. Hence, when MPS-Sb : SnO<sub>2</sub> (Sb = 0%)/PEGDA 575 formulations *without any other photocatalytic molecule/particle* are irradiated with light with wavelengths well above 340 nm a direct excitation of the electron from the valence band into the conduction band can no longer occur [8, 17]. Still very similar changes in the IR spectra of the formulations are observed during irradiation with 365, 408, 545, or 650 ± 5 nm to those when these formulations were irradiated with 315 nm (Figure 1(a)). These changes are also found when the nanoparticles are doped with Sb (Figure 1) [12, 18].

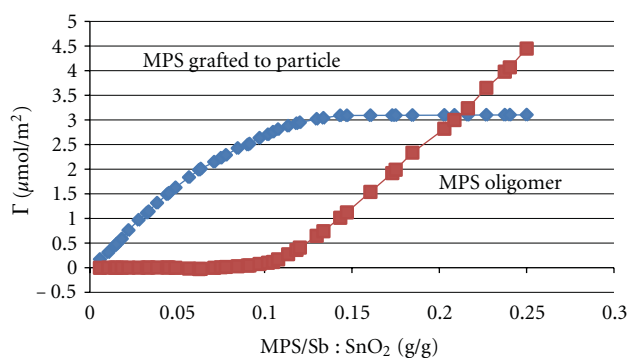
Using the same starting formulations, but without Sb : SnO<sub>2</sub> particles or any other photoinitiator, a change in the IR spectra during irradiation with light ≥ 365 nm is no longer observed. Hence, MPS-Sb : SnO<sub>2</sub> nanoparticles (Sb ≥ 0%) photocatalyze the radical polymerization of the (meth)acrylate C=C bonds according to the mechanism proposed in Scheme 4 even when the energy of the light quanta is (far) too small to transfer an electron from the valence band into the conduction band of these nanoparticles.

During irradiation the C=C bonds in the IR spectra at 1637, 1620, 1408, 986, 814, and 810 cm<sup>-1</sup> disappear [12]. At 1637 cm<sup>-1</sup> the methacrylate MPS C=C and the acrylate C=C bonds absorb IR radiation, whereas at 1620 and 1408 cm<sup>-1</sup> only the acrylate C=C bonds absorb [18]. Hence, the methacrylate as well as the acrylate C=C bonds polymerize during irradiation (see also later on).

The energy of the light quanta of wavelengths ≥ 365 nm is (far) too small to transfer an electron from the valence band directly into the conduction band. Hence, energy levels in the band gap of the Sb : SnO<sub>2</sub> nanoparticles are likely to be involved in the initiation of the radical polymerization. Our Sb : SnO<sub>2</sub> particles (Sb = 0%) are always doped with N and these particles, contrary to what was reported before for



SCHEME 2: Schematic presentation of grafting of 3-metacryloxypropyltrimethoxysilane (MPS) to OH-groups of the Sb : SnO<sub>2</sub> particle surface and formation of MPS oligomers.



SCHEME 3: Amount of MPS grafted on the surface of the Sb : SnO<sub>2</sub> nanoparticles surface and amount of MPS oligomer formed as a function of initial MPS/Sb : SnO<sub>2</sub> ratios used in the grafting reaction [12].

non-doped SnO<sub>2</sub>, absorb visible light (Table 1, Figure 2) [12, 13]. This suggests that these levels in the band gap are formed by N-doping. This is confirmed by a recent publication that shows that N-doped SnO<sub>2</sub> films can photocatalyze the oxidation of methylene blue under visible light illumination [19, 20].

During illumination of the MPS-Sb : SnO<sub>2</sub> (Sb = 0%) / PEGDA 575 mixture with 315, 365, 408, 545, or 650 nm, always an increase in absorption and shift in intensity of the plasmon band of the particles are observed in the IR spectra (Figure 3). The plasmon band absorption is due to the reflection of the electric field of the incident IR light by the combined oscillations of the electrons in the conduction band of the Sb : SnO<sub>2</sub> particles [21–23]. These observed changes show that electrons are also transferred into the conduction band of our particles during irradiation with light of wavelengths  $\geq 365$  nm [24]. Hence, the occurrence of these photocatalyzed polymerizations may be explained by band gap narrowing through N-doping and/or by the involvement of N-related energy levels of these nanoparticles

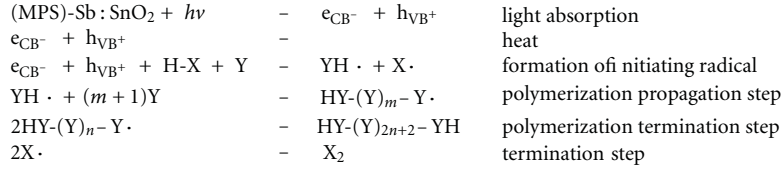
in the transfer of an electron into the conduction band (see also later on).

The (MPS)-Sb : SnO<sub>2</sub> particles (Sb >0%) are also doped with N, and these particles also absorb visible light (Table 1, Figure 2) [12, 13]. Similar changes in the plasmon absorption band of their PEGDA formulations are found during irradiation with 315, 365, 408, 545, or 650 nm in the IR spectra of their PEGDA formulations (Figure 3) [21–23]. Hence, the same conclusions can be drawn. During irradiation electrons are transferred into the conduction band and an activated electron initiates the C=C bond polymerization (Scheme 4). That these reactions occur even when the energy of the light quanta is well below 3.4 eV may be explained by band gap narrowing through N-doping and/or by the involvement of N-related energy levels of these nanoparticles in the transfer of an electron into the conduction band.

Especially at high Sb-doping levels the plasmon band may absorb also radiation at wavelengths <1200 nm. Hence, a small part of the measured absorptions at 545 and 650 nm in Figure 2 may be actually contributed to this plasmon band. Lack of information in the literature and limitations of our equipment made it impossible to determine the contribution of the plasmon band to the absorption below 1200 nm, and therefore we neglect this aspect in the discussion below.

### 3.2. Quantum Yields at Different Wavelengths of Irradiation.

It is well known that the rate of a reaction which is photocatalyzed by a semiconductive inorganic particle/layer depends on the surface area and crystallinity of these activators [5]. Hence, in this work well-characterized Sb : SnO<sub>2</sub> nanoparticles of varying composition, but with similar nanoparticle sizes and crystallinities, are used (Table 1). To be certain that these particles are well dispersed before and during irradiation in the acrylate monomer their surfaces were grafted in advance with MPS [13, 14, 25]. PEGDA 575 was chosen as acrylate monomer to minimize the influence of viscosity variations on the rate of the acrylate polymerization during irradiation.



SCHEME 4: The photocatalytic radical polymerization of (meth)acrylate C=C bonds initiated by the Sb : SnO<sub>2</sub> particles. (MPS)-Sb : SnO<sub>2</sub> means the Sb : SnO<sub>2</sub> particles grafted or not grafted with MPS; Y is PEGDA 575 monomer, grafted MPS, and/or MPS oligomer (Scheme 2). H-X is a hydrogen donor.

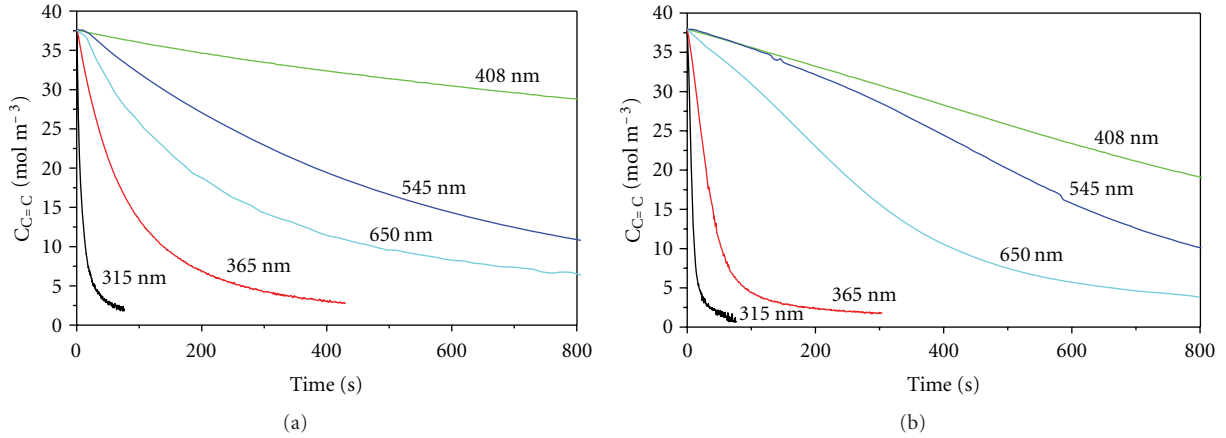


FIGURE 1: The decreases in the C=C bond concentration over time (at 1637 cm<sup>-1</sup>) during irradiation of MPS-Sb : SnO<sub>2</sub>/PEGDA formulations using incident light of 315, 365, 408, 545, or 650 ± 5 nm. MPS/Sb : SnO<sub>2</sub> = 0.19 g/g; *c*<sub>particle</sub> = 10 vol%. (a) Sb = 0%; (b) Sb = 7%.

To determine the rates of the photocatalyzed polymerizations of the (meth)acrylate C=C bonds during irradiation with 315, 365, 408, 545, or 650 ± 5 nm we used real-time FT-IR spectroscopy (Figure 1). For MPS-Sb : SnO<sub>2</sub> (Sb ≥ 2%) nanoparticle/PEGDA mixtures always an S-shape relation was found between the decrease in C=C bond concentration and irradiation time (Figure 1). Hence, for these particles the initial rate of polymerization  $R_{ini}^\lambda$  appears to be always lower than the maximum rate of polymerization  $R_{max}^\lambda$ , and therefore both were determined independently using (1a)–(4) (Scheme 4):

$$R_{ini}^\lambda = K_{ini}^\lambda \{c_{(c=c)}_{t=0} - c_{(c=c)}_t\} \times \left\{ I_0 \left( 1 - 10^{-\varepsilon \cdot c_{particle} \cdot d} \right) d^{-1} \right\}^{1/2}, \quad (2)$$

$$R_{max}^\lambda = K_{max}^\lambda \{c_{(c=c)}_{t1} - c_{(c=c)}_{t2}\} \times \left\{ I_0 \left( 1 - 10^{-\varepsilon \cdot c_{particle} \cdot d} \right) d^{-1} \right\}^{1/2}, \quad (3)$$

$$K_{ini/max}^\lambda = k_{p(ini/max)}^\lambda \left\{ \Phi \left( k_{t(ini/max)}^\lambda \right)^{-1} \right\}^{1/2}. \quad (4)$$

In these relations the  $(c_{c=c})_{t=0}$  [mol m<sup>-3</sup>] is the initial concentration of the C=C bonds just before the irradiation starts and the  $C_{(c=c)t}$  [mol m<sup>-3</sup>] is the C=C bond concentration

at time *t* [s]. The rate  $R_{ini/max}^\lambda$  [mol m<sup>-3</sup> s<sup>-3</sup>] is a function of the propagating ( $k_p$ ) and terminating polymerization rate constants  $k_t$  [m<sup>3</sup> mol<sup>-1</sup> s<sup>-1</sup>], the quantum yield for the formation of the initiating radical  $\Phi$  [mol J<sup>-1</sup>], the incident radiation intensity  $I_0$  [J m<sup>-2</sup> s<sup>-1</sup>], the  $\varepsilon$  of the absorbing Sb : SnO<sub>2</sub> particles at a certain wavelength, the Sb : SnO<sub>2</sub> particle concentration  $c_{particle}$  [mol m<sup>-3</sup>], the thickness of the irradiated film *d* [m], and the relative quantum efficiency at the initial stage of the reaction ( $K_{ini}^\lambda$ ; m<sup>3/2</sup> s<sup>-1/2</sup> J<sup>-1/2</sup>) or at the maximum rate of the reaction ( $K_{max}^\lambda$ ; m<sup>3/2</sup> s<sup>-1/2</sup> J<sup>-1/2</sup>). A similar approach was used for the determination of the polymerization rates of (meth)acrylate C=C bonds photocatalyzed by an organic photoinitiator or inorganic particle [2, 3, 12, 26–28].

Recently, we showed that the polymerizations of the (meth)acrylate C=C bonds photocatalyzed by MPS-Sb : SnO<sub>2</sub> (Sb ≥ 0%) nanoparticles using radiation of 315 nm can be explained by (1a)–(4). To test whether these equations also explain our results for illuminations with wavelengths of light above 340 nm, experiments with 365 nm were done with two different light intensities, one nine times lower than the other using for both the same starting MPS-Sb : SnO<sub>2</sub>/PEGDA dispersion. The ratio of these  $R_{max}^{1637}$  values appeared to be 3, in agreement with the proportionality of  $\sqrt{I_0}$  of (3).

From the decrease in the C=C bond absorptions at 1637 or 1620 cm<sup>-1</sup> over time, the initial and maximum relative quantum efficiencies *K* are calculated (for Sb = 7% initial and

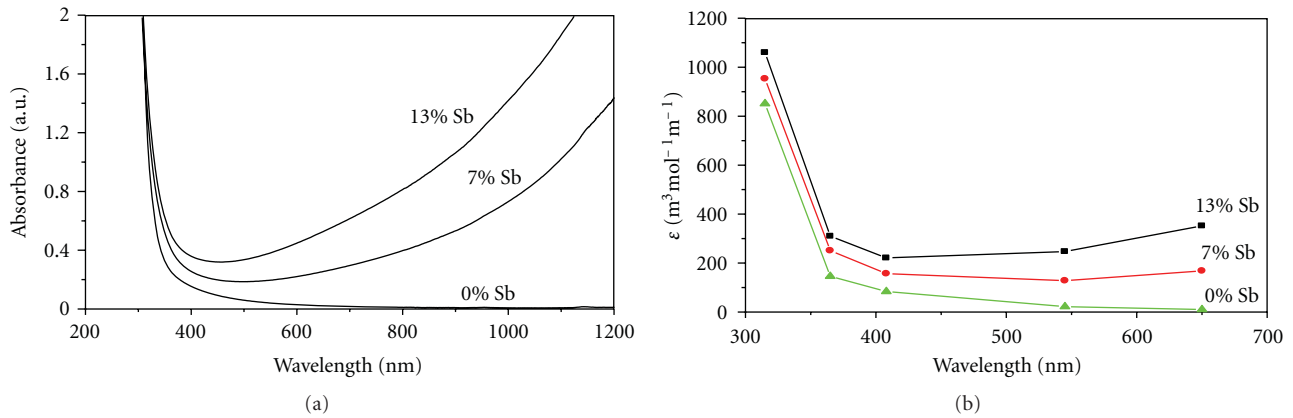


FIGURE 2: (a) UV/Vis absorbance spectra of Sb : SnO<sub>2</sub> nanoparticles in aqueous dispersion. The Sb : SnO<sub>2</sub> particle concentration is 0.23 wt%. (b) Molar extinction coefficients,  $\epsilon$ , of Sb : SnO<sub>2</sub> nanoparticles as a function of wavelength for different Sb-doping levels, determined from (a).

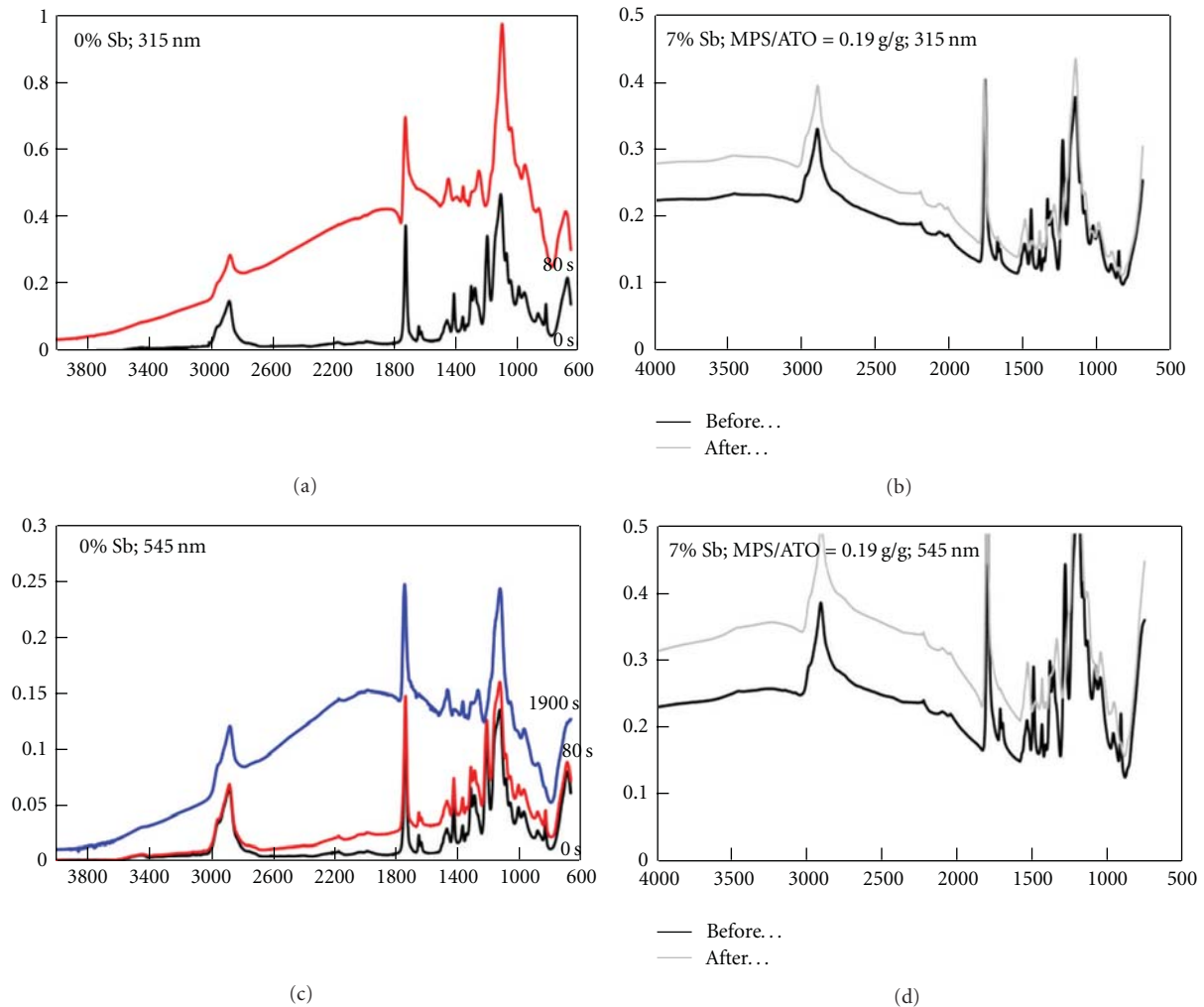


FIGURE 3: Infrared absorption spectra before and during irradiation of Sb : SnO<sub>2</sub> (Sb  $\geq$  0%) / PEGDA 575 formulations (Sb = 0% or Sb = 7%). MPS/Sb : SnO<sub>2</sub> = 0.19 g/g. Incident wavelength of radiation: 315 or 545 nm. The results obtained fusing incident radiation of 365, 408 or 650 nm are similar.

maximum; for Sb = 0% only initial) (Table 3). Because the incident radiation intensities used were sometimes different, the measured  $R$  and calculated  $K$  values were also corrected for these differences using (2) and (3) ( $R^*$ ,  $K^*$ ). Table 3 and Figure 4 show that the  $K^*$  values depend on the incident wavelength of light used. The C=C acrylate bonds of the monomer (PEGDA 575) absorb at 1637 and 1620  $\text{cm}^{-1}$  and methacrylate C=C bonds (grafted MPS and MPS oligomer) absorb at 1637  $\text{cm}^{-1}$  [18]. A comparison made between the rates measured at these wavenumbers will give more insight into the polymer networks formed.

First the discussion is focused on the MPS-Sb:SnO<sub>2</sub> nanoparticles doped with Sb 7% (Figure 4(b); Tables 3(a) and 3(b)). For these particles the measured  $R_{\text{max}}^{*1637}$  values for radiation of 365, 408, 545, and 650 nm are within the experimental error equal to the  $R_{\text{max}}^{*1620}$ . Hence, at this moment in time the propagation step of the C=C bond polymerization at time  $t = t_{\text{max}}$  can be described as the reaction between a polymer fragment with an acrylate end group radical and an acrylate monomer. This means that the differences found in the relative quantum yield  $K_{\text{max}}^{*1637}$  for the different incident light wavelengths in Table 3b are caused by a difference in the quantum yield  $\Phi_{\text{Sb-7\%}}$  for the formation of the initiating radical (4).

For the Sb = 7% particles the value of  $K_{\text{ini}}^{*1620}$  is always about 40% lower than the  $K_{\text{ini}}^{*1637}$  value (Tables 3(a), 3(b) and Figure 4b). These lower values were also reported earlier for similar formulations when radiation of 315 nm was used and can be explained by the large preference of a methacrylate radical end group to react with a methacrylate C=C double bond [12]. This phenomenon is well known for radical initiated polymerizations of mixtures of acrylate and methacrylate C=C bonds [12, 14, 29]. Hence, the C=C propagation step at the initial part of the polymerization reaction can be partly described as a reaction between a polymer fragment with a methacrylate radical end group and a methacrylate MPS C=C bond. Moreover, the ratios of  $K_{\text{ini}}^{*1637}$  and  $K_{\text{max}}^{*1637}$  and the ratios of  $K_{\text{ini}}^{*1637}$  and  $K_{\text{ini}}^{*1620}$  are similar for the different wavelengths of radiation used (Table 3). This confirms that the dependency of  $K_{\text{ini}}^*$  and  $K_{\text{max}}^*$  on the incident wavelength of radiation is mainly caused by the dependency of the quantum yield  $\Phi_{\text{Sb-7\%}}$  on this wavelength and that the lowering of  $K_{\text{ini}}^{*1637}$  and of  $K_{\text{ini}}^{*1620}$  with respect to  $K_{\text{max}}^{*1637}$  is caused by the preference of the methacrylate radical end group to react with a methacrylate double bond or, in other words, by a decrease in the contribution of  $k_p k_t^{-1/2}$  to  $K_{\text{ini}}^*$  (4).

For Sb:SnO<sub>2</sub> particles without Sb-doping no S-shape relation between the decrease in the C=C bond absorption and irradiation time is found and the rate at the initial stage of the reaction is the largest rate measured. For convenience we still call these rates initial.

As has been discussed before acrylate C=C bonds absorb at 1620 and 1637  $\text{cm}^{-1}$ , whereas methacrylate C=C bonds absorb only at 1637  $\text{cm}^{-1}$  [18]. The methacrylate C=C bond concentration is about 10% of the acrylate C=C bond concentration in the starting formulations of Table 3 [12]. Still for formulations containing particles without Sb-doping

the value of  $K_{\text{ini}}^{*1620}$  is about 45% lower than  $K_{\text{ini}}^{*1637}$  (Table 3(c), Figure 4(a)). Hence, for these formulations too, the propagation step at the initial part of the polymerization reaction is mainly a reaction between a polymer fragment with a methacrylate radical end group and a methacrylate C=C bond, and the differences in these two  $K^*$  values for each wavelength of irradiation can be explained by the differences in  $k_p k_t^{-1/2}$  for methacrylates versus acrylates C=C bonds.

Table 3(c) also shows that the  $K_{\text{ini}}^{*1637}/K_{\text{ini}}^{*1620}$  ratios for particles without Sb-doping are very similar and independent of the wavelength of irradiation used. This suggests that the large variations reported for  $K_{\text{ini}}^{*1637}$  in this table can be explained also by a strong dependency of  $\Phi_{\text{Sb-0\%}}$  on the incident radiation wavelength used. The  $K_{\text{ini}}^{*1637}$  values are always larger when particles without Sb-doping are used in respect to the  $K_{\text{ini}}^{*1637}$  values for particles with Sb-doping of 7%. This can be explained by a strong influence of Sb-doping on  $\Phi$  ( $\Phi_{\text{Sb-0\%}} > \Phi_{\text{Sb-7\%}}$ ) (Figure 4).

When we compare the results of the particles with Sb = 0% and Sb = 7% it is important to realize that the surfaces of both particles are grafted with a monolayer MPS and the amount of MPS oligomer present in both dispersions is very similar (Scheme 3). Moreover, these particles have a similar crystallinity, they are well dispersed in the starting formulation, and their surface areas in contact with the liquid is similar too (Table 1). Hence, the differences in MPS grafting, MPS oligomer concentration, particle crystallinity, and surface areas between these particles are small and cannot explain that the  $K_{\text{ini}}^{*1637}$  and  $K_{\text{ini}}^{*1620}$  values are always larger for particles with Sb = 0% than for particles with Sb = 7% (Figure 4). These differences can be explained by a strong influence of Sb-doping on  $\Phi$  ( $\Phi_{\text{Sb-0\%}} > \Phi_{\text{Sb-7\%}}$ ) and suggest a more efficient formation of YH radicals (Scheme 1) for particles with Sb = 0%. We cannot directly measure for particle formulations with Sb = 0% the rates of the reactions between a polymer fragment with an acrylate end group and an acrylate C=C bond, but we can estimate the corresponding  $K_{\text{max}}^{*1637}$  values ( $K_{\text{max}}^{*1637}$ )<sub>corr</sub> using the corresponding  $k_p k_t^{-1/2}$  values of particles with Sb = 7% (Figure 4(a)). The ( $K_{\text{max}}^{*1637}$ )<sub>corr</sub> confirms that  $\Phi$  is also dependent on Sb-doping.

When the Sb:SnO<sub>2</sub> particles are not doped with Sb, deep impurity (donor) energy levels, which are efficient hole scavengers, are likely to be present in the crystals [30, 31]. The much higher  $\Phi_{\text{Sb-0\%}}$  than  $\Phi_{\text{Sb-7\%}}$  may be explained also by the presence of these energy levels (for more details see below).

### 3.2.1. Influence of MPS Grafting and MPS Oligomers.

Sb:SnO<sub>2</sub> nanoparticles can be kept well dispersed over a longer period of time in acrylate monomer dispersions when the surfaces of these particles are grafted with MPS before adding them to the PEGDA monomer. Without this surface modification the particles in the acrylate monomer agglomerate before, during, and after processing [2, 12, 15, 22] and this agglomeration becomes visible by the naked eye during irradiation in our experiments. This agglomeration influences the surface area of the particles in contact with the

TABLE 3: (a)  $R_{\max}^{1637}$ ,  $R_{\max}^{*1637}$ ,  $K_{\max}^{*1637}$ , and  $\Phi_{\lambda}/\Phi_{315}$  measured at  $1637 \text{ cm}^{-1}$  using different wavelengths of irradiation ( $\lambda$ ). Sb doping: 7%.<sup>a,b</sup> (b)  $R_{\text{ini}}^{*1637}$ ,  $K_{\text{ini}}^{*1637}$ ,  $K_{\text{ini}}^{*1637}/K_{\text{max}}^{*1637}$  and  $K_{\text{ini}}^{*1637}/K_{\text{ini}}^{*1620}$  measured at  $1637 \text{ cm}^{-1}$ , and  $1620 \text{ cm}^{-1}$  using different wavelengths of irradiation ( $\lambda$ ). Sb doping: 7%.<sup>a,b</sup> (c)  $R_{\text{ini}}^{*1637}$  and  $K_{\text{ini}}^{*1637}$  measured at  $1637 \text{ cm}^{-1}$  and  $1620 \text{ cm}^{-1}$  different wavelengths of irradiation ( $\lambda$ ). Sb doping: 0%.<sup>a,b</sup>

(a)

$\lambda$ [nm]	$R_{\max}^{1637}$ [mol m <sup>-3</sup> s <sup>-1</sup> ]	$R_{\max}^{*1637}$ [mol m <sup>-3</sup> s <sup>-1</sup> ]	$K_{\max}^{*1637}$ [m <sup>3/2</sup> s <sup>-1/2</sup> J <sup>-1/2</sup> ]	$\Phi_{\lambda}/\Phi_{315}$
315	3.0	4.2	$3 \times 10^{-4}$	1
365	0.65	0.65	$1 \times 10^{-4}$	0.4
408	0.025	0.025	$0.04 \times 10^{-4}$	0.01
545	0.035	0.033	$0.07 \times 10^{-4}$	0.02
650	0.081	0.23	$1 \times 10^{-4}$	0.3

<sup>a</sup> MPS/Sb : SnO<sub>2</sub> = 0.19 g/g;  $c_{\text{particle}} = 10 \text{ vol}\%$ .

<sup>b</sup>  $R_{\max}^{*1637}$  values are  $R_{\max}^{1637}$  values corrected for differences in  $I_0$ , and these  $R_{\max}^{*1637}$  values are within experimental error equal to  $R_{\max}^{1620}$ . The  $K_{\max}^{*1637}$  values were calculated from the  $R_{\max}^{*1637}$  values.

(b)

$\lambda$ [nm]	$R_{\text{ini}}^{*1637}$ [mol m <sup>-3</sup> s <sup>-1</sup> ]	$R_{\text{ini}}^{*1620}$ [mol m <sup>-3</sup> s <sup>-1</sup> ]	$K_{\text{ini}}^{*1637}$ [m <sup>3/2</sup> s <sup>-1/2</sup> J <sup>-1/2</sup> ]	$K_{\text{ini}}^{*1620}$ [m <sup>3/2</sup> s <sup>-1/2</sup> J <sup>-1/2</sup> ]	$K_{\text{ini}}^{*1637}/K_{\text{max}}^{*1637}$	$K_{\text{ini}}^{*1637}/K_{\text{ini}}^{*1620}$
315	2.58	1.50	$2.0 \times 10^{-4}$	$1.0 \times 10^{-4}$	0.5	1.5
365	0.47	0.39	$0.5 \times 10^{-4}$	$0.3 \times 10^{-4}$	0.6	1.5
408	0.023	0.015	$0.03 \times 10^{-4}$	$0.02 \times 10^{-4}$	0.7	1.5
545	0.023	0.015	$0.04 \times 10^{-4}$	$0.03 \times 10^{-4}$	0.6	1.3
650	0.180	0.132	$0.6 \times 10^{-4}$	$0.44 \times 10^{-4}$	0.6	1.4

<sup>a</sup> MPS/Sb : SnO<sub>2</sub> = 0.19 g/g;  $c_{\text{particle}} = 10 \text{ vol}\%$ .

<sup>b</sup> The  $K_{\max}^{*1637}$  values used are shown in Table 3(a). The  $K_{\text{ini}}^{*1637}$  corrected for differences in  $I_0$ . The values  $K_{\text{ini}}^{*1637}$  were calculated from the corresponding  $R_{\text{ini}}^{*1637}$  values.

(c)

$\lambda$ [nm]	$R_{\text{ini}}^{*1637}$ [mol m <sup>-3</sup> s <sup>-1</sup> ]	$R_{\text{ini}}^{*1620}$ [mol m <sup>-3</sup> s <sup>-1</sup> ]	$K_{\text{ini}}^{*1637}$ [mol m <sup>-3/2</sup> s <sup>-1/2</sup> J <sup>-1/2</sup> ]	$K_{\text{ini}}^{*1620}$ [mol m <sup>-3/2</sup> s <sup>-1/2</sup> J <sup>-1/2</sup> ]	$K_{\text{ini}}^{*1637}/K_{\text{ini}}^{*1620}$
315	6.4	3.5	$3.4 \times 10^{-4}$	$1.90 \times 10^{-4}$	1.8
365	0.39	0.21	$0.7 \times 10^{-4}$	$0.4 \times 10^{-4}$	1.9
408	0.016	0.0081	$0.04 \times 10^{-4}$	$0.02 \times 10^{-4}$	2.0
545	0.061	0.037	$0.26 \times 10^{-4}$	$0.16 \times 10^{-4}$	1.7
650	0.31	0.23	$6 \times 10^{-4}$	$4 \times 10^{-4}$	1.5

<sup>a</sup> MPS/Sb : SnO<sub>2</sub> = 0.19 g/g;  $c_{\text{particle}} = 10 \text{ vol}\%$ .

<sup>b</sup> The  $R_{\text{ini}}^{*1637}$  are  $R_{\text{ini}}$  values corrected for differences in  $I_0$ . The  $K_{\text{ini}}^{*1637}$  values and  $K_{\text{ini}}^{*1637}$  ratios were calculated from the corresponding  $R_{\text{ini}}^{*1637}$  values shown.

liquid monomer, and quantitatively reproducible data were not obtained by us for the C=C bond disappearance rates when Sb : SnO<sub>2</sub> particles without MPS grafting were used in our experiments. Therefore, in general, starting formulations containing MPS grafted Sb : SnO<sub>2</sub> particles were used.

The amount of methacrylate (MPS) moieties grafted on the surface of our Sb : SnO<sub>2</sub> particles surface and the amount of methacrylate (MPS) oligomer present in the starting formulation depend on the MPS/Sb : SnO<sub>2</sub> ratio used in the grafting reaction (Schemes 2 and 3) [2, 12, 22, 25]. It has been shown that these amounts are hardly influenced by the surface and bulk composition of our Sb : SnO<sub>2</sub> nanoparticles (Scheme 3). The results for starting mixtures containing Sb : SnO<sub>2</sub> (Sb = 7%) particles which were grafted in advance with variable MPS/Sb : SnO<sub>2</sub> ratios (MPS/Sb : SnO<sub>2</sub>  $\geq 0$ ) are shown in Figure 5(a). The largest influence is found when a monolayer of MPS is present (MPS/Sb : SnO<sub>2</sub>  $\geq 0.08 \text{ g/g}$ ). The influence of MPS oligomer seems to be small (Scheme 3).

To calculate the rate constants for the different starting mixtures of Figure 5(a), a variation in the (meth)acrylate C=C bond concentration at the start of the reaction has to be taken into account. As the molecular weight and the number of C=C double bonds of these monomers/moieties are different, a change in the MPS/PEGDA ratio will change the total double bond concentration  $c_{(\text{C}=\text{C})t=0}$ . To facilitate the interpretation of these results (2)–(4) were modified into (5)–(7) using (8):

$$R_{\text{ini}}^m{}^\lambda = \left\{ K_{\text{ini}}^\lambda (c_{\text{C}=\text{C}})_t - (c_{\text{C}=\text{C}})_{t=0} \right\} \left\{ (c_{\text{C}=\text{C}})_{t=0} \right\}^{-1} \times \left\{ I_0 \left( 1 - 10^{-\varepsilon(\lambda) \cdot c_{\text{particle}} \cdot d} \right) d^{-1} \right\}^{1/2}, \quad (5)$$

$$R_{\text{max}}^m{}^\lambda = K_{\text{max}}^\lambda \left\{ c_{(\text{C}=\text{C})t1} - c_{(\text{C}=\text{C})t2} \right\} \left\{ (c_{\text{C}=\text{C}})_{t=0} \right\}^{-1} \times \left\{ I_0 \left( 1 - 10^{-\varepsilon(\lambda) \cdot c_{\text{particle}} \cdot d} \right) d^{-1} \right\}^{1/2}, \quad (6)$$

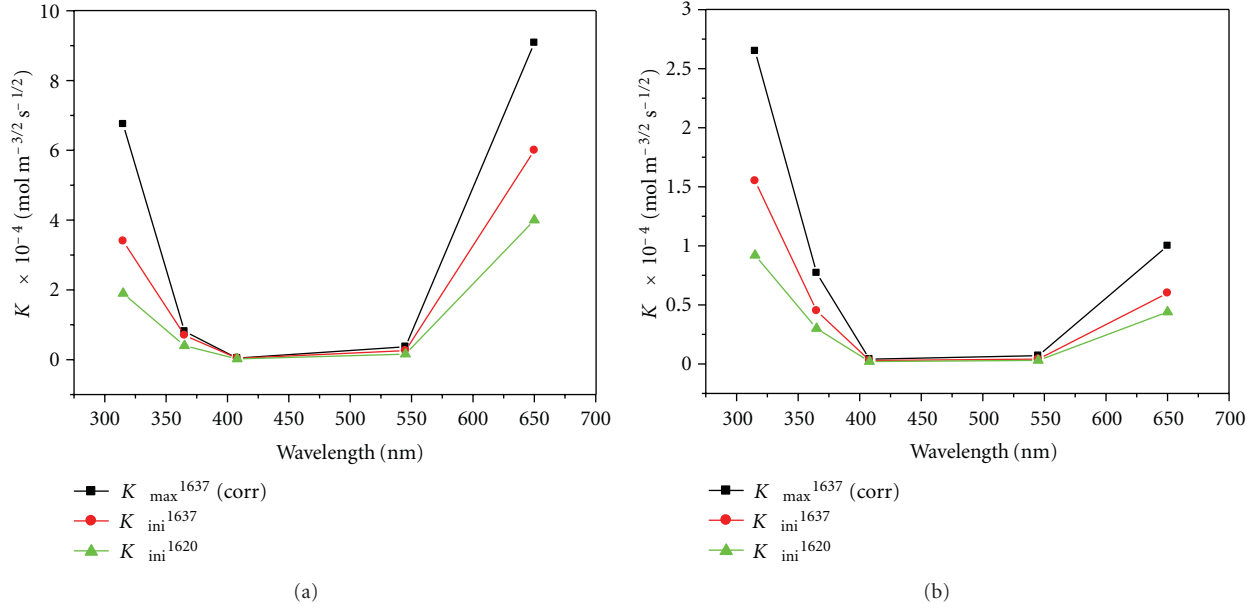


FIGURE 4: The influence of the wavelength of illumination on the  $K^*$  values for starting MPS-Sb:SnO<sub>2</sub>/PEGDA formulations against the wavelength of radiation  $\lambda$  (nm). (a) Sb = 0%; (b) Sb = 7%.

$$K_{ini/max}^{\lambda,m} = K_{ini/max}^{\lambda} \{(c_{c=c})_{t=0}\}^{-1} \quad (7)$$

$$= k_p^{\lambda} \left( \frac{k_t}{k_{t(ini/max)}} \right)^{-1} \{(c_{c=c})_{t=0}\}^{-1},$$

$$R_{ini/max}^{\lambda,m} = R_{ini/max}^{\lambda} \{(c_{c=c})_{t=0}\}^{-1}. \quad (8)$$

This means that the presented  $R_{ini/max}^m$  values in Table 4 using incident radiation of 365 nm depend not only on the concentration of the C=C double bonds at time  $t$  or  $t_{max}$   $\{t_{max} = (t_1 - t_2)/2\}$  but also on the C=C bond concentration at time  $t = 0$ . The corrected  $K_{ini/max}^m$  values are shown in Table 4 and Figure 5(b) as  $K_{ini/max}^{**}$ .

Figure 5(b) shows that the  $K_{max}^{**}$  values determined at 1637 cm<sup>-1</sup> are, within experimental error, identical to those determined at 1620 cm<sup>-1</sup>. The acrylate C=C bonds absorb at 1620 cm<sup>-1</sup> and both methacrylate C=C and acrylate C=C bonds at 1637 cm<sup>-1</sup>. Hence, these  $K_{max}^{**}$  values are the relative quantum yields for the reaction between a polymer fragment with an acrylate radical end group and an acrylate C=C bond. The  $K_{max}^{**}$  values are hardly influenced when the particles are grafted with a monolayer of MPS (MPS/Sb:SnO<sub>2</sub> ratios  $\geq 0.08$ ). Variable amounts of MPS oligomer are present in these starting formulations, but they seem not to influence these  $K_{max}^{**}$  values. When the surface of the particles is covered with less than a monolayer MPS (MPS/Sb:SnO<sub>2</sub> ratio  $< 0.08$ ), the rate is increased showing that the amount of grafted MPS influences these  $K^{**}$  values. Figure 5(b) also shows that the  $K_{ini}^{**}$  values are always lower than the  $K_{max}^{**}$  values. These lower values were also reported earlier for similar formulations when radiation of 315 nm was

used and can be explained by the large preference of a methacrylate radical end group to react with a methacrylate C=C double bond. This results into lower  $K_{ini}^{**}$  values and a preferred consumption of the methacrylate C=C bonds (different  $k_p/\sqrt{k_t}$  values) at the initial stage of the reaction. This preference, which is discussed above in more detail, is well known for radical polymerizations in methacryl/acryl C=C bond mixtures [12, 14, 32]. The influence of the  $k_p/\sqrt{k_t}$  values at the initial stage of the reaction becomes larger when the amount of methacrylate MPS C=C bonds present is larger (Figure 5(b), Table 4). The similarity found for the ratios of  $K_{ini}^{*1637}/K_{ini}^{*1620}$  can only be explained by a lowering of the  $\Phi_{Sb=7\%}^{365}$  when increasing amounts of MPS/Sb:SnO<sub>2</sub> ratios are used in the grafting reaction of the particles.

When the particles are not grafted with MPS the reproducibility in the measured C=C rates is much lower, because of the variation in the agglomeration of the nanoparticles before and during the reaction. Still the  $K_{ini}$  values calculated for the nongrafted particles are always much larger than those for the nanoparticles grafted with MPS. This confirms that the grafting of the surface of the Sb:SnO<sub>2</sub> particles lowers  $\Phi_{Sb=7\%}^{365}$ . Similar influences of the MPS/Sb:SnO<sub>2</sub> ratios on the rate of C=C bond disappearance were reported when the formulations containing Sb:SnO<sub>2</sub> (Sb = 0%) particles were irradiated with 315  $\pm$  5 nm [12]. Hence, it is likely that MPS grafting of the surface of the Sb:SnO<sub>2</sub> (Sb  $\geq 0\%$ ) nanoparticles lowers the quantum efficiency of the formation of the initiating radical for C=C polymerization for all irradiating wavelengths of light between 300 and 650 nm.

After irradiation with 315, 365, 408, 545, or 650 nm, we always obtained a hard transparent thin layer (trans-

TABLE 4: The influence of the MPS/Sb : SnO<sub>2</sub> grafting ratio on the  $K_{ini}^m$ ,  $K_{ini}^{**}/K_{ini}^{**}$ , and  $K_{ini}^{**}/K_{ini}^{**}$  for Sb : SnO<sub>2</sub>/PEGDA 575 formulations.<sup>a</sup>

MPS/Sb : SnO <sub>2</sub>	$R_{ini}^{m 1637}$ [s <sup>-1</sup> ]	$R_{ini}^{m 1620}$ [s <sup>-1</sup> ]	$R_{max}^{m 1637}$ [s <sup>-1</sup> ]	$R_{max}^{m 1620}$ [s <sup>-1</sup> ]	$K_{ini}^{** 1637}/K_{max}^{** 1637}$	$K_{ini}^{** 1637}/K_{ini}^{** 1620}$
0	(0.020) <sup>b</sup>	(0.023) <sup>b</sup>				(0.90) <sup>a</sup>
0.051	0.012	0.011	0.024	0.025	0.42	1.1
0.080	0.011	0.0084	0.020	0.020	0.41	1.2
0.12	0.0098	0.0090	0.019	0.020	0.41	1.1
0.15	0.0095	0.0077	0.016	0.016	0.48	1.3
0.196	0.0038	0.0093	0.017	0.018	0.55	1.5

<sup>a</sup> Sb = 7%, incident wavelength of radiation 365 ± 5 nm. <sup>b</sup> Experimental error above 40%.

parency > 98%, haze < 1%) when MPS grafted Sb : SnO<sub>2</sub> (Sb > 0%) nanoparticles were used in PEGDA 575 starting formulations which did not contain any other photocatalytic molecule/particle. The layers were so hard because the MPS grafted surface groups also reacted and the nanoparticles were chemically connected to the polymer network and were forming cross-links through the polymer matrix. The methacrylate C=C bonds present react at the initial stage of the polymerization reaction. Hence, the structure of the polymer network formed at the end of the cure will depend on the ratio between methacrylate C=C and acrylate C=C bonds initially present in the formulation.

When Sb : SnO<sub>2</sub> (Sb ≥ 0%) nanoparticles, of which the surfaces were not grafted with MPS, were used in these PEGDA 575 starting formulations viscous thin layers are obtained after cure. These layers are no longer transparent. The particles agglomerate further during the cure and become visible for the eye. At the end of the cure reaction, still a large number of acrylate C=C bonds are present (Figure 5(a)).

In the experiments discussed above incident radiation with a very narrow wavelength distribution was used. We found the same photocatalytic properties for (MPS)-Sb : SnO<sub>2</sub> (Sb ≥ 0%) particles when in our experiments incident radiation with a broad wavelength distribution (visible or ultraviolet > 300 nm + visible) was used. However, the overall efficiency of the photocatalyzed polymerization, the structure of the polymer, and the particle network formed through the layer depended on the wavelength and intensity distribution of the lamp used in the experiment.

**3.3. Influence of Sb-Doping.** In this section the influence of Sb-doping (0–13 vol.%) on the photocatalytic properties of the Sb : SnO<sub>2</sub> nanoparticles is discussed. All the Sb : SnO<sub>2</sub>/PEGDA formulations discussed in this chapter contain Sn : SbO<sub>2</sub> particles which are covered with a monolayer of grafted MPS and contain very similar amounts of MPS oligomer. For all these formulations the  $(C_{c=c})_{t=0}$  is the same. These formulations are irradiated with light of 315 or 365 nm, and the measured relative conversions of the C=C bonds over time at 1637 cm<sup>-1</sup> are shown in Figures 6(a) and 6(b), respectively. The corresponding  $R$  and  $K$  data are shown in Figure 7 after correcting them for differences in incident radiation intensities and in absorption coefficients of the Sb : SnO<sub>2</sub> particles ( $R_{ini}^*$ ,  $R_{max}^*$ ,  $K_{ini}^*$ , and  $K_{max}^*$ ) (Table 2, Figure 2).

The presented conversions in Figure 6 show that for all Sb-doping levels the rates of the C=C bond polymerization are always much faster for irradiation with 315 nm than those with 365 nm. This is confirmed by the calculated  $K^*$  values shown in Figure 7. For both incident wavelengths of radiation used the  $K_{max}^{* 1637}$  and  $K_{max}^{* 1620}$  values for particles with Sb ≥ 2% are, within experimental error, identical. Hence, all these  $K$  values are the relative quantum efficiencies of the propagation and termination reaction of a polymer fragment with an acrylate radical end group and a C=C acrylate monomer. This suggests that the observed dependence of  $K_{max}^*$  on Sb-doping should be explained by the dependency of  $\Phi$  on Sb-doping.

Figure 7 also shows that the  $K_{ini}^*$  values measured at 1637 cm<sup>-1</sup> are always much larger than the  $K_{ini}^*$  values measured at 1620 cm<sup>-1</sup>. Hence, at the initial stage of the polymerization reaction methacrylate radicals and C=C bonds as well as acrylate radicals and C=C bonds are involved in the formation of the polymer. Although the methacrylate C=C bond concentration is only about one tenth of the total C=C bond concentration in these mixtures, the reaction between a methacryl radical and a methacryl C=C bond is preferred [12, 14, 32]. Still the ratios  $K_{ini}^{* 1637}/K_{max}^{* 1637}$  and  $K_{ini}^{* 1637}/K_{ini}^{* 1620}$  are within experimental error independent of the Sb-doping level and wavelength of radiation (Table 5).

Hence, also at the initial stage of the polymerization reactions the variations in  $K_{ini}^*$  presented in Figure 7 with respect to Sb-doping level are likely to be caused by variations in  $\Phi$  only. This suggests that these  $K$  values can be corrected for corresponding  $k_p(k_t)^{-1/2}$  values of the polymerization reaction between a polymer fragment with an acrylate end group and an acrylate C=C bond. Using this approach and the data of Table 3 and Figure 7, the ratios between the different  $\Phi$  values for different Sb-doping levels are calculated and presented in Table 5. These data confirm that our Sb-doped Sb : SnO<sub>2</sub> nanoparticles always have a lower  $\Phi$  and that the influence on  $\Phi$  of Sb-doping strongly depends on the wavelength of light used. For a fixed wavelength the differences in  $\Phi$  for particles with Sb ≥ 2% are small. Combining the data of Table 5 with the data reported earlier for particles with Sb of 7% and 0%, the ratios of both  $\Phi$ 's are calculated for visible light too (Figure 8). From this graph we conclude that the influence of Sb-doping on  $\Phi$  is strongly dependent on the wavelength of irradiation used. For each wavelength the value of  $\Phi$  is always larger for formulations with Sb : SnO<sub>2</sub> (Sb = 0%) than for formulations

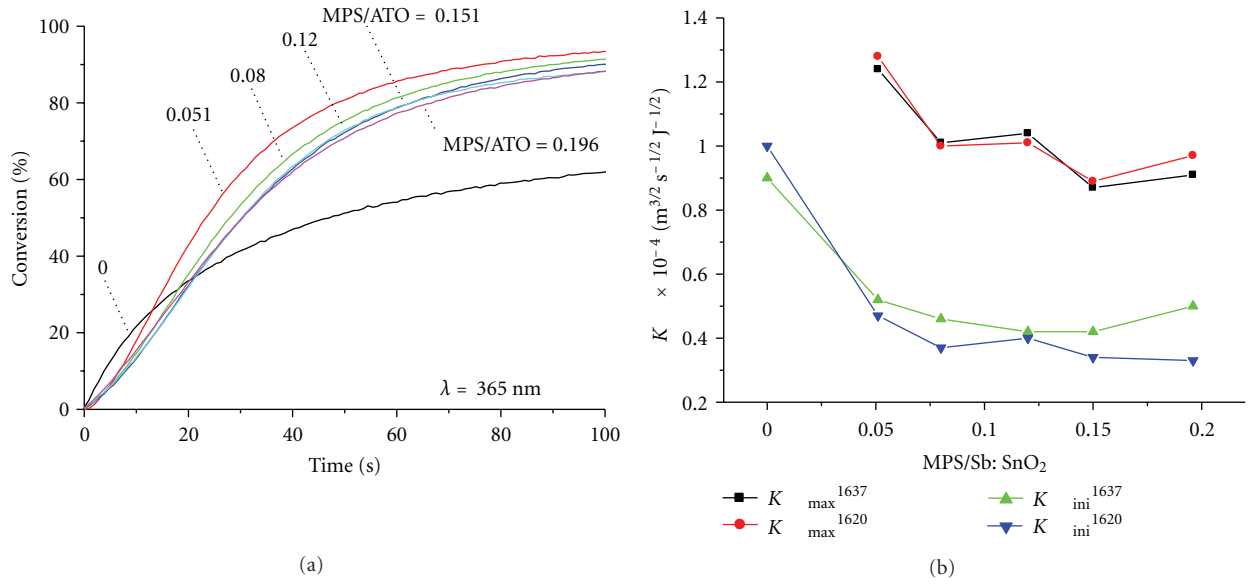


FIGURE 5: (a) Influence of the amount of MPS present in the starting formulation on the conversion % of the C=C bonds over time;  $\lambda = 365$  nm, Sb = 7%, and  $c_{particle} = 10$  vol%. (b)  $K^{**}$  values calculated from (a).

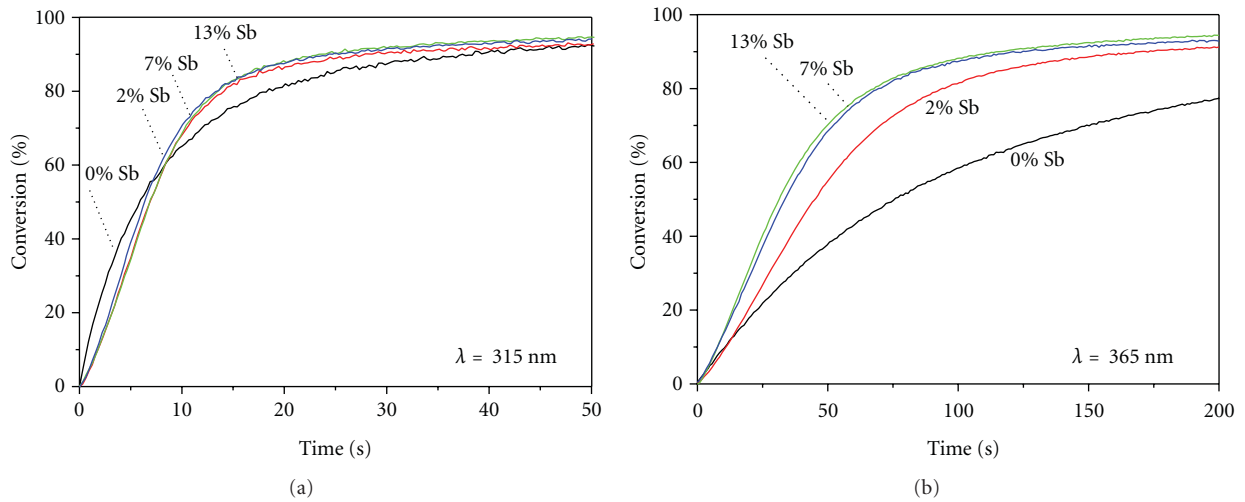


FIGURE 6: Influence of the Sb-doping level of the nanoparticles on the conversion % of the C=C bonds over time measured at  $1637\text{ cm}^{-1}$ . (a)  $\lambda = 315$  nm; (b)  $\lambda = 365$  nm.

TABLE 5: Influence of Sb-doping on  $K_{ini}^{1637}/K_{max}^{1637}$  and  $K_{ini}^{1637}/K_{ini}^{1620}$ ;  $\lambda = 315$  or  $365$  nm.

$\lambda$ [nm]	Sb %	$K_{ini}^{1637}/K_{max}^{1637}$	$K_{ini}^{1637}/K_{ini}^{1620}$	$\Phi_{Sb \geq 2\%}/\Phi_{Sb=0\%}$ <sup>a</sup>
315	0		1.8	
365	0		1.8	
315	2	0.6	1.8	0.35
365	2	0.6	1.8	0.68
315	7	0.6	1.7	0.40
365	7	0.6	1.6	0.90
315	13	0.5	1.5	0.46
365	13	0.6	1.6	0.74

<sup>a</sup>  $K^*$  values corrected for differences in  $k_p(k_t)^{-1/2}$ .

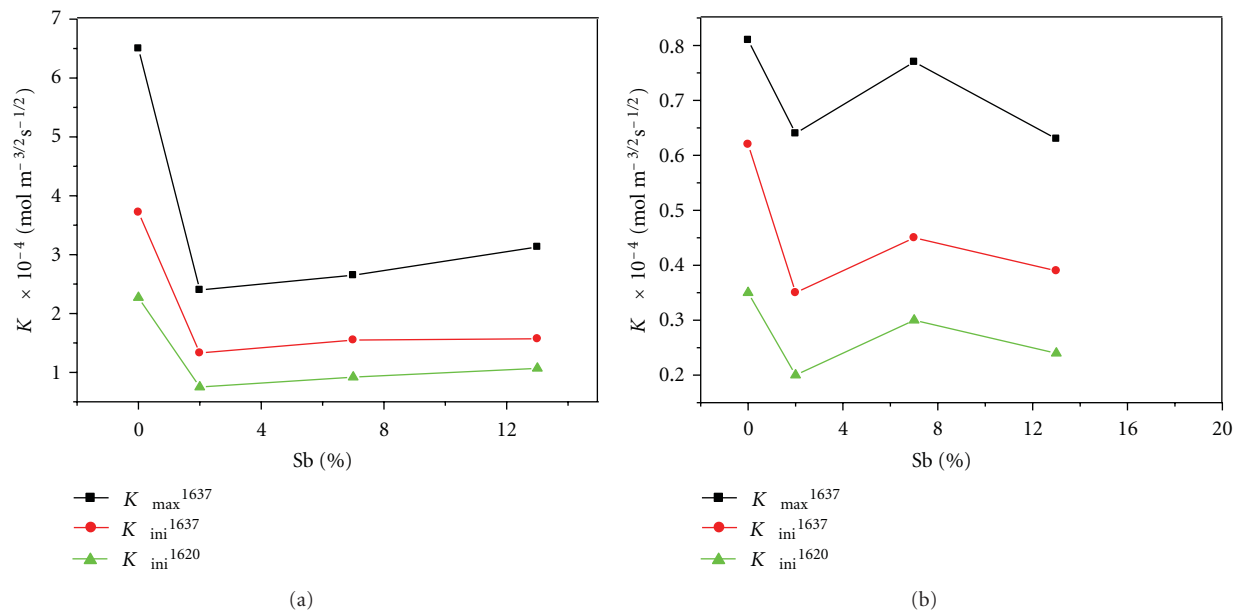


FIGURE 7: The influence of the Sb-doping level on  $K_{\max}^{1637}$ ,  $K_{\max}^{1637}$ , and  $K_{\text{ini}}^{1620}$  calculated from the data given in Figure 6. When Sb = 0% the  $K_{\max}^{1637}$  values shown are actually the  $K_{\max}^{1637} \text{ (corr.)}$  values. (a)  $\lambda = 315 \text{ nm}$ ; (b)  $\lambda = 365 \text{ nm}$ .

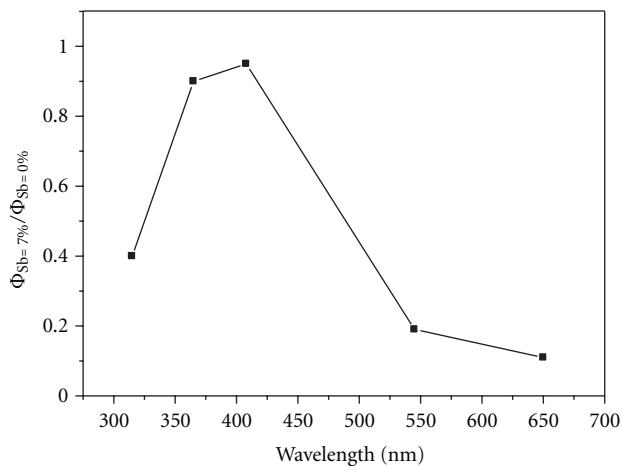


FIGURE 8: The dependency of the ratio  $\Phi_{\text{Sb}=7\%}/\Phi_{\text{Sb}=0\%}$  versus the wavelength of illumination.

with Sb : SnO<sub>2</sub> (Sb  $\geq$  2%). These data also suggest that further optimization of the amount of Sb-doping and of N-doping (see also later on) used may enlarge the  $\Phi$  for visible light of Sb : SnO<sub>2</sub> (Sb > 0%) nanoparticles considerably.

**3.4. Why Is  $\Phi$  Dependent on the Wavelength of Irradiation, MPS Grafting and Sb Doping?** We showed above that the  $\Phi$ 's for the formation of the radical, which initiates the (meth)acrylate C=C bond polymerization, are dependent on the wavelength of illumination used, the amount of the methacrylate group grafted on the particle surface, and the Sb-doping level of the particles. The MPS-Sb : SnO<sub>2</sub>

nanoparticles used are (almost) monocrystalline, have a similar surface area and are well dispersed in the formulations before and during processing (Table 1) [12, 13]. Hence, the observed differences in quantum yields are mainly related to differences in surface and/or bulk group composition of these nanoparticles.

Undoped SnO<sub>2</sub> particles/films are, in general, n-type semiconductive materials due to native oxygen vacancies. They have a band gap of 3.6 eV–3.8 eV and a Fermi level of about 0.35–0.5 eV below the conduction band [16, 17]. This band gap difference corresponds with light quanta energies between 320 and 340 nm. When the Sb : SnO<sub>2</sub> (Sb=0%)/PEGDA formulations are irradiated with light of 315 nm, the photocatalytic properties are explained by a direct transfer of an electron from the valence band into the conduction band. However, for irradiation wavelengths  $\geq$  365 nm, the energy of the light quantum is too small to initiate this transition and the observed photocatalytic properties of the Sb : SnO<sub>2</sub> particles at or above 365 nm have to be explained differently.

Recently it has been shown that N-doping can shift the band gap of crystalline SnO<sub>2</sub> films to 624 nm and that these N-doped films photocatalyze the oxidation of methylene blue in water during irradiation with visible light [19]. The authors detected in the XPS spectra of these films three N 1s related peaks, namely, at 396, 399, and 402 eV. They suggest that the energy level related to the peak at 396 eV is the one responsible for the observed photocatalysis under visible illumination. All our Sb : SnO<sub>2</sub> nanoparticles are doped with N (Table 1), but in their XPS spectra only one broad peak at about 400 eV and no signal at 396 eV is observed (Figure 9). The peak at 400 eV is likely to be a combination of two peaks (399 and 402 eV). The maximum of this broad peak

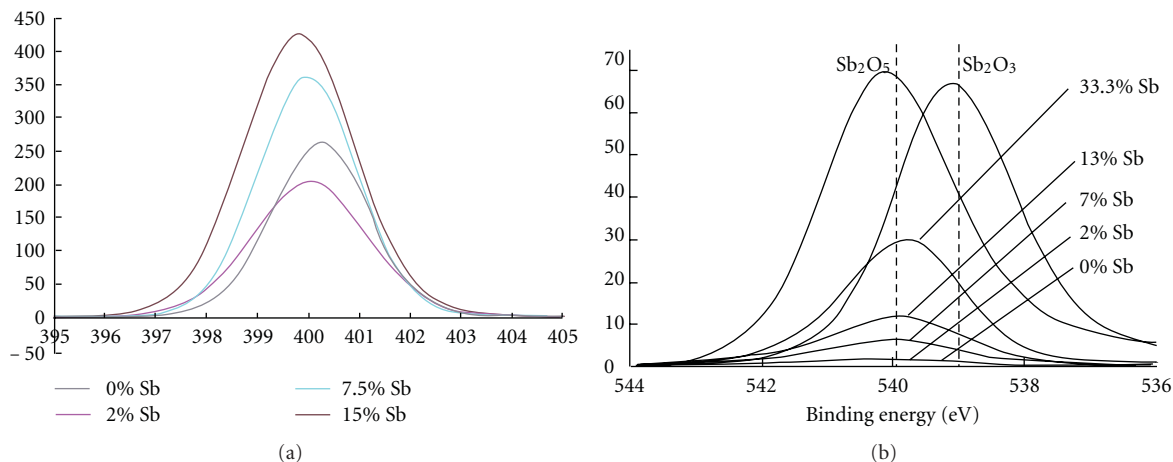


FIGURE 9: (a) XPS spectra of the N 1s band of the Sb : SnO<sub>2</sub> nanoparticles; (b) XPS spectra of the Sb 3d<sub>3/2</sub> of several Sb : SnO<sub>2</sub> nanoparticles.

gradually shifts to 399 eV when the Sb-doping level of the nanoparticles is increased, which can be explained by a dependency of the intensities of the 399 and 402 eV peaks and of the concentrations of the two N forms in the bulk on Sb-doping level. Hence, it is likely that for our nanoparticles the energy levels related to the 399 and/or 402 eV peaks initiate the photocatalyzed C=C bond polymerizations for radiation wavelengths  $\geq 365$  nm. XPS is a surface technique, and its penetration depth of a few nanometers will not probe the whole volume of our particles (diameter about 7 nm) or the crystalline SnO<sub>2</sub> films mentioned above, and this may explain the discrepancies in energy levels from which the photocatalysis occurs in both materials.

Density functional theory calculations on different N-doped SnO<sub>2</sub> structures suggest that N-doping raises the top level of the valence band, forms states in the gap between valence and conduction band, and may lower the bottom of the conduction band [32]. Hence, all these changes facilitate the visible light photocatalytic activities of the MPS-Sb : SnO<sub>2</sub> (Sb = 0%) particles discussed here. Because after irradiation the number of electrons in the conduction band of our nanoparticles increased for all the wavelengths used (Figure 3), it is likely that the polymerization starts with a reaction with the activated electron in the conduction band.

As was reported earlier [13], our Sb : SnO<sub>2</sub> nanoparticles are semiconductive and contain only Sb(V) ions at lower Sb-doping levels. At higher doping level also Sb(III) is present, probably mainly near/at the surface of the particles (Table 1) [12, 16]. The Sb(V) ions have probably replaced some Sn ions in the original crystal structure and have donated an extra electron to the conduction band upon substitutional replacement [16]. UPS EELS and photoemission measurements confirm the filling of the conduction band by Sb-doping and suggest a shift of the Fermi level into the conduction band and a band gap narrowing. The increase in number of electrons in the conduction band by Sb-doping has been confirmed for our nanoparticles by an increase in intensity/shift of the peak maximum of the plasmon band (Figure 3).

Band structure calculations at high Sb-doping levels in SnO<sub>2</sub> (Sb doping about 25%) suggest the formation of a Sb 5s-like band in the SnO<sub>2</sub> gap with a free electron character at the  $\Gamma$ -point. This could be a half filled metallic band below the conduction band. Hence, it is likely that the Sb-doping levels of our nanoparticles result into energy levels at or close to the conduction band [16, 33]. These Sb(V) energy levels may be expected to be about 0.03 eV to 0.15 eV below the minimum of the conduction band [30, 34]. Moreover, we found that Sb-doping always lowers the  $\Phi$  (Table 5, Figure 8). This suggests that Sb-doping levels function as scavengers of the activated electrons in the conduction band. However, Sb-doping lowers also the number of oxygen vacancies in SnO<sub>2</sub> and seems to influence the ratio between the two N-doping energy levels observed in our Sb : SnO<sub>2</sub> nanoparticles (Figure 9). These changes in bulk composition may be responsible for the lowering of  $\Phi$  with Sb-doping, and then it is likely that a half filled band close to the conduction band or the lowering of the bottom of the conduction band is involved in shifting the absorption of the radiation to at least 650 nm and the occurrence of radical C=C bond polymerization photocatalyzed by our Sb : SnO<sub>2</sub> (Sb  $\geq$  2%) nanoparticles for illuminations with light between 365 and 650 nm. This half filled band may not be present at Sb-doping levels lower than 2%.

Grafting the surface of the Sb : SnO<sub>2</sub> particles with MPS lowers  $\Phi$ . The lowest values are obtained when the surface is grafted with a monolayer of MPS. Still photocatalysis continues although at a lower rate. This may be explained by the initial formation of an MPS radical on the surface of the particle, which reacts further with a much slower rate with a C=C double bond outside the particle as compared to a direct transfer of an electron from the particle surface to a C=C bond outside the particle, even when almost all the methacrylate C=C bonds are disappeared. Another explanation may be that the initially formed grafted MPS radical reacts first preferably with the other grafted MPS molecules forming a more or less closed chemically connected apolar acrylate shield, which limits later on the

transfer of another electron after absorption of a new light quantum to the outside of the particle.

#### 4. Conclusions

- (1) By absorption of radiation of 365, 408, 545, or  $650 \pm 5$  nm Sb:SnO<sub>2</sub> (Sb  $\geq$  0%) nanoparticles photocatalyze the (meth)acrylate C=C bond radical polymerization present in MPS-Sb:SnO<sub>2</sub>/acrylate monomer starting formulations.
- (2) Although the energy of the light quanta of these wavelengths is too small to directly activate an electron from the valence band into the conduction band, the shift in peak position and/or the increase in the absorption the plasmon band during illumination of these formulations suggest that still this polymerization starts with a transfer of an activated electron present in the conduction band of the particle to a C=C double bond outside or at the surface of the MPS-Sb:SnO<sub>2</sub> nanoparticle. All the nanoparticles studied are always doped with N in the bulk, in which energy levels may be responsible for these photocatalyzed C=C bond polymerizations.
- (3) The relative quantum efficiencies for the polymerization of the C=C bonds can be determined quantitatively and depend on the quantum yields ( $\Phi$ 's) for the formation of the radical which initiates the polymerization and the rate constants of the propagating and terminating polymerization reactions.
- (4) The  $\Phi$  appears to be dependent on the wavelength of irradiation, the amount of Sb-doping, and the amount of MPS grafting of the particle surface.
- (5) It is likely that methacrylate grafting of the surface of the Sb:SnO<sub>2</sub> (Sb  $\geq$  0%) nanoparticles lowers  $\Phi$  for all irradiating wavelengths of light between 300 and 650 nm. This may be explained by the scavenger role of the grafted MPS moieties on the surfaces of the nanoparticles for the activated electrons in the conduction band. MPS grafting of these particles is essential for obtaining transparent (>98%) hard layers with a low haze (<1%).
- (6) Sb-doping always lowers  $\Phi$ . The decrease in  $\Phi$  may be caused by a scavenging of the activated electrons by Sb-doping energy levels. Sb-doping lowers also the number of oxygen vacancies in the Sb:SnO<sub>2</sub> (Sb > 0%) nanoparticles. These oxygen vacancies may initiate the formation of other radicals, which can initiate also the C=C bond polymerization reaction.
- (7) MPS-Sb:SnO<sub>2</sub> nanoparticles are attractive new photocatalysts under visible light to initiate the polymerization of (meth)acrylate monomers.

#### References

- [1] A. Mills and S. K. Lee, "A web-based overview of semiconductor photochemistry-based current commercial applications,"

- Journal of Photochemistry and Photobiology*, vol. 152, no. 1–3, pp. 233–247, 2002.
- [2] C. Damm, "An acrylate polymerisation initiated by iron doped titanium dioxide," *Journal of Photochemistry and Photobiology*, vol. 181, no. 2–3, pp. 297–305, 2006.
  - [3] A. J. Hoffman, H. Yee, G. Mills, and M. R. Hoffmann, "Photo-initiated polymerization of methyl methacrylate using Q-sized ZnO colloids," *Journal of Physical Chemistry*, vol. 96, no. 13, pp. 5540–5546, 1992.
  - [4] R. Ojah and S. K. Dolui, "Photopolymerization of methyl methacrylate using dye-sensitized semiconductor based photocatalyst," *Journal of Photochemistry and Photobiology*, vol. 172, no. 2, pp. 121–125, 2005.
  - [5] *Encyclopedia of Polymer Science and Technology*, vol. 10, 2004.
  - [6] F. E. Osterloh, "Inorganic materials as catalysts for photochemical splitting of water," *Chemistry of Materials*, vol. 20, no. 1, pp. 35–54, 2008.
  - [7] R. Asahi, T. Morikawa, T. Ohwaki, K. Aoki, and Y. Taga, "Visible-light photocatalysis in nitrogen-doped titanium oxides," *Science*, vol. 293, no. 5528, pp. 269–271, 2001.
  - [8] W. S. Tung and W. A. Daoud, "A new approach toward nanosized ferrous ferric oxide and iron-doped titanium dioxide photocatalysts," *Applied Materials & Interfaces*, vol. 1, pp. 2453–2461, 2009.
  - [9] J. Zhu, W. Zheng, B. He, J. Zhang, and M. Anpo, "Characterization of Fe-TiO photocatalysts synthesized by hydrothermal method and their photocatalytic reactivity for photodegradation of XRG dye diluted in water," *Journal of Molecular Catalysis*, vol. 216, no. 1, pp. 35–43, 2004.
  - [10] U. Gesenhues, "Al-doped TiO pigments: influence of doping on the photocatalytic degradation of alkyd resins," *Journal of Photochemistry and Photobiology*, vol. 139, no. 2–3, pp. 243–251, 2001.
  - [11] D. Wu, Y. Jiang, Y. Yuan, J. Wu, and K. Jiang, *The Journal of Nanoparticle Research*, vol. 13, no. 7, pp. 2875–2886, 2011.
  - [12] J. C. M. Brokken-Zijp, O. L. J. van Asselen, W. E. Kleinjan, R. van de Belt, and G. de With, "Photocatalysed (meth)acrylate polymerization by (antimony-doped) tin oxide nanoparticles and photoconduction of their crosslinked polymer nanoparticle composites," *Journal of Nanotechnology*, vol. 2010, Article ID 579708, 16 pages, 2010.
  - [13] W. E. Kleinjan, R. van de Belt, Z. Chen, and G. de With, "Antimony-doped tin oxide nanoparticles for conductive polymer nanocomposites," *Journal of Materials Research*, vol. 23, no. 3, pp. 869–880, 2008.
  - [14] W. Posthumus, *UV-Curable Acrylate Metal Oxide Nanocomposite Coatings*, Ph.D. thesis, Eindhoven University of Technology, Eindhoven, The Netherlands, 2004.
  - [15] W. Posthumus, P. C. M. M. Magusin, J. C. M. Brokken-Zijp, A. H. A. Tinnemans, and R. Van Der Linde, "Surface modification of oxidic nanoparticles using 3-methacryloxypropyltrimethoxysilane," *Journal of Colloid and Interface Science*, vol. 269, no. 1, pp. 109–116, 2004.
  - [16] M. Batzill and U. Diebold, "The surface and materials science of tin oxide," *Progress in Surface Science*, vol. 79, no. 2–4, pp. 47–154, 2005.
  - [17] S. Shanthi, C. Subramanian, and P. Ramasamy, "Investigations on the optical properties of undoped, fluorine doped and antimony doped tin oxide films," *Crystal Research and Technology*, vol. 34, no. 8, pp. 1037–1046, 1999.
  - [18] D. Lin-Vien, N. B. Colthup, W. G. Fatley, and J. C. Grasselli, *The Handbook of Infrared and Raman Characteristic Frequencies of Organic Molecules*, Academic Press, San Diego, Calif, USA, 1991.

- [19] S. S. Pan, Y. D. Shen, X. M. Teng et al., "Substitutional nitrogen-doped tin oxide single crystalline submicrorod arrays: vertical growth, band gap tuning and visible light-driven photocatalysis," *Materials Research Bulletin*, vol. 44, no. 11, pp. 2092–2098, 2009.
- [20] S. S. Pan, Y. X. Zhang, X. M. Teng, G. H. Li, and L. Li, "Optical properties of nitrogen-doped SnO<sub>2</sub> films: effect of the electronegativity on refractive index and band gap," *Journal of Applied Physics*, vol. 103, no. 9, Article ID 93103, 2008.
- [21] L. J. Huijbregts, H. B. Brom, J. C. M. Brokken-Zijp, W. E. Kleinjan, and M. A. J. Michels, "Dielectric quantification of conductivity limitations due to nanofiller size in conductive powders and nanocomposites," *Physical Review*, vol. 77, no. 7, Article ID 075322, 6 pages, 2008.
- [22] C. McGinley, H. Borchert, M. Pflughoeft et al., "Dopant atom distribution and spatial confinement of conduction electrons in Sb-doped SnO<sub>2</sub> nanoparticles," *Physical Review*, vol. 64, no. 24, Article ID 245312, 9 pages, 2001.
- [23] T. Nütz, U. Z. Felde, and M. Haase, "Wet-chemical synthesis of doped nanoparticles: blue-colored colloids of n-doped SnO<sub>2</sub>:Sb," *Journal of Chemical Physics*, vol. 110, no. 24, Article ID 12142, 9 pages, 1999.
- [24] U. Zum Felde, M. Haase, and H. Weller, "Electrochromism of highly doped nanocrystalline SnO<sub>2</sub>:Sb," *Journal of Physical Chemistry*, vol. 104, no. 40, pp. 9388–9395, 2000.
- [25] V. A. Soloukhin, J. C. M. Brokken-Zijp, and G. De With, "Conductive ATO-acrylate nanocomposite hybrid coatings: experimental results and modeling," *Journal of Polymer Science*, vol. 45, no. 16, pp. 2147–2160, 2007.
- [26] A. J. Hoffman, G. Mills, H. Yee, and M. R. Hoffmann, "Q-sized CdS: synthesis, characterization, and efficiency of photoinitiation of polymerization of several vinylic monomers," *Journal of Physical Chemistry*, vol. 96, no. 13, pp. 5546–5552, 1992.
- [27] R. Mehnert, A. Pincus, I. Janorsky, R. Stowe, and A. Berejka, *UV & EB Curing Technology and Equipment*, vol. 1, John Wiley & Sons, Chichester, UK, 1998.
- [28] G. R. Tryson and A. R. Shultz, "Calorimetric study of acrylate photopolymerization," *Journal of Polymer Science*, vol. 17, no. 12, pp. 2059–2075, 1979.
- [29] J. Jansen, E. Houben, P. H. G. Tummens, D. Wienke, and J. Hoffmann, "Real-time infrared determination of photoinitiated copolymerization reactivity ratios: application of the Hilbert transform and critical evaluation of data analysis techniques," *Macromolecules*, vol. 37, no. 6, pp. 2275–2286, 2004.
- [30] C. S. Rastomjee, R. G. Egdell, M. J. Lee, and T. J. Tate, "Observation of conduction electrons in Sb-implanted SnO<sub>2</sub> by ultraviolet photoemission spectroscopy," *Surface Science*, vol. 259, no. 3, pp. L769–L773, 1991.
- [31] F. Gu, S. F. Wang, M. K. Lü, G. J. Zhou, D. Xu, and D. R. Yuan, "Photoluminescence properties of SnO<sub>2</sub> nanoparticles synthesized by sol-gel method," *Journal of Physical Chemistry*, vol. 108, no. 24, pp. 8119–8123, 2004.
- [32] X. Sun, R. Long, X. Cheng, X. Zhao, Y. Dai, and B. Huang, "Structural, electronic, and optical properties of N-doped SnO<sub>2</sub>," *Journal of Physical Chemistry*, vol. 112, no. 26, pp. 9861–9864, 2008.
- [33] K. C. Mishra, K. H. Johnson, and P. C. Schmidt, "Electronic structure of antimony-doped tin oxide," *Physical Review*, vol. 51, no. 20, pp. 13972–13976, 1995.
- [34] C. G. Fonstadt and R. H. Redicker, "Electrical properties of high quality stannic oxide crystals," *Journal of Applied Physics*, vol. 42, no. 7, p. 2911, 1971.

## Research Article

# Photodegradation of Chloridazon Using Coreshell Magnetic Nanocomposites

Dina Mamdouh Fouad<sup>1</sup> and Mona Bakr Mohamed<sup>2</sup>

<sup>1</sup> Chemistry Department, Faculty of Science, Assiut University, 71516 Assiut, Egypt

<sup>2</sup> National Institute of Laser Enhanced Science, NILES, Cairo University, 12613 Cairo, Egypt

Correspondence should be addressed to Dina Mamdouh Fouad, dinafouad93@hotmail.com

Received 5 March 2011; Accepted 2 June 2011

Academic Editor: Menka Jain

Copyright © 2011 D. M. Fouad and M. B. Mohamed. This is an open access article distributed under the Creative Commons Attribution License, which permits unrestricted use, distribution, and reproduction in any medium, provided the original work is properly cited.

A new synthesized magnetic nanoparticle of  $\text{Fe}_3\text{O}_4$  and coreshell  $\text{Fe}_3\text{O}_4@Au$  is prepared chemically. A comparative study between the photocatalytic activity between  $\text{Fe}_3\text{O}_4$  and core shell  $Au\text{-Fe}_3\text{O}_4$  nanoparticles has been studied on the effect of UV and sun light on the photodegradation of chloridazon. The particle has been prepared using chemical methods and the particle size and shape have been examined via transmission electron microscopy (TEM). Analysis of the degradation of 20 ppm chloridazon under ultraviolet (UV) and visible light was analyzed with high-performance liquid chromatography (HPLC) and UV-Visible Spectra. Influence of different parameters on the activity photodegradation rate has been studied. The results indicate that the  $\text{Fe}_3\text{O}_4@Au$  nanoparticles are much more active catalyst in presence of sun light than pure  $\text{Fe}_3\text{O}_4$  nanomaterials which have maximum absorption at 560 nm.

## 1. Introduction

Magnetic nanoparticles (NPs) have attracted significant interest, due to their numerous attributes such as their low toxicity and biocompatibility; the increasing attention in these materials as well as other composites is determined by the novel magnetic, electronic, optical, and chemical properties, which are different to those of the bulk materials because of the extreme small sizes and the large specific surface areas, and magnetic properties that enable them to be directed by an external magnetic field, in addition to their possibility to separate them from a reaction mixture [1–7]. Iron oxide nanoparticles could be easily oxidized by oxygen present in air and also can react between its self-forming aggregates. Many trials have been carried out to modify the surface during the synthesis or coating process [8–10]. A special class of particular interest of nanocomposite materials is nanoshell particles or core/shell nanocomposites. These core/shell nanocomposites are highly functional materials consisting of thin coatings (1–20 nm) of one particular material deposited on core particles of another different material utilizing certain procedures [11, 12].

Nanocomposites core/shell has attracted a lot of attention owing to their novel-tailored properties which are different from the single-component counterparts (the single core or shell). Now it is possible to synthesize these nanocomposites in desired size and shape and with controlled improved properties such as increased stability, surface area, magnetic, optical, and catalytic properties [13]. Gold surface allows the attachment of molecules with a relative ease using a variety of thiol linkers [14–16]; gold exhibits strong absorption in the visible region. This strong color originates from the excitation of the electrons in the conduction band and is called *surface plasmon resonance*. The surface plasmon resonance is the coherent excitation of the free surface electrons leading to coherent oscillation [17–20].

The herbicide n-chloridazon (5-amino-4-chloro-2-phenyl-3(2H)-pyridazinone; n-CLZ) is a selective systemic herbicide, which can cause apathy, dyspnoea, hyperventilation, hypersalivation (sheep-foam hypersalivation), paralysis, tonic-clonic convulsions, and death in clonic convulsions [21, 22].

Available fate data indicate that n-CLZ is mobile in a variety of soil types and therefore, has the potential to enter

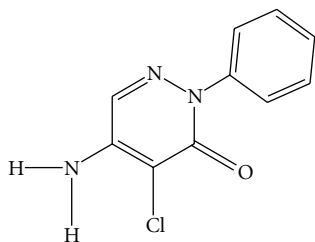


FIGURE 1: Structure of chloridazon.

surface and groundwater [23, 24]. Few scientific reports deal with the presence and photodegradation of chloridazon [25]. Our main goal is to find away to eliminate the excess of chloridazon from water and soil using sunlight. It was essential to find a photocatalysis used for photodegradation of chloridazon to nontoxic primary material such as  $\text{CO}_2$  and  $\text{H}_2\text{O}$ . In this work, we synthesize  $\text{Fe}_3\text{O}_4$  nanoparticles capped with PVP and use this material as a catalyst. The prepared particles have been used as a seed to grow layer of gold shell on their surfaces. Comparative study between the catalytic activity of both particles has been evaluated in presence of UV and visible sunlight.

## 2. Experimental

**2.1. Materials.** n-chloridazon (5-amino-4-chloro-2-phenyl-3(2H)-pyridazinone; n-CLZ) was obtained from Fluka (99% HPLC grade) and used as received; hydrogen tetrachloroaurate trihydrate ( $\text{HAuCl}_4 \cdot 3\text{H}_2\text{O}$ ); from Sigma-Aldrich, (99.9%), Polyvinyl pyrrolidone, PVP-K30; from Fluka (Av. Wt. 22000); Trisodium citrate from Sigma-Aldrich, (99%), Sterile sodium chloride physiological saline 0.9% (ADWIC) and Ferric chloride anhydrous from LOBA Chemicals (98%); Sodium borohydride from Sigma (98%), Sodium carbonate from Sigma (99%), and L-Ascorbic acid from Sigma-Aldrich.

HPLC grade solvents (purity 99%) such as methanol, ethanol, were purchased from Aldrich and high purity water are used in the experiments purified with the milli-Q system. All chemicals were used without any further purification (Figure 1).

### 2.2. Synthesis of Nanoparticles

**2.2.1. Synthesis of Gold Nanoparticles by Citrate Method.** Spherical gold nanoparticles in aqueous solution were prepared according to a method described by Turkevich. Simply, the method is a chemical reduction of gold ions by sodium citrate in aqueous solution. Sodium citrate serves also as a capping materials prevents aggregation and further growth of the particles. 5 mL of 1% sodium citrate solution was added to a boiling solution 40 mL of a chlorouric acid ( $\text{HAuCl}_4$ ) solution containing 5 mg of gold ions. The solution was boiled for 30 minutes and was then left to cool down to room temperature. The produced gold particles have average diameter of 15.0 nm as determined by TEM analysis.

**2.2.2. Preparation of  $\text{Fe}_3\text{O}_4$ .** Magnetite nanospheres  $8 \pm 2$  nm size is synthesized by coprecipitation method using ascorbic acid reduction of  $\text{FeCl}_3$  (231). A 100 mL beaker is cleaned in aqua regia (3 parts HCl, 1 part  $\text{HNO}_3$ ) and rinsed with DDI water. 0.25 g of  $\text{FeCl}_3$  powder is dissolved in 25 mL Sterile Saline with stirring for five minutes at room temperature. 0.6 g  $\text{NaCO}_3$  powder dissolved 10 mL Sterile Saline is added to  $\text{FeCl}_3$  solution with continued stirring for 10 minutes; the solution turned viscous with brown color. Directly adding 0.12 g powder of ascorbic acid to the previous solution with vigorous stirring for 15 minutes, the color of solution turned black, and formation of magnetite nanoparticles is capped with ascorbic acid. We complete the solution to 50 mL with Sterile Saline in measuring flask.

**2.2.3. Preparation of  $\text{Fe}_3\text{O}_4$ @Au Nanoparticles.** The magneto-optical (magnetite/gold) core shell nanocomposites were prepared chemically by reducing gold (III) chloride to gold in the presence of presynthesized magnetite nanoparticles (MNPs). During the reduction process, a reddish color is developed indicating the formation of Au nanoparticles; magnetite nanoparticles behave like “seeds” or nucleation sites for the resultant  $\text{Fe}_3\text{O}_4$ @Au nanocomposites. Ultraviolet-visible (UV-vis) absorption spectrometry confirms the formation of the resultant  $\text{Fe}_3\text{O}_4$ /Au nanocomposites. TEM has been used to characterize as-prepared bimetallic nanocomposites. 10.0 mL of presynthesized MNPs were placed in a 100 mL flask equipped with a small magnet bar for the sake of stirring. Then, a 10.0 mL Au precursor solution (aq. soln. of  $\text{HAuCl}_4 \cdot 3\text{H}_2\text{O}$ , 1 mM with 1.0 PVP) was added into the flask. The reaction mixture was allowed to boil under reflux. Upon boiling, up to 1.0 mL of the reducing solution (0.1 M trisodium citrate in water) was slowly injected into the flask under stirring to avoid mass production of pure gold nanoparticles. The color of the solution turned to reddish upon reduction. The absorption spectrum is recorded, and additional citrate may be added in order to predominate the characteristic plasmon band for the GNPs, which indicate the surface coverage of MNPs with a layer of gold.

Investigation and examination of particle size and shape have been investigated using Transmission electron microscopy (TEM) (JEM 100CXII) operated at High Voltage 120 KV. Absorption spectra have been measured using UV-Vis spectrophotometer.

**2.2.4. Photodegradation Mechanism of Chloridazon.** The photodegradation of chloridazon has been monitored using UV-Visible spectrophotometer (Evolution 300) (thermo scientific) and HPLC (Bischoff). Different concentrations of chloridazon ( $1 \times 10^{-4}$  and  $5 \times 10^{-4}$ ) have been prepared by dissolving the required amounts in 10 mL methanolic solution.

Equal amounts of chloridazon solution and the catalyst have been mixed and irradiated at the same time to the light. The UV-Vis absorption spectra have been recorded at different time intervals.

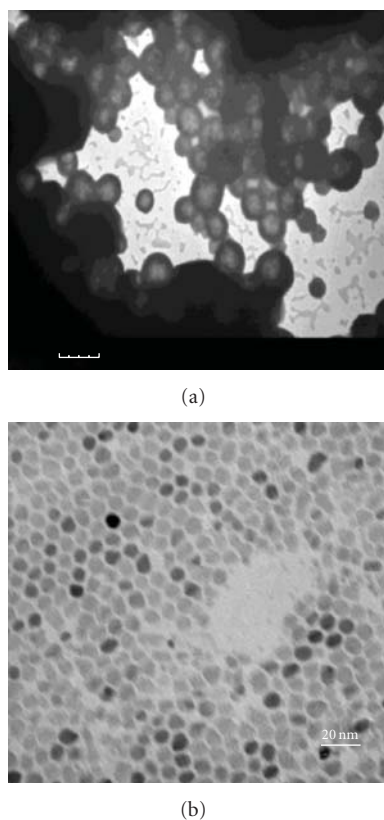


FIGURE 2: (a, b) TEM image of the prepared magnetite nanoparticles capped with ascorbic acid shows that these particles have spherical shape with average size of  $8.0 \pm 2.0$  nm.

### 3. Results

**3.1. Characterization of Magnetite Nanoparticles.** Physico-chemical properties of magnetite nanoparticles can be characterized via TEM imaging and vibrating sample magnetometry (VSM) measurements.

The TEM images of the synthesized magnetite nanoparticles show that these particles have average size of  $8.0 \pm 2.0$  nm with spherical shape as shown in Figures 2(a) and 2(b).

The magnetic measurements are done using VSM on an unoriented, random assembly of particles at room temperature; a hysteresis loop was generated from which the intrinsic coercivity ( $H_c$ ), remnant magnetization ( $M_r$ ), and saturation magnetization ( $M_s$ ) were calculated. The saturation magnetization of the product is  $5.2$  emu/g much smaller than that ( $68.7$  emu/g) of the  $Fe_3O_4$  nanoparticles sized about  $70$  nm prepared through a hydrothermal method without any surfactants [26].

**3.2. Characterization of the Prepared of Biocompatible Magneto-Optical Nanocomposite.** Magneto-optical core shell nanocomposite formed of Magnetite and gold is synthesized, where aqueous solution of gold nanoparticles capped with citrate and the core shell Magnetite-gold nanoshell were prepared as shown in the experimental section. The average size of the particles is determined from the transmission

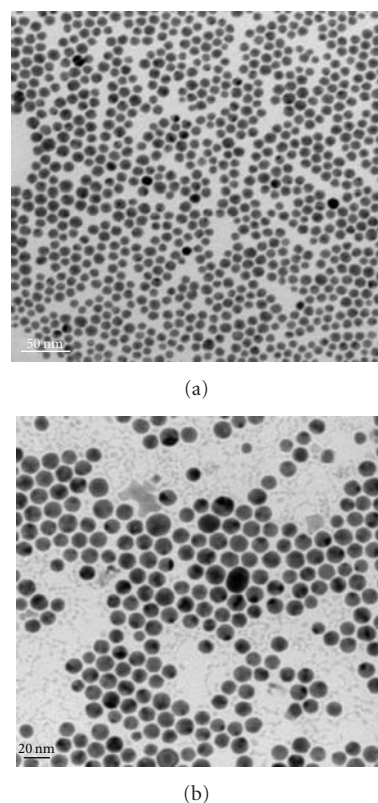


FIGURE 3: TEM images of Magneto-optical nanocomposite (magnetite-gold core shell nanocomposite) and is found to be (a)  $15$  nm, (b)  $1.1$  nm for the spherical gold nanoparticles, and core shell.

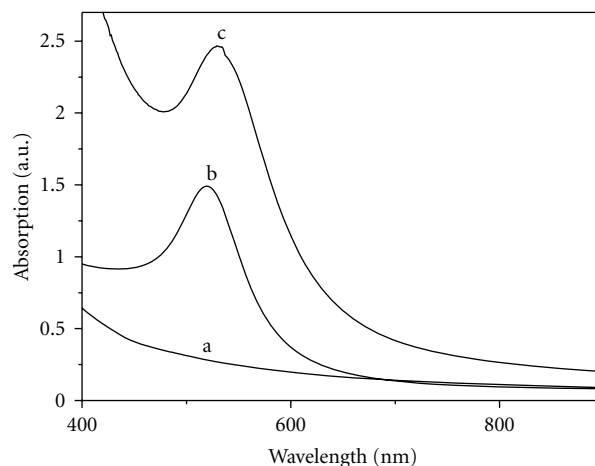


FIGURE 4: Absorption spectra of (a)  $Fe_3O_4$  and (b)  $Fe_3O_4@Au$  and (c) Au.

electron microscopic (TEM) images and is found to be  $15$  nm  $\pm$   $1.1$  nm for the spherical gold nanoparticles, and core shell is about  $18$  nm, (Figures 3(a) and 3(b)). Figure 4 presents the absorption band of  $Fe_3O_4@Au$ ,  $Fe_3O_4$ , and Au.

**3.3. Exposure to Different Concentrations Nanocomposites.** Different factors which affect the rate of photodegradation

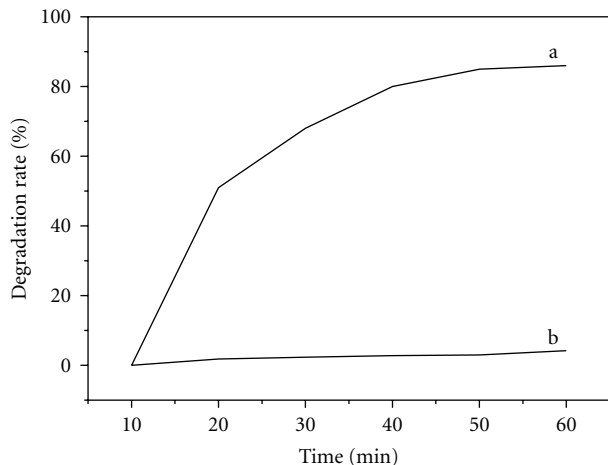


FIGURE 5: Effect of different concentration of  $\text{Fe}_3\text{O}_4\text{@Au}$  on degradation of  $10^{-5}$  M chloridazon: (a)  $10^{-4}$  M  $\text{Fe}_3\text{O}_4\text{@Au}$  and (b)  $10^{-5}$  M  $\text{Fe}_3\text{O}_4\text{@Au}$ .

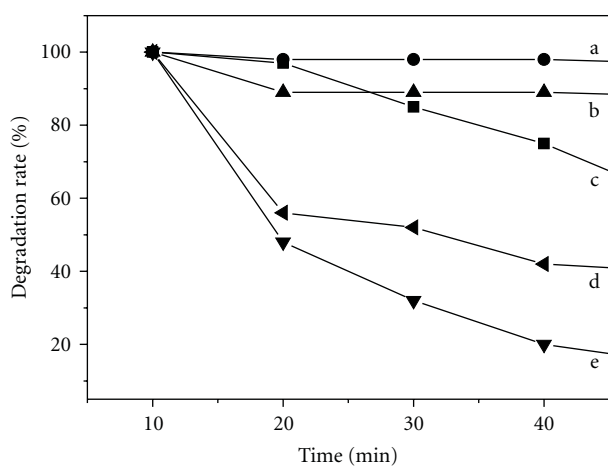


FIGURE 6: Normalized Curve shows Effect of different light sources, (a) in presence of  $\text{Fe}_3\text{O}_4$  in dark (b) in presence of  $\text{Fe}_3\text{O}_4\text{@Au}$  in dark (c) in presence of  $\text{Fe}_3\text{O}_4\text{@Au}$  in sun, (d) in presence of  $\text{Fe}_3\text{O}_4$  in UV lamp, and (e) in presence of  $\text{Fe}_3\text{O}_4\text{@Au}$  in UV lamp.

such as the catalyst concentration and the irradiation time have been investigated [27–29]. Figure 5 shows the degradation of chloridazon with different concentrations  $\text{Fe}_3\text{O}_4\text{@Au}$  nanoparticle. The rate of photodegradation has been determined by the exposure of the chloridazon-catalyst mixture to light, the rate of photodegradation and how it depends on the catalyst concentration have been studied. It is worth to mention that only 10% of the pesticides are degraded using  $10^{-5}$  M, but in case of the  $10^{-4}$ , 80% of the pesticides are degraded in less than one hour. Degradation of chloridazon with various amounts of the catalysts was studied. The results clearly emphasize that higher amount of the nanoparticles increases the production of the free radicals which accelerates the rate of degradation reaction [30].

TABLE 1: RT and integration area of HPLC peaks about products after 15 mins of photoreaction in presence of  $\text{Fe}_3\text{O}_4\text{@Au}$ .

RT (min)	3.58	7.2
Integration area (%)	19	79.14

TABLE 2: RT and integration area of HPLC peaks about products after 60 mins of photoreaction in presence of  $\text{Fe}_3\text{O}_4\text{@Au}$ .

RT (min)	3.58	7.2
Integration area (%)	36	49.47

3.4. *Exposure to Different Light Sources.* Photocatalytic reaction rate depends largely on the radiation absorption of the photocatalyst [31]. It has been reported that the degradation rate increases as the light intensity increases.

By subjecting the mixtures containing the chloridazon with the nanocomposites to sun light degradation will only occur for visible light responsive catalyst which is in our case  $\text{Fe}_3\text{O}_4\text{@Au}$ . Figure 6(c) presented that about 20% was degraded after one hour. This leads to the higher photocatalytic activity under UV-visible light. Figures 6(d) and 6(e) show that UV-C attributed a high rate of degradation of chloridazon for both nanoparticles  $\text{Fe}_3\text{O}_4$  and  $\text{Fe}_3\text{O}_4\text{@Au}$  since after 1 hour about 80% of chloridazon was degraded since high-energy source would excite more electrons from a vacancies band to conduction band; simultaneously the quantum efficiency of the nanocomposites is increased [32].

3.5. *Exposure to Different Irradiation Time.* The effect of irradiation time under the different conditions of nanocomposite concentrations and different light sources was investigated. The results shown in Figure 7 suggest that the degradation degree obviously increases with increasing the irradiation time and the increase in the rate of degradation showed the significance for using  $\text{Fe}_3\text{O}_4$  and  $\text{Fe}_3\text{O}_4\text{@Au}$  as nanocatalysts. To validate our investigations, we compared the results obtained with those obtained by a previously prepared photo-nanocatalyst synthesized by our group. As shown in Figure 7(c) chloridazon is degraded with  $\text{ZnO@Au}$  nanoparticle in quite a same trend as  $\text{Fe}_3\text{O}_4\text{@Au}$ .

3.6. *HPLC Measurements.* Chloridazon has one sharp peak at retention time 7; the decrease in the area of this band intensity and the area under the peak reflects the decomposition of the chloridazon, by subjecting the chloridazon nanocomposite mixture to UV lamp for 1 hour and comparing the results with the degradation of chloridazon subjected to UV lamp without any addition of nanoparticle. The results shown in Figure 8 illustrates that by the addition of the different synthesized nanoparticles to chloridazon a marked decrease in the peak area and the integration area percentage was obtained, while chloridazon showed photostability under the same conditions without any nanoparticles (Tables 1 and 2).

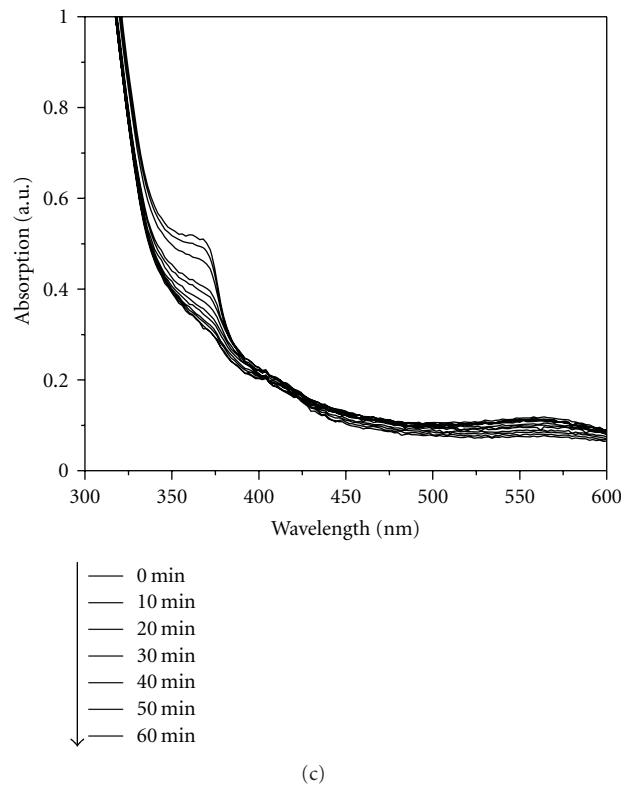
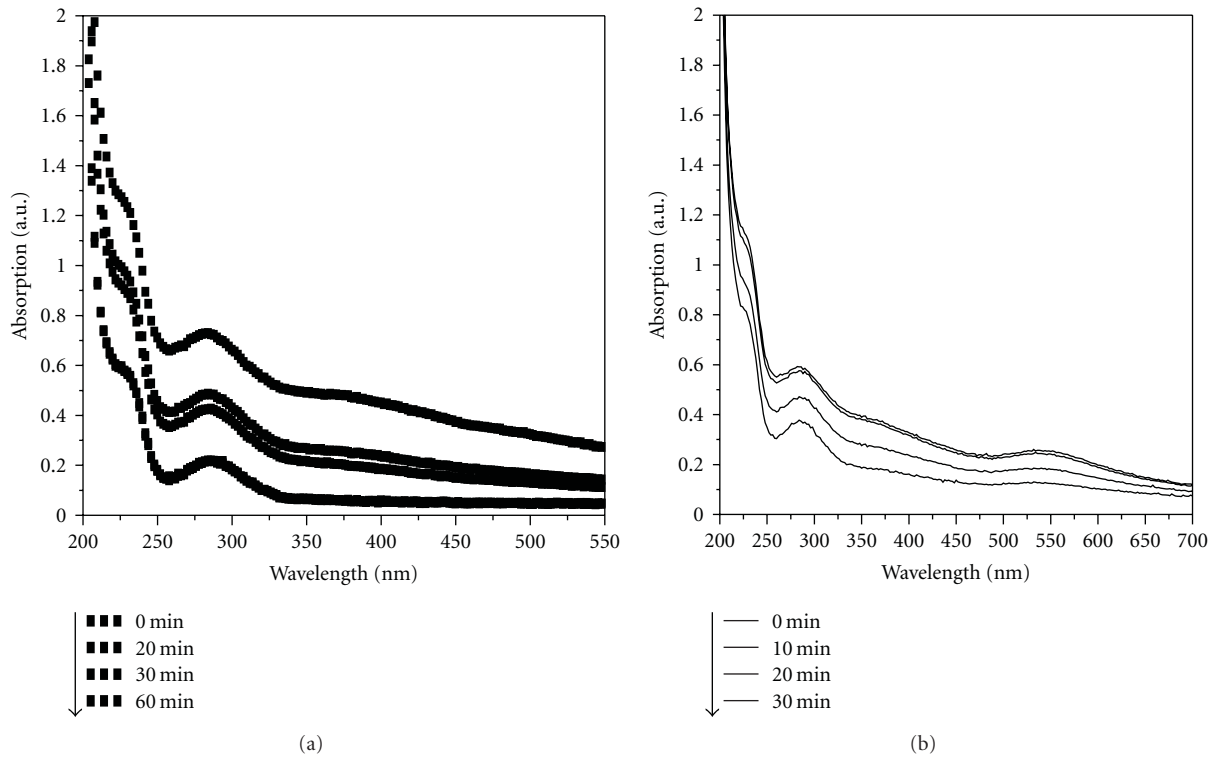


FIGURE 7: Time-dependent photodegradation of cholridazon in UV lamp. (a) Addition of  $10^{-4}$   $\text{Fe}_3\text{O}_4$ . (b) Addition of  $10^{-4}$   $\text{Fe}_3\text{O}_4@\text{Au}$ . (c) Addition of  $\text{ZnO}@\text{Au}$ .

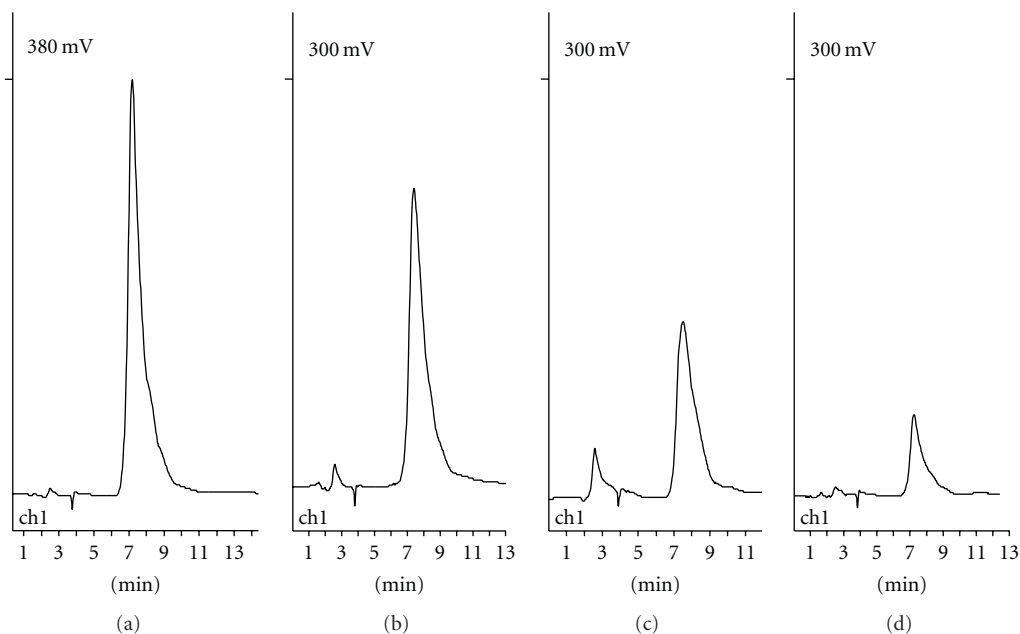


FIGURE 8: HPLC chromatograms for the photodegradation of 20 mg/L<sup>-1</sup> chloridazon using different synthesized nanoparticles: (a) chloridazon, (b) in absence of nanocomposites, (c) in presence of Fe<sub>3</sub>O<sub>4</sub>, and (d) in presence of Fe<sub>3</sub>O<sub>4</sub>@Au.

#### 4. Conclusion

Fe<sub>3</sub>O<sub>4</sub>@Au has turned out to have high efficiency in photodegradation in comparison to the Fe<sub>3</sub>O<sub>4</sub> due to the presence of the gold which has the plasmonic phenomena having a great influence in accelerating the oxidation of the pesticides.

#### References

- [1] D. Q. Jian, X. Meng, L. Ru-Ping, P. Hua-Ping, and L. Fen, "Synthesis and characterization of ferrocene modified Fe<sub>3</sub>O<sub>4</sub>@Au magnetic nanoparticles and its application," *Biosensors and Bioelectronics*, vol. 24, no. 8, pp. 2649–2653, 2009.
- [2] W. Nan, Z. Lihua, W. Dali, W. Mingqiong, L. Zhifen, and T. Heqing, "Sono-assisted preparation of highly-efficient peroxidase-like Fe<sub>3</sub>O<sub>4</sub> magnetic nanoparticles for catalytic removal of organic pollutants with H<sub>2</sub>O<sub>2</sub>," *Ultrasonics Sonochemistry*, vol. 17, no. 3, pp. 526–533, 2010.
- [3] W. Nan, Z. Lihua, W. Mingqiong, W. Dali, and T. Heqing, "Sono-enhanced degradation of dye pollutants with the use of H<sub>2</sub>O<sub>2</sub> activated by Fe<sub>3</sub>O<sub>4</sub> magnetic nanoparticles as peroxidase mimetic," *Ultrasonics Sonochemistry*, vol. 17, no. 1, pp. 78–83, 2010.
- [4] A. G. Tarek, F. Kyoko, K. Shigeru, S. Shigeo, and K. Toshinori, "Preparation and characterization of magnetically separable photocatalyst (TiO<sub>2</sub>/SiO<sub>2</sub>/Fe<sub>3</sub>O<sub>4</sub>): effect of carbon coating and calcination temperature," *Journal of Hazardous Materials*, vol. 154, no. 1–3, pp. 572–577, 2008.
- [5] Z. Ling, W. Wenzhong, Z. Lin, S. Meng, and S. Songmei, "Fe<sub>3</sub>O<sub>4</sub> coupled BiOCl: a highly efficient magnetic photocatalyst," *Applied Catalysis B*, vol. 90, no. 3–4, pp. 458–462, 2009.
- [6] T. F. Hsu, T. L. Hsiung, W. James, C. H. Huang, and H. P. Wang, "In situ XANES studies of TiO<sub>2</sub>/Fe<sub>3</sub>O<sub>4</sub>@C during photocatalytic degradation of trichloroethylene," *Nuclear Instruments and Methods in Physics Research A*, vol. 619, no. 1–3, pp. 98–101, 2010.
- [7] W. Jiang, C. Jiang, Z. Cao, X. Gong, and Z. Zhang, "Fabrication and characterization of photocatalytic activity of Fe<sub>3</sub>O<sub>4</sub>-doped CdS hollow spheres," *Journal of Physics and Chemistry of Solids*, vol. 70, no. 3–4, pp. 782–786, 2009.
- [8] L. Zhang, W. Wang, M. Shang, S. Sun, and J. Xu, "Bi<sub>2</sub>WO<sub>6</sub>@carbon/Fe<sub>3</sub>O<sub>4</sub> microspheres: preparation, growth mechanism and application in water treatment," *Journal of Hazardous Materials*, vol. 172, no. 2–3, pp. 1193–1197, 2009.
- [9] Z. Q. Zou, M. Ibisate, Y. Zhou, R. Aebersold, Y. N. Xia, and H. Zhang, "Synthesis and evaluation of superparamagnetic silica particles for extraction of glycopeptides in the microtiter plate format," *Analytical Chemistry*, vol. 80, no. 4, pp. 1228–1234, 2008.
- [10] D. K. Kim, Y. Zhang, J. Kehr, T. Klason, B. Bjelke, and M. Muhammed, "Characterization and MRI study of surfactant-coated superparamagnetic nanoparticles administered into the rat brain," *Journal of Magnetism and Magnetic Materials*, vol. 225, no. 1–2, pp. 256–261, 2001.
- [11] R. Davies, G. A. Schurr, P. Meenan et al., "Engineered particle surfaces," *Advanced Materials*, vol. 10, no. 15, pp. 1264–1270, 1998.
- [12] A. C. Templeton, W. P. Wuelfing, and R. W. Murray, "Monolayer-protected cluster molecules," *Accounts of Chemical Research*, vol. 33, no. 1, pp. 27–36, 2000.
- [13] S. Kalele, S. W. Gosavi, J. Urban, and S. K. Kulkarni, "Nanoshell particles: synthesis, properties and applications," *Current Science*, vol. 91, no. 8, pp. 1038–1052, 2006.
- [14] G. K. Kouassi and J. Irudayaraj, "Magnetic and gold-coated magnetic nanoparticles as a DNA sensor," *Analytical Chemistry*, vol. 78, no. 10, pp. 3234–3241, 2006.
- [15] C. Minard-Basquin, R. Kügler, N. N. Matsuzawa, and A. Yasuda, "Gold-nanoparticle-assisted oligonucleotide immobilisation for improved DNA detection," *IEEE Proceedings Nanobiotechnology*, vol. 152, no. 2, pp. 97–103, 2005.

- [16] L. M. Demers, C. A. Mirkin, R. C. Mucic et al., "A fluorescence-based method for determining the surface coverage and hybridization efficiency of thiol-capped oligonucleotides bound to gold thin films and nanoparticles," *Analytical Chemistry*, vol. 72, no. 22, pp. 5535–5541, 2000.
- [17] U. Kreibig and M. Vollmer, *Optical Properties of Metal Clusters*, Springer, New York, NY, USA, 1995.
- [18] G. C. Papavassiliou, "Optical properties of small inorganic and organic metal particles," *Progress in Solid State Chemistry*, vol. 12, no. 3-4, pp. 185–271, 1979.
- [19] C. F. Bohren and D. R. Huffman, *Absorption and Scattering of Light by Small Particles*, John Wiley & Sons, New York, NY, USA, 1983.
- [20] J. A. Creighton and D. G. Eadon, "Ultraviolet-visible absorption spectra of the colloidal metallic elements," *Journal of the Chemical Society, Faraday Transactions*, vol. 87, no. 24, pp. 3881–3891, 1991.
- [21] EPA, *Registration Eligibility Decision (RED) Document for Pyrazon*, US Environmental Protection Agency, 2005.
- [22] H. Mlynarcikova, J. Legath, J. Guzy, N. Kovalkovicova, and S. Ivanko, "Effect of chloridazon on the animal organism," *General Physiology and Biophysics*, vol. 18, pp. 99–104, 1999.
- [23] C. Tomlin, *The e-Pesticide Manual. Version 2.2*, British Crop Production Council, Hampshire, UK, 12th edition, 2002.
- [24] F. F. Céspedes, M. V. Sánchez, S. P. García, and M. F. Pérez, "Modifying sorbents in controlled release formulations to prevent herbicides pollution," *Chemosphere*, vol. 69, no. 5, pp. 785–794, 2007.
- [25] G. Buttiglieri, M. Peschka, T. Frömel et al., "Environmental occurrence and degradation of the herbicide n-chloridazon," *Water Research*, vol. 43, no. 11, pp. 2865–2873, 2009.
- [26] J. Wan, Y. Yao, and G. Tang, "Controlled-synthesis, characterization, and magnetic properties of Fe<sub>3</sub>O<sub>4</sub> nanostructures," *Applied Physics A*, vol. 89, no. 2, pp. 529–532, 2007.
- [27] A. J. Maira, K. L. Yeung, J. Soria et al., "Gas-phase photo-oxidation of toluene using nanometer-size TiO<sub>2</sub> catalysts," *Applied Catalysis B*, vol. 29, no. 4, pp. 327–336, 2001.
- [28] J. Krýsa, M. Keppert, J. Jirkovský, V. Štengl, and J. Šubrt, "The effect of thermal treatment on the properties of TiO<sub>2</sub> photocatalyst," *Materials Chemistry and Physics*, vol. 86, no. 2-3, pp. 333–339, 2004.
- [29] M. Saquib and M. Muneer, "TiO<sub>2</sub>/mediated photocatalytic degradation of a triphenylmethane dye (gentian violet), in aqueous suspensions," *Dyes and Pigments*, vol. 56, no. 1, pp. 37–49, 2003.
- [30] B. Neppolian, H. Jung, and H. Choi, "Photocatalytic degradation of 4-chlorophenol using TiO<sub>2</sub> and Pt-TiO<sub>2</sub> nanoparticles prepared by sol-gel method," *Journal of Advanced Oxidation Technologies*, vol. 10, no. 2, pp. 369–374, 2007.
- [31] D. Curco, J. Gimenez, A. Addardak, S. Cervera-Marcch, and S. Esplugas, "Effects of radiation absorption and catalyst concentration on the photocatalytic degradation of pollutants," *Catalysis Today*, vol. 76, no. 2–4, pp. 177–188, 2002.
- [32] X. Yibing and Y. Chunwei, "Photocatalysis of neodymium ion modified TiO<sub>2</sub> sol under visible light irradiation," *Applied Surface Science*, vol. 221, no. 1–4, pp. 17–24, 2004.

## Research Article

# Structure and Optical Properties of Doped SiO<sub>2</sub> Mesoporous Glasses

**G. Hernández-Padrón,<sup>1</sup> M. Hernández-Ortiz,<sup>2</sup> H. A. Durán-Muñoz,<sup>2</sup> M. García-Garduño,<sup>3</sup> and V. M. Castaño<sup>4</sup>**

<sup>1</sup>Departamento de Nanotecnología, Centro de Física Aplicada y Tecnología Avanzada, UNAM Campus Juriquilla, 76230, QRO, Mexico

<sup>2</sup>Programa de Posgrado en Ciencia de Materiales del Departamento de Investigación en Polímeros y Materiales, Universidad de Sonora, 83000, SON, Mexico

<sup>3</sup>División de Estudios de Posgrado e Investigación, Facultad de Odontología, UNAM, 04510, D.F., Mexico

<sup>4</sup>Departamento de Ingeniería Molecular de Materiales, Centro de Física Aplicada y Tecnología Avanzada, UNAM Campus Juriquilla, 76230, QRO, Mexico

Correspondence should be addressed to G. Hernández-Padrón, [genoveva@servidor.unam.mx](mailto:genoveva@servidor.unam.mx)

Received 31 March 2011; Accepted 19 May 2011

Academic Editor: Hongmei Luo

Copyright © 2011 G. Hernández-Padrón et al. This is an open access article distributed under the Creative Commons Attribution License, which permits unrestricted use, distribution, and reproduction in any medium, provided the original work is properly cited.

Monolithic mesoporous silica glasses were synthesized. The presence of Cu<sup>2+</sup> and Fe<sup>3+</sup> cations during the synthesis of sol-gel precursors leads to different morphologies and pore sizes. The materials are characterized via IR and Raman scattering spectra to detect surface groups and -Si-O-Si- rings (i.e., 3–6 Si atoms) and morphology is examined through electron microscopy. N<sub>2</sub> sorption isotherms reveal details of the mesoporous structure of the materials, which are endowed with significantly large surface areas and pore volumes. Vapor percolation occurs in these samples because of a void arrangement consisting of pore bulges delimited by narrower necks. The optical characterization shows the luminescence spectrum and thermoluminescent behavior subjected to successive exposures of beta particles.

## 1. Introduction

Nowadays, a number of novel materials have been investigated, from organometallics, catalysis [1], semiconductors [2], carbonaceous materials [3], to optical fibers, and so forth, aiming to develop a new generation of nanotechnology-based mesosystems [4]. The development of nanostructured materials represents special significance for optical applications. Among the materials widely investigated due to their optical properties, silica ion-doped have been proved to be competitive candidates [5]. In addition, they represent very attractive materials for selective separation and adsorption of chemical for sensing [6].

The modification of its surface to design silica materials provides a wide range of special applications. Their proper development allows studying the structural behavior at molecular level and their interactions. The sol-gel process [7–9] has acquired much interest in recent years for pro-

viding inorganic materials in which it is possible to control particle size and shape, as well as the final arrangement of the colloidal particles, in order to obtain interesting materials with improved properties. In this work, we show the nanostructure differences between of several materials synthesized by two alternative routes that employ sol-gel process.

FT-IR and surface-enhanced Raman scattering (SERS) spectroscopies have been employed as auxiliary techniques for the study of structure at the molecular level of the optical glasses based on silica [10]. Raman scattering and IR were used to determine the interaction and the structural and molecular modifications induced by the doping element and the heat treatment. IR spectroscopy was used to determine the incorporation Cu<sup>2+</sup> in the silica network.

The structural properties, particle size distribution, porous size, and surface area depend strongly of the condensation and hydrolysis rate of the gelation; therefore, the



FIGURE 1: MG<sub>1</sub>-Cu, MG<sub>2</sub>-Cu, MG<sub>3</sub>-Cu, and MG<sub>1</sub>-undoped at 110°C.



FIGURE 2: MG<sub>2</sub>-Fe and MG<sub>2</sub>-Cu at 500°C.

heat and/or use of doping metal must be tightly controlled to obtain an ordered structural arrangement.

The thermoluminescence phenomena occurred when a phosphor material is heated previously exposed to ionizing and nonionizing radiation. This is considered as an effective technique to understanding of the creation of defects generates a glow curve which is a graphical representation of light emission as a function of temperature and is related with trapping levels in the band gap, the main goal of analyzing trapping levels is to obtain several kinetic parameters [11]. The glow curves obtained for each material are different, and each glow peak is ascribed to the recombination centres and is related to the traps [12]. The luminescence properties of several silicate as gemstone exhibit good response thermo-luminescent (TL), and a number of methods to synthesize TL materials have been reported based on traditional approaches to modify the band structure of the materials as well as the characteristic of their electron traps, thus controlling to some extent the corresponding TL response [13, 14].

In this work, a series of SiO<sub>2</sub> xerogels, some of them doped with Cu<sup>2+</sup> and Fe<sup>3+</sup> ions, are synthesized by the sol-gel procedure. Porous glasses are created by precursor gels after thermal treatment at 500°C. The surface and pore morphology characteristics depicted by porous glasses are studied by surface-enhanced Raman scattering (SERS),

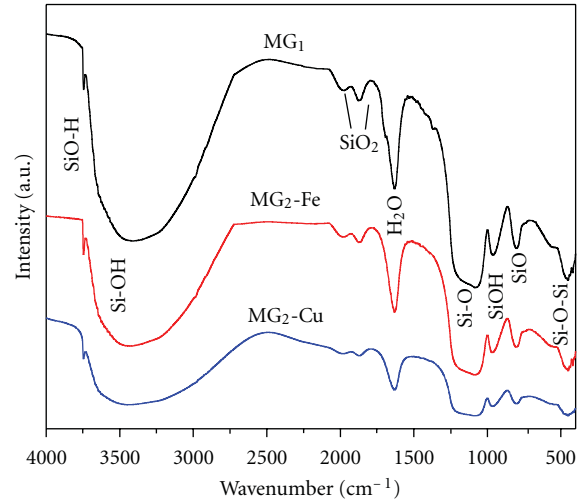


FIGURE 3: FT-IR spectra of MG<sub>1</sub>, MG<sub>2</sub>-Cu doped, and MG<sub>2</sub>-Fe doped.

TEM, and N<sub>2</sub> sorption analyses. Some optical properties were measured as the behavior of the glow curve through the technique of thermally stimulated luminescence and luminescence spectrum response.

## 2. Experimental

Mixtures of tetraethylorthosilicate (TEOS) (98% Aldrich), triple distilled water and ethanol produced SiO<sub>2</sub> gels. Doping cations came from either Cu(NO<sub>3</sub>)<sub>2</sub>·2.5H<sub>2</sub>O (Aldrich 99 wt.%) or Fe(NO<sub>3</sub>)<sub>2</sub>·9H<sub>2</sub>O (Baker 99 wt.%). Each sol synthesis was performed in a Nalgene flask at room temperature by dissolving the appropriate amount of TEOS in ethanol under a gentle stirring. Separately, suitable quantities of Cu<sup>2+</sup> or Fe<sup>3+</sup> nitrates were dissolved in water. The Cu<sup>2+</sup> or Fe<sup>3+</sup> solution was then poured inside the flask containing the TEOS mixture. The reaction system was subjected to stirring during 20 min; afterward 0.25 cm<sup>3</sup> of concentrated HCl mixed with 0.25 cm<sup>3</sup> of concentrated HF were added drop by drop while continuing the stirring for further 30 min. The resulting SiO<sub>2</sub> sol was then poured into a Nalgene cylinder where gelation rapidly occurred. Each gel was dried at 110°C for 48 h and the resulting xerogel calcined at 500°C during 24 h then obtaining SiO<sub>2</sub> cylindrical monoliths.

Molar TEOS: H<sub>2</sub>O: ethanol ratios of: 1:4:6 (MG<sub>1</sub>), 1:1:4 (MG<sub>2</sub>) and 1:3:6 (MG<sub>3</sub>) were chosen to produce an assortment of transparent monolithic glass materials. For all samples, the amounts of Cu(NO<sub>3</sub>)<sub>2</sub>·2.5H<sub>2</sub>O or Fe(NO<sub>3</sub>)<sub>2</sub>·9H<sub>2</sub>O employed for the synthesis of cation-doped xerogels corresponded to 10<sup>-3</sup> and 6 × 10<sup>-4</sup> mol per one mol of TEOS, respectively. Figure 1, shows the samples MG<sub>1</sub>-Cu, MG<sub>2</sub>-Cu, MG<sub>3</sub>-Cu, and MG<sub>1</sub>-undoped at 110°C, respectively. On the other hand, Figure 2 shows the samples MG<sub>1</sub>, MG<sub>1</sub>-Fe, and MG<sub>1</sub>-Cu at 500°C.

FT-IR silica glass spectra were measured on a Bruker Vector 33 spectrometer by means of the Diffuse Reflectance

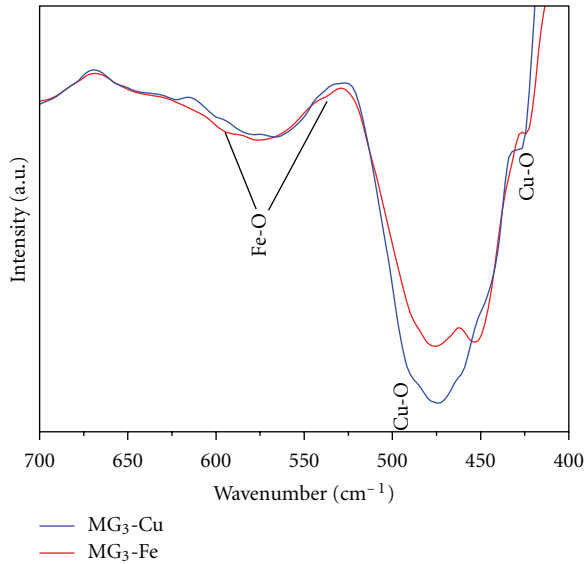


FIGURE 4: FT-IR spectra at 700–400  $\text{cm}^{-1}$  interval, for  $\text{MG}_3\text{-Cu}$  doped and  $\text{MG}_3\text{-Fe}$  doped.

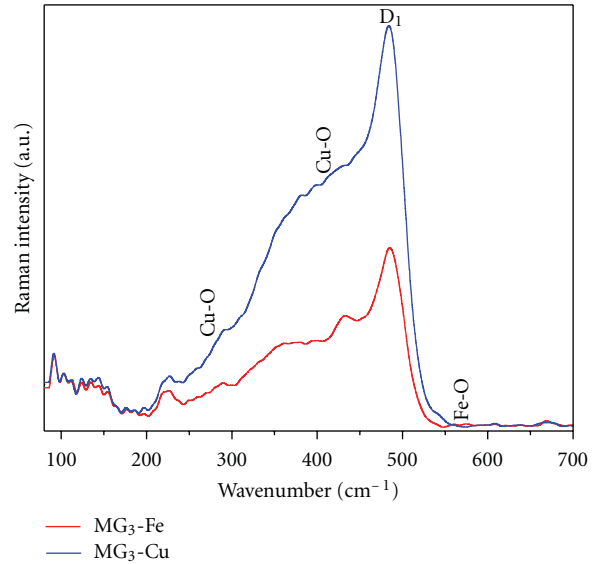


FIGURE 6: Raman scattering spectra at 80–700  $\text{cm}^{-1}$  of  $\text{MG}_3\text{-Cu}$  and  $\text{MG}_3\text{-Fe}$  doped.

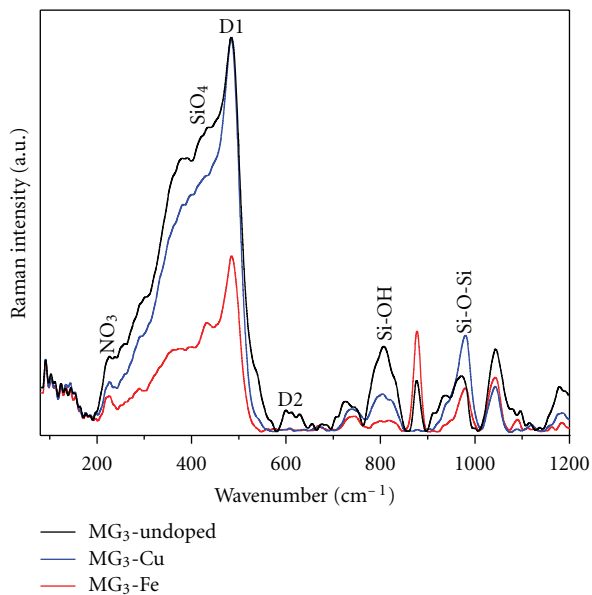


FIGURE 5: Raman scattering spectra of  $\text{MG}_3$ ,  $\text{MG}_3\text{-Cu}$ , and  $\text{MG}_3\text{-Fe}$ .

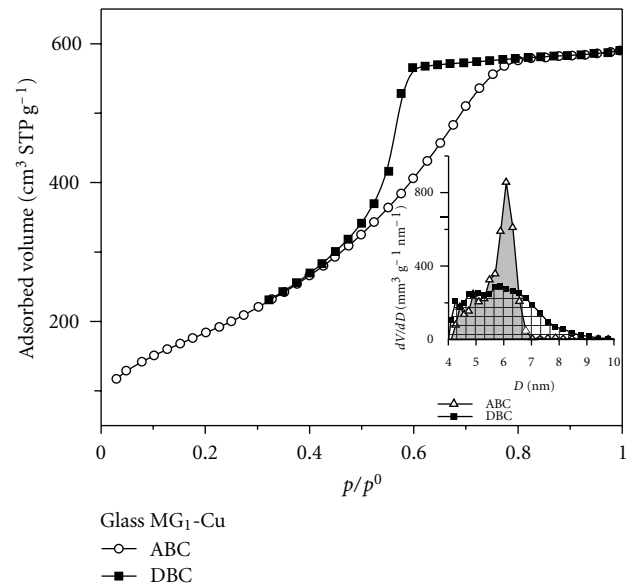


FIGURE 7:  $\text{N}_2$  sorption on (a)  $\text{MG}_3\text{-Cu}$ .

technique. Glasses were also analyzed by Raman scattering spectroscopy by mounting the cylindrical glass specimens transversally in the sampling compartment of a Senterra Bruker Raman scattering instrument with a laser 785 nm. Transmission electron microscopy (TEM) of powdery glass samples was performed in a JEOL JEM-1010 instrument.

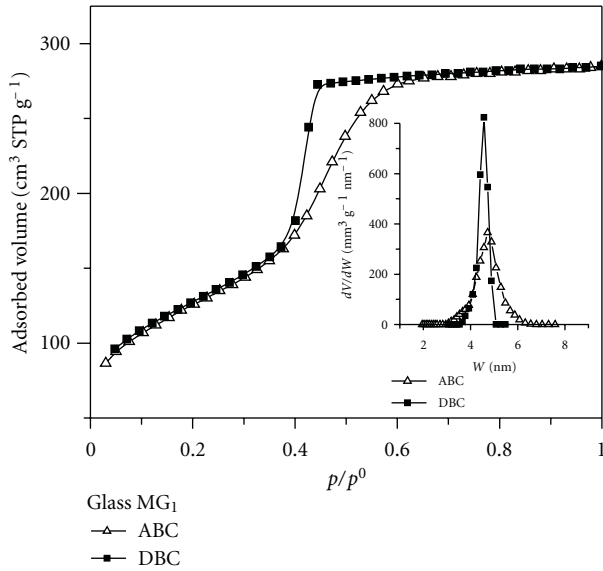
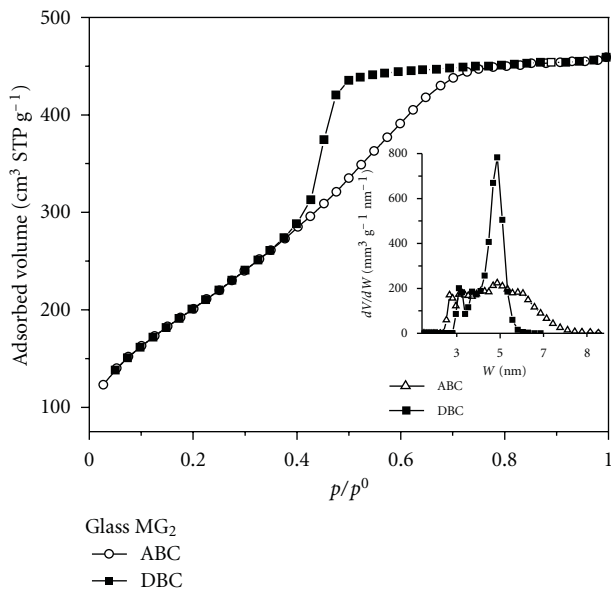
$\text{N}_2$  sorption isotherms at 76 K of powdery samples were measured in a Quantachrome Autosorb 1 instrument. The  $\text{N}_2$  and He gases were UHP grade (Praxair, 99.99%). All samples were outgassed at 200°C overnight prior to the sorption run.

TL measurements and beta irradiation were performed in a Risø TL/OSL model TL/OSL-DA-15 unit equipped

with a  $^{90}\text{Sr}$  beta source 3.33  $\text{Gy min}^{-1}$  dose rate. The TL signal was integrated from room temperature up to 650 K under  $\text{N}_2$  atmosphere using a heating rate of 1°C s $^{-1}$ . The luminescence spectra were obtained prior to the UV excitation by using a Perkin Elmer spectrofluorometer model LS50-B at room temperature.

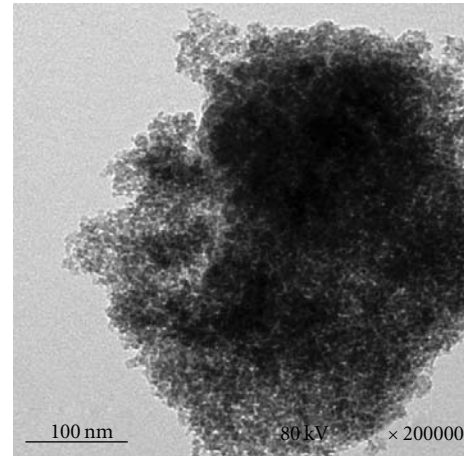
### 3. Results and Discussion

**3.1. FT-IR and Dispersive Surface-Enhanced Raman Scattering.** Figure 3 shows IR spectra of cation-undoped  $\text{MG}_1$ ,  $\text{MG}_2\text{-Cu}$ , and  $\text{MG}_2\text{-Fe}$  silica samples treated at 500°C. These

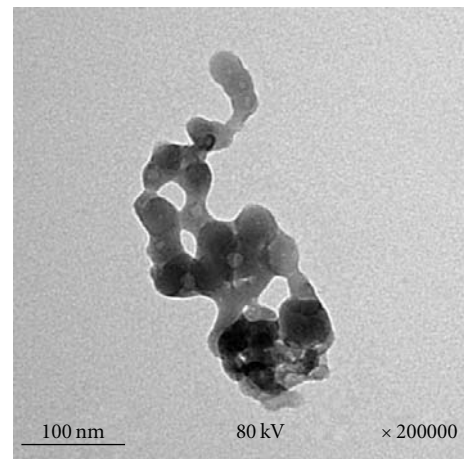
FIGURE 8: N<sub>2</sub> sorption on (a) MG<sub>1</sub> undoped.FIGURE 9: N<sub>2</sub> sorption on (a) MG<sub>2</sub> undoped.

spectra present a sharp peak at  $3746 \text{ cm}^{-1}$  due to the fundamental OH stretching vibration of the surface silanol groups (Si-OH). The wide band appearing between  $3600 \text{ cm}^{-1}$  and  $3500 \text{ cm}^{-1}$  corresponds to OH vibrations of Si-OH groups existing on the surface or hydrogen-bonded to molecular water. The peak at  $1370 \text{ cm}^{-1}$  has been interpreted as a signal proceeding from a highly disordered structure [15]. Signals characteristic of silica glass are found at  $1085 \text{ cm}^{-1}$  and  $800 \text{ cm}^{-1}$  and correspond to symmetric and asymmetric Si-O stretching modes while the band displayed at  $450 \text{ cm}^{-1}$  is due to the Si-O-Si bending model [15, 16].

In the case of FT-IR spectra of Cu-doped silica glasses (Figure 3), the vibration modes of the Cu-O groups [17, 18]



(a)



(b)

FIGURE 10: TEM micrographs of (a) MG<sub>3</sub>-Cu and (b) MG<sub>3</sub>-Fe.

should appear at  $420$ ,  $425$  and  $528 \text{ cm}^{-1}$ ; however, these peaks are hidden by the wide band centered at  $450 \text{ cm}^{-1}$  and which is assigned to Si-O-Si groups. The vibrations modes of Fe-O groups should appear at  $636$  and  $560 \text{ cm}^{-1}$  [19]. For Cu-doped MG<sub>1</sub> and Fe-doped MG<sub>2</sub> samples, the absence of the  $1370 \text{ cm}^{-1}$  band is indicative that these samples possess a more ordered structure than the cation-undoped specimens. Finally, three-member Si-O rings are detected at  $3746 \text{ cm}^{-1}$ .

Observing the Cu-O and Fe-O groups for the doped monolithic glasses in Figure 4, it is possible to see the spectra at  $700\text{--}400 \text{ cm}^{-1}$  interval to observe the Cu-O and Fe-O groups of the MG<sub>3</sub>-Cu-doped and MG<sub>3</sub>-Fe-doped samples, respectively.

The Raman scattering spectra of MG<sub>3</sub>, MG<sub>3</sub>-Cu, and MG<sub>3</sub>-Fe calcined samples are shown in Figure 5. The Si-O-Si and SiO<sub>4</sub> characteristic bands depicted at  $980 \text{ cm}^{-1}$  and  $430 \text{ cm}^{-1}$ , respectively, are indicative of the existence of a 3D glass network. The two signals occurring at  $485$  and  $610 \text{ cm}^{-1}$  are called D<sub>1</sub> and D<sub>2</sub> defect bands; D<sub>1</sub> is attributed to the emergence of 4-member Si-O rings, while D<sub>2</sub> is interpreted as a symmetrical stretching vibration of O atoms

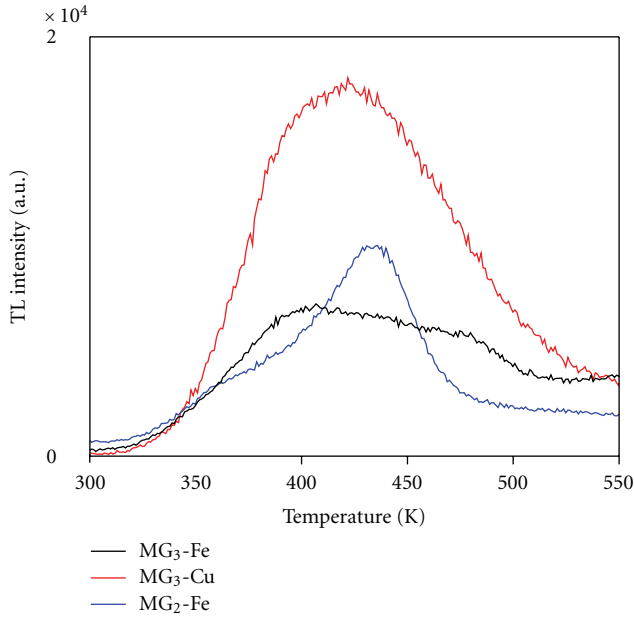


FIGURE 11: TL glow curves of SiO<sub>2</sub> glasses with different doping concentrations irradiated using a 400 Gy dose.

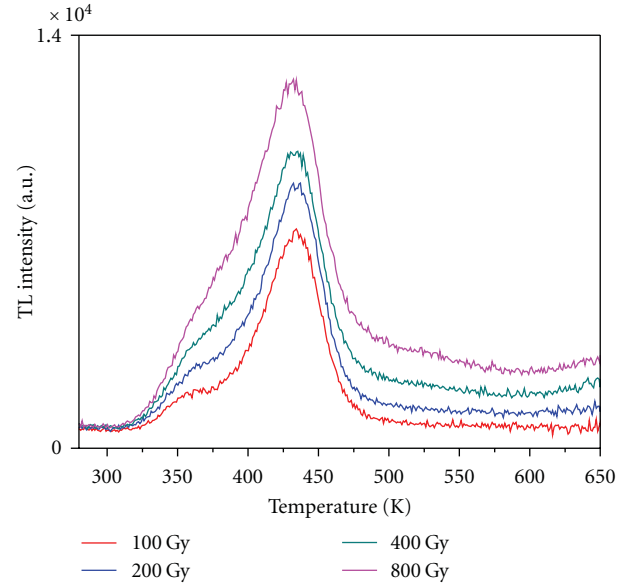


FIGURE 13: TL glow curves of MG<sub>2</sub>-Fe at different doses in the interval 100–800 Gy.

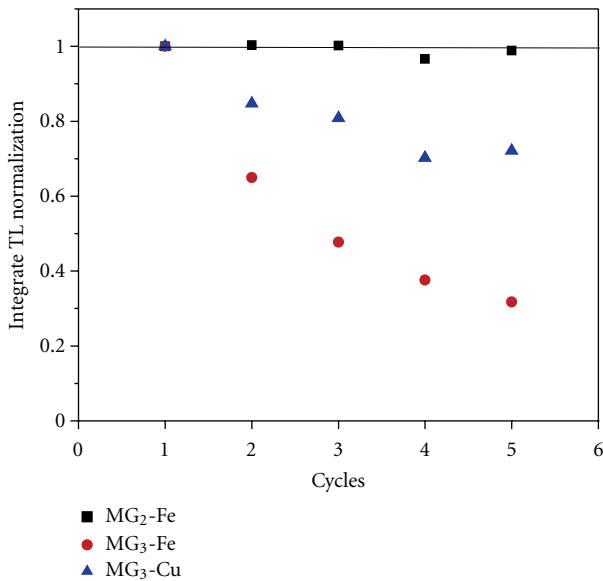


FIGURE 12: Reproducibility of the TL glow of silica glasses after being exposed 5 times to beta particles for 100 Gy dose each.

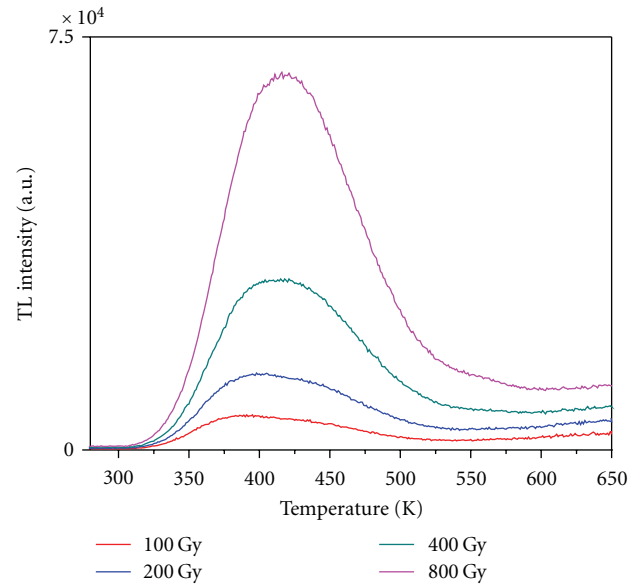


FIGURE 14: TL glow curves of MG<sub>3</sub>-Cu obtained by exposing to beta irradiation for different doses: 100–800 Gy.

constituting the Si-O three-member rings [20]. The Raman scattering spectrum of sample MG<sub>1</sub>-Cu depicts a band at 280 cm<sup>-1</sup>; this signal can be due to the crystalline lattice of Cu(NO<sub>3</sub>)<sub>2</sub> [21]. In this case, it is possible to observe the spectra at 700–80 cm<sup>-1</sup> interval, as shown in Figure 6, the Cu-O and Fe-O groups for the MG<sub>3</sub>-Cu-doped and MG<sub>3</sub>-Fe-doped samples, respectively.

3.2. *N<sub>2</sub> Sorption.* Table 1 shows the textural properties of nine SiO<sub>2</sub> glasses: in this results, we can see that the porosity glasses is adequate for catalysis system, and these properties

were obtained using a mixed of two different catalyst (HCl and HF) that obtained with only one catalyst. The biggest areas were obtained of the porous glasses with Cu-doped cation, and the best textural properties were obtained with the MG<sub>3</sub> group. On the other hand, with the Fe-doped cation was decreased the pore sizes of the SiO<sub>2</sub> glasses.

The N<sub>2</sub> sorption isotherms and pore-size distributions (PSD) of three SiO<sub>2</sub> glasses one Cu-doped (MG<sub>1</sub>-Cu) and two cation-undoped (MG<sub>1</sub> and MG<sub>2</sub>), are shown in Figures 7, 8, and 9. Also, they display the PSD functions that have been calculated by the nonlocal functional density theory

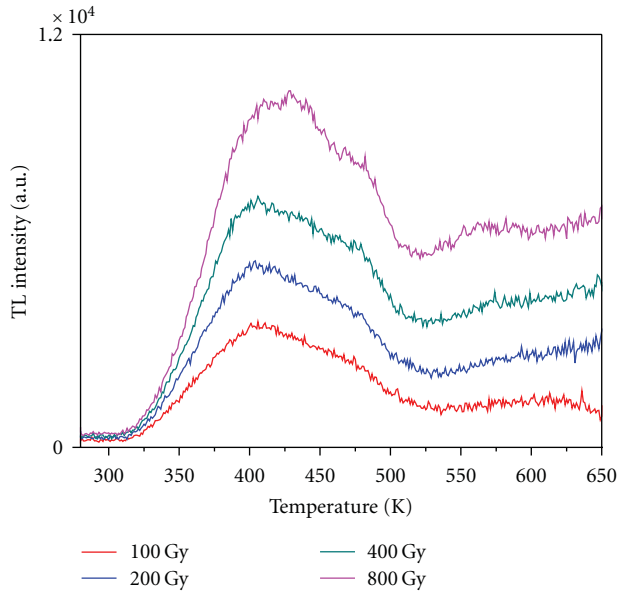


FIGURE 15: TL glow curves of  $\text{MG}_3\text{-Fe}$  at different doses in the interval 100–800 Gy.

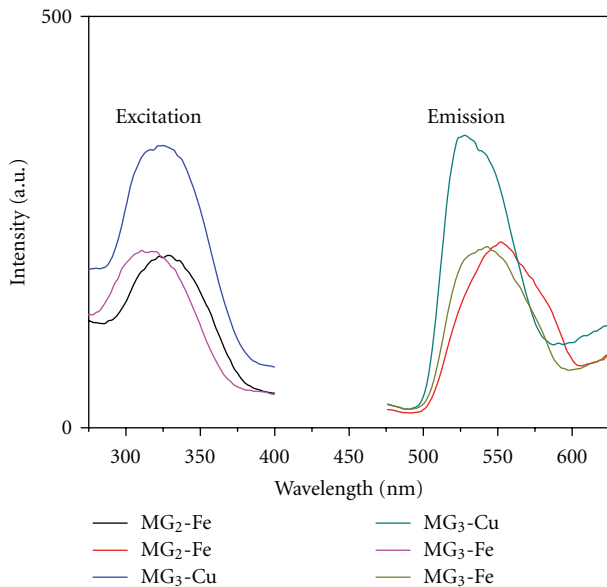


FIGURE 16: Excitation and emission spectra of  $\text{MG}_2\text{-Fe}$ ,  $\text{MG}_3\text{-Cu}$ , and  $\text{MG}_3\text{-Fe}$  taken at room temperature.

(NLDFT) procedure [22]. All isotherms correspond to IUPAC Type IV shapes while depicting IUPAC H2 hysteresis loops. An important characteristic of these isotherms is the existence of a plateau during the development of desorption boundary curve (DBC) of the hysteresis loop; on the other hand, the adsorption boundary curves (ABC) display a sloping behavior. Main textural parameters (i.e., surface area, pore volume, and mean pore size) of the glass specimens are presented in Table 1.

An interesting characteristic of porous glasses consists of the appreciable overlap between the PSD functions obtained

from the ABC and DBC isotherms. The DBC-PSD result depicts a mode value higher than the ABC-PSD outcome in all cases; this means that a pore-blocking phenomenon is taking place along the DBC.

Another interesting feature of all PSD distributions consists in pointing out that the DBC percolation peak protrudes above the ABC curve by about one third of its total area (compare the shaded peak area versus the crosshatched area in Figure 5); this means that an average connectivity ( $C$ ) of about four corresponds to the cavities of porous glass. This is due to the fact that according to percolation theory [23], the shoulder of the DBC isotherm requires a fraction of  $1/C - 1$  open bonds in order to create a percolation vapor path into the inner pores of the glass substrate. Therefore, the pore structure of glasses prepared by the sol-gel method resembles a fractal 3D network of interconnected (deformed) tetrahedral [24].

TEM photographs (Figure 10) of porous glasses reveal the fractal nature of the precursory  $\text{SiO}_2$  gels: the morphologies of the vitreous solids are similar to structures created by diffusion-limiting processes for the samples the Cu-O and Fe-O groups for the  $\text{MG}_3\text{-Cu}$ -doped and  $\text{MG}_3\text{-Fe}$ -doped samples, respectively.

**3.3. Optical Measurement.** The TL response induced by an irradiation dose of 400 Gy in  $\text{SiO}_2$  glasses with impurities:  $\text{MG}_2\text{-Fe}$ ,  $\text{MG}_3\text{-Cu}$ , and  $\text{MG}_3\text{-Fe}$ , is presented in Figure 9. Specimens display complex TL glow curve structure and support exposure to high doses [25]. Those Fe-doped show TL glow curve with two maxima, while  $\text{MG}_3\text{-Cu}$  has only one TL peak around of 420 K. Silica glasses TL glow curves after successive exposures to beta particles are present in Figure 10. Each was obtained by irradiating the same monolith during a dose of 100 Gy. The reproducibility of the TL glow curves for  $\text{MG}_2\text{-Fe}$  irradiated 5 times is  $\pm 2\%$  better samples realized with other reagent concentration. Figures 11–15 illustrate the TL glow curves of the irradiated samples, respectively, at different laboratory doses, in the interval of 100–800 Gy. As can be seen, the maxima of the curves for the Fe-doped samples appear in the same position regardless doses, which indicates that first-order processes are involved in the TL phenomenon [26]. On the other hand, the Cu-doped specimen not have the same conduct; however, all samples do not present saturation of the TL response for the used doses. Therefore, cation-doped directly influences in the creation of various traps and recombination centres of  $\text{SiO}_2$  nanostructures mesoporous glasses.

Figure 14 shows the luminescence spectrums comparison of  $\text{MG}_2\text{-Fe}$ ,  $\text{MG}_3\text{-Cu}$ , and  $\text{MG}_3\text{-Fe}$  taken at room temperature without annealing. Silica glasses  $\text{MG}_3$  excitation band is centered at 314 nm, and the emission is centered at 525 nm, while the  $\text{MG}_2$  monolith present excitation and emission band centered in 330 and 550, respectively (Figure 16). There are small shift in the spectra for each specimen type, but there are not important differences between the spectra for distinct doping. In both samples, the main emission occurs around the green.

TABLE 1: Textural properties of porous glasses.

Sample	MG <sub>1</sub>	MG <sub>1</sub> -Fe	MG <sub>1</sub> -Cu	MG <sub>2</sub>	MG <sub>2</sub> -Fe	MG <sub>2</sub> -Cu	MG <sub>3</sub>	MG <sub>3</sub> -Fe	MG <sub>3</sub> -Cu
$A_{\text{BET}}/\text{m}^2 \text{g}^{-1}$	449	352	680	766	134	711	298	970	629
$V^{\text{P}}/\text{mm}^3 \text{g}^{-1}$	440	322	609	706	181	605	3630	1908	1749
$\overline{W}_{\text{DBC}}/\text{nm}$	4.7	3.4	6.0	4.8	3.5	3.7	4.8	6.0	6.8

$A_{\text{BET}}$   $\equiv$  BET area;  $V^{\text{P}}$   $\equiv$  pore volume;  $\overline{W}_{\text{DBC}}$   $\equiv$  DBC mean pore widths.

## 4. Conclusions

The sol-gel process assisted by supercritical drying is an efficient method to fabricate highly porous monolithic silica materials. A variety of porous glasses of outstanding surface areas and mesopore volumes can be synthesized by the sol-gel procedure. Thermal treatment of precursory gels produces mesoporous substrates free of micropores and of well-defined pore volumes. The effect of doping cations consists in decreasing the pore sizes of the resultant glasses.

## Acknowledgments

The authors would like to thank M. A. Lourdes Palma Tirado for technical support by TEM, M. en C. Alicia Del Real López for technical support by EDX analysis, M. en C. Carmen Peza Ledesma by help in textural properties measurement, and M. en C. Guillermo Vázquez Sánchez for the processing photographs.

## References

- [1] M. Esparza, M. L. Ojeda, A. Campero et al., "Development and sorption characterization of some model mesoporous and microporous silica adsorbents," *Journal of Molecular Catalysis A*, vol. 228, no. 1-2, pp. 97–110, 2005.
- [2] F. Schlottig, M. Textor, U. Georgi, and G. Roewer, "Template synthesis of SiO<sub>2</sub> nanostructures," *Journal of Materials Science Letters*, vol. 18, no. 8, pp. 599–601, 1999.
- [3] S. A. Mahadik, M. S. Kavale, S. K. Mukherjee, and A. R. Venkateswara, "Transparent superhydrophobic silica coatings on glass by sol-gel method," *Applied Surface Science*, vol. 257, no. 2, pp. 333–339, 2010.
- [4] A. de Keizer, E. M. van der Ent, and L. K. Koopal, "Surface and volume charge densities of monodisperse porous silicas," *Colloids and Surfaces A*, vol. 142, no. 2-3, pp. 303–313, 1998.
- [5] G. Chunlei, J. Miao, Y. Liu, and Y. Wang, "Meso-macroporous monolithic CuO—CeO<sub>2</sub>/c-Al<sub>2</sub>O<sub>3</sub> catalysts and their catalytic performance for preferential oxidation of CO," *Journal of Materials Science*, vol. 45, no. 20, pp. 5660–5668, 2010.
- [6] D. D. Xiaobo Liu and H. Wencheng, "The structure and mechanism of porous silica films by sol-gel method using poly(ethylene glycol) and side-chain polyether modified polydimethylsiloxane with terminal Si—CH<sub>3</sub> as templates," *Journal of Materials Science*. In press.
- [7] C. Sanchez, L. Rozes, F. Ribot et al., "'Chimie douce': a land of opportunities for the designed construction of functional inorganic and hybrid organic-inorganic nanomaterials," *Comptes Rendus Chimie*, vol. 13, no. 1-2, pp. 3–39, 2010.
- [8] A. Mc Cormick, "Recent progress in the study of the kinetics of sol-gel SiO<sub>2</sub> synthesis reactions," in *Sol-Gel Processing and Applications*, Y. A. Attia, Ed., pp. 1–16, Plenum Press, New York, NY, USA, 1994.
- [9] W. Stöber, A. Fink, and E. Bohn, "Controlled growth of monodisperse silica spheres in the micron size range," *Journal of Colloid and Interface Science*, vol. 26, no. 1, pp. 62–69, 1968.
- [10] L. L. Hench and J. Livage, "The sol-gel process," *Chemical Reviews*, vol. 90, no. 1, pp. 34–72, 1990.
- [11] V. Pagonis, G. Kitis, and C. Furetta, *Numerical and Practical Exercises in Thermoluminescence*, Springer, New York, NY, USA, 2006.
- [12] C. Furetta, S. Guzmán, B. Ruiz, and E. Cruz-Zaragoza, "The initial rise method extended to multiple trapping levels in thermoluminescent materials," *Applied Radiation and Isotopes*, vol. 69, no. 2, pp. 346–349, 2011.
- [13] V. Correcher, J. M. Gomez-Ros, J. Garcia-Guinea, M. Lis, and L. Sanchez-Muñoz, "Calculation of the activation energy in a continuous trap distribution system of a charoite silicate using initial rise and TL glow curve fitting methods," *Radiation Measurements*, vol. 43, no. 2–6, pp. 269–272, 2008.
- [14] D. Mendoza-Anaya, C. Angeles, P. Salas, R. Rodríguez, and V. M. Castaño, "Nanoparticle-enhanced thermoluminescence in silica gels," *Nanotechnology*, vol. 14, no. 12, pp. L1–L4, 2003.
- [15] J. C. Cheang, A. Oliver, J. Roiz et al., "Optical properties of Ir<sup>2+</sup>-implanted silica glass," *Nuclear Instruments and Methods in Physics Research B*, vol. 175–177, pp. 490–494, 2001.
- [16] C.-K. Wu, "Stable silicate glasses containing up to 10 weight percent of water," *Journal of Non-Crystalline Solids*, vol. 41, no. 3, pp. 381–398, 1980.
- [17] J. R. Martínez, F. Ruiz, Y. V. Vorobiev, F. Pérez-Robles, and J. González-Hernández, "Infrared spectroscopy analysis of the local atomic structure in silica prepared by sol-gel," *Journal of Chemical Physics*, vol. 109, no. 17, pp. 7511–7514, 1998.
- [18] T. Woignier, C. Fernandez-Lorenzo, J. L. Sauvajol, J. F. Schmit, J. Phalippou, and R. Sempere, "Raman study of structural defects in SiO<sub>2</sub> aerogels," *Journal of Sol-Gel Science and Technology*, vol. 5, no. 3, pp. 167–172, 1995.
- [19] M. Vilarigues and R. C. da Silva, "The effect of Mn, Fe and Cu ions on potash-glass corrosion," *Journal of Non-Crystalline Solids*, vol. 355, no. 31–33, pp. 1630–1637, 2009.
- [20] H.-Y. Zhu, R. Jiang, L. Xiao, and W. Li, "Preparation, characterization and adsorption application for removal of hazardous azo dye," *Journal of Hazardous Materials*, vol. 179, no. 1–3, pp. 251–257, 2010.
- [21] V. M. Miskowski, S. Franzen, A. P. Shreve et al., "Distortional isomers of a mixed-valence binuclear Cu complex," *Inorganic Chemistry*, vol. 38, pp. 2546–2547, 1999.
- [22] P. I. Ravikovitch and A. V. Neimark, "Characterization of micro- and mesoporosity in SBA-15 materials from adsorption data by the NLDFT method," *Journal of Physical Chemistry B*, vol. 105, no. 29, pp. 6817–6823, 2001.
- [23] R. P. Iczkowski, "Electrical conductivity of partially saturated porous solids," *Industrial and Engineering Chemistry Fundamentals*, vol. 7, no. 4, pp. 572–576, 1970.

- [24] G. Mason and D. W. Mellor, "Simulation of drainage and imbibition in a random packing of equal spheres," *Journal of Colloid and Interface Science*, vol. 176, no. 1, pp. 214–225, 1995.
- [25] G. Zgrablich, V. Mayagoitia, F. Rojas et al., "Molecular processes on heterogeneous solid surfaces," *Langmuir*, vol. 12, no. 1, pp. 129–138, 1996.
- [26] J. Morales, R. Bernal, C. Cruz-Vazquez, E. G. Salcido-Romero, and V. M. Castaño, "Thermoluminescence of tequila-based nanodiamond," *Radiation Protection Dosimetry*, vol. 139, no. 4, pp. 1–4, 2010.

## Research Article

# Light-Emitting Polymer Nanocomposites

**Kyle Gipson, Brett Ellerbrock, Kathryn Stevens, Phil Brown, and John Ballato**

*Center for Optical Materials Science and Engineering Technologies (COMSET) and The School of Materials Science and Engineering, Clemson University, Clemson, SC 29634, USA*

Correspondence should be addressed to John Ballato, jballat@clemson.edu

Received 15 March 2011; Accepted 28 April 2011

Academic Editor: Hongmei Luo

Copyright © 2011 Kyle Gipson et al. This is an open access article distributed under the Creative Commons Attribution License, which permits unrestricted use, distribution, and reproduction in any medium, provided the original work is properly cited.

Inorganic nanoparticles doped with optically active rare-earth ions and coated with organic ligands were synthesized in order to create fluorescent polymethyl methacrylate (PMMA) nanocomposites. Two different aromatic ligands (acetylsalicylic acid, ASA and 2-picolinic acid, PA) were utilized in order to functionalize the surface of  $Tb^{3+} : LaF_3$  nanocrystals. The selected aromatic ligand systems were characterized using infrared spectroscopy, thermal analysis, rheological measurements, and optical spectroscopy. Nanoparticles produced *in situ* with the PMMA contained on average 10 wt% loading of  $Tb^{3+} : LaF_3$  at a 6 : 1 La : Tb molar ratio and ~7 wt% loading of 4 : 1 La : Tb molar ratio for the PA and ASA systems, respectively. Measured diameters ranged from  $457 \pm 176$  nm to  $150 \pm 105$  nm which is indicative that agglomerates formed during the synthesis process. Both nanocomposites exhibited the characteristic  $Tb^{3+}$  emission peaks upon direct ion excitation (350 nm) and ligand excitation (PA : 265 nm and ASA : 275 nm).

## 1. Introduction

Rare-earth (RE) ions doped into inorganic matrices have been utilized as luminescent additives in applications such as light-emitting devices, lasers, optical amplifiers, and biological fluorescence labeling [1]. RE ions are ideal additives due to their ability to produce intense narrow spectral bands in the visible range of the electromagnetic spectrum and exhibit long excited-state lifetimes as a result of f-f electronic transitions [2, 3].

With respect to many inorganic materials, polymer matrices have the potential to offer improved production rates, lower cost, and improved processability. However, polymers exhibit inherently high vibrational energies which tend to quench many of the transitions of rare-earth ions thus limiting their application as optical materials [4]. RE ions are typically incompatible with organic polymers; although, PMMA has been shown suitable when utilized as a matrix for certain RE ion ligand complexes [5].

In this research, the method utilized to overcome high vibrational energy observed in PMMA is to incorporate optically active RE ions into low vibrational energy inorganic nanoparticles which then are dispersed into a polymer matrix by the use of selective organic ligands. The inorganic

component is rare-earth ion phosphor, (terbium III), doped lanthanum trifluoride ( $LaF_3$ ) nanocrystals. Terbium (III) ( $Tb^{3+}$ ) emits green fluorescence as a result of a strong electronic transition,  $^5D_4 \rightarrow ^7F_5$ , occurring near 543 nm.  $Tb^{3+}$  exhibits absorption levels at shorter wavelengths in the ultraviolet (UV) to visible color region (390–780 nm) [6]. Consequently, RE ions like  $Tb^{3+}$  are incorporated into an inorganic host that is surface-treated or capped with UV light harvesting ligands to boost the absorption capability of the RE.

$Tb^{3+}$  is incorporated into the inorganic crystal structure of lanthanum trifluoride,  $LaF_3$  to create the doped nanocrystal ( $Tb^{3+} : LaF_3$ ).  $LaF_3$ , was chosen as the host matrix for terbium due to the low phonon energy it exhibits which minimizes the quenching potential of  $Tb^{3+}$  ion emissions [7–10]. The organic portion refers to UV light harvesting ligands that bind to the surface of the nanocrystal to form a coordination complex. The ligands purpose is to enhance emissions and aid in dispersion within the organic polymer matrix. Light harvesting refers to the ability of the ligand to absorb light from short wavelengths and transfer the energy to the rare-earth ion which emits light at longer wavelengths [3, 11]. The light-harvesting ligand capped nanocrystal complex is considered to be the complete nanoparticle.

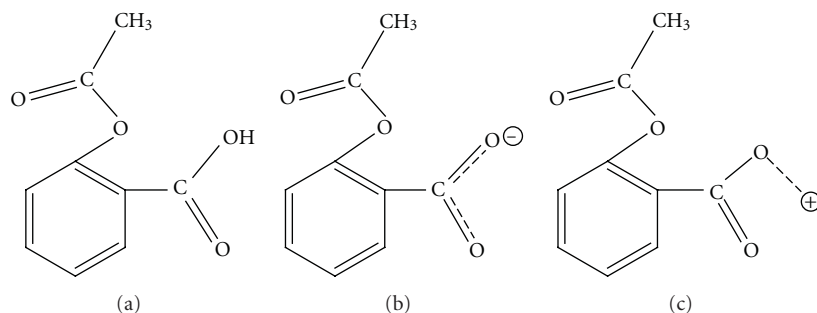


FIGURE 1: ASA molecule (a), ASA anion (b), and ASA chelation of cation (c).

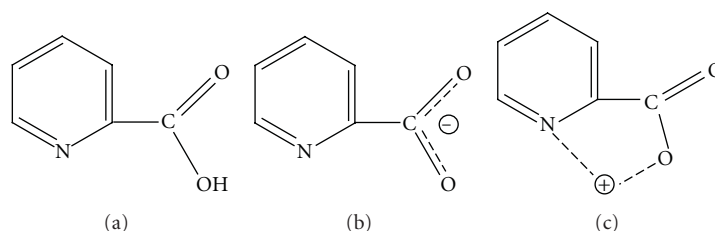


FIGURE 2: PA molecule (a), PA anion (b), and PA chelation of cation (c).

Aromatic acids have been used as ligands to sensitize and enhance lanthanide fluorescence by reducing the probability of radiationless (heat) energy transfer from the RE ion to the solvent [12]. Both acetylsalicylic acid (ASA) and 2-picolinic acid (PA) are aromatic acids and bidentate ligands. ASA deprotonates the carboxyl group which forms dianions with the ability to coordinate cations like RE ions [13]. The structures of ASA are depicted in Figure 1: (a) molecule, (b) anion where the hydrogen of carboxyl group was ionized, and (c) chelated structure of cation where the oxygen of the carboxyl group bonds to the cation. PA chelates cations through the nitrogen atom of the pyridine ring and the oxygen anion of deprotonated carboxyl group as illustrated in Figure 2. In Figure 2, (a) is the molecule, (b) is the anion where the hydrogen of carboxyl group was ionized, and (c) is the chelated structure of cation where the oxygen of the carboxyl group acts with the nitrogen atom to bond with the cation [14].

The incorporation and distribution of nanoparticles has been shown to affect the viscoelastic properties of polymers [15]. The focus of this research is to develop light-emitting polymer nanocomposites via solution/precipitation chemistry in order to understand the influence of the nanoparticles on the thermal, rheological, and photoluminescence characteristics of the resultant polymer nanocomposite.

## 2. Experimental

**2.1. Materials.** The PMMA ( $M_w \approx 130$  k—Plaskolite West, Inc.) was used as received. Anhydrous tetrahydrofuran, THF (99%—Acros), methanol (99.8%—BDH), and ultrapure water (18.2 M $\Omega$ ·cm) were used as solvents. Lanthanum (III) nitrate hexahydrate, La (La(NO<sub>3</sub>)<sub>3</sub>·6H<sub>2</sub>O, 99.99%—Sigma-Aldrich) and terbium (III) nitrate hydrate, Tb<sup>3+</sup>

(Tb(NO<sub>3</sub>)<sub>3</sub>·6H<sub>2</sub>O, 99.9%—Sigma-Aldrich), acetylsalicylic acid, ASA (MP Biomedicals, LLC), 2-picolinic acid, PA (99%—Alfa Aesar), ammonium fluoride (99.3%—Fisher Scientific), ammonium hydroxide (28–30% ACS—BDH Aristar-VWR), ethanol-EtOH (99.5%—Acros), and acetone (99.9%—BDH) were used as received.

**2.2. Synthesis.** The nanoparticles were produced by the scheme shown in Figure 3.

**2.3. Characterization.** Dried precipitated polymer and precipitated polymer nanocomposite samples were analyzed by attenuated total reflectance—Fourier transform infrared (ATR-FTIR) spectroscopy. The spectra were acquired on a Thermo-Fisher Nicolet Magna 550 FTIR spectrometer equipped with a Thermo-SpectraTech Foundation Series Diamond ATR accessory, Nic-Plan microscope, and Omnic software. The spectral resolution was set at 8 cm<sup>-1</sup> and 160 scans were conducted at room temperature.

Glass transition temperature ( $T_g$ ) was determined by a Universal TA Instruments—2920 MDSC V2.6A differential scanning calorimeter (DSC). Approximately 5 mg of sample was placed in a hermetic sample pan for measurements. The instrument was equilibrated at a temperature of 25°C. The temperature ramp rate was set at 20°C/min to a maximum of 300°C. The samples were removed, quenched with liquid nitrogen, and then rerun under the same heating regimen. The traces were analyzed using TA Instruments Universal Analysis 2000 version 4.4a software.

Percent nanocrystal loading was determined by a Universal TA Instruments—TGA Q5000 V3.5 Build 252 thermogravimetric analysis instrument (TGA). Samples weighing

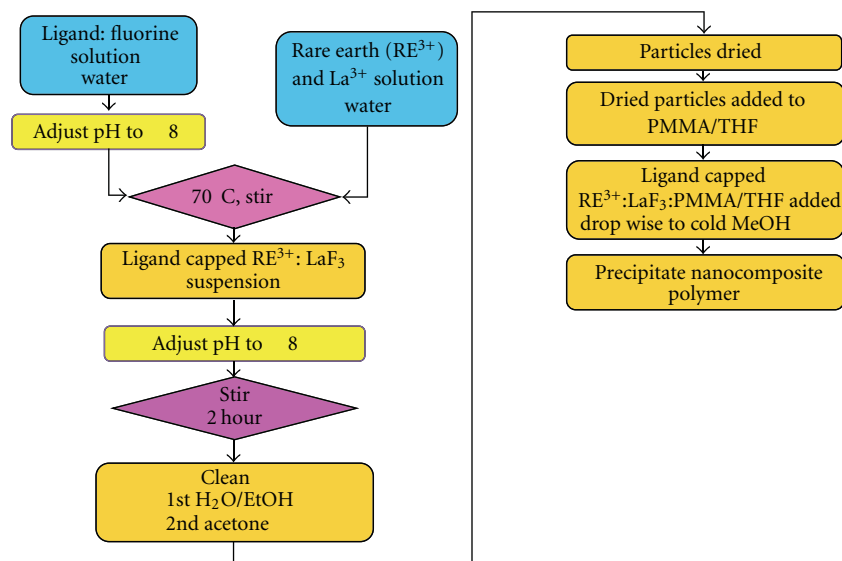


FIGURE 3: Flow chart of nanoparticle synthesis.

approximately 5 mg were loaded into a platinum pan and then placed in the instrument under nitrogen. The temperature ramp rate was  $10^{\circ}\text{C}/\text{min}$  to  $650^{\circ}\text{C}$ . Nanoparticle loading values were determined from the percent of material remaining at  $495^{\circ}\text{C}$  using TA Instruments Universal Analysis 2000 version 4.4a software.

Size and size distribution of particles were measured on a Malvern Dynamic Light Scattering (DLS) Zetasizer Nano Series Nano ZS at room temperature. Teflon spheres were used to ball-mill the dried samples into a fine powder before a resuspension in a neat solvent. The average of three samples was used to determine the size and size distributions.

Viscosity measurements were performed using a TA Instruments—ARES LS/M 0012701 Rheometer equipped with the TA Orchestrator version 7.1.2.3 software package. Dynamic frequency sweep tests were performed under a nitrogen environment in the frequency range of 0.1 to 500 rad/s at  $220^{\circ}\text{C}$ . Cone and plate geometry was used where the plates had a diameter of 25 mm and the cone angle was set at 0.1 rad. The gap distance during the measurements was set at 0.056 mm and the strain was maintained at 5%.

A Perkin Elmer Lambda 900 UV-Vis-NIR Spectrometer with UV Winlab Version 3.00.03 software was utilized to gather optical absorption data. Scans were performed with a 1 nm slit size in the UV and visible range of 260–380 nm. Samples were prepared by dispersing the ligand into water and measurements were done at room temperature.

Photoluminescence measurements were performed with a Jobin-Yvon Fluorolog Tau 3 Fluorometer with 4 nm emission bandpass. The data were collected at 1 nm intervals with 50 ms integration time. All measurements were performed at room temperature. Excitation spectra were fit with Lorentzian curves correcting for a constant background in Igor Pro 6.1 (Wavemetrics, Portland, Oregon) for full width at half maximum (FWHM) measurements.

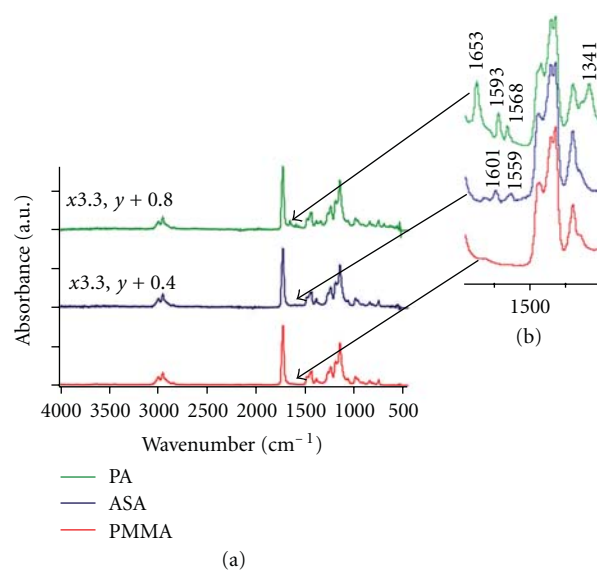


FIGURE 4: Absorbance as a function of wavenumber—infrared spectra of undoped precipitated PMMA (red), ASA capped nanocrystals incorporated into precipitated PMMA (blue), and PA capped nanocrystals incorporated into precipitated PMMA (green) in the range of  $4000\text{--}500\text{ cm}^{-1}$  (a) and inset—range  $1700\text{--}1300\text{ cm}^{-1}$  (b).

### 3. Results and Discussion

**3.1. Characterization of Ligand Capped Nanoparticles.** Figure 4 shows the FT-IR spectra comparison of undoped precipitated PMMA, ASA and PA capped nanocrystals loaded into PMMA. The region of interest is located in the range of  $1700\text{--}1300\text{ cm}^{-1}$ , inset of Figure 4. Absorption peaks at  $1601\text{ cm}^{-1}$  and  $1559\text{ cm}^{-1}$  were observed in FT-IR spectrum for the ASA, doped PMMA and suggest benzene ring stretching. The spectrum for the PA doped system exhibits absorption peaks at around  $1653\text{ cm}^{-1}$ ,  $1593\text{ cm}^{-1}$ ,

TABLE 1: Percent loadings and glass transition temperature of ligand capped nanocrystals in PMMA.

Ligand	Ligand to nanoparticle ratio	Calculated loading	Experimental loading	Inflection point $T_g$ , °C
ASA	2 : 1	10%	9%	120
	3 : 1	10%	9%	121
	4 : 1	10%	10%	121
	5 : 1	10%	10%	121
PA	2 : 1	10%	7%	121
	3 : 1	10%	7%	122
	4 : 1	10%	7%	120
	5 : 1	10%	8%	121
undoped PMMA precipitated			0%	122

TABLE 2: Elemental composition and corresponding atomic percentage of nanoparticles in PMMA at different ligand:nanoparticle ratios.

Element	Atomic percentage							
	PA				ASA			
	2 : 1	3 : 1	4 : 1	5 : 1	2 : 1	3 : 1	4 : 1	5 : 1
La	61.2	46.4	49.1	30.8	43.0	30.4	32.6	30.8
Tb	6.6	8.0	8.1	4.9	9.1	8.2	7.7	7.3
F	32.2	45.6	42.7	64.3	47.9	61.4	59.5	60.0

and  $1568\text{ cm}^{-1}$  which can be associated with aromatic ring stretching of the pyridine ring of picolinic acid. The IR peak observed at approximately  $1341\text{ cm}^{-1}$  could correspond to the C-N stretching vibrations of the PA ligand. Therefore, both ligands are present in the PMMA matrix.

The loading of the inorganic components ( $\text{Tb}^{3+}:\text{LaF}_3$ ) and  $T_g$  obtained from TGA and DSC, respectively, are presented in Table 1. PMMA loaded with ASA ligand capped nanoparticles (hence forth referred to as the ASA system) contained  $\sim 10\text{ wt}\%$  inorganic material. Whereas the PMMA loaded with PA ligand capped nanoparticles (PA system) contained inorganic material on the order of  $7\text{ wt}\%$ . However, the measured amounts of inorganic material for each ligand sample were kept constant experimentally. The difference in inorganic material amounts might be attributed to loss of product during the cleaning steps of the particle synthesis.

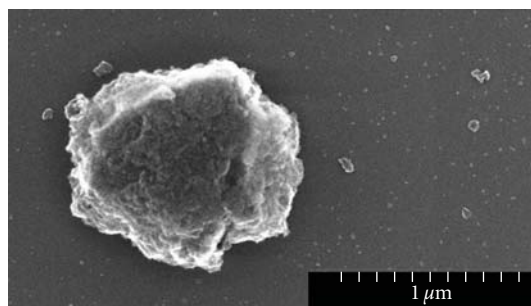
No significant change in  $T_g$  was observed between the undoped PMMA and the nanoparticle-loaded PMMA systems. The glass transition inflection point was used to determine the  $T_g$  and the average of two sample runs is stated as the  $T_g$  for each sample in Table 1.

The results of the elemental composition of the nanoparticles determined by EDS analysis are summarized in Table 2. This data confirms that the resulting nanoparticles consisted of  $\text{Tb}^{3+}:\text{LaF}_3$  at a  $6:1$  and  $4:1$  (La:Tb) molar ratio for the PA and ASA systems, respectively.

Suspensions containing different ligand:nanoparticle ratios of PA: $\text{Tb}^{3+}:\text{LaF}_3$  and ASA: $\text{Tb}^{3+}:\text{LaF}_3$  were measured

TABLE 3: Agglomerate diameters and complex viscosity percent difference of ligand capped nanocrystals in PMMA.

Ligand	Ligand to nanoparticle ratio	Diameter (nm)	Complex viscosity percent difference
ASA	2 : 1	$252 \pm 66$	81%
	3 : 1	$420 \pm 116$	66%
	4 : 1	$349 \pm 85$	58%
	5 : 1	$233 \pm 41$	68%
PA	2 : 1	$444 \pm 138$	44%
	3 : 1	$150 \pm 105$	82%
	4 : 1	$457 \pm 176$	53%
	5 : 1	$242 \pm 24$	70%

FIGURE 5: STEM image of polymer nanocomposite showing the presence of 50–1000 nm ligand capped  $\text{Tb}^{3+}:\text{LaF}_3$  agglomerates.

by dynamic light scattering to determine the size of the nanoparticles. Previous work of Ellerbrock using the same nanoparticle synthesis route found that  $\text{Tb}^{3+}:\text{LaF}_3$  particles without ligand measured  $6 \pm 1\text{ nm}$  in diameter [16]. The average diameter for PA: $\text{Tb}^{3+}:\text{LaF}_3$  and ASA: $\text{Tb}^{3+}:\text{LaF}_3$  are presented in Table 3. The large diameters produced suggest that particulate agglomerates formed. Figure 5 shows a representative illustration of agglomerates ranging from 50–1000 nm within the nanocomposite. Due to the measured agglomerate diameters being on the order of the excitation wavelength of the rare-earth ion ( $\sim 350\text{ nm}$ ), the light is scattered resulting in reduced light emission. Additionally, synthesis parameters have been suggested as the cause of agglomerate formation as they can cause changes in the electrostatic nature of nanoparticles in solutions [17].

No significant difference was observed between the size of the agglomerates resuspended in water versus those resuspended in THF for either PA or ASA ligand at nanoparticle ratios of  $2:1$ ,  $3:1$ , and  $4:1$ . However, a significant particle size difference was observed at the  $5:1$  ratio between the two resuspension methods. The agglomerate sizes in water for ASA and PA systems were measured at  $893 \pm 418\text{ nm}$  and  $1080 \pm 192\text{ nm}$ , respectively. The agglomerate sizes in THF/PMMA were measured at  $233 \pm 41\text{ nm}$  for ASA and  $242 \pm 24\text{ nm}$  for PA. This diameter variation could be attributed to the mechanical action of the grinding process necessary to achieve the resuspension. Representative histograms of the diameter size distribution for PA: $\text{Tb}^{3+}:\text{LaF}_3$  and

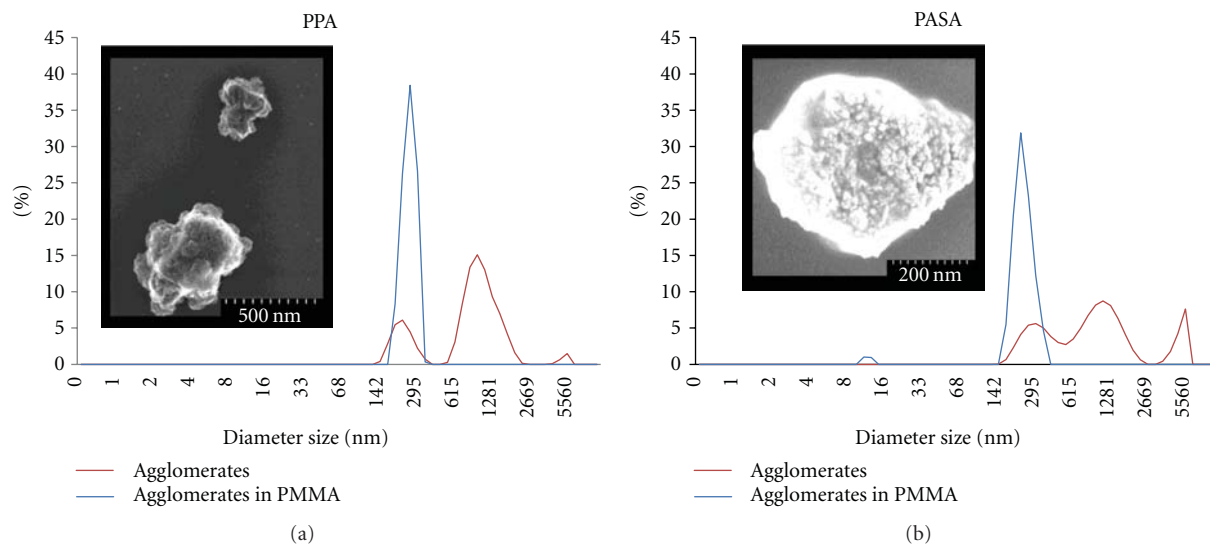


FIGURE 6: PA: Tb<sup>3+</sup>: LaF<sub>3</sub> (a) and ASA: Tb<sup>3+</sup>: LaF<sub>3</sub> (b) agglomerate diameters in water (red) and dispersed in PMMA/THF (blue) at 5: 1 ligand to nanoparticle ratio. STEM images (inset) show representative agglomerates found in the polymer nanocomposite.

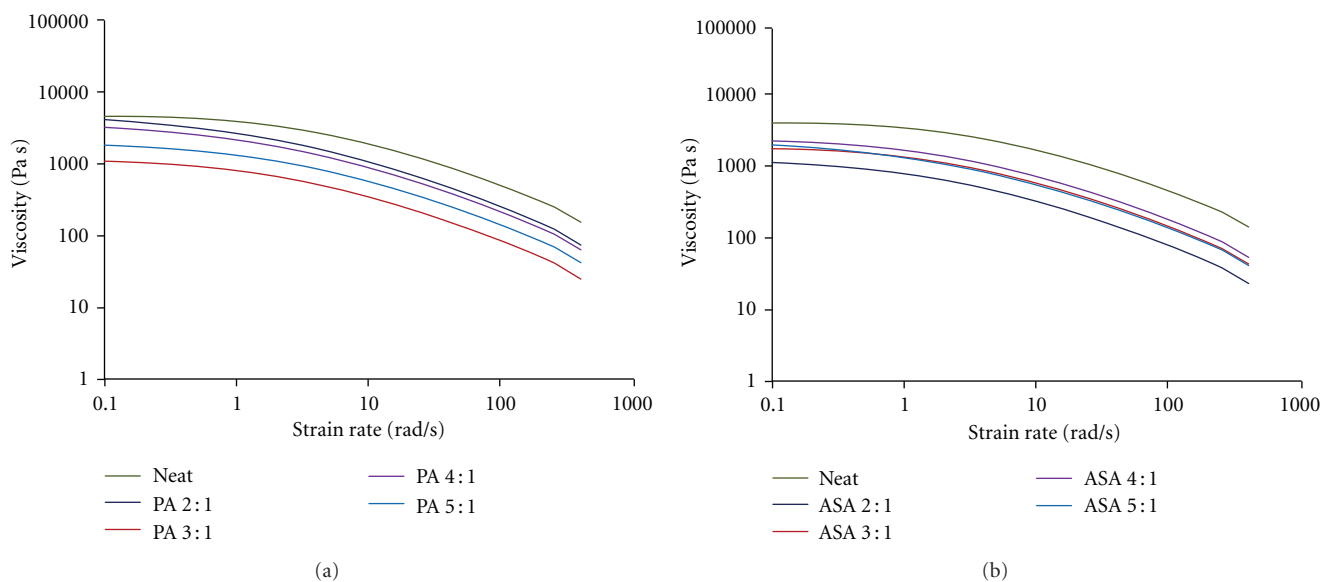


FIGURE 7: Complex viscosity as a function of frequency at 220°C for neat PMMA and PMMA nanocomposites of PA: Tb<sup>3+</sup>: LaF<sub>3</sub> (a) and ASA: Tb<sup>3+</sup>: LaF<sub>3</sub> (b) at varying ligand to nanoparticle ratios.

ASA: Tb<sup>3+</sup>: LaF<sub>3</sub> at the 5: 1 ligand to nanoparticle ratio with STEM images in the inset are illustrated in Figures 6 (a) and 6 (b), respectively.

Viscosity measurements were made by evaluating the relationship between complex viscosity and frequency. The relationship of complex viscosity to frequency is representative of the shear viscosity versus shear rate based on the Cox-Merz rule which states that the magnitudes of complex and shear viscosity data can be compared at equal values of frequency and shear rate [18]. Figure 7 shows the measured complex viscosity with varying frequency for neat PMMA and the nanocomposite PMMA with ligand to nanoparticle ratios of 2: 1, 3: 1, 4: 1, and 5: 1. All of the samples exhibited

a traditional shear thinning behavior where Newtonian fluid behavior occurred at low frequencies and shear thinning behavior occurring at higher frequencies in a similar manner to the nanoparticle loading samples. The incorporation of nanoparticles caused a reduction in the viscosity of the composites for all the ratios studied as seen in Figure 7. The calculated values of percent difference in the average complex viscosity at 10 rad/s between the neat PMMA and nanocomposite PMMA are displayed in Table 3. In the case of PA capped nanoparticles, the reduction in average agglomerate size (from ~450 nm to 150 nm) corresponded with the lower values for the measured complex viscosity values (44% to 82% reduction in complex viscosity), in that the lower the

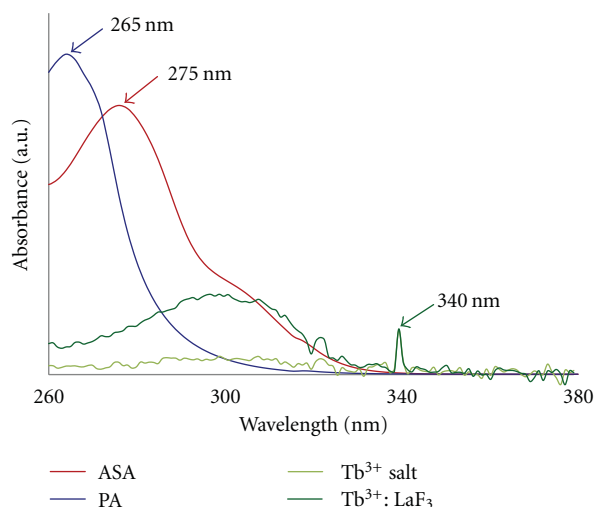


FIGURE 8: Absorption spectra of PA (blue), ASA (red) ligand,  $Tb^{3+}$  salt (light green), and  $Tb^{3+} : LaF_3$  (dark green) in water.

agglomerate size the lower the viscosity observed. This trend was not seen in the case of the ASA system.

Overall, the lower viscosity values could be the result of the nanoparticles acting to break up the structure interfering with the local intermolecular hydrogen bonding, and enabling polymer chains to slip past the nanoparticles resulting in less resistance [19]. An alternative hypothesis might also be attributed to a small decrease of polymer molecular entanglement density as a function of the high aspect ratio of the nanoparticles causing disruption in the polymer chain entangled network [20], allowing the chains to slip past one another hence lowering the viscosity. Therefore, it is fair to extrapolate that the particles act as transient lubricants which may lead to a lower processing temperature profile for melt extrusion [21, 22].

Figure 8 shows the UV-Vis spectra for the PA ligand (blue), ASA ligand (red),  $Tb^{3+}$  salt, that is,  $Tb(NO_3)_3 \cdot 6H_2O$ , (light green) and  $Tb^{3+} : LaF_3$  (dark green) in water. The peak value for the PA ligand was measured at 265 nm and for the ASA ligand was 275 nm. These values were used as the ligand excitation wavelength to evaluate the energy transfer of the ligand to the RE ion. The peak value for the  $Tb^{3+}$  salt and  $Tb^{3+} : LaF_3$ , respectively, was measured at 340 nm.

Figure 9 (a) is the excitation spectrum of  $Tb^{3+} : LaF_3$  which demonstrates the presence of peaks within the UV region that are representative of  ${}^7F_6 \rightarrow {}^5D_3$ ,  ${}^7F_6 \rightarrow {}^5G_1$ , and  ${}^7F_6 \rightarrow {}^5L_6$  ground state absorptions of the  $Tb^{3+}$  ion [23]. The characteristic  $Tb^{3+}$  emission peaks that occur within the visible region at 490, 543, 585, and 621 nm coincide with  ${}^5D_4 \rightarrow {}^7F_6$ ,  ${}^5D_4 \rightarrow {}^7F_5$ ,  ${}^5D_4 \rightarrow {}^7F_4$ , and  ${}^5D_4 \rightarrow {}^7F_3$  transitions, respectively and are shown in Figure 9 (b). The most intense emission band was observed at 543 nm where green light is emitted. The luminescence of the various ratios of ligand to rare-earth PMMA nanocomposites when excited with UV light at the wavelength of 365 nm is visually apparent from the images in Figure 10.

Upon excitation of the  $Tb^{3+}$  absorption band at 350 nm ( $\lambda_{ex}$ ), the emission spectrum generates the characteristic

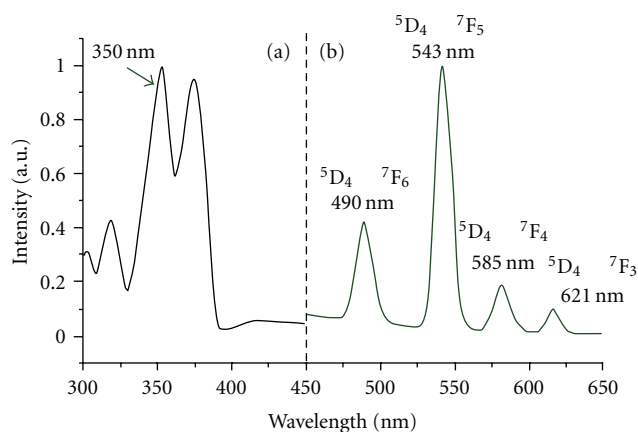


FIGURE 9: Characteristic (a) excitation spectrum ( $\lambda_{em} = 542$  nm) and (b) emission peaks of  $Tb^{3+} : LaF_3$  ( $\lambda_{ex} = 375$  nm) [23].

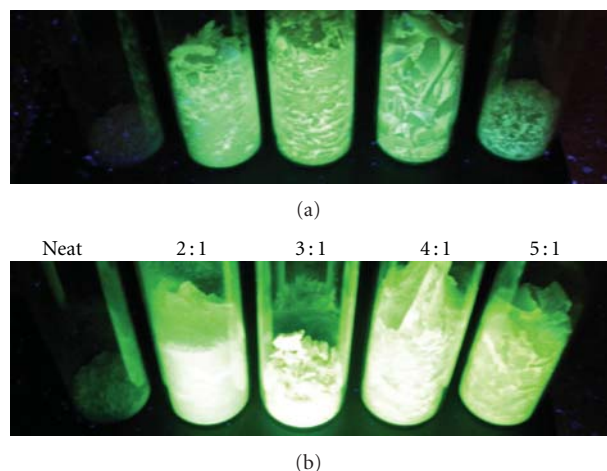


FIGURE 10: Neat PMMA and PMMA nanocomposites composed of varying ratios of (a) PA :  $Tb^{3+} : LaF_3$  and (b) ASA :  $Tb^{3+} : LaF_3$  under UV light.

emission peaks found in Figure 9 (b). When the UV light harvesting organic ligand is excited the emission is effectively sensitized due to the energy transfer to the RE ion [24]. In the case where the ligand is excited the characteristic emission spectra peaks of the ion would exist if energy transfer to  $Tb^{3+}$  is successful. Analysis of the UV-Vis spectra (Figure 8) suggests that the excitation wavelength for PA is 265 nm and ASA is 275 nm hence both nanocomposites exhibited the characteristic  $Tb^{3+}$  emission peaks.

Sharp emission spectra (FWHM < 5 nm) are generally preferred than broad emission spectra (FWHM = 50–200 nm) which organic dyes typically produce for photonic devices [25]. Sharp or narrow emission peaks are preferred as a result of improving color saturation where saturation is the perceived intensity relative to its own brightness [26]. In order to characterize the photoluminescence of the optical polymer nanocomposites the spectra were normalized at the characteristic peak of 543 nm and Lorentzian fits were applied. The FWHM at the 490 nm emission peaks was measured. The 490 nm peak of  $Tb^{3+}$  is considered to occur as

TABLE 4: FWHM values for PMMA nanocomposites composed of varying ratios of PA : Tb<sup>3+</sup> : LaF<sub>3</sub>.

Ligand	Ligand to nanoparticle ratio	FWHM of 490 nm peak—direct ion excitation ( $\lambda_{\text{ex}} = 350$ nm)	FWHM of 490 nm peak—ligand excitation ( $\lambda_{\text{ex}} = 265$ nm)
PA	2 : 1	9.64 ± 0.36 nm	8.51 ± 0.20 nm
	3 : 1	9.01 ± 0.19 nm	8.53 ± 0.18 nm
	4 : 1	9.18 ± 0.34 nm	8.50 ± 0.20 nm
	5 : 1	9.81 ± 0.39 nm	8.95 ± 0.20 nm

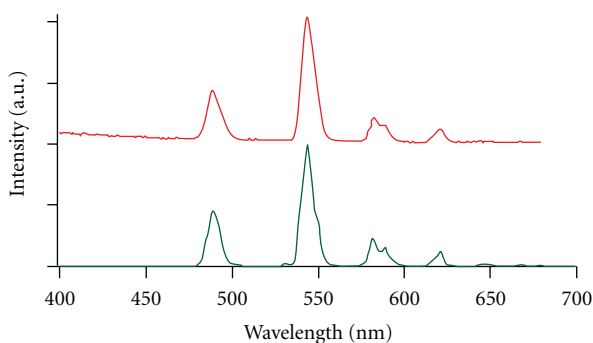


FIGURE 11: Emission of Tb<sup>3+</sup> doped LaF<sub>3</sub> in PMMA nanocomposites composed of 2:1 PA ligand to ion ratio at two different excitation wavelengths (red— $\lambda_{\text{ex}} = 350$  nm and green— $\lambda_{\text{ex}} = 265$  nm). The spectra are normalized to the 540 nm peak.

the result of an electric dipole transition which by nature is affected by changes in the environment [27]. The ASA system under direct ion or ligand excitation produced FWHM values  $\approx 11$  nm regardless of ligand to ion ratio. The PA system produced FWHM values from ligand excitation that were lower than values produced by direct ion excitation as shown in Table 4. Representative emission spectra of PMMA PA : Tb<sup>3+</sup> : LaF<sub>3</sub> nanocomposite excited at 350 nm (direct ion excitation—red) and 265 nm (ligand excitation—green) are shown in Figure 11.

#### 4. Conclusions

Light-emitting polymer nanocomposites were produced via solution/precipitation chemistry using ligand capped nanocrystals doped with Tb<sup>3+</sup> ions loaded into PMMA. The incorporation of ligand (ASA and PA) : Tb<sup>3+</sup> : LaF<sub>3</sub> nanoparticles within the PMMA matrix was verified by ATR-FTIR spectroscopy (organic) and TGA (inorganic). The absorbance spectrum obtained from ATR-FTIR spectroscopy of the ASA system produced absorption peaks at 1601 cm<sup>-1</sup> and 1559 cm<sup>-1</sup> which corresponds with benzene ring stretching. The PA : Tb<sup>3+</sup> : LaF<sub>3</sub> absorbance spectrum exhibited absorption peaks at 1653 cm<sup>-1</sup>, 1593 cm<sup>-1</sup>, and 1568 cm<sup>-1</sup> which suggest that the pyridine ring of picolinic acid is stretching. The peak located at  $\sim 1341$  cm<sup>-1</sup> could be associated with C-N stretching vibrations of the PA ligand.

Thermogravimetric analysis of PMMA nanocomposites showed that the ASA : Tb<sup>3+</sup> : LaF<sub>3</sub> contained system  $\sim 10$  wt%

inorganic material, whereas the PA : Tb<sup>3+</sup> : LaF<sub>3</sub> system contained approximately 7 wt% inorganic material. The EDS analysis confirmed that PA : Tb<sup>3+</sup> : LaF<sub>3</sub> was on average at a 6 : 1 molar ratio of La<sup>3+</sup> to Tb<sup>3+</sup> and ASA : Tb<sup>3+</sup> : LaF<sub>3</sub> was on average at a 4 : 1 molar ratio of La to Tb<sup>3+</sup>.

The average diameter for PA : Tb<sup>3+</sup> : LaF<sub>3</sub> and ASA : Tb<sup>3+</sup> : LaF<sub>3</sub> at varying ligand to nanoparticle ratios produced agglomerates with diameters > 200 nm in PMMA. The resuspension liquid (water or THF) showed no significant difference in agglomerate size for PMMA nanocomposites of PA : Tb<sup>3+</sup> : LaF<sub>3</sub> and ASA : Tb<sup>3+</sup> : LaF<sub>3</sub> at ligand : nanoparticle ratios of 2 : 1, 3 : 1, and 4 : 1. However, a significant particle size difference was observed at the 5 : 1 ratio where those resuspended in water were measured at 893 ± 418 nm and 1080 ± 192 nm for ASA and PA systems, respectively. For the same ratio resuspended in THF values were measured at 233 ± 41 nm for ASA and 242 ± 24 nm for PA.

The rheology measurements for all samples produced traditional shear thinning curves. The addition of the agglomerates caused a reduction in the viscosity of all PMMA nanocomposites as compared to neat PMMA. The PA : Tb<sup>3+</sup> : LaF<sub>3</sub> PMMA nanocomposites exhibited a reduction in viscosity that corresponded with the reduction in the size of the agglomerates. The ASA nanocomposite demonstrated lower viscosity values but did not exhibit the same trend with respect to agglomerate size.

Green light was produced by direct ion and ligand excitation of ASA and PA PMMA nanocomposite. All emission spectra exhibited the corresponding characteristic emission of trivalent terbium.

#### Acknowledgments

The authors acknowledge the support and fellowship funding at the time of this work provided by the South East Alliance for Graduate Education and the Professoriate (SEAGEP) on the National Science Foundation Award HRD-0450279, Center of Optical Materials Science and Engineering Technologies (COMSET), and School of Materials Science and Engineering at Clemson University. A note of gratitude is given to Dr. Gregory Von White II, Courtney Kucera, and Kim Ivey for their help with this paper.

#### References

- [1] Z. L. Wang, Z. W. Quan, P. Y. Jia et al., "A facile synthesis and photoluminescent properties of redispersible CeF<sub>3</sub>, CeF<sub>3</sub>:Tb<sup>3+</sup>, and CeF<sub>3</sub>:Tb<sup>3+</sup>/LaF<sub>3</sub> (core/shell) nanoparticles," *Chemistry of Materials*, vol. 18, no. 8, pp. 2030–2037, 2006.
- [2] P. K. Sharma, R. Nass, and H. Schmidt, "Effect of solvent, host precursor, dopant concentration and crystallite size on the fluorescence properties of Eu(III) doped yttria," *Optical Materials*, vol. 10, no. 2, pp. 161–169, 1998.
- [3] V. Bekiari and P. Lianos, "Multicolor emission from terpyridine-lanthanide ion complexes encapsulated in nanocomposite silica/poly(ethylene glycol) sol-gel matrices," *Journal of Luminescence*, vol. 101, no. 1-2, pp. 135–140, 2003.
- [4] E. Brunet, O. Juanes, and J. Rodriguez-Ubis, "Supramolecularly organized lanthanide complexes for efficient metal excitation and luminescence as sensors in organic and biological

- applications," *Current Chemical Biology*, vol. 1, no. 1, pp. 11–39, 2007.
- [5] H. Jiu, L. Zhang, G. Liu, and T. Fan, "Fluorescence enhancement of samarium complex co-doped with terbium complex in a poly(methyl methacrylate) matrix," *Journal of Luminescence*, vol. 129, no. 3, pp. 317–319, 2009.
- [6] R. R. Tang, G. L. Gu, and Q. Zhao, "Synthesis of Eu(III) and Tb(III) complexes with novel pyridine dicarboxamide derivatives and their luminescence properties," *Spectrochimica Acta—Part A*, vol. 71, no. 2, pp. 371–376, 2008.
- [7] Z. Wang, M. Li, C. Wang, J. Chang, H. Shi, and J. Lin, "Photoluminescence properties of LaF<sub>3</sub>:Eu<sup>3+</sup> nanoparticles prepared by refluxing method," *Journal of Rare Earths*, vol. 27, no. 1, pp. 33–37, 2009.
- [8] L. G. Jacobssohn, K. B. Sprinkle, C. J. Kucera et al., "Synthesis, luminescence and scintillation of rare earth doped lanthanum fluoride nanoparticles," *Optical Materials*, vol. 33, no. 2, pp. 136–140, 2010.
- [9] B. Kokuoz, J. R. DiMaio, C. J. Kucera, D. D. Evanoff, and J. Ballato, "Color kinetic nanoparticles," *Journal of the American Chemical Society*, vol. 130, no. 37, pp. 12222–12223, 2008.
- [10] B. Kokuoz, C. Kucera, J. R. DiMaio, and J. Ballato, "Organic—inorganic hybrid nanoparticles with enhanced rare-earth emissions," *Optical Materials*, vol. 31, no. 9, pp. 1327–1330, 2009.
- [11] Y. Luo, X. Yu, W. Su et al., "Energy transfer in a ternary system composed of Tb(DBM)<sub>3</sub>Phen, Eu(DBM)<sub>3</sub>Phen, and poly(N-vinylcarbazole)," *Journal of Materials Research*, vol. 24, no. 10, pp. 3023–3031, 2009.
- [12] S. Maji and K. S. Viswanathan, "Ligand-sensitized fluorescence of Eu<sup>3+</sup> using naphthalene carboxylic acids as ligands," *Journal of Luminescence*, vol. 128, no. 8, pp. 1255–1261, 2008.
- [13] I. G. Binev, B. A. Stamboliyska, and Y. I. Binev, "The infrared spectra and structure of acetylsalicylic acid (aspirin) and its oxyanion: an ab initio force field treatment," *Journal of Molecular Structure*, vol. 378, no. 3, pp. 189–197, 1996.
- [14] L. C. Thompson, "Complexes of the rare earths. VIII. Picolinic acid," *Inorganic Chemistry*, vol. 3, no. 9, pp. 1319–1321, 1964.
- [15] R. Dangtungee, J. Yun, and P. Supaphol, "Melt rheology and extrudate swell of calcium carbonate nanoparticle-filled isotactic polypropylene," *Polymer Testing*, vol. 24, no. 1, pp. 2–11, 2005.
- [16] B. M. Ellerbrook, *Fabrication of fluorescent nanoparticle-polymer composites for photoactive-based materials*, M.S. thesis, 2010.
- [17] L. Ravina, *Everything You Want to Know about Coagulation & Flocculation*, Zeta-Meter, Staunton, Va, USA, 4th edition, 1993.
- [18] R. Bird, R. Armstrong, and O. Hassager, Eds., *Dynamics of Polymeric Liquids, Volume 1, Fluid Mechanics*, vol. 1, John Wiley & Sons, New York, NY, USA, 1977.
- [19] H. Barnes, *A Handbook of Elementary Rheology*, vol. 1, The University of Wales Institute of Non-Newtonian Fluid Mechanics, Wales, UK, 2000.
- [20] S. G. Hatzikiriakos, N. Rathod, and E. B. Muliawan, "The effect of nanoclays on the processibility of polyolefins," *Polymer Engineering and Science*, vol. 45, no. 8, pp. 1098–1107, 2005.
- [21] H. E. Sliney, "Rare-earth fluorides and oxides—an exploratory study of their use as solid lubricants at temperatures to 1800°F (1000°C)," 1–26.
- [22] Z. Zhang, L. Yu, W. Liu, and Q. Xue, "Effect of LaF<sub>3</sub> nanocluster modified with succinimide on the lubricating performance of liquid paraffin for steel-on-steel system," *Tribology International*, vol. 34, no. 2, pp. 83–88, 2001.
- [23] J. Wang, S. Bo, L. Song, J. Hu, X. Liu, and Z. Zhen, "One-step synthesis of highly water-soluble LaF<sub>3</sub>:Ln<sup>3+</sup> nanocrystals in methanol without using any ligands," *Nanotechnology*, vol. 18, no. 46, article 465606, 2007.
- [24] J. Mezyk, D. Di Nuzzo, A. Mech, R. Tubino, and F. Meinardi, "Exciton-exciton annihilation in organic lanthanide complexes," *Journal of Chemical Physics*, vol. 132, article 024504, 2010.
- [25] M. A. Diaz-Garcia, S. F. De Avila, and M. G. Kuzyk, "Energy transfer from organics to rare-earth complexes," *Applied Physics Letters*, vol. 81, no. 21, pp. 3924–3926, 2002.
- [26] M. D. Fairchild, "In color appearance models: CIECAM02 and beyond," in *Proceedings of the IS&T/SID 12th Color Imaging Conference*, pp. 1–68, Scottsdale, Ariz, USA, November 2004.
- [27] P. R. Selvin and J. E. Hearst, "Luminescence energy transfer using a terbium chelate: improvements on fluorescence energy transfer," *Proceedings of the National Academy of Sciences of the United States of America*, vol. 91, no. 21, pp. 10024–10028, 1994.

## Research Article

# A Novel Route for Development of Bulk Al/SiC Metal Matrix Nanocomposites

Payodhar Padhi<sup>1</sup> and Sachikanta Kar<sup>2</sup>

<sup>1</sup>Department of Mechanical Engineering, Konark Institute of Science & Technology, Bhubaneswar 752050, India

<sup>2</sup>Department of Consultancy & Quality, Central Tool Room & Training Center, Bhubaneswar 752024, India

Correspondence should be addressed to Payodhar Padhi, payodharpadhi@gmail.com

Received 15 March 2011; Revised 5 May 2011; Accepted 6 May 2011

Academic Editor: Baoquan Sun

Copyright © 2011 P. Padhi and S. Kar. This is an open access article distributed under the Creative Commons Attribution License, which permits unrestricted use, distribution, and reproduction in any medium, provided the original work is properly cited.

Addition of nano particles, even in quantities as small as 2 weight percent can enhance the hardness or yield strength by a factor as high as 2. There are several methods for the production of metal matrix nanocomposites including mechanical alloying, vertex process, and spray deposition and so forth. However, the above processes are expensive. Solidification processing is a relatively cheaper route. During solidification processing, nano particulates tend to agglomerate as a result of van der Waals forces and thus proper dispersion of the nano particulate in metal matrix is a challenge. In the present study a noncontact method, where the ultrasonic probe is not in direct contact with the liquid metal, was attempted to disperse nanosized SiC particulates in aluminum matrix. In this method, the mold was subjected to ultrasonic vibration. Hardness measurements and microstructural studies using HRTEM were carried out on samples taken from different locations of the nanocomposite ingot cast by this method.

## 1. Introduction

The mechanical properties of nanoparticle dispersion strengthened MMCs are far superior to those of micrometric dispersion strengthened MMCs with a similar volume composition of particulate. For example, the tensile strength of an Al-1 vol.% Si<sub>3</sub>N<sub>4</sub> (10 nm) composite has been found to be comparable to that of an Al-15 vol.% SiCp (3.5 μm) composite, the yield stress of the nanometric MMC being significantly higher than that of the micrometric MMC [1–7]. Particles larger than 1.5 μm tend to act as microconcentrators and are susceptible to cleavage [1]. On the other hand, particles in the range of 200–1500 nm have been found to cause the formation of cavities and pits caused by poor interphase cohesion [1]. Particles smaller than 200 nm generally bond well with the matrix, which is key to the excellent mechanical properties of nanoscale particulate MMCs [1].

There are several methods for the production of metal matrix nanocomposites including mechanical alloying, vertex process, and spray deposition [8, 9]. But the above processes are expensive. Solidification processing is a relatively cheaper route. However, when the nanoparticles are mixed with liquid metal during the casting, they agglomerate due to interparticle van der Waals force. Dispersion of the

nanoparticles in the liquid media will require large amount of force to break the bonds in between the particles. The mechanical means used in the conventional methods to cast MMCs will not be sufficient to deagglomerate the nanoparticles. Also, when the nanopowder is added into the melt the viscosity of the melt increases significantly. This hinders the mixing process. The lower the particle size is the higher will be the viscosity of the melt [10], and the higher is the volume fraction of particulate, the higher will be the viscosity [10]. Therefore, it is very difficult to uniformly disperse nanoparticles in metal matrix.

Yang et al. [8] overcame the problem of agglomeration by using ultrasonic waves. The ultrasonic wave generates non-linear effects in the liquid-like transient acoustic cavitation and acoustic streaming, which are responsible for refining microstructures, degassing of liquid metal, and dispersing the nanoparticles [8]. Acoustic cavitation refers to the formation, growth, and implosive collapse of bubbles in the liquid. Cavitation collapse can locally raise the temperature to as high as ~20000 K [11]. It raises the pressure adjacent to the collapse to as high as 1000 atm. The heating and cooling rate of ~10<sup>9</sup> K/s and liquid jet streams of ~400 km/h have been reported during the cavitation [12–15].

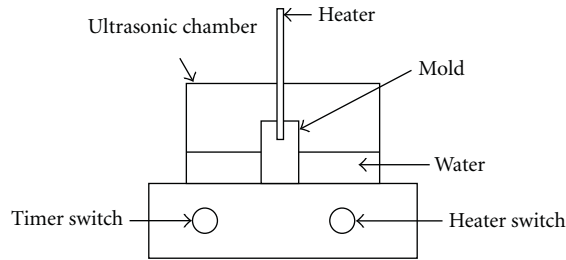


FIGURE 1: Schematic diagram for experimental setup.

TABLE 1: Compositions commercially pure Aluminium.

Element	Fe	Mg	Si	Al
Wt%	0.96	0.43	0.26	Balance

When sound wave propagates through the liquid, alternating high-pressure (compression) and low-pressure (rarefaction) cycles are generated. During the low-pressure cycle, small bubbles or voids are nucleated. After the bubbles reach the critical size, they collapse violently during the high-pressure cycle. During the collapse of bubbles, high-pressure shock waves are generated. They propagate through the liquid at velocities above the speed of sound and break up the agglomerations, thus breaking the interparticle van der Waals forces [8]. Eskin et al. [14] fabricated both Al-SiC and Mg-SiC nanocomposites using ultrasonic wave of 20 kHz frequency and 600 W power. In the method adopted by Yang et al. the source of the ultrasonic wave or the probe was dipped into the liquid metal [2, 10].

However, the above technique has several drawbacks such as the oscillating probe may dissolve in liquid metal thus contaminating the liquid [16]. Moreover, the intensity of cavitation is not uniform. It is maximum near the probe, and it gradually decreases as one moves away from the probe. Further, the direct contact of probe with liquid metal is not possible for continuous casting.

To overcome the above difficulties, a noncontact method was attempted to mix up nanosized particulates in aluminum matrix. A simple setup was made to carry out the preliminary study for nanoparticle distribution by the non-contact method. In this method, the mold is subjected to ultrasonic vibration. A simple setup was made to cast MMNCs weighing up to 305 gm. The method was successful in uniformly dispersing the nanosized particulates of SiC in Al matrix.

## 2. Noncontact Ultrasonic Method of Casting Metal Matrix Nanocomposites

The experimental setup is shown in Figure 1. The setup consists of an ultrasonic generator which generates ultrasonic

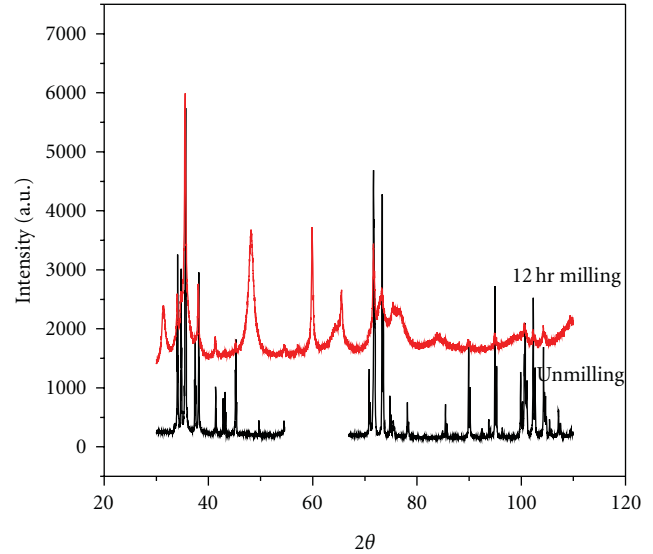


FIGURE 2: X-ray diffraction of both milled (12 hrs) and unmilled SiC powders.

waves at a frequency of 35 kHz (Bandelin-Germany Make—Model: RK-100H), an ultrasonic chamber, steel die, and hanging heating filament. Sufficient water was kept around the die for effective transmission of ultrasonic waves from the sides of the chamber. Mold was preheated to avoid thermal cracking. The preheated mold was kept in the ultrasonic chamber, and the chamber was subjected to vibration at a frequency of 35 kHz. Liquid aluminum and SiC particulate (2-3 wt%) having average size of 12.3 nm were simultaneously poured into the vibrating mold. After the simultaneous pouring, the heating element was immediately brought down above the liquid metal in order to delay the solidification. The vibration was carried out for a period of five minute to ensure complete mixing. The castings were cut in both longitudinal and transverse section and polished for microstructural evaluation.

### 2.1. Starting Material

**2.1.1. Commercially Pure Aluminium.** The composition of commercially pure aluminum used for casting Al matrix nanocomposites is shown in Table 1.

**2.1.2. Ceramic Particulate.** SiC nanoparticles were used as reinforcements. These were prepared by ball milling. SiC powder was milled for 12 hours. The nanopowders were characterized using high-resolution X-ray diffractometer (PHILLIPS, X-PERT-PRO) and high-resolution transmission electron microscope (JEOL, JEM-2100). Figure 2 shows the X-Ray diffractograms of milled and unmilled SiC powders. Based on Scherrer's equation, the X-ray diffractograms were analysed for estimating the crystallite size of SiC. Using this method, the estimated crystallite size for SiC was ~ 12.3 nm. Figure 3 shows the HRTEM photograph of SiC. It can be seen from Figure 3 that the particle size of SiC varied from ~10 nm to ~20 nm.

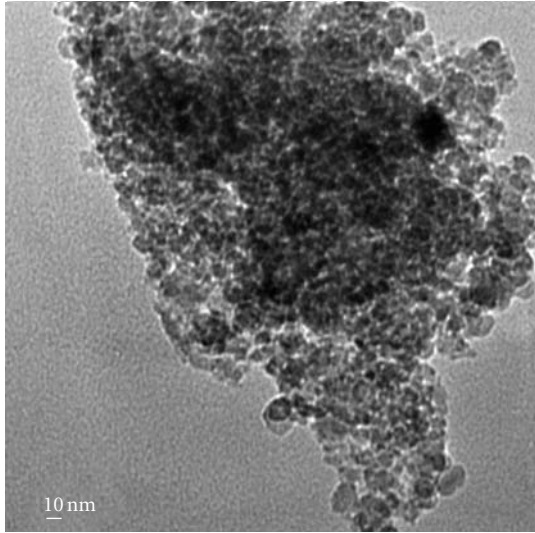


FIGURE 3: HRTEM photograph of SiC Powders.

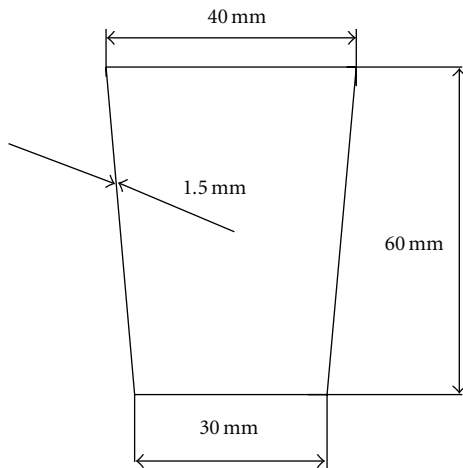


FIGURE 4: Schematic diagram of stainless steel mold.

2.1.3. *Experimental Setup.* The descriptions of the ultrasonic vibrator, mold, and the heating system are as follows.

- (a) Ultrasonic vibrator: Ultrasonic Bath (Bandelin-Germany Make—Model: RK-100H) was used to generate the ultrasonic wave of 35 kHz frequency. At the base of the chamber was a mesh on which the mold was fixed. The mold was surrounded by sufficient water so that effective transmission of ultrasonic waves to liquid metal could take place. The time period of vibration could be varied from 1 minute to 30 minute.
- (b) Mold: the mold was made of stainless steel and its geometry is shown in Figure 4.
- (c) Heating system: Figures 5 and 6 show the heating system. It consisted of a ceramic cylinder with a central hole surrounded by another six holes, all parallel to the axis of the cylinder. Through these holes, heating coil (1000 W) was passed. The heating system was lowered and lifted using a pulley system.

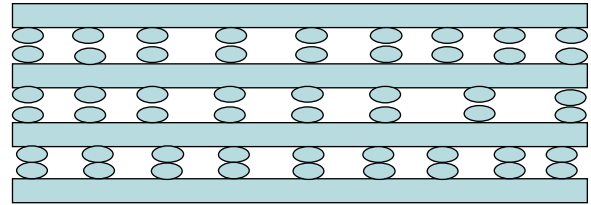


FIGURE 5: Schematic diagram of heater.

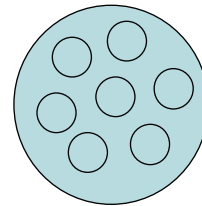


FIGURE 6: Cross sectional view of heater.

### 3. Procedure for Characterization of Cast Ingot

3.1. *Specimen Preparation for Microstructural Study.* The specimens were cut with low-speed abrasive cutter for microstructural analysis. Three different grades (60, 400, and 600 grits) of emery papers were used to polish the specimen surface. Then, using alumina fine powder cloth polishing for about 20 minute was carried out. The surface was cleaned with alcohol solution. Finally, diamond polishing was done and the specimen surface was cleaned with acetone. The specimens were etched with Keller's reagent. The etching was done for 30 seconds. Etched specimens were cleaned in acetone using an ultrasonic vibrator and dry hot air. The specimens were cold mounted in order to achieve a uniform flatness of specimen surface and the cold mount base.

3.2. *Preparation of Specimens for TEM Study.* Thin slice of specimen was cut out using low-speed diamond cutter. The first stage of thinning was done by placing the specimen over a belt grinder. The slice was then attached to a block using suitable adhesive and subjected to thinning using emery paper (6 grit). The thickness of the specimen was reduced below  $100\ \mu\text{m}$ . Finally, discs of 3 mm diameter were punched out of the specimen using mechanical punch (Gaton Model 642). Then, prethinning of the discs was carried out using a dimple grinder (Gaton Model-656). By dimpling, the centre regions of the discs were thinned to  $\sim 20\ \mu\text{m}$  from a thickness of  $\sim 100\ \mu\text{m}$ . The prethinned discs were finally subjected to ion milling (Gaton Precision Polishing System Model 691). The difference between the top and bottom gun angles of the ion milling machine was  $3.5^\circ$ . The vacuum inside the ion beam milling chamber was  $10^{-6}$  Torr. A beam of 5 KeV was used for ion milling. As a result of ion milling, a hole was formed in the centre and the region around the hole was thin enough to be examined under a TEM.

3.3. *TEM Characterization.* For TEM analysis, High-resolution TEM (JEOL, JEM-2100) was used. The TEM

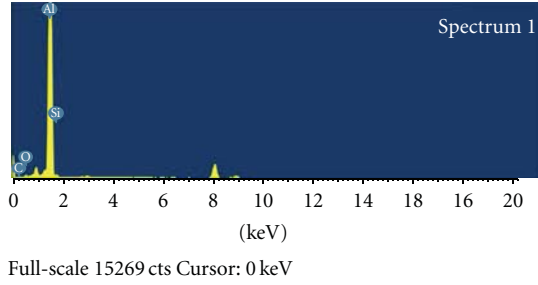


FIGURE 7: EDAS of Al-SiC nanocomposites.

operated at an accelerating voltage of 200 kV. Bright field images of nanoparticulates spread in the Al matrix were taken and selected area diffraction patterns were recorded. EDAX was also carried out.

#### 4. Results of Characterization of Cast Metal Matrix Nanocomposites

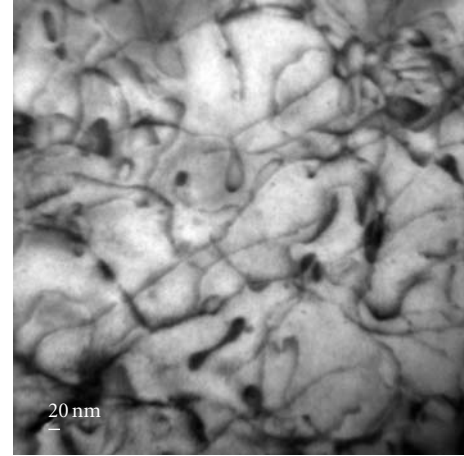
**4.1. Commercially Pure Al.** Commercially pure Al was cast by the noncontact ultrasonic method, without addition of any particulate. The microhardness was  $\sim 51$  Hv, which is much higher than the commercially pure Al used in the present study.

**4.2. SiC Nanocomposite.** MMNCs with two different volume fractions of SiC namely, 0.0263 and 0.016, were cast. The total weight of the ingot having 2.63 volume percentage (3 wt%) of SiC was 310 gm and that of the ingot having 1.6 volume percentage (2 wt%) of SiC was 205 gm. The cast ingots were longitudinally cut for the hardness and microstructural characterization of the ingot.

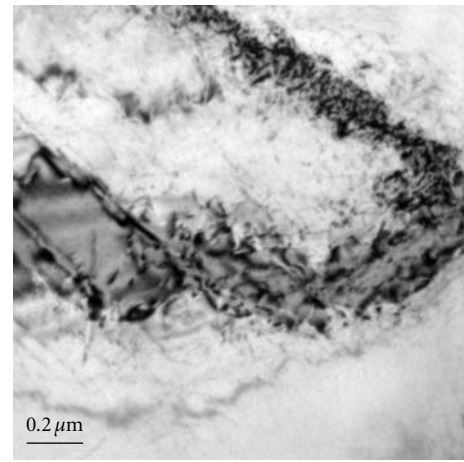
**4.3. Results of TEM Studies.** Figure 7 shows EDAS of Al-SiC nanocomposites confirming the SiC nanoparticles in the composites. TEM samples were made from different regions of the cast. From the qualitative observation, it can be inferred that the SiC nanoparticles have got dispersed uniformly within the ingot. However within a length scale of  $1 \mu\text{m}$ , one can observe segregation of the nanoparticles. It is possible that the nanoparticles have segregated in the grain boundary region. Figure 8 shows the TEM micrographs of Al-2 wt% SiC nanocomposite taken at different magnifications. Figure 8(a) shows the SiC nanoparticles spread uniformly. They are possibly surrounded by subgrains. Figure 8(b) shows the SiC nanoparticles segregated along a line, which is possibly a grain boundary.

#### 5. Discussions

**5.1. Distribution of Nanoparticles in Al matrix.** From the microhardness values taken from different locations of the ingot, it is clear that the distribution of nanoparticles is uniform across the ingot. It appears that, in the liquid metal nanoparticles were uniformly dispersed and the segregation of the particles near the grain boundaries is due to pushing



(a)



(b)

FIGURE 8: TEM micrographs of Al-SiC nanocomposites.

of the nanoparticles during the growth of the grains. As the grains grew, the nanoparticles were pushed into the remaining liquid regions. In majority of metal-ceramic combinations [17] gives the critical velocity for engulfment of particulate in solidified metal:

$$V_{cr} = \frac{0.157}{\eta} \Delta\sigma^{2/3} \sigma_{sl} \left(\frac{a}{R}\right)^{4/3}, \quad (1)$$

where  $V_{cr}$  is the critical solidification front velocity,  $\Delta\sigma = 2\sigma_{cs} - \sigma_{cl} - \sigma_{sl}$ ,  $\sigma_{ij}$  being the interfacial energy between phases  $i$  and  $j$  ( $l = \text{liquid}$ ,  $g = \text{gas}$ ,  $c = \text{ceramic}$ , and  $s = \text{solidified metal}$ ),  $\eta$  is the dynamic viscosity of liquid metal,  $a$  is the diameter of the atom in liquid metal, and  $R$  is the particle radius.

As evident from the equation, the critical velocity required for engulfment of nanoparticles will be very high and thus a large fraction of nanoparticles will be pushed near the grain boundaries. The mechanism of uniform distribution of nanoparticle within liquid metal subjected to ultrasonic vibration is well understood. Nanoparticles have a tendency to agglomerate due to van der Waals forces. Thus, during

casting of nanocomposites, high-intensity ultrasound has been used for mixing, dispersing, and deagglomeration the nanoparticles [10]. When sound wave propagates into the liquid, alternating high-pressure (compression) and low-pressure (rarefaction) cycles are generated. During the low-pressure cycle, small bubbles or voids get nucleated in the liquid. When the bubble reaches a critical size at which it can no longer absorb energy, they collapse violently during the high-pressure cycle. The process of bubble formation and collapse is called cavitation. During the collapse of bubbles, high-pressure shock waves are generated and propagate through the liquid at velocities above the speed of sound, which keep the nanoparticles uniformly dispersed.

## 6. Conclusions

- (1) In certain locations, we achieved uniform distributions of SiC nanoparticles in the aluminium matrix.
- (2) TEM studies reveal segregation of particles near the grain boundaries suggesting pushing of nanoparticles during grain growth.
- (3) More number of experiments are required to find out the degree of uniform distributions of nano particles.

## References

- [1] Y. C. Kang and S. L. Chan, *Materials Chemistry and Physics*, vol. 65, p. 436, 2004.
- [2] J. Hashim, L. Looney, and M. S. J. Hashmi, "Metal matrix composites: production by the stir casting method," *Journal of Materials Processing Technology*, vol. 92-93, pp. 1-7, 1999.
- [3] J. Hashim, L. Looney, and M. S. J. Hashmi, "Particle distribution in cast metal matrix composites—part I," *Journal of Materials Processing Technology*, vol. 123, no. 2, pp. 251-257, 2002.
- [4] J. Hashim, L. Looney, and M. S. J. Hashmi, "Particle distribution in cast metal matrix composites—part II," *Journal of Materials Processing Technology*, vol. 123, no. 2, pp. 258-263, 2002.
- [5] A. Ourdjini, K. C. Chew, and B. T. Khoo, "Settling of silicon carbide particles in cast metal matrix composites," *Journal of Materials Processing Technology*, vol. 116, no. 1, pp. 72-76, 2001.
- [6] A. Kolsgaard and S. Brusethaug, "Settling of SiC particles in an AlSi7Mg melt," *Materials Science and Engineering A*, vol. 173, no. 1-2, pp. 213-219, 1993.
- [7] S. Charles and V. P. Arunachalam, "Effect of particle inclusions on the mechanical properties of composites fabricated by liquid metallurgy," *Indian Journal of Engineering and Materials Sciences*, vol. 10, no. 4, pp. 301-305, 2003.
- [8] Y. Yang, J. Lan, and X. Li, "Study on bulk aluminum matrix nano-composite fabricated by ultrasonic dispersion of nano-sized SiC particles in molten aluminum alloy," *Materials Science and Engineering A*, vol. 386, no. 1-2, pp. 284-290, 2004.
- [9] B. S. Murty and K. Hono, "Al- Mg- and Fe-based nanocomposites by rapid solidification processing," *Transactions of the Indian Institute of Metals*, vol. 58, no. 4, pp. 769-775, 2005.
- [10] T. Hielscher, "Ultrasonic production of nano-size dispersions and emulsions," in *Proceedings of European Nanosystems Conference (ENS '05)*, Paris, France, December 2005.
- [11] D. J. Flannigan and K. S. Suslick, "Plasma formation and temperature measurement during single-bubble cavitation," *Nature*, vol. 434, no. 7029, pp. 52-55, 2005.
- [12] K. S. Suslick, *Ultrasound: Its Chemical, Physical, and Biological Effects*, VCH, New York, NY, USA, 1988.
- [13] G. I. Eskin, "Broad prospects for commercial application of the ultrasonic (cavitation) melt treatment of light alloys," *Ultrasonics Sonochemistry*, vol. 8, no. 3, pp. 319-325, 2001.
- [14] G. I. Eskin, "Cavitation mechanism of ultrasonic melt degassing," *Ultrasonics Sonochemistry*, vol. 2, no. 2, pp. S137-S141, 2001.
- [15] G. I. Eskin and D. G. Eskin, "Production of natural and synthesized aluminum-based composite materials with the aid of ultrasonic (cavitation) treatment of the melt," *Ultrasonics Sonochemistry*, vol. 10, no. 4-5, pp. 297-301, 2003.
- [16] C. Vivés, "Progress in fluid flow research: turbulence and applied MHD," in *Effects of Oscillatory Electromagnetic Force Fields on Microstructure of Solidifying Aluminum Alloys*, vol. 162, chapter 40, pp. 601-617, AIAA, 1998.
- [17] G. Kaptay, "Interfacial criteria for producing metal matrix composites and ceramic particle stabilized metallic foams," *Materials Science Forum*, vol. 414-415, pp. 419-424, 2003.

## Research Article

# Process Modeling of Deagglomeration of Ceramic Nanoparticles in Liquid Metal during Synthesis of Nanocomposites

Payodhar Padhi,<sup>1</sup> Biranchi Narayan Dash,<sup>1</sup> and Sachi Kanta Kar<sup>2</sup>

<sup>1</sup>Department of Mechanical Engineering, Konark Institute of Science & Technology, Bhubaneswar, India

<sup>2</sup>Central Tool Room & Training Centre, Bhubaneswar, India

Correspondence should be addressed to Payodhar Padhi, payodharpadhi@gmail.com

Received 15 March 2011; Accepted 21 April 2011

Academic Editor: Guifu Zou

Copyright © 2011 Payodhar Padhi et al. This is an open access article distributed under the Creative Commons Attribution License, which permits unrestricted use, distribution, and reproduction in any medium, provided the original work is properly cited.

The cavitation phenomenon is well known to lead to deagglomeration and uniform dispersion of nanoparticles in liquid metal. The nature of flow leading to deagglomeration, the rate of deagglomeration, and the effect of frequency of them has been systematically investigated. It is extremely difficult to experimentally know about them and thus modeling the phenomenon is indispensable. The same has been attempted in the present study. The present study attempts to model the process of deagglomeration and dispersion of ceramic nanoparticles in the vicinity of cavitation using FLUENT 6.2.16. For this a simple representative volume element has been modeled.

## 1. Introduction

The phenomenon of bubble cavitation has been found to be useful for de-agglomeration and uniform dispersion of nano-particles in liquid metal. There are many researchers who have described the bubble dynamics in details [1–11] but dispersion of nanoparticles due to collapse of bubbles in liquid metal is still a hot topic for research. The nature of flow leading to deagglomeration, the rate of deagglomeration, and the effect of frequency of them need to be systematically investigated. It is extremely difficult to experimentally know about them and thus modeling the phenomenon is indispensable. The same has been attempted in the present study. The present study attempts to model the process of deagglomeration and dispersion of ceramic nanoparticles in the vicinity of cavitation using FLUENT 6.2.16. [12]. For this a simple representative volume element has been considered.

## 2. Mathematical Model

A two-dimensional representative volume element (RVE), which is shown in Figure 1, was selected to understand the

flow behavior and kinetics of deagglomeration at mesoscopic scale. The two-dimensional representative volume element consists of a single agglomerate consisting of nanoparticles. The agglomerate was assumed to be circular. The flow at the boundaries AB, BC, and CD was assumed negligible for computational simplicity. On one side (DA) of the representative volume element, a surface of bubble (assumed static) with 100  $\mu\text{m}$  diameter generates pressure shock wave as a result of collapse. Therefore, pressure boundary condition was applied in the semicircular portion of the side DA (shown in Figure 1) and no slip condition was applied in the remaining portion of DA. The semicircular boundary, taken as the bubble wall, was subjected to a sinusoidal pressure variation using user-defined function (UDF) in FLUENT 6.2.16. Thus it has been assumed that bubble collapse is taking place at the same location of the RVE after regular intervals of time.

Although during the collapse the dimension of the bubble changes, for simplicity it has been kept static. Since the size of bubble is small compared to the representative volume element and through the mathematical model only a rough estimate of the dispersion time is aimed at, the assumption is justified. Also convective movement of the bubble has been ignored. The assumption of negligible flow

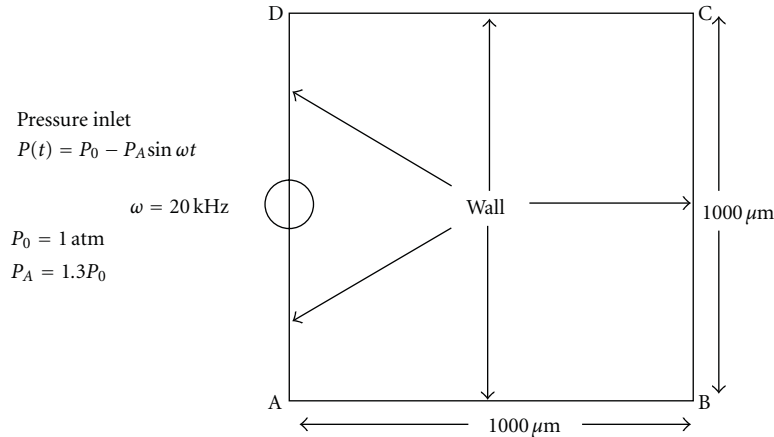


FIGURE 1: Schematic diagram of the domain with semicircular bubble wall.

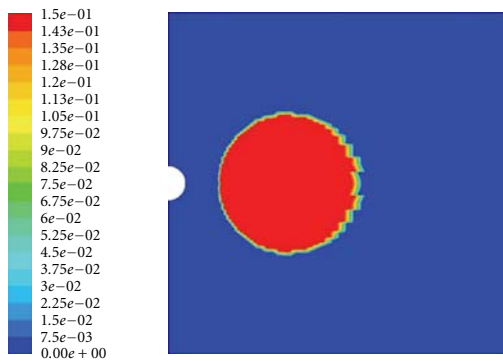


FIGURE 2: Contour of particulate volume fraction at time  $t = 0$  s.

at the boundaries does not make the problem far away from reality because the pushing effect of cavitation of different bubbles will be resulting in cancellation of flow along a boundary line surrounding each of the bubble.

It has been further assumed that size distribution is not present in the nanoparticles, that is, all the particles are of same size. Eulerian multiphase granular flow was assumed and solved using FLUENT 6.2.16. The volume element was divided into  $2 \times 10^4$  control volumes. The region nearby the bubble was finely meshed to get the accurate calculation in that region as very high pressure is generated in the domain, which is affected largely by the region nearby bubble.

The Eulerian granular multiphase model solves a set of momentum and continuity equations for each phase. Coupling is achieved through the pressure and interphase exchange coefficients. In this problem, a combination of two phases, namely, fluid and solid has been taken. This is called granular flow problem. In granular flows, the properties are obtained from application of kinetic theory [13]. The standard  $k-\epsilon$  model [14] has been considered assuming the flow to be fully turbulent.

The Shyamal et al. Equation [13], which takes into consideration the van der Waals force amongst the particles, was used for the particle-particle interaction.

Since Al is most widely used material as a matrix in composites, for the modeling of the nanoparticle deagglomeration we have chosen Aluminum as matrix material. The reinforcement in the matrix has been taken as SiC nanoparticles of 30 nm size. Along with this we have assumed that about 15 ppm air is entrapped in the aluminum melt.

### 3. Results and Discussions

FLUENT 6.2.16 was run to simulate the mathematical model. The computational time step for solving the unsteady state problem was  $0.1 \mu\text{s}$ . During the simulation of the model the output data files, namely, those containing information on velocity field and volume fraction (particulate) field were saved after every 100 time steps for computations up to the first 1000 time steps. Later on the frequency for saving the data files was reduced, that is, data files were saved after every 5000 time steps for the next 50000 time steps and after every 10000 time steps for the remaining computation.

The contours of volume fraction of particulate were plotted from the saved data files. Figure 2 shows the initial distribution of nanoparticles with respect to the source of the shock wave, that is, the location where periodic cavitations is occurring. Figure 3(a) shows the movement of the agglomerate of the nanoparticles in the first  $100 \mu\text{s}$ . The lump moves towards the right boundary wall. As it moves its shape also changes. Apart from this convective movement the nanoparticles have diffused out to a small extent. Since bubble wall has been taken as semicircular, the shock wave generated by the bubble will be circular in nature. It can be seen from Figure 3(a), in which the nanoparticles lying on the symmetry axis, being closer to the bubble, have moved more compared to those at other locations. It can be seen from Figure 3(b) that after an initial drift towards the right wall the agglomerate bifurcates, and a spiral pattern on both the sides of the axis of symmetry is formed. Within the spiral pattern, a narrow band of zones with high volume fraction of nanoparticles can be observed. This convective effect is due to high fluid velocity created by the pressure field. A gradual

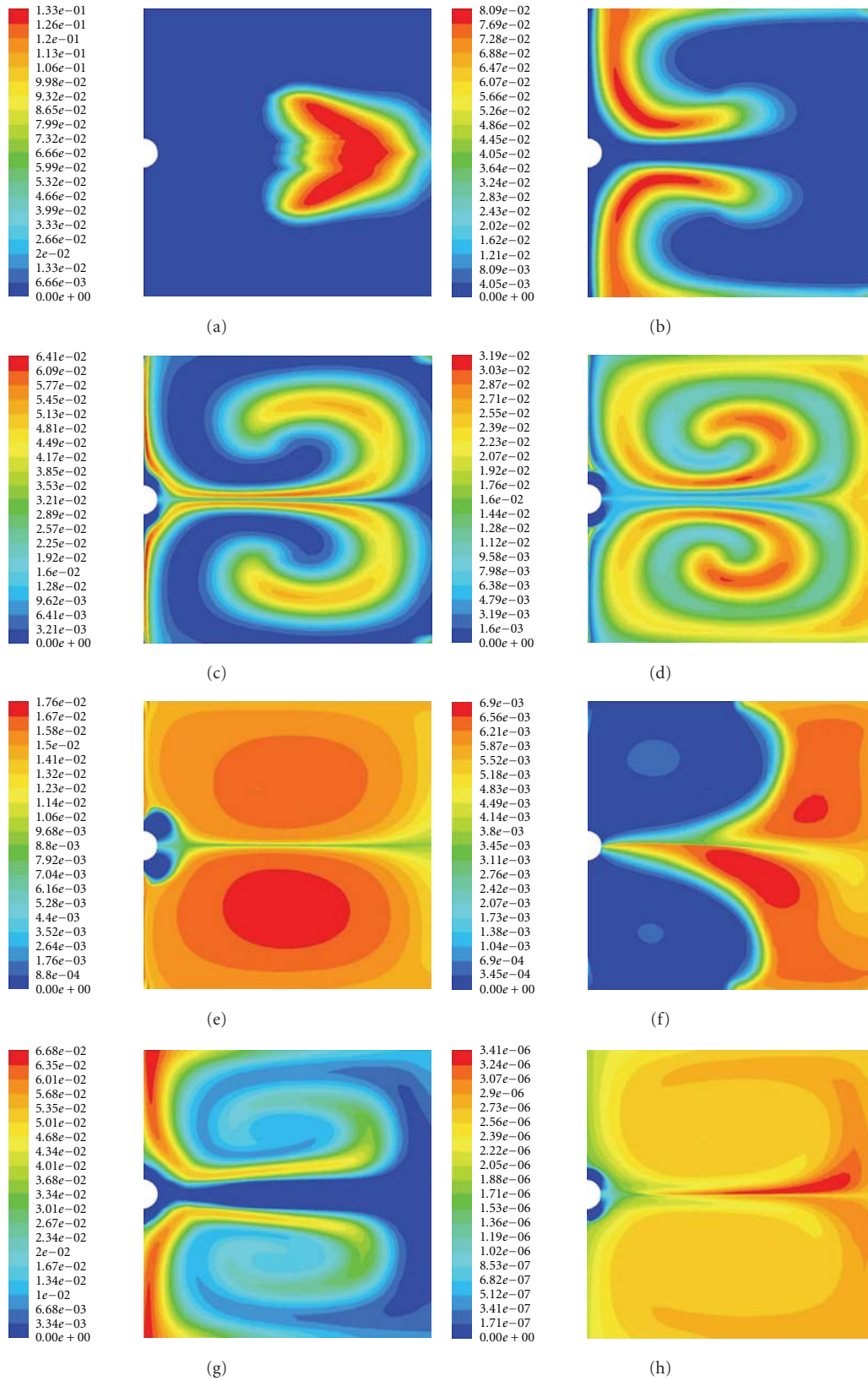


FIGURE 3: (a) Contour of particulate volume fraction at time  $t = 100 \mu\text{s}$ . (b) Contour of particulate volume fraction at time  $t = 1 \text{ ms}$ . (c) Contour of particulate volume fraction at time  $t = 2 \text{ ms}$ . (d) Contour of particulate volume fraction at time  $t = 4 \text{ ms}$ . (e) Contour of particulate volume fraction at time  $t = 15 \text{ ms}$ . (f) Contour of particulate volume fraction at time  $t = 50 \text{ ms}$ . (g) Contour of particulate volume fraction at time  $t = 0.4 \text{ s}$ . (h) Contour of particulate volume fraction at time  $t = 4.2 \text{ s}$ .

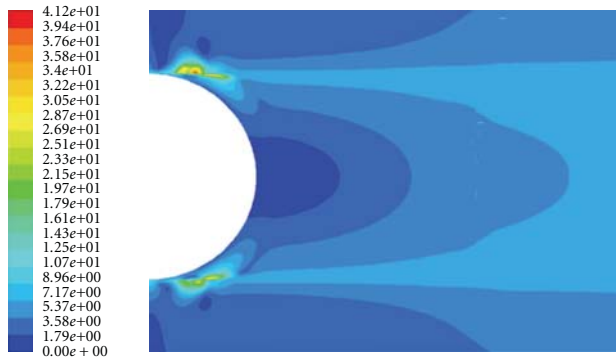


FIGURE 4: Contour of magnitude of velocity (liquid Al) at time  $t = 0.1 \mu\text{s}$ .

dispersion of the nanoparticles can be seen in Figures 3(b)–3(e).

After the formation of spiral bands, as shown in Figures 3(b)–3(e), nano-particle depleted zones formed on both sides of the bubble. At 50 ms (Figure 3(f)) of simulation time almost half of the domain got depleted and nanoparticles were pushed towards the right side of the boundary. But in the nondepleted zone dispersion of nanoparticles has taken place. Thus a spiral pattern forms again. In earlier figures we have seen that how the nanoparticle agglomerate is moving away from the bubble. In subsequent figures, we have seen spiral loops and then nanoparticle-depleted regions. In Figure 3(h), which is the contour after 4.2 s, it can be noted that over a very large area the concentration of nanoparticle does not vary significantly. In the rest of the region, except very close to bubble gradient the concentration can be seen but this gradient can be neglected as it is very small. The volume fraction of particle did not change much with time, over a large area, after 4.2 s. we can conclude that almost homogeneous distribution was achieved after 4.2 s throughout.

The contour of magnitude of velocity (liquid Al) is shown in Figure 4. It can be seen that the maximum velocity of the fluid can rise up to 41 m/s local to the bubble. In the intense flow field, which spatially varies over the agglomerate zone, different parts of the agglomerate are pushed in different direction, facilitating the movement of its different parts in different direction. Such a flow, with sharp variation in the velocity field is generated by the pressure shock wave with very low wavelength.

#### 4. Conclusions

A flow within a representative volume element with a single agglomerated lump of the nanoparticles, as a result of periodic cavitation, has been simulated. After  $\sim 4.2$  s significant dispersion took place and the distribution of nanoparticles was almost uniform. Thus the phenomenon of deagglomeration due to cavitation could be simulated at mesoscale. Intense convective flow with significantly large gradient in the velocity fields, at the mesoscale, results in the dispersion.

#### References

- [1] K. S. Suslick, *Ultrasound: Its Chemical, Physical, and Biological Effects*, Vancouver Coastal Health, New York, NY, USA, 1988.
- [2] G. I. Eskin, *Ultrasonic Treatment of Light Alloy Melts*, Gordon and Breach, Amsterdam, The Netherlands, 1998.
- [3] G. I. Eskin, Yu. P. Pimenov, and G. S. Makarov, "Effect of cavitation melt treatment on the structure refinement and property improvement in cast and deformed hypereutectic Al-Si alloys," *Materials Science Forum*, vol. 242, pp. 65–70, 1997.
- [4] G. I. Eskin, "Broad prospects for commercial application of the ultrasonic (cavitation) melt treatment of light alloys," *Ultrasonics Sonochemistry*, vol. 8, no. 3, pp. 319–325, 2001.
- [5] G. I. Eskin, B. I. Semenov, and D. N. Lobkov, "Concept and control means for the formation of crystalline structure of castings in new casting methods," *Litejnoe Proizvodstvo*, no. 9, p. 2, 2001.
- [6] D. G. Eskin, M. L. Kharakterova, G. I. Eskin, and YU. P. Pimenov, "Structure and phase composition of hypereutectic siluminos intended for deformation," *Izvestia Akademii nauk SSSR. Metall*, no. 2, pp. 91–98, 1997.
- [7] Y. Yang, J. Lan, and X. Li, "Study on bulk aluminium matrix nano-composite fabricated by ultrasonic dispersion of nano-sized SiC particles in molten aluminium alloy," *Materials Science and Engineering A*, vol. 380, pp. 378–383, 2004.
- [8] Y. Yang and X. Li, "Ultrasonic cavitation-based nanomanufacturing of bulk aluminum matrix nanocomposites," *Journal of Manufacturing Science and Engineering*, vol. 129, no. 2, pp. 252–255, 2007.
- [9] G. I. Eskin and D. G. Eskin, "Production of natural and synthesized aluminum-based composite materials with the aid of ultrasonic (cavitation) treatment of the melt," *Ultrasonics Sonochemistry*, vol. 10, no. 4-5, pp. 297–301, 2003.
- [10] B. P. Michael, "Single-bubble sonoluminescence," *Reviews of Modern Physics*, vol. 74, no. 2, pp. 425–484, 2002.
- [11] T. Hielscher, "Ultrasonic production of nano-size dispersions and emulsions," in *Dans European Nano Systems Workshop (ENS '05)*, Paris, France, 2005.
- [12] FLUENT Tutorials.
- [13] M. Syamlal, W. Rogers, and T. J. O'Brien, *MFIX Documentation, I, Theory Guide*, National Technical Information Service, Springfield, Va, USA, 1993, DOE/METC-94112K2K4, NTIS/DE9400087.
- [14] D. G. Schaeffer, "Instability in the evolution equations describing incompressible granular flow," *Journal of Differential Equations*, vol. 66, no. 1, pp. 19–50, 1987.

## Research Article

# Structure and Properties of Multiwall Carbon Nanotubes/Polystyrene Composites Prepared via Coagulation Precipitation Technique

I. N. Mazov,<sup>1,2</sup> V. L. Kuznetsov,<sup>1,2</sup> D. V. Krasnikov,<sup>2</sup> N. A. Rudina,<sup>1</sup> A. I. Romanenko,<sup>2,3</sup>  
O. B. Anikeeva,<sup>2,3</sup> V. I. Suslyayev,<sup>4</sup> E. Yu. Korovin,<sup>4</sup> and V. A. Zhuravlev<sup>4</sup>

<sup>1</sup> Department of Physical Methods of Investigations, Boreskov Institute of Catalysis, Novosibirsk, Russia

<sup>2</sup> Physical Faculty, Novosibirsk State University, Novosibirsk 630090, Russia

<sup>3</sup> Department of Thermodynamic Investigations, Nikolaev Institute of Inorganic Chemistry, Novosibirsk 630090, Russia

<sup>4</sup> Faculty of Radiophysics, National Research Tomsk State University, Tomsk 634050, Russia

Correspondence should be addressed to I. N. Mazov, ilya.mazov@gmail.com

Received 9 February 2011; Revised 25 April 2011; Accepted 28 April 2011

Academic Editor: Baoquan Sun

Copyright © 2011 I. N. Mazov et al. This is an open access article distributed under the Creative Commons Attribution License, which permits unrestricted use, distribution, and reproduction in any medium, provided the original work is properly cited.

Coagulation technique was applied for preparation of multiwall carbon nanotube- (MWNT-)containing polystyrene (PSt) composite materials with different MWNT loading (0.5–10 wt.%). Scanning and transmission electron microscopies were used for investigation of the morphology and structure of produced composites. It was shown that synthesis of MWNT/PSt composites using coagulation technique allows one to obtain high dispersion degree of MWNT in the polymer matrix. According to microscopy data, composite powder consists of the polystyrene matrix forming spherical particles with diameter ca. 100–200 nm, and the surface of MWNT is strongly wetted by the polymer forming thin layer with 5–10 nm thickness. Electrical conductivity of MWNT/PSt composites was investigated using a four-probe technique. Observed electrical percolation threshold of composite materials is near to 10 wt.%, mainly due to the insulating polymer layer deposited on the surface of nanotubes. Electromagnetic response of prepared materials was investigated in broadband region (0.01–4 and 26–36 GHz). It was found that MWNT/PSt composites are almost radiotransparent for low frequency region and possess high absorbance of EM radiation at higher frequencies.

## 1. Introduction

Carbon nanotubes attract high attention as perspective material due to their high mechanical strength, Young's modulus, thermal and electrical conductivity, and chemical stability. One of the most interesting ways of application of multiwall carbon nanotubes (MWNT) is their usage for synthesis of MWNT-reinforced composite materials. Introduction of carbon nanotubes in polymer matrix leads to significant increase of material's properties, such as mechanical strength, electrical conductivity, fracture toughness, and electromagnetic shielding properties [1–3]. In recent decade many works were done in the field of the development of preparation techniques and investigation of properties of MWNT-reinforced plastic composites, based on such

matrices as epoxy resin [4], polymethylmethacrylate [5], polyurethanes [6], polystyrene [7], and polypropylene and polyethylene [7, 8]. Nowadays several preparation methods were successfully used for synthesis of CNT-containing composites, melt mixing [9], solvent cast technique [10], *in situ* polymerization [11, 12], coagulation precipitation [13], and so forth. Among these methods coagulation precipitation technique described by Du et al. [14] is one of the most promising because of its experimental simplicity, potential scalability, and ability for usage for synthesis of various thermoplastic-based polymer composites. In this method the filler material and polymer matrix precursor are dissolved in appropriate medium, treated (with ultrasound, mechanical stirring, or any other necessary technique) for disaggregation and distribution of filler, and produced mixture is poured in

appropriate solvent, providing dissolution of the suspension medium with further precipitation of the matrix material with incorporated filler. Using this technique, it is possible to achieve high degree of distribution of filler (e.g., carbon nanotubes) in the matrix due to relatively high amount of the solvent with low viscosity as compared with pure matrix. Successful application of the coagulation precipitation technique depends strongly on the right choice of the solvent medium and disaggregation method.

In the present work coagulation precipitation technique was applied for preparation of MWNT-containing polystyrene composites with various CNT content, and investigation of their morphological, structural, electrophysical, and electromagnetic properties was performed.

## 2. Experimental and Methodology

Multiwall carbon nanotubes (MWNT) with average diameter 20–22 nm were produced on site by CVD decomposition of ethylene over bimetallic FeCo catalysts at 680°C. Synthesized MWNTs were purified by reflux with HCl (1 : 1), rinsed with distilled water, and dried in air at 60°C overnight.

Polystyrene (PSt) with molecular weight ca. 75 000–100 000 was dissolved in dimethylformamide (DMF) to form concentration 0.05 g/mL.

Coagulation technique described elsewhere [15] for preparation of MWNT/PMMA composites was applied for synthesis of MWNT/PSt composites as follows. Necessary amount of purified MWNTs was placed in the water-cooled glass reaction vessel, 80 mL of PSt/DMF solution and 40 mL of pure DMF were added to MWNT, and the mixture was sonicated (22 KHz, 800 W) during 1 hour. After sonication MWNT/PSt/DMF suspension became uniformly black and was poured into ca. 1000 mL of distilled water (55–60°C). Immediately after mixing with water precipitation of MWNT/PSt composite takes place leading to formation of spongy deposit with color changing from light gray to black depending on MWNT loading. MWNT/PSt composites with MWNT content 0.5, 1.0, 2.0, 4.0, and 10.0 wt.% were prepared using described technique.

Produced deposit was filtered, rinsed with water (500 mL for 3 times) and dried in air at 60°C overnight, milled in rotary mill, and dried once more at 60°C in vacuum ( $10^{-2}$  torr) for 4 hours until the constant weight. Composite powder was hot pressed at 115–120°C between polished steel plates with pressure up to 200 kg/cm<sup>2</sup> to form films with dimensions ca. 60 mm  $\varnothing$   $\times$  0.3 mm.

Scanning and transmission electron microscopy investigations were performed using JSM6460LV and JEM-2010 microscopes, correspondingly. For SEM analysis polymer films were broken and glued to the copper plate using silver glue with fresh break upwards. In order to avoid charging effects composites were gold coated with layer thickness 60–80 Å. TEM analysis was performed for powder samples deposited on the copper grid from ethanol suspension using horn ultrasonicator.

Electrical conductivity of composite films was measured using four-probe technique in temperature range 4.2–300 K

with silver wire (0.1 mm in diameter) contacts attached to the sample using silver glue. The low conductivity threshold of the experimental setup was  $10^{-11}$  S/cm.

Electromagnetic response properties (reflection, absorbance, and transmission coefficients on power) were measured in 0.01–4 and 26–36 GHz frequency ranges. For low-frequency range coaxial cell with 16 mm O.D. and 6.95 mm I.D. connected to the transmittance and reflectance measurement unit R2-4M (Mikran, Russia) was used. High frequency measurement was performed using open horn measurement cell, connected with HP Agilent PNA E8363B vector network analyzer.

## 3. Results and Discussion

*Structure of carbon nanotubes* was investigated by means of transmission electron microscopy. The typical TEM image of MWNTs used for synthesis of composites is shown on Figure 1.

The average diameter of MWNTs was determined statistically after analysis of 400–450 individual nanotubes on 10–15 TEM images and Gatan software package and made the value of 22–24 nm. No additional purification was used for removal of possible excessive amorphous carbon—according to our previous studies [16] the amount of amorphous species on the surface of MWNTs does not exceed 0.5 at.%. The residual metal particles are situated mainly inside of carbon nanotubes, the quantity of the metal was estimated by X-ray fluorescent analysis and was found to be ca. 0.5 wt.%.

*Investigation of the internal structure of composite films* was performed using scanning electron microscopy in order to obtain data on the dispersion state of MWNTs in the polystyrene matrix. Optical microscopy was used. On Figure 2 SEM images of fresh breaks of the composite films with MWNT concentration 0.5, 1.0, 2.0, 4.0, and 10 wt.%, and reference pure polystyrene film are shown. Carbon nanotubes are well distributed in the polymer matrix for all concentrations, noting that the increase of CNT content does not lead to formation of visible agglomerates in the bulk volume of the polymer. MWNTs are covered with the polymer layer, which remains intact after breakage of the composite film (see Figure 2(d) e.g.) indicating good wetting of the CNT surface with the polystyrene.

Transmission electron microscopy images of initial MWNT/PSt composite powders are presented on Figure 3. Polystyrene forms spherical particles with approximate diameter 50–200 nm either separated or linked with each other (Figure 3(a)), which may be freestanding or situated on the surface of nanotubes (Figures 3(b) and 3(c)). The surface of MWNTs is covered with the layer of amorphous polystyrene with thickness up to 10–20 nm or forming drop-like particles on the surface of nanotubes (see Figures 3(b), 3(c), and 3(d)). The average value of the contact angle between polystyrene particles and carbon nanotubes lays in range 18–28 degrees, indicating good wetting of the CNT surface with the polymer.

Wetting of the nanotube surface with polymer may be of crucial importance to obtain good disaggregation of

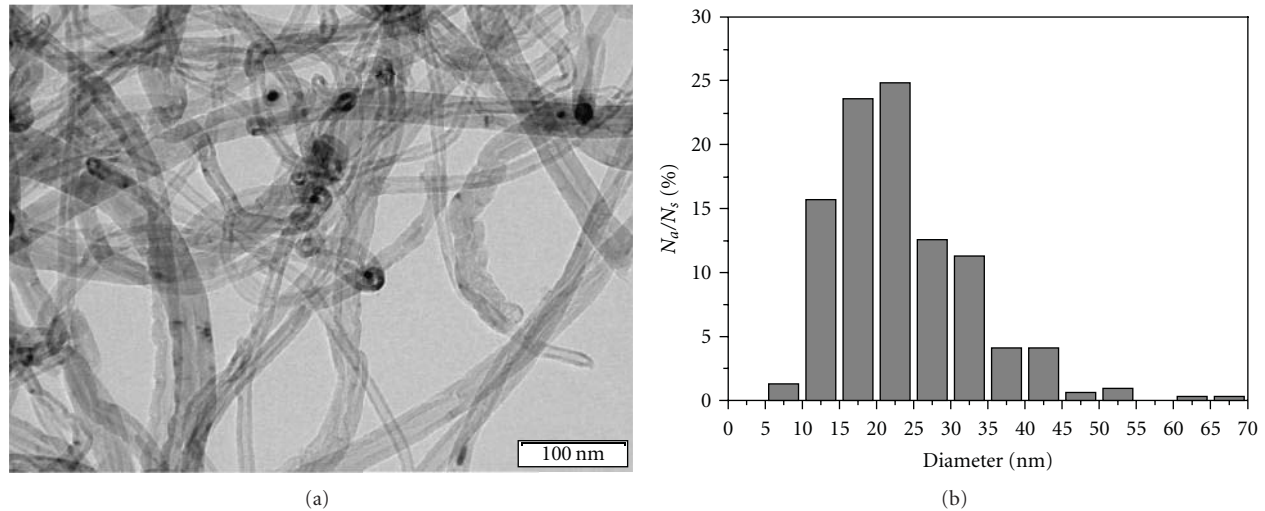


FIGURE 1: Initial multiwall carbon nanotubes, (a) TEM image of MWNTs, (b) statistical distribution of MWNTs.

MWNTs and subsequent high dispersion state of nanotubes in polystyrene matrix due to change of the interaction behavior from “CNT-polystyrene” in the case of low wetting to “polystyrene-polystyrene” in the case of the high wetting. Nevertheless, the presence of the insulating polymer layer on the surface of conductive nanotube can significantly change the electrical conductivity of resulting composite.

Thus according to the microscopy data it is reasonable to conclude that coagulation precipitation of the polystyrene/MWNT mixture from DMF solution allows one to produce composite material with highly disaggregated nanotubes. As it was early mentioned by Du et al. [14] for SWNT/PMMA composites precipitation of the dissolved polymer leads to wrapping of the disaggregated nanotubes with polymer chains, thus preventing further agglomeration of CNTs and in our case leading to insulating of the nanotubes by relatively dense polymer layer with thickness comparable with MWNT diameter. Agglomeration of MWNTs during deposition and further film processing does not occur mainly due to the polymer layer formed on the surface of the nanotubes, preventing strong van der Waals interactions between individual CNTs, which are produced from agglomerates during ultrasonication in DMF which is known as a well-dispersing agent for carbon nanostructures [17] because of its high polarity and free electron pair of the nitrogen atom which interacts with distributed  $\pi$ -system of CNT allowing good wetting of the surface and further disaggregation of tangled agglomerates.

Thus in our case highly dispersed nanotubes are covered with the polymer layer immediately after disaggregation and this may be of crucial importance to further formation of the distributed network of CNTs in the bulk polymer matrix.

*Electrical resistivity measurements* of MWNT/PSt composite films were performed using four-probe technique, applied earlier for investigation of electrophysical properties of MWNTs and MWNT-containing polymer composites [18]. It is well known that introduction of continuous carbon

nanotubes in the dielectric polymer matrix allows to increase conductivity of the resulting composite for several orders of magnitude. Conductive composite materials can be characterized by the percolation threshold which for multiwall carbon nanotubes lays in range from ca. 0.005 wt.% [19] to 3-4 wt.% [20] depending on the electrophysical properties of initial nanotubes and peculiarities of the composites' preparation (alignment and dispersion of nanotubes etc.).

Earlier we have observed percolation threshold ca. 0.5 wt.% for the same type of nanotubes incorporated in the polymethylmethacrylate (PMMA) matrix and prepared using the same coagulation technique [21]. Composite materials investigated in this work show better distribution of MWNTs in the polymer matrix, but at the same time surprisingly low electrical conductivity for these materials was found. Significant conductivity ( $4.4 \times 10^{-4}$  S/cm) was observed only for composite sample with 10.0 wt.% loading of CNTs; all other samples show electrical resistivity higher than  $10^9$  Ohm/cm which was the sensitivity threshold for the setup used for measurements. For comparison MWNT/PMMA composites with the same type of nanotubes showed higher electrical conductivity

This phenomenon can be described taking into consideration the above-mentioned wetting of the nanotubes' surface and formation of polystyrene layer on it. It is well known that electrical percolation proceeds in systems formed with conductive inclusions in the insulating matrix, but in the case of MWNT/PSt composites the clearly observed 3-dimensional network in the bulk volume of the polymer is constructed of *nonconductive* objects due to the strong wetting occurring between carbon nanotube surface and polystyrene and subsequent covering of the surface of each nanotube with polystyrene layer. In this case electrical conductivity may occur only for relatively dense systems with high CNT content in which numerous potential electric contacts are presented. Despite high disaggregation degree and homogeneous distribution of MWNTs for composites with

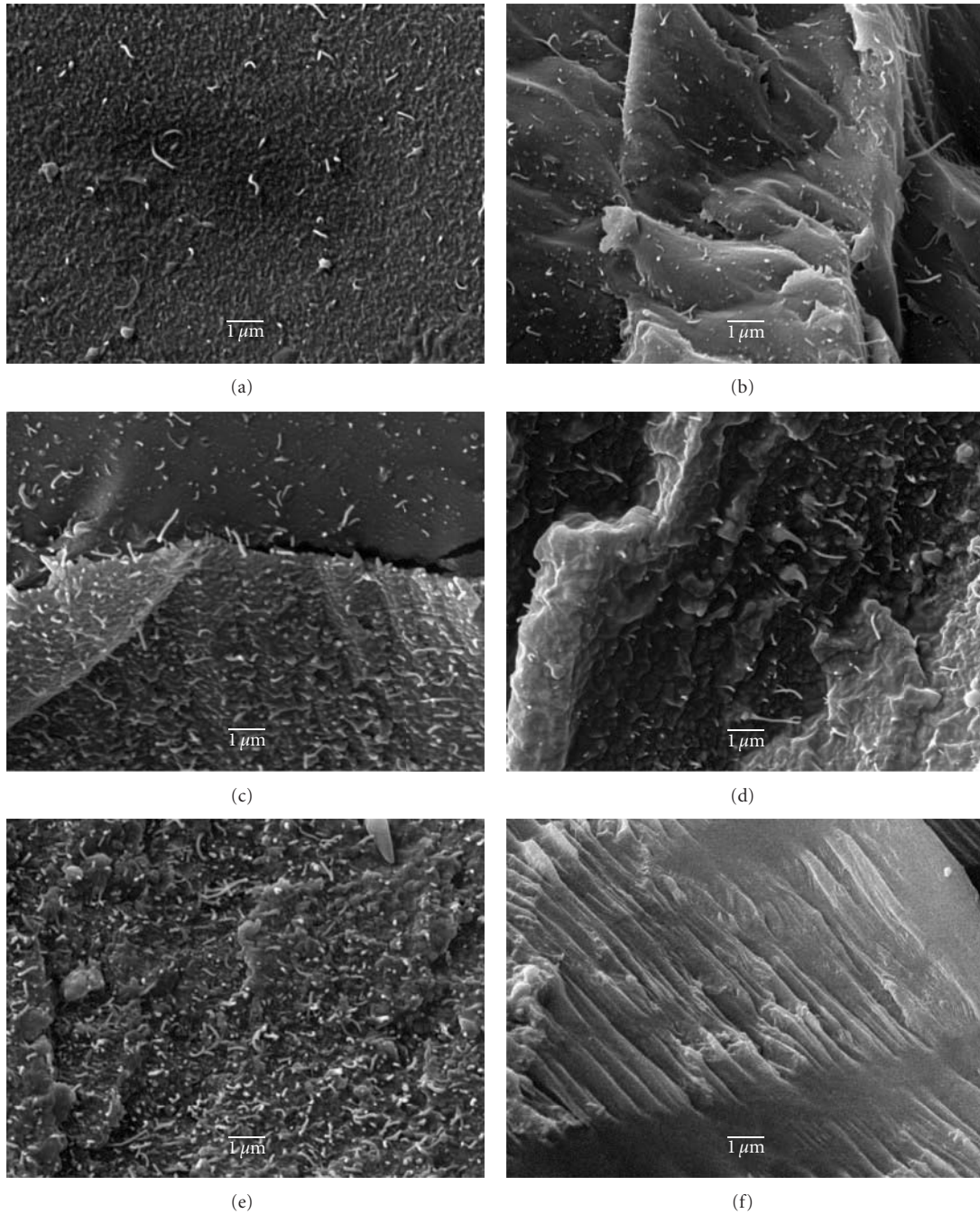


FIGURE 2: SEM micrographs of the MWNT/PSt composite films (gold-coated fresh breaks) with CNT loading 0.5 (a), 1.0 (b), 2.0 (c), 4.0 (d), and 10.0 (e) wt.%. On Figure (f) pure PSt film is shown for comparison.

low concentrations of nanotubes, formation of geometrical CNT network is not enough to form electrically conductive system.

Nevertheless, this phenomenon may be used for the design of CNT-based composites with tailorable properties, for example nonconductive coatings with enhanced mechanical, tribological, and thermal properties or for synthesis of EM-shielding coating with low reflection ability due to low electrical conductivity.

*Electromagnetic response* of produced composites was investigated in frequency range 0.01–4 and 26–36 GHz. In the low frequency region reflection and transmission coefficients for composite materials were measured directly in the coaxial cell, and it was found that nonconductive composites are almost radiotransparent in frequency range 0.01–4 GHz. In the microwave frequency region 26–36 GHz transmission ( $T$ ) and reflection ( $R$ ) coefficients were measured using open horn measurement cell. Absorption coefficient ( $A$ ) of the

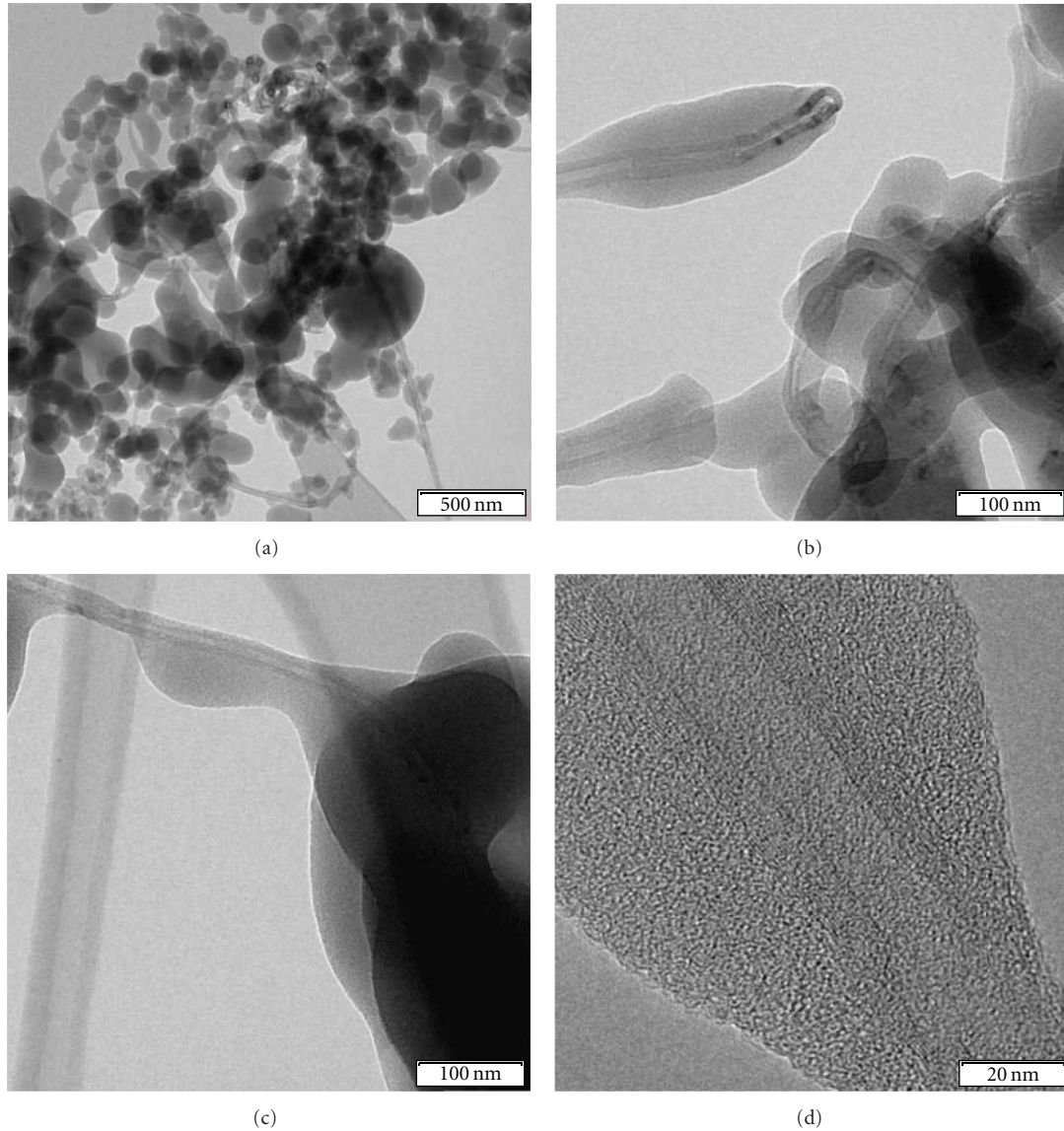


FIGURE 3: TEM images of MWNT/PSt composite powders with different MWNT loading. Carbon nanotubes covered with polystyrene. (a) 2 wt.% of MWNTs in PSt, 2–10 wt.% of MWNTs in PSt, 3, 4–0.5 wt.% of MWNTs in PSt. The polymer is presented in form of spherical particles (a) and the layer on the surface of CNT (b, c, d).

EM radiation in the sample can be calculated as  $A(\%) = 100 - R - T$ .

Data on the dependences electromagnetic response of MWNT/PSt composites with various MWNT loading at fixed frequencies are shown in Figure 4. Increase of the EM radiation frequency leads to the simultaneous growth of the absorbance coefficient and, what is the most surprising, to the sharp diminishing of the reflectance of EMI even for composites with high MWNT loading.

EM properties of all composite materials are changing with increase of the MWNT content in the material. Only slight changes can be seen for the composite with 0.5 wt.% MWNT loading—it is almost radiotransparent in all frequency range. Increase of the MWNT content leads to drastic increase of the EM absorbance and reflectance with

subsequent drop of the EM transmittance coefficient. It is noteworthy that absorbance coefficient  $A$  for the samples with high MWNT loading increases more sharply as compared with the reflectance coefficient  $R$  especially for higher frequencies.

Analyzing data on the EM response of the composites versus MWNT loading and frequency, one can see percolation-like behavior. At the same time no significant electrical conductivity was observed for all samples excluding 10 wt.% sample. Such behavior can be explained taking into consideration structural data for MWNT/PSt composites: (a) high wetting of MWNT surface with polystyrene allows one to obtain high degree of MWNT distribution in the polymer body with formation of the percolative 3-dimensional nanotube network; (b) the surface of each individual

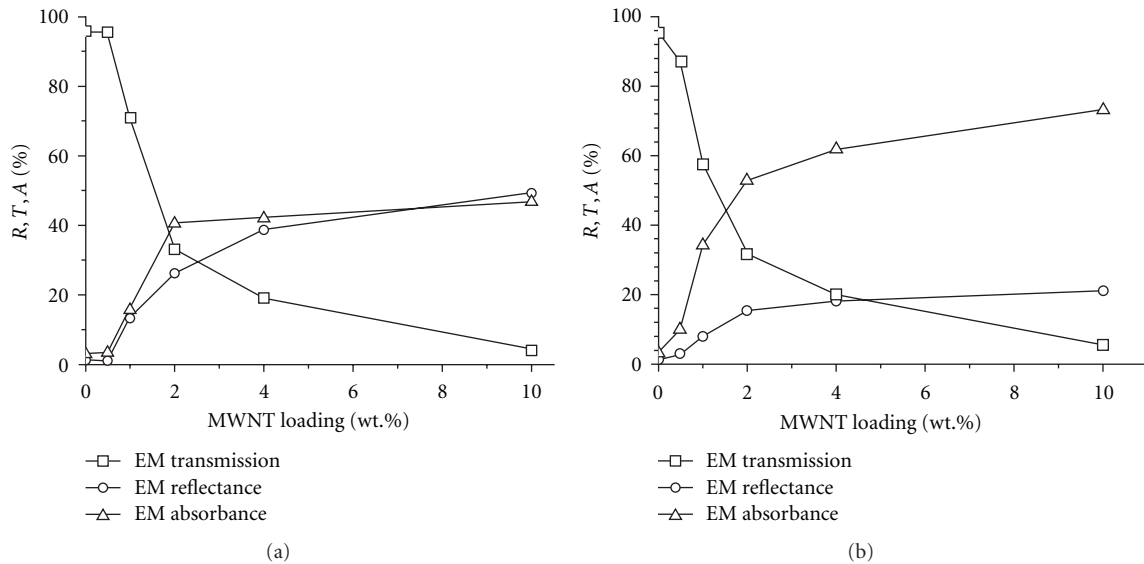


FIGURE 4: Electromagnetic response of MWNT/PSt composites at fixed frequency versus MWNT loading. (a) EM response at 29 GHz, (b) EM response at 34 GHz.

nanotube is covered with the polystyrene thus the above-mentioned nanotube network is consisted of *insulating* objects; (c) the surface conductivity cannot be measured at low MWNT loadings due to insulation between nanotubes on the surface and in the volume of the polymer composite; (d) microwave probing of such material leads to high EM absorbance and relatively low reflectance from the bulk volume of the material.

The last point should be considered separately. The characteristic wavelength for the microwave radiation is  $\sim 0.7$  cm, which is much higher than the size of the individual nanotube and MWNT agglomerate and the thickness of the composite sample. Thus it is possible to suggest that incident EM wave interacts with the whole composite sample, and this interaction is facilitated due to the absence of surface conductivity and possible skin effects.

Earlier we have observed the effect of high EM shielding for MWNT/PMMA composite materials with the same MWNT loadings in the microwave region [22]. In the case of PMMA-based composites the surface wetting of nanotubes was low, and the surface conductivity of all samples was higher as compared with PSt-based composites with electrical percolation threshold at ca. 0.5 wt.% of MWNTs.

Thus for conductive MWNT/PMMA samples observed earlier high shielding efficiency was achieved mainly due to the reflectance of EM radiation from the surface of the composite film.

In the case of low-conductive MWNT/PSt composite materials high electromagnetic response may be attributed with various mechanisms of dissipation of EM radiation—such as mechanical resonances of disaggregated carbon nanotubes in polymer media, metamaterial-like absorbance due to formation of inductance-capacitor (LC) circuits in the carbon nanotube network.

The detailed clarification of the nature of strong EM absorbance by low-conductive MWNT-composites needs further detailed investigations.

#### 4. Conclusions

Polystyrene-based composite materials containing multi-wall carbon nanotubes were synthesized via coagulation technique. According to electron microscopy study carbon nanotubes are well distributed in the polystyrene matrix forming 3-dimensional uniform network.

High wetting of the nanotube surface with polymer results in formation of the polystyrene layer with thickness 5–15 nm just after the coagulation, the polymer on MWNTs. Finally that prevents electrical contacts between nanotubes in the composite. The insulation of each nanotube is the main reason of low electrical conductivity for low loadings of CNTs in composite neither shortening or dispersion state of CNT.

Significant electrical conductivity was observed only for materials with 10 wt.% of MWNT content with corresponding conductivity value  $4.4 \times 10^{-4}$  S/cm. We have found that EM response of MWNT/PSt composite materials with high CNT loading has high contribution of absorbance in GHz frequency range in contrast to highly conductive MWNT/PMMA composites investigated earlier where the main contribution into the EM response is reflectance.

Electromagnetic response of the CNT/PSt composite does not depend only on the electrical conductivity of the composites—the interaction of EM radiation with nanotubes occurs at low loadings—namely, 1-2 wt.%, thus allowing to conclude that formation of the insulated network of CNT interacting with EM radiation proceeds even at low CNT loadings (which is in agreement with SEM data concerning formation of uniform CNT distribution in

polystyrene matrix). Detailed mechanism of such high EM absorbance is not clear and needs further investigations.

MWNT-containing composites with polystyrene matrix can be used for synthesis of tailorable materials with variable electrical and electromagnetic properties.

## Acknowledgments

This work was partially supported by ITSC Project no. B-1708, Russian state Contracts nos. 16.740.11.0016 and 16.740.11.0146, and RFBR Grant no. 11-03-00351-a.

## References

- [1] H. Xu, S. M. Anlage, L. Hu, and G. Gruner, "Microwave shielding of transparent and conducting single-walled carbon nanotube films," *Applied Physics Letters*, vol. 90, no. 18, Article ID 183119, 2007.
- [2] G. M. Odegard, S. J. V. Frankland, and T. S. Gates, "Effect of nanotube functionalization on the elastic properties of polyethylene nanotube composites," *AIAA Journal*, vol. 43, no. 8, pp. 1828–1835, 2005.
- [3] Y. Yang, M. C. Gupta, and K. L. Dudley, "Towards cost-efficient EMI shielding materials using carbon nanostructure-based nanocomposites," *Nanotechnology*, vol. 18, no. 34, Article ID 345701, 2007.
- [4] Y. Zhou, F. Pervin, L. Lewis, and S. Jeelani, "Fabrication and characterization of carbon/epoxy composites mixed with multi-walled carbon nanotubes," *Materials Science and Engineering A*, vol. 475, no. 1-2, pp. 157–165, 2008.
- [5] S.-M. Yuen, C.-M. Ma, C.-Y. Chuang et al., "Effect of processing method on the shielding effectiveness of electromagnetic interference of MWCNT/PMMA composites," *Composites Science and Technology*, vol. 68, no. 3-4, pp. 963–968, 2008.
- [6] R. Zhang, A. Dowden, H. Deng, M. Baxendale, and T. Peijs, "Conductive network formation in the melt of carbon nanotube/thermoplastic polyurethane composite," *Composites Science and Technology*, vol. 69, no. 10, pp. 1499–1504, 2009.
- [7] D. Xu and Z. Wang, "Role of multi-wall carbon nanotube network in composites to crystallization of isotactic polypropylene matrix," *Polymer*, vol. 49, no. 1, pp. 330–338, 2008.
- [8] S. Kanagaraj, F. R. Varanda, T. V. Zhil'tsova, M. S. A. Oliveira, and J. A. O. Simões, "Mechanical properties of high density polyethylene/carbon nanotube composites," *Composites Science and Technology*, vol. 67, no. 15-16, pp. 3071–3077, 2007.
- [9] C. McClory, T. McNally, M. Baxendale, P. Pötschke, W. Blau, and M. Ruether, "Electrical and rheological percolation of PMMA/MWCNT nanocomposites as a function of CNT geometry and functionality," *European Polymer Journal*, vol. 46, no. 5, pp. 854–868, 2010.
- [10] P. Slobodian, A. Lengálová, P. Sáha, and M. Šlouf, "Poly (methyl methacrylate)/multi-wall carbon nanotubes composites prepared by solvent cast technique: composites electrical percolation threshold," *Journal of Reinforced Plastics and Composites*, vol. 26, no. 16, pp. 1705–1712, 2007.
- [11] E. N. Konyushenko, J. Stejskal, M. Trchová et al., "Multi-wall carbon nanotubes coated with polyaniline," *Polymer*, vol. 47, no. 16, pp. 5715–5723, 2006.
- [12] S. J. Park, M. S. Cho, S. T. Lim, H. J. Choi, and M. S. Jhon, "Electrorheology of multiwalled carbon nanotube/poly(methyl methacrylate) nanocomposites," *Macromolecular Rapid Communications*, vol. 26, no. 19, pp. 1563–1566, 2005.
- [13] S. R. Tatro, L. M. Clayton, P. A. O. Muisener, A. M. Rao, and J. P. Harmon, "Probing multi-walled nanotube/poly(methyl methacrylate) composites with ionizing radiation," *Polymer*, vol. 45, no. 6, pp. 1971–1979, 2004.
- [14] F. Du, J. E. Fischer, and K. I. Winey, "Coagulation method for preparing single-walled carbon nanotube/poly(methyl methacrylate) composites and their modulus, electrical conductivity, and thermal stability," *Journal of Polymer Science Part B*, vol. 41, no. 24, pp. 3333–3338, 2003.
- [15] I. N. Mazov, V. Kuznetsov, S. Moseenkov et al., "Electromagnetic shielding properties of MWCNT/PMMA composites in Ka-band," *Physica Status Solidi (B)*, vol. 246, no. 11-12, pp. 2662–2666, 2009.
- [16] A. I. Romanenko, O. B. Anikeeva, T. I. Buryakov et al., "Electrophysical properties of multiwalled carbon nanotubes with various diameters," *Physica Status Solidi (B)*, vol. 246, no. 11-12, pp. 2641–2644, 2009.
- [17] F. Inam, H. Yan, M. J. Reece, and T. Peijs, "Dimethylformamide: an effective dispersant for making ceramic-carbon nanotube composites," *Nanotechnology*, vol. 19, no. 19, Article ID 195710, 5 pages, 2008.
- [18] A. I. Romanenko, O. B. Anikeeva, T. I. Buryakov et al., "Influence of surface layer conditions of multiwall carbon nanotubes on their electrophysical properties," *Diamond and Related Materials*, vol. 19, pp. 964–967, 2010.
- [19] A. Moisala, Q. Li, I. A. Kinloch, and A. H. Windle, "Thermal and electrical conductivity of single- and multi-walled carbon nanotube-epoxy composites," *Composites Science and Technology*, vol. 66, no. 10, pp. 1285–1288, 2006.
- [20] W. K. Park, J. H. Kim, S. S. Lee, J. Kim, G. W. Lee, and M. Park, "Effect of carbon nanotube pre-treatment on dispersion and electrical properties of melt mixed multi-walled carbon nanotubes/poly(methyl methacrylate) composites," *Macromolecular Research*, vol. 13, no. 3, pp. 206–211, 2005.
- [21] J. Macutkevic, D. Seliuta, G. Valusis et al., "Dielectric properties of MWCNT based polymer composites close and below percolation threshold," *Physica Status Solidi (C)*, vol. 6, no. 12, pp. 2814–2816, 2009.
- [22] I. N. Mazov, V. Kuznetsov, S. Moseenkov et al., "Electromagnetic shielding properties of MWCNT/PMMA composites in Ka-band," *Physica Status Solidi (B)*, vol. 246, no. 11-12, pp. 2662–2666, 2009.

## Research Article

# Self-Organization of ZnO Nanoparticles on UV-Curable Acrylate Nanocomposites

J. A. Burunkova, I. Yu. Denisyuk, and S. A. Semina

Saint Petersburg State University of Information Technologies, Mechanics and Optics, Kronverskiy Avenue, 49, Saint Petersburg 197101, Russia

Correspondence should be addressed to I. Yu. Denisyuk, denisiuk@mail.ifmo.ru

Received 14 February 2011; Revised 30 March 2011; Accepted 11 April 2011

Academic Editor: Hongmei Luo

Copyright © 2011 J. A. Burunkova et al. This is an open access article distributed under the Creative Commons Attribution License, which permits unrestricted use, distribution, and reproduction in any medium, provided the original work is properly cited.

Our work focused on synthesis and investigation of nanoparticles role in structuring of homogenous nanocomposite based on ZnO nanoparticles in UV-curable monomers mixture. Due to strong interaction between nanoparticles surface and polymerizable carboxylic acid, nanoparticles were distributed homogeneously, and density of nanocomposite increased also in comparison with pure polymer matrix. Light scattering, plasticity, and water sorption non-monotonically depends on the concentration of nanoparticles concentration. UV-curable active matrix polymerization on the surface of ZnO nanoparticles was investigated using IR spectroscopy. The set of structural modifications of polymeric nanocomposites were observed by ASM, light scattering, Brinell hardness, and water sorption. Suggestions that the nanoparticles in the polymerization process play the role of photocatalysts and provide structuring effect on the nanocomposite were discussed.

## 1. Introduction

Nanocomposites based on metal nanoparticles and their oxides into a polymer matrix are intensively developing fields of physics and chemistry of nanosized state. Structural organization of such nanosized particles is an important problem, and without solving it, it will be difficult to make nanocomposite material suitable for practical application. The need to improve the stability of nanocomposites is attracting attention to new ways to control their morphology, structural organization, and architecture [1]. Investigation of self-regulating systems in which synthesis of the polymer matrix and the growth of nanoparticles take place simultaneously can be the best solution to the problem of stabilization of nanoparticles polymers and their structural organization. In other words, the aim is to develop methods for creating nanocomposites with architecture “microcapsulated nanoparticles in a polymer shell” formed *in situ*. This is done by generating a polymerized matrix of cluster dispersions, thereby limiting the growth of nanoparticles. There are many ways to do this: polymerization of vinyl monomers in the intensive mechanical dispersing of metals (initiators are freshly formed metal surface), the introduction

of organometallic compounds to the polymerizing system, which decompose at temperatures close to the temperature of polymerization,  $\gamma$ -coirradiation of the precursor and the monomer at room temperature, polymerization of metal containing monomers, and so forth [1–3].

Nanostructured ZnO has attracted intensive research efforts for its unique properties and versatile applications in transparent electronics, ultraviolet (UV) light emitters, photocatalysis, photoprotecting, piezoelectric devices, chemical sensors, and spin electronics [4, 5]. Based on these remarkable physical properties and the motivation of device miniaturization, large effort has been focused on the synthesis, characterization, and device application of ZnO nanomaterials [6, 7]. In order to change the surface physicochemical properties of ZnO nanomaterials for the special applications, the methods such as chemical adsorption or grafting and physical wrapping were widely used [8].

There are different synthesis methods for ZnO nanopowder preparation [9–13]. Li et al. [9] and Vaezi and Sadrezaad [10] performed some studies in the field of ZnO nanopowder preparation via precipitation routes. They used a zinc salt and varied the pH and some other parameters. Chu et al. [11] used zinc acetate, citric acid, and ammonia

and succeeded in obtaining its ZnO nano particles. Westin et al. [12] and Pillai et al. [13] used a sol-gel method to produce ZnO nanoparticles and applied the prepared powder to a varistor application and observed very high electrical properties.

In spite of the diversity of researches, there are few papers on the optical grade nanomaterials in which a high concentration of nanoparticles is combined with good optical properties.

The difficulty of these task consists in that a high concentration of structuring additives is usually accompanied by significant light scattering on them or by fluctuations in their concentration.

This work is a continuation of our research in the field of nanostructuring of polymers for optical purposes [14–16] and the last work on SiO<sub>2</sub>-based nanocomposite investigation [17]. Nanocomposites were prepared by UV curing of acrylic monomers in the presence of nanoparticles embedded in a curable matrix. Morphology of the material depends on nature and concentration of nanoparticles strongly.

The aim of the work is to study the structural changes of UV-curable polymeric ZnO nanocomposites and the main factors that determine their properties, such as mechanical characteristics, sorption and optical properties. Our work shows that addition of nanoparticles strongly interacting with polymer matrix will not result in worsening its homogeneity in contrary to filled polymers.

It has been found that ZnO nanoparticles are actively involved in the process of UV curing. Introduction in the polymerizable composition of ZnO nanoparticles leads to the formation of transparent and less scattering nanocomposite with good processability.

## 2. Experimental

**Chemicals.** We used monomers 2-Carboxyethyl acrylate (2Carb, Aldrich No. 552348), Bisphenol A glycerolate (BisA, Aldrich No. 41,116-7). For structuring nanomodification we used ZnO nanoparticles with a size of 20 nm (Russian local supplier).

Polymer films (thickness from 12 to 100 microns) were obtained from the previously prepared solutions containing monomer, nanoparticles, and its UV curing. The drop of solution is trapped between two polyester films to prevent inhibitory effects of oxygen. All experiments were accomplished at room temperature in air without special inert atmosphere. UV curing was made by a mercury lamp (100 W) used at the mercury line at 365 nm.

Transmission spectra of the films were measured on a spectrophotometer Perkin-Elmer 555 UV-Vis. For the IR spectra we used Fourier IR spectrometer FSM 1201 Manufacturer Company “Monitoring.” Samples were prepared by pressing pellets with KBr.

Refractive index is measured on an Abbe refractometer in accordance with the recommendations of the European standard ASTM D542.

In this paper we study sorption of water vapor by gravimetric method.

Hardness is measured by Brinell hardness method with “Bulat-T1” device.

Light scattering is measured by the photometric sphere method in accordance with the recommendations of the European standard ASTM D1003.

Investigation of the surface profile of samples was made with an atomic force microscope Ntegra used in contact mode.

## 3. Results

We find some effects at mixing of nanoparticles with monomers mixture. At ZnO introduction in the composition of the monomer BisA/2Carb (30/70) above a concentration of 8 wt.% the viscosity of solutions increases greatly. At higher concentrations (14 wt.% and higher) viscosity of the solution continues to grow and the mixture becomes solid at room temperature.

Transparent nanocomposites were obtained up to 14 wt.% of ZnO nanoparticles with formation of transparent film after UV curing. More than 14 wt.% of ZnO particles addition to the monomer mixture resulted in turbid films. The system becomes heterogeneous.

The films are transparent in the visible and UV spectral region. A significant decrease in optical transmission is observed at high concentrations of ZnO (more than 14 wt.%).

The calculated (1) and experimental (2) values of the refractive index nanocompositions are shown in Figure 1(a). For the theoretical calculation of the refractive index, Maxwell-Garnett’s model of effective medium has been used [18]:

$$\frac{\epsilon_{\text{eff}} - \epsilon_2}{\epsilon_{\text{eff}} + 2\epsilon_2} = f_1 \frac{\epsilon_1 - \epsilon_2}{\epsilon_1 + 2\epsilon_2}, \quad (1)$$

Where  $\epsilon_1$  is the permittivity of the medium,  $\epsilon_2$  is the permittivity of inclusions,  $\epsilon_{\text{eff}}$  is the permittivity of the composite medium,  $f_1 = (1/V)\sum_i V_i$  is the volumetric filling factor, ( $V_i$  is the volume of  $i$ th particle,  $V$  is the volume of the composite environment).

This model is applicable when the volume filling factor:  $f_1 \leq 1/3$ , that is, fraction of inclusions is small. The experimentally obtained values for the film samples are higher than theoretically calculated. This effect can be explained by the following: according our recent results, there is interaction between nanoparticles and polymer matrix. Model of Maxwell-Garnett is applicable in the case when nanoparticles are distributed in any matrix. As a result of interaction between nanoparticles and polymer matrix this model condition is not accomplished. [19]. Refractive index of composition with maximum ZnO concentration (14 wt.%) is increased by 0.045 compared with the polymer without nanoparticles.

Figure 1((b), curve 3) shows that at increasing ZnO concentration, scattering of nanocomposite decreases, but near 4 wt.% there is a maximum of scattering. We think that near this concentration takes place a reorganization of polymer inner structure from polymeric structure with

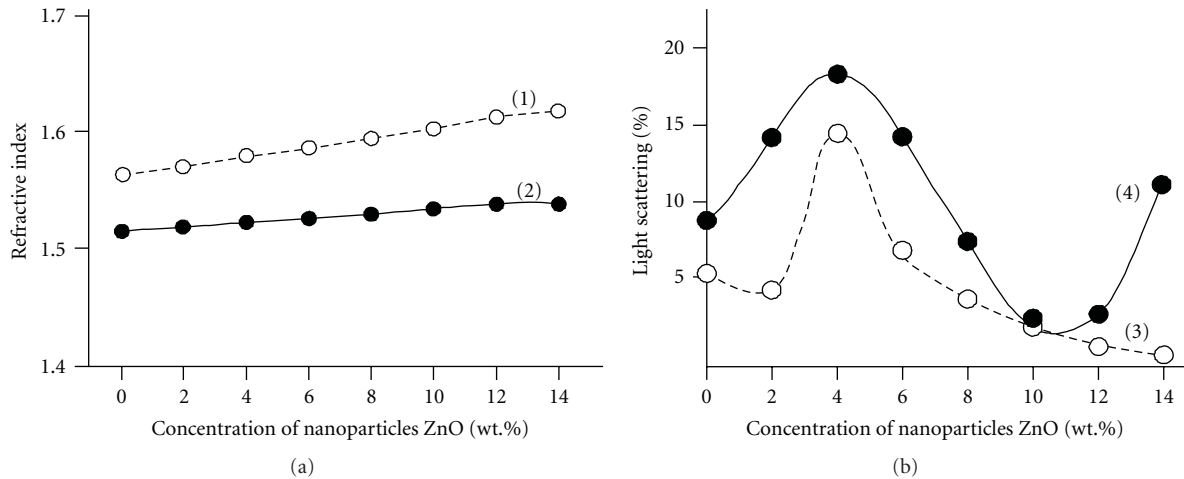


FIGURE 1: Refractive index (a): experimental RI (1) and calculation RI (2), light scattering (b): before (3) and after (4) water sorption of the composition BisA/2Carb (30/70) versus ZnO nanoparticles concentrations.

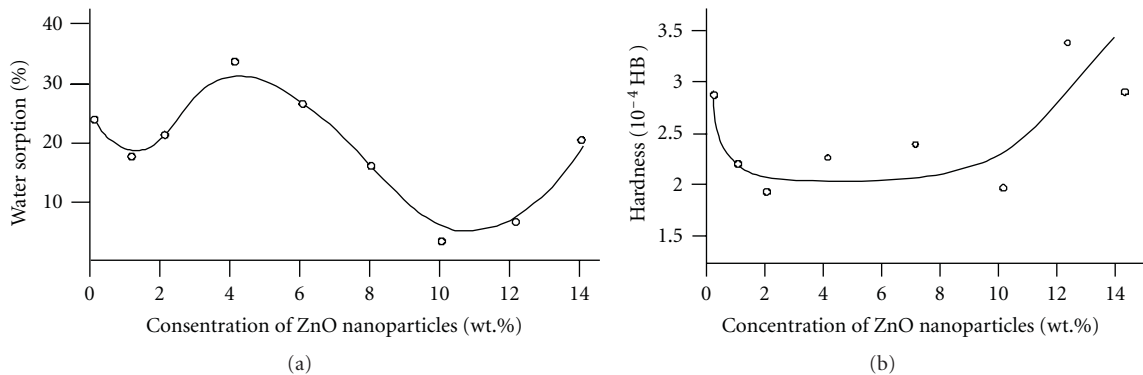


FIGURE 2: Sorption of water (a) and hardness (b) of composite BisA/2Carb (30/70) versus concentrations of ZnO.

inclusion of nanoparticles to self-organized nanocomposite structure (see Figure 3).

When the concentration of ZnO is more than 14 wt.%, light scattering is independent of the concentration of nanoparticles. ZnO amount is sufficient for uniform distribution in volume, and homogeneous polymer composites are formed. In this structure, the light scattering decreases compared to pure polymer, approximately twice.

The water sorption experiments were conducted to study changes in the internal volume of the polymer as a result of effect of free volume filling by ZnO nanoparticles (Figure 1 (b), curve 4)).

Water sorption properties of nanocomposite have strong dependence on nanoparticles concentration (Figure 2(a)). There is a sorption maximum near 4% (reorganization of polymer inner structure). At higher nanoparticles concentration (12 wt. % ZnO) water sorption increases, perhaps as a result of disordering of the nanocomposite.

For pure polymer value, water sorption is 23%. The introduction of 10 wt.% nanoparticles achieved reduction in water sorption by 5 times compared with the pure composition.

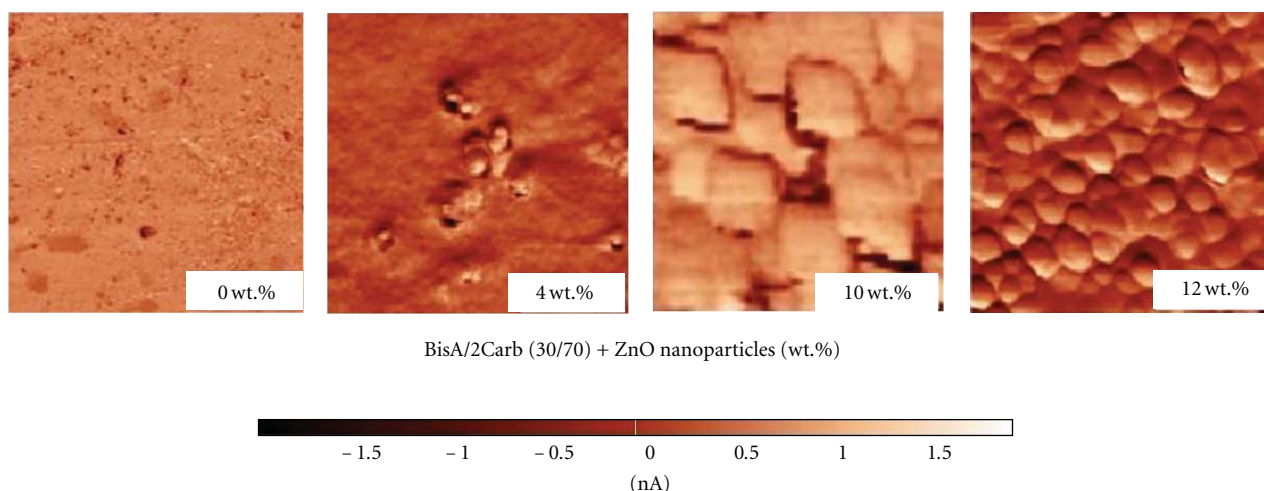
The hardness investigation of films is an indirect way to study the effect of ZnO on the structural change of nanocomposites (Figure 2(b)).

At the introduction of ZnO up to 10 wt.% the hardness of the films decreases. Further, the hardness of the film increases and reaches the one of pure polymer.

The changes of the polymer nanocomposite properties (water sorption, light scattering, hardness) confirmed that nanoparticles influence on the polymer structure by means of possible interactions of ZnO with active groups of the polymer [20].

The investigation of the surface relief of the nanocomposites made by atomic force microscopy is shown in Figure 3.

As can be seen from Figure 3, there are essential changes in the composition structure as compared with the original by introduction at 4 wt.% ZnO nanoparticles. The formation of separate polymer regions of structured ZnO was observed clearly. The grain uniform structure are observed throughout the material when ZnO concentration achieves 10 wt.%. Apparently, formation of this structure is due to the ability of nanoparticles to create weak bonds with the active groups



BisA/2Carb (30/70) + ZnO nanoparticles (wt.%)

FIGURE 3: Relief of polymer films with the introduction of 0 wt.% (a), 4 wt.% (b), 8 wt.% (c), 12 wt.% (d) ZnO nanoparticles (AFM). The size of photos  $5 \times 5$  mkm.

of the monomer molecules and to work as centers of polymerization.

When the ZnO concentration is more than 10 wt.%, free polymer phase disappears and all available polymers form spheres on nanoparticles surface.

At low concentrations of nanoparticles, modified polymer areas are not enough and composites are heterogeneous. Heterogeneous structures are reflected in their properties. With increasing ZnO concentration, size and number of hybrid fields are growing, thus it is conditioned by forming of a completely different structure of the material.

The formation of submicron spheres around each nanoparticle is the cause of formation of quasi-homogeneous materials, in which light scattering does not exceed the pure polymer. Indeed (Figure 3), submicron spheres formed around each nanoparticle possess almost identical diameters. This fact can be explained by identical growth rates of these spheres. The result is structure consisting of sphere particles located in the self-organized quasilattice. Eventually, the above-named effects lead to a homogeneous distribution of nanoparticles and the formation of a homogeneous environment.

Determination of possibility and mechanism of polymerization on surface of ZnO nanoparticles were investigated by mean of FTIR nanocomposite spectra (Figure 4). FTIR spectra of monomers mixture BisA/2Car (30/70) may be seen as peaks at  $1737$ ,  $1410$  and  $1188$ ,  $1050$   $\text{cm}^{-1}$ . The first peak corresponds to valency vibration of carboxylic group, next three—to combination of flat deformation vibration of hydroxide group and valency vibration of C-O links in carboxylic acids [21].

At preparation of nanocomposite FTIR spectra change essentially, peak  $1720$   $\text{cm}^{-1}$  (C-O group) keep and peak  $1410$ – $1450$   $\text{cm}^{-1}$  (valency vibration of carboxylate anion) will intensify. It is important to notice that the peak at  $500$   $\text{cm}^{-1}$  corresponds to Zn-O vibration. A peaks appears between  $1620$ – $1550$   $\text{cm}^{-1}$ . This area is typical of asymmetric valency vibration of carboxylic anion. According to informa-

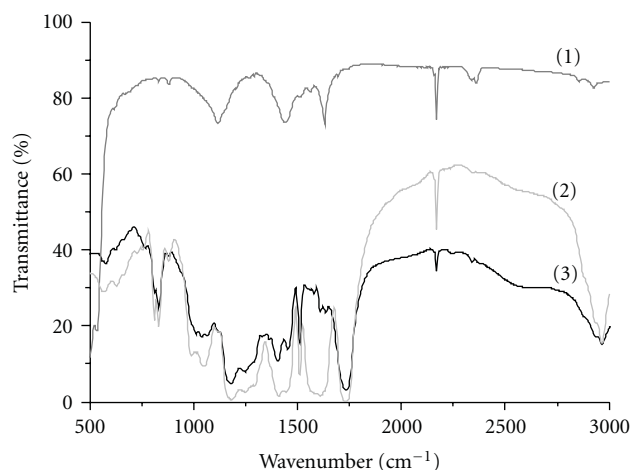


FIGURE 4: FTIR spectra: nanoparticles ZnO (1), composition 2Carb/BisA (70/30) + 12 wt.% ZnO (2), and pure 2Carb/BisA (70/30) (3).

tion of works [22–25] interaction of inorganic nanoparticles ZnO and carbonyl group results in change in IR spectra, as metal atoms can be connected to carbonyl oxygen by electron pair transfer. The increase of peak intensity O-H at  $1550$   $\text{cm}^{-1}$  can be a result of formation of a complex between the polymer and nanoparticle.

Next, in nanocomposite peaks appearing at  $1640$ – $1650$   $\text{cm}^{-1}$ , they are typical for C=C valency vibration in  $\text{CH}_2=\text{CHR}$ , and peak  $990$   $\text{cm}^{-1}$  is typical for C-H deformation vibration in  $\text{CH}_2=\text{CHR}$ .  $\text{CH}_2=\text{CHR}$  groups can photopolymerize on ZnO surface, acting as photoinitiator. Principal scheme of described process is shown in Figure 5.

#### 4. Discussion on Obtained Results

Our results show that ZnO nanoparticles can be involved in UV polymerization process with formation of bonds

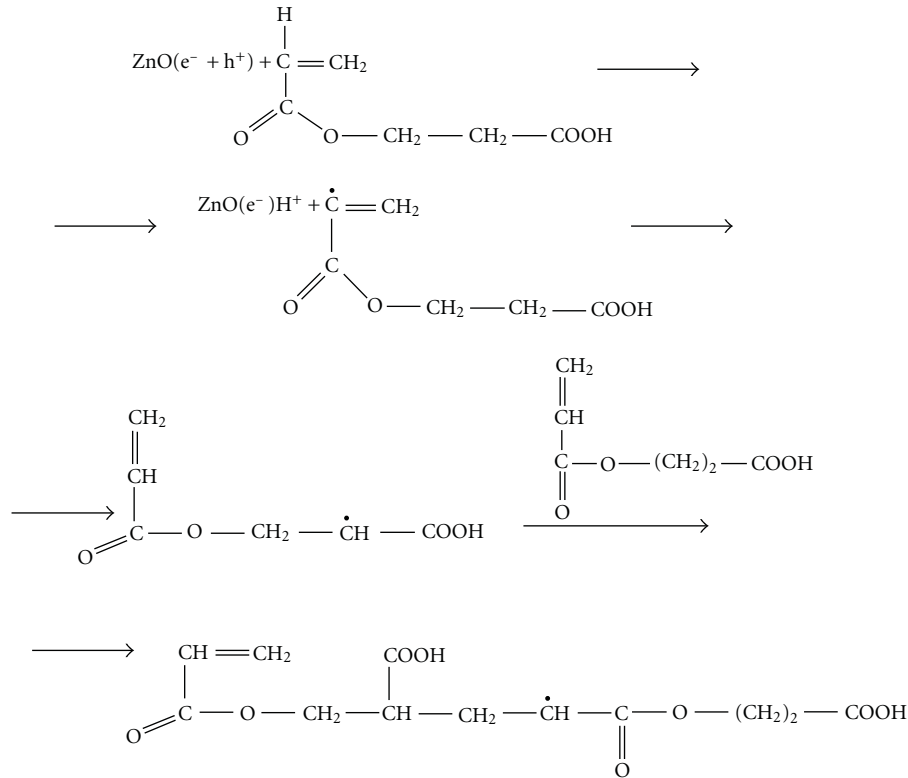


FIGURE 5: Scheme of photocatalysis process.

between nanoparticle surfaces and polymers. Thus, the ZnO nanoparticles act as centers of formation of a new polymer phase—the nanocomposite, other than with the pure polymer properties.

According to FTIR spectra of ZnO nanocomposites we assume that nanoparticles act as photocatalysts in polymerization and became as a centers of polymerization as a result of interaction with carboxylic group of one of the composition monomers. Our hypotheses are proved by formation of micron size spheres in nanocomposite around each nanoparticle (Figure 3). Nanosized semiconductor clusters have the potential of photooxidation and photocatalysis through the combined effects of photoelectrons production at UV light absorption and high surface area in which electron-transfer-induced polymerization takes place. According to results of the work in [26], during the photocatalytic process, the illumination of a semiconductor photocatalyst with ultraviolet (UV) radiation activates the catalyst, establishing a redox environment in the aqueous solution. Semiconductors act as sensitizers for light-induced redox processes due to their electronic structure, which is characterized by a filled valence band and an empty conduction band. So, light absorption by semiconductor nanoparticles will result in photocatalytic process in its surface including photopolymerization processes. The work in [27] shows possibility of this process of methyl methacrylate photopolymerization initiation by  $\text{TiO}_2$  nanoparticles. In our experiments we obtain similar

process that is proved by FTIR and atomic force microscopy results (formation of equal spheres around each nanoparticle as a center of polymerization and chemical bonding between nanoparticles surface and polymer).

Formation of spheres around each nanoparticles as a result of photopolymerization on its surface results in transformation of polymer structure: at augmentation of nanoparticles concentration all proprieties of composition have sudden extremums at the same values of nanoparticles concentration. Characteristic points are 4 and 10 wt%. According AFM photos between 2 and 4 wt% of nanoparticles, new phase of polymer generated on nanoparticles surface will occupy mostly part of nanocomposite volume. It results in structuring of material, light scattering, and water sorption will decrease. At nanoparticles concentration more than 10 wt %, all volume of polymers will be involved in formation of new phase; perhaps next increasing of nanoparticles concentration will result in competition between nanoparticles as the center of polymerization resulted in missequencing of material. AFM photo shows that structures consisting of micro spheres occupy all volume, and light scattering and water sorption increase. Above-listed effects are proved by missequencing of nanocomposite.

Certainly these suggestions are our hypothesis only. Future investigation of nanocomposite with active nanoparticles is needed to understand the causes of these strange effects of composite reorganization.

## 5. Conclusion

The sorption of water vapor, Brinell hardness, optical transmission, refractive index, and light scattering of film polymer ZnO nanocomposites were studied.

Composites are transparent in the visible spectrum at high concentrations of ZnO nanoparticles (14 wt.%). With the introduction of 14 wt.% ZnO the refractive index composite increases to 0.045. With the introduction of 10 wt.% ZnO the sorption decreases five times. Hardness, until a maximum concentration of nanoparticles 12 wt.% ZnO, does not exceed the hardness of the pure polymer, while light scattering is not increased.

Nonmonotonic changes in the properties, the AFM data, and the IR spectra demonstrate the ability of nanoparticles to act as centers of polymerization and to form a granular structure in the nanocomposite.

## Acknowledgment

The work was made under support of Russian Ministry of Education Grant GK P995 under Federal Program "Teaching and scientific personnel of innovative Russia," 2009–2013.

## References

- [1] A. S. Rosenberg, G. I. Dzhardimalieva, and A. D. Pomogailo, "Polymer composites of nano-sized particles isolated in matrix," *Polymers for Advanced Technologies*, vol. 9, no. 8, pp. 527–535, 1998.
- [2] A. D. Pomogailo and V. S. Savost'yanov, *Synthesis and Polymerization of Metal-Containing Monomers*, CRC Press, Boca Raton, Fla, USA, 1994.
- [3] A. S. Pomogailo, A. S. Rozenberg, G. I. Dzhardimalieva, and M. Leonowicz, "Polymer nanocomposites on the base of metal carboxylates," *Advances in Materials Science*, vol. 1, no. 1, pp. 19–27, 2001.
- [4] M. J. Height, S. E. Pratsinis, O. Mekasuwandumrong, and P. Praserthdam, "Ag-ZnO catalysts for UV-photodegradation of methylene blue," *Applied Catalysis B*, vol. 63, no. 3-4, pp. 305–312, 2006.
- [5] L. Guedri-Knani, J. L. Gardette, M. Jacquet, and A. Rivaton, "Photoprotection of poly(ethylene-naphthalate) by zinc oxide coating," *Surface and Coatings Technology*, vol. 180-181, pp. 71–75, 2004.
- [6] Z. Y. Fan and J. G. Lu, "Zinc oxide nanostructures: synthesis and properties," *Journal of Nanoscience and Nanotechnology*, vol. 5, no. 10, pp. 1561–1573, 2005.
- [7] X. Fang, Y. Bando, U. K. Gautam et al., "ZnO and ZnS nanostructures: ultraviolet-light emitters, lasers, and sensors," *Critical Reviews in Solid State and Materials Sciences*, vol. 34, no. 3-4, pp. 190–223, 2009.
- [8] P. Liu and T. Wang, "Poly(hydroethyl acrylate) grafted from ZnO nanoparticles via surface-initiated atom transfer radical polymerization," *Current Applied Physics*, vol. 8, no. 1, pp. 66–70, 2008.
- [9] Y. Li, G. Li, and Q. Yin, "Preparation of ZnO varistors by solution nano-coating technique," *Materials Science and Engineering B*, vol. 130, no. 1–3, pp. 264–268, 2006.
- [10] M. R. Vaezi and S. K. Sadrnezhad, "Nanopowder synthesis of zinc oxide via sol-chemical processing," *Materials & Design*, vol. 28, no. 2, pp. 515–519, 2007.
- [11] S.-Y. Chu, T.-M. Yan, and S.-L. Chen, "Analysis of ZnO varistors prepared by the sol-gel method," *Ceramics International*, vol. 26, no. 7, pp. 733–737, 2000.
- [12] G. Westin, A. Ekstrand, M. Nygren, R. Österlund, and P. Merkelbach, "Preparation of ZnO-based varistors by the sol-gel technique," *Journal of Materials Chemistry*, vol. 4, no. 4, pp. 615–621, 1994.
- [13] S. C. Pillai, J. M. Kelly, D. E. McCormack, and R. Ramesh, "Self-assembled arrays of ZnO nanoparticles and their application as varistor materials," *Journal of Materials Chemistry*, vol. 14, no. 10, pp. 1572–1578, 2004.
- [14] M. I. Fokina, I. Yu. Denisyuk, Y. É. Burunkova, and L. N. Kaporskiĭ, "Formation of microstructures based on UV-hardenable acrylates," *Journal of Optical Technology*, vol. 75, no. 10, pp. 664–669, 2008.
- [15] I. Yu. Denisyuk, T. R. Williams, and J. E. Burunkova, "Hybrid optical material with nanoparticles at high concentrations in UV-curable polymers—technology and properties," *Molecular Crystals and Liquid Crystals*, vol. 497, pp. 142–153, 2008.
- [16] T. R. Williams, I. Yu. Denisyuk, and J. E. Burunkova, "Filled polymers with high nanoparticles concentration—synthesis, optical and rheological properties," *Journal of Applied Polymer Science*, vol. 116, no. 4, pp. 1857–1866, 2010.
- [17] J. A. Burunkova, I. Yu. Denisyuk, N. N. Arefeva, and S. A. Semena, "Influence of SiO<sub>2</sub> nanoaddition on the self-organization via UV-polymerization of acrylate nanocomposites," *Molecular Crystals and Liquid Crystals*, vol. 536, no. 1, pp. 10–16, 2011.
- [18] A. P. Vinogradov, *Electrodynamics of Composite Materials*, Aditorial URSS, Moscow, Russia, 2001.
- [19] J. E. Spanier and I. P. Herman, "Use of hybrid phenomenological and statistical effective-medium theories of dielectric functions to model the infrared reflectance of porous SiC films," *Physical Review B*, vol. 61, no. 15, pp. 10437–10450, 2000.
- [20] S. Jiguet, A. Bertsch, M. Judelewicz, H. Hofmann, and P. Renaud, "SU-8 nanocomposite photoresist with low stress properties for microfabrication applications," *Microelectronic Engineering*, vol. 83, no. 10, pp. 1966–1970, 2006.
- [21] R. M. Silverstein, G. C. Bassler, and T. C. Morrill, *Spectrometric Identification of Organic Compounds*, John Wiley & Sons, New York, NY, USA, 4th edition, 1981.
- [22] X. Lu, Y. Zhao, and C. Wang, "Fabrication of PbS nanoparticles in polymer-fiber matrices by electrospinning," *Advanced Materials*, vol. 17, no. 20, pp. 2485–2488, 2005.
- [23] X. Lu, Y. Zhao, C. Wang, and Y. Wei, "Fabrication of CdS nanorods in PVP fiber matrices by electrospinning," *Macromolecular Rapid Communications*, vol. 26, no. 16, pp. 1325–1329, 2005.
- [24] J. Bai, Y. Li, C. Zhang, X. Liang, and Q. Yang, "Preparing AgBr nanoparticles in poly(vinyl pyrrolidone) (PVP) nanofibers," *Colloids and Surfaces A*, vol. 329, no. 3, pp. 165–168, 2008.
- [25] A. H. Kupcov and G. N. Jijin, *Raman Scattering and Fourier-IR Polymers Spectra*, Fismatlit, Moscow, Russia, 2001.
- [26] D. Beydoun, R. Amal, G. Low, and S. McEvoy, "Role of nanoparticles in photocatalysis," *Journal of Nanoparticle Research*, vol. 1, no. 4, pp. 439–458, 1999.
- [27] C. Dong and X. Ni, "The photopolymerization and characterization of methyl methacrylate initiated by nanosized titanium dioxide," *Journal of Macromolecular Science, Part A*, vol. 41, no. 5, pp. 547–563, 2004.

## Research Article

# Carbon-Based Fibrous EDLC Capacitors and Supercapacitors

**C. Lekakou, O. Moudam, F. Markoulidis, T. Andrews, J. F. Watts, and G. T. Reed**

*Faculty of Engineering and Physical Sciences, University of Surrey, Guildford, Surrey GU2 7XH, UK*

Correspondence should be addressed to C. Lekakou, c.lekakou@surrey.ac.uk

Received 4 February 2011; Accepted 20 March 2011

Academic Editor: Huisheng Peng

Copyright © 2011 C. Lekakou et al. This is an open access article distributed under the Creative Commons Attribution License, which permits unrestricted use, distribution, and reproduction in any medium, provided the original work is properly cited.

This paper investigates electrochemical double-layer capacitors (EDLCs) including two alternative types of carbon-based fibrous electrodes, a carbon fibre woven fabric (CWF) and a multiwall carbon nanotube (CNT) electrode, as well as hybrid CWF-CNT electrodes. Two types of separator membranes were also considered. An organic gel electrolyte PEO-LiClO<sub>4</sub>-EC-THF was used to maintain a high working voltage. The capacitor cells were tested in cyclic voltammetry, charge-discharge, and impedance tests. The best separator was a glass fibre-fine pore filter. The carbon woven fabric electrode and the corresponding supercapacitor exhibited superior performance per unit area, whereas the multiwall carbon nanotube electrode and corresponding supercapacitor demonstrated excellent specific properties. The hybrid CWF-CNT electrodes did not show a combined improved performance due to the lack of carbon nanotube penetration into the carbon fibre fabric.

## 1. Introduction

There is much interest in electrochemical double-layer capacitors (EDLCs) due to the quick response and high mobility of the ions of the electrolyte and the increase of energy storage due to the double capacitor layer effect. Carbon-based electrodes attract a lot of research as they offer the possibility of a good conductor of large surface area. Much research has focused on porous carbon electrodes [1–5] which supply large surface area but are poor conductors, offering reduced power density. The next step is to consider fibrous carbon materials [6] of good conductivity to ensure high power density, whereas the high surface area of their fibrous structure could provide good energy density. Such materials have the advantage of having been considered and applied in the field of structural composites from which there is a wealth of research and expertise on their processing and their impregnation by viscous and viscoelastic fluids [7–9]. Furthermore, there is increased interest in fibrous materials and textiles for wearable electronics for everyday use, biomedical monitoring and, other specific applications for which a wearable unit for energy storage and supply would be most useful. As a result, it would be worthwhile to explore the use of carbon-based fibrous materials as EDLC electrodes. Shirshova et al. [10] tested high conductivity, nonactivated

carbon fibre fabrics as electrodes for capacitor devices with a polymer gel electrolyte, poly(ethylene glycol) diglycidyl ether (PEGDGE), which resulted in very low capacitance, whereas their activated carbon fabrics had high resistance.

Carbon nanotubes have the advantage of forming electrically conductive networks and possibly being able to also store energy [11]. Pushparaj et al., 2007 [12], used as electrode MWNTs aligned perpendicularly to the current collector and embedded in cellulose, and they fabricated supercapacitors with a maximum power density of 1.5 kW/kg for an RTIL electrolyte. Shi et al. [13] reported that growing carbon nanotubes directly on the nickel foam current collector lowered the internal resistance. Ma et al. [14] reported the inclusion of MWNTs in phenolic resin mixtures and carbonisation of the mixture at 850°C, which yielded electrodes of a specific capacitance of 15–25 F/cm<sup>3</sup> using 38 wt% H<sub>2</sub>SO<sub>4</sub> as electrolyte. Binderless carbon or MWNT electrodes [15] have been considered, and they might have lower resistance in the absence of a polymeric binder while they are also of lower cost. However, the results of Bordjiba et al. [15] cannot be compared directly to the results of the present study, as they used mainly activated carbon as their electrode and only a small percentage of MWNTs and an aqueous KOH electrolyte, whereas the present study uses nonactivated fibrous carbon electrodes and an organic

electrolyte. Guo et al. [16] found that carbon nanotubes embedded in electrospun carbon nanofibres (CNFs) doubled the capacitance of CNFs using 1 M H<sub>2</sub>SO<sub>4</sub> electrolyte.

The electrolyte is very important in the performance of a capacitor, and more specifically the ion mobility and the electrochemical stability of the electrolyte (defining the potential range of use of the electrolyte). Aqueous electrolytes have low electrical resistance, high ion mobility but low maximum voltage around 1 V [17]. This means that they are highly suitable for very low voltage applications but for medium and high voltage applications assemblies of many in-series connected low voltage cells are required for the capacitor bank. An in-series connection of  $N$  cells with a cell capacitance  $C$  and a cell resistance  $R$  reduces the total capacitance to  $C/N$  and increases the total resistance to  $NR$ . Hence, this study has included an organic electrolyte with relatively high working voltage. Lithium ion electrolytes have been used in both battery and capacitor applications. The anion ClO<sub>4</sub> has moderate binding ability with aprotic solvents [18]. The PMMA-EC-PC-TEAClO<sub>4</sub> gel electrolyte has a working potential range of  $-2.5$  to  $+2.5$  V and exhibited a maximum capacitance of  $3.7$ – $5.4$  mF cm<sup>-2</sup> [19]. Polyethylene oxide is an ionomer supplying anions [18], hence, it has been incorporated in the gel electrolyte in this study. Furthermore, ion mobility in a porous electrode is linked to the relative sizes of pores and ions [20]. In recent studies [21, 22], TEABF<sub>4</sub> is a popular organic electrolyte that can be used in cyclic voltammetry up to 3 V without any degradation; however, the size of TEA<sup>+</sup> is rather large [20] in comparison with the size of Li<sup>+</sup> ions and ions of aqueous electrolytes, hence it was decided to use a Li<sup>+</sup>-based organic electrolyte in this study. Further developments on supercapacitors in latest studies are based on adding pseudocapacitance compounds to the carbon fibrous electrodes [22, 23] which increase the overall capacitance but introduce redox processes that would reduce the lifetime of the capacitor device.

The present study considers the fabrication and testing of novel EDLC cells with carbon-based fibrous electrodes without any binder, two different types of separator membranes, and an organic gel electrolyte, PEO-LiClO<sub>4</sub>-EC-THF. Two different types of electrically conductive fibrous carbon material were explored as electrodes on their own or as a combination: a carbon fibre plain woven fabric (CWF) and multiwall carbon nanotubes (MWNTs). The purpose of the organic gel electrolyte was a relatively high working voltage, fast moving small Li<sup>+</sup> ions and the fabrication of a homogeneous, compliant EDLC. The carbon fibre fabric consisted of tows comprising many microfibrils and resulting in a structure of dual porosity including meso- and micropores. Impregnation of this fabric by a viscous electrolyte would be channelled preferentially into the mesopores and might leave unfilled micropores [24, 25]. As a result, care was taken during the fabrication to perform impregnation slowly and for a long time to ensure maximum impregnation of micropores. In the case of MWNTs, dispersion was very important to achieve maximum surface area and maximum number of conductive paths in the MWNT network. Two types of separator membranes were used alternatively: a filter membrane with  $0.8$  μm pores and a glass microfibre filter

(GF/F) with  $0.7$  μm average pore size. All EDLC cells were tested in cyclic voltammetry, charge-discharge, and impedance tests. Two EDLC cells exhibited excellent performance: the CWF-GF/F cell demonstrated excellent performance per unit area, and the CNT-GF/F cell demonstrated excellent specific properties (per unit mass).

## 2. Materials

**2.1. Carbon Fibre Plain Woven Fabric Electrodes.** An engineering carbon fibre fabric was used of plain weave, A0186, from Folthergill Engineered Fabrics, of a nominal thickness of  $270$  μm and areal density of  $19.9$  mg/cm<sup>2</sup>. The carbon fabric was used as received, and the carbon was not activated in any way.

**2.2. Carbon Nanotube (CNT) Electrodes.** Multiwall carbon nanotubes (MWNTs) ElicarBMW from Thomas Swan Ltd were used, with the following parameters: outer diameter of  $10$ – $30$  nm, tens of microns length, and  $>92\%$  purity. In a previous dielectrophoresis study in Araldite epoxy by our group [26], it was determined that they have high electrophoretic mobility  $\mu = 0.0025$  μm mm/Vs and zeta potential of  $67$  mV.

In this study,  $0.3\%$  w/v MWNTs were dispersed in THF first via sonication for 1 hr and afterwards via high shear mixing at  $18,000$  rpm for 1 hr. The mixture was deposited with a syringe drop by drop onto an aluminium tape current collector. THF was allowed to evaporate, and a thin MWNT mat was formed.

**2.3. Separator.** Two types of separators were tried:

Super poly(estersulphone) filter membrane by PALL:  
 $0.8$  μm pores, measured thickness of  $290$  μm;

GF/F filter, a glass microfibre filter by Whatman with  
 $0.7$  μm average pore size and a nominal thickness of  
 $420$  μm.

**2.4. Electrolyte.** The electrolyte was a PEO-LiClO<sub>4</sub>-EC-THF organic gel electrolyte consisting of  $0.5$  g polyethylene oxide (PEO,  $M_v = 100,000$ ,  $n_d = 1.45$ ),  $0.21$  g LiClO<sub>4</sub>, and  $0.29$  g ethylene carbonate (EC) in  $10$  mL THF. All substances were purchased from Sigma-Aldrich. Processing of the electrolyte was carried out after gently heating it as EC solidifies at  $35^\circ\text{C}$ .

## 3. Experimental Methods

**3.1. Fabrication of Capacitor Cells.** Figure 1 presents the EDLC capacitor cells fabricated and tested in this study. In each case, the separator porous membrane was dip-coated in the electrolyte gel, sandwiched between the electrodes, and the whole cell was sealed under gradually increasing pressure up to  $5$  kPa. Generally, each carbon fibre woven fabric-based capacitor cell was  $2$  cm<sup>2</sup>, and each CNT-based capacitor cell was  $1$  cm<sup>2</sup>.

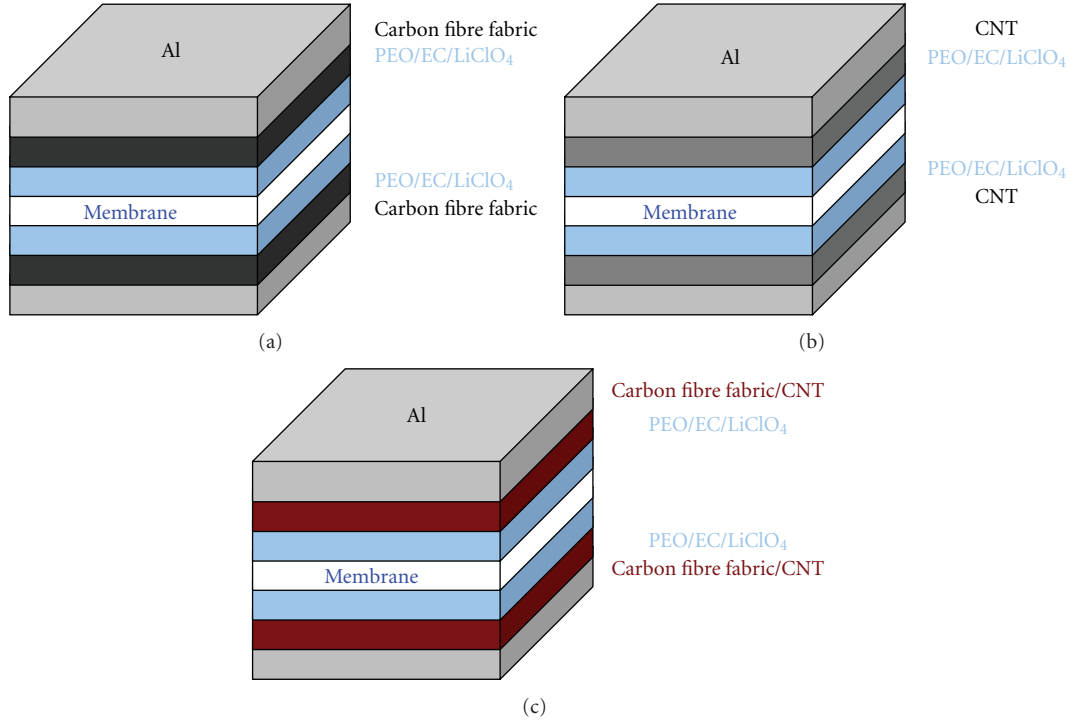


FIGURE 1: Diagrams of EDLC cells fabricated and tested in this study.

The following types of capacitor cells were fabricated and tested:

- (i) carbon fibre woven fabric electrodes and GF/F filter separator (CFW-GF/F);
- (ii) carbon fibre woven fabric electrodes and Supor filter separator (CFW-Supor);
- (iii) carbon nanotube electrodes and GF/F filter separator (CNT-GF/F);
- (iv) carbon nanotube electrodes and Supor filter separator (CNT-Supor);
- (v) hybrid CFW-CNT electrodes and GF/F filter separator (CFW-CNT-GF/F);
- (vi) hybrid CFW-CNT electrodes and Supor filter separator (CFW-CNT-Supor).

**3.2. Testing of the Capacitor Cells.** The fabricated capacitor cells were tested using a VersaSTAT4 Electrochemical System in cyclic voltametry, charge-discharge, and impedance tests. Cyclic voltametry (CV) was performed initially within 0 to +3 V to find the maximum breakdown potential of the electrolyte and subsequently within 0 to 2.5 V. The area of the I-V envelope gave the power,  $P$ , and power density,  $P_{sp}$ , of the full capacitor cell (by dividing by the mass of the two carbon-based electrodes). Considering the current at the midpoint,  $I_m$ , and the scan rate,  $dV/dt$ , the capacitance,  $C_{CV}$ , was determined:

$$C_{CV} = \frac{I_m}{dV/dt}. \quad (1)$$

Charge-discharge tests were also used to determine capacitance:

$$C_{CD} = \frac{I}{dV/dt} \quad (2)$$

while impedance,  $Z$ , testing provided more data of the capacitance as function of frequency,  $f$  (angular frequency  $\omega = 2\pi f$ ), where

$$Z = Z' + jZ'', \quad (3)$$

the real part of impedance  $Z'$  is the resistance  $R$ , the imaginary part of impedance,  $Z''$ , is the sum of the capacitive reactance  $X_C$  (depending on capacitance  $C$ ) and the inductive reactance  $X_L$  (depending on inductance  $L$ ):

$$C = -\frac{1}{\omega X_C}, \quad (4)$$

$$X_L = \omega L.$$

The maximum energy  $E_{max}$  stored in the capacitor is given by

$$E_{max} = \frac{1}{2}CV_{max}^2. \quad (5)$$

The maximum power of the capacitor  $P_{max}$  depends on its equivalent series resistance ESR according to the relation, where ESR values in this study included both electrolyte and interface resistances:

$$P_{max} = \frac{V^2}{4ESR}. \quad (6)$$

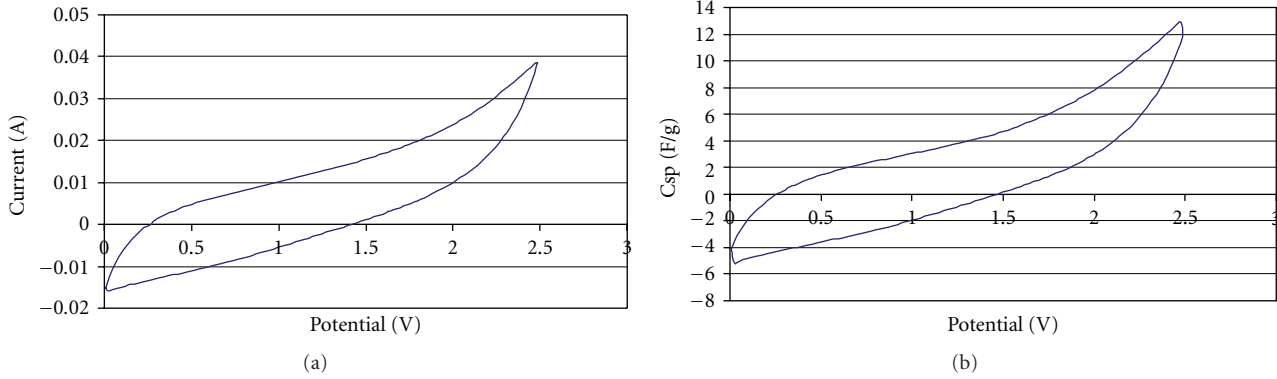


FIGURE 2: Cyclic voltammetry of EDLC CWF-GF/F capacitor from 0 to 2.5 V at a rate of 0.15 V/s and specific capacitance of electrode; each carbon electrode has an area of 2 cm<sup>2</sup> and mass of 40 mg.

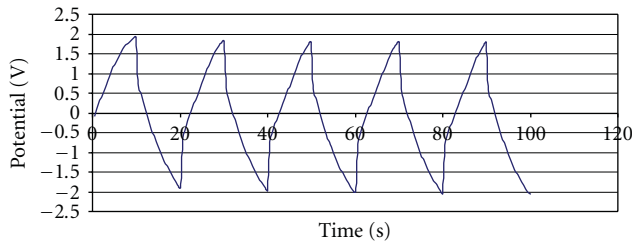


FIGURE 3: Charge-discharge testing of EDLC CWF-GF/F capacitor at constant current steps of -5 mA and +5 mA; each carbon electrode has an area of 1 cm<sup>2</sup> and mass of 20 mg.

## 4. Results

### 4.1. Carbon Fibre Woven Fabric- (CFW-) Based Capacitors.

Figure 2 presents the results from cyclic voltammetry for the CWF-based electrode capacitors with a GF/F filter as separator. From the plots, a maximum potential of 2.3 V may be considered for the electrolyte of LiClO<sub>4</sub>/EC/PEO, which is higher than previously reported (1 V for [27] using LiClO<sub>4</sub>-EC-PC-Polyurethane electrolyte) for similar electrolytes in a carbon cloth electrode, demonstrating the excellent pairing of the electrolyte and the CWF electrode in this study. In fact, the present study has reached the highest possible potential for LiClO<sub>4</sub>, where beyond this, electrolyte breakdown occurs.

Figure 3 presents the results of the charge-discharge test from which the electrode capacitance has been determined as  $C_{\text{Discharge,max}} = 0.076 \text{ F/cm}^2$  or 3.81 F/g. This yields the corresponding energy  $E = 0.20 \text{ J/cm}^2$  and  $E_{\text{sp}} = 2.8 \text{ Wh/kg}$ .

Figure 4 displays the Nyquist plot from the impedance testing of an EDLC CWF-GF/F capacitor, which displays an ESR of 6.1 ohm, yielding a maximum power density for the EDLC cell of 2.7 kW/kg. Figure 5 presents the AC capacitance of the EDLC CWF-GF/F cell as a function of AC frequency, showing that there is a large fall of capacitance of two orders of magnitude within the first 500 Hz, thereafter the capacitance falls much more slowly. In general, the results of capacitance, power density, and energy density for the EDLC CWF-GF/F electrode and capacitor cell demonstrate that

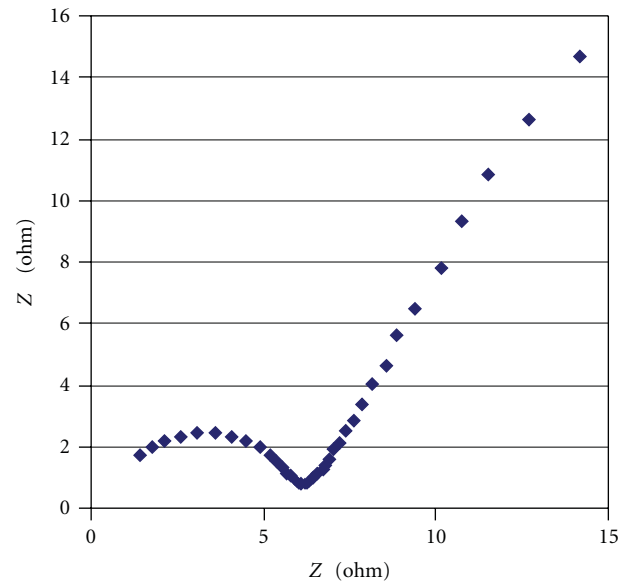


FIGURE 4: Nyquist plot from impedance testing of EDLC CWF-GF/F capacitor between 10 kHz and 1 Hz; each carbon electrode has an area of 2 cm<sup>2</sup> and mass of 40 mg.

its performance is higher than other fibre fabric capacitors reported in the literature (e.g., several orders of magnitude better than Shirshova et al.'s work [10]) and that it is at the levels of current commercial supercapacitors.

The same experiments were repeated using as separator the thinner *Supor* poly(estersulphone) filter membrane. The main performance results are presented in Table 1. It is clear that the EDLC CWF-*Supor* cell is inferior in both ESR and capacitance, yielding much lower power and energy densities. It is thought that the reason for this is the large surface area of the microfiber GF/F filter separator and its large absorbance of the electrolyte, which lowers ESR while it also increases capacitance. These good properties of the glass fibre papers have also been observed by other investigators with different electrolytes (e.g., Staiti et al. [28] with H<sub>2</sub>SO<sub>4</sub> as electrolyte).

TABLE 1: Summary of performance results of the various types of electrodes combined with two different types of separators. ( $P_{CV}$ : power from cyclic voltammetry 0 to 2.5 V at 0.2 V/s.  $P_{CV, sp}$ : power density from cyclic voltammetry at 0.2 V/s.  $P_{max}$ : maximum power on the basis of the ESR determined from the impedance test.  $P_{max, sp}$ : maximum power density.  $E_{max}$ : maximum energy.  $E_{max, sp}$ : maximum energy density).

Cell	CFW-GF/F	CFW-Supor	CNT-GF/F	CNT-Supor	CFW-CNT-GF/F	CFW-CNT-Supor
$P_{CV}$ (W/cm <sup>2</sup> )	0.035 <sub>0.15 V/s</sub>	0.012	0.004	0.004	0.004	0.006
$P_{CV, sp}$ (kW/kg)	1.768 <sub>0.15 V/s</sub>	0.320	20	1.84	0.245	0.265
$P_{max}$ (W/cm <sup>2</sup> )	0.207	0.012	0.011	0.024	0.01	0.014
$P_{max, sp}$ (kW/kg)	10.4	0.292	113	12.1	0.52	0.60
$C_{CV}$ (F/cm <sup>2</sup> )	0.08 <sub>0.15 V/s</sub>	0.015	0.002	0.008	0.053	0.008
$C_{CV, sp}$ (F/g)	3.78 <sub>0.15 V/s</sub>	0.095	12.487	5.2	2.6	0.38
$C_D$ (F/cm <sup>2</sup> )	0.08 <sub>5 mA/cm<sup>2</sup></sub>	No test	0.001 <sub>20 μA/cm<sup>2</sup></sub>	No test	No test	No test
$C_{D, sp}$ (F/g)	3.81 <sub>5 mA/cm<sup>2</sup></sub>	No test	6.39 <sub>20 μA/cm<sup>2</sup></sub>	No test	No test	No test
$E$ (J/cm <sup>2</sup> )	0.20 <sub>0.15 V/s</sub>	0.040	0.007	0.02	0.085	0.013
$E_{max, sp}$ (Wh/kg)	2.80 <sub>0.15 V/s</sub>	0.280	9.2	2.94	1.17	0.164

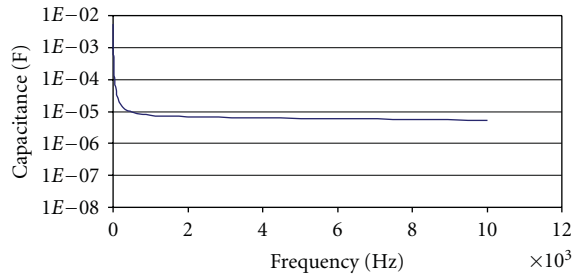


FIGURE 5: Capacitance as a function of frequency from impedance testing of EDLC CWF-GF/F capacitor between 10 kHz and 1 Hz; each carbon electrode has an area of 2 cm<sup>2</sup> and mass of 40 mg.

**4.2. Carbon Nanotube- (CNT-) Based Capacitors.** First, EDLC cells were fabricated with CNT electrodes (deposited on Al current collectors) and a GF/F filter separator. The cells were subjected to cyclic voltammetry, charge-discharge, and impedance tests. Figure 6 presents the results from cyclic voltammetry plotted as current versus potential and capacitance versus potential graphs. From the graphs, a maximum potential of 2.3 V may be considered for the electrolyte of LiClO<sub>4</sub>/EC/PEO, same as for the CWF electrodes. The I-V curves display a bump at -1.1 and +1.1 V, indicating redox reactions at the CNTs. The first results show clearly that the areal power and capacitance (per cm<sup>2</sup>) are lower than the corresponding properties of the CWF-GF/F cell (see Table 1) but the CNT-GF/F cell has much higher specific properties, such as power density,  $P_{sp}$ , and specific capacitance,  $C_{sp}$ , due to the very small mass of each CNT electrode.

Figure 7 presents the results of the charge-discharge test from which the capacitance has been determined as  $C_{Discharge, max} = 0.0013$  F/cm<sup>2</sup> or 6.39 F/g. This yields the corresponding energy  $E = 3.4$  mJ/cm<sup>2</sup> and  $E_{sp} = 4.7$  Wh/kg with excellent charge/discharge energy efficiency at 97%.

Figure 8 displays the Nyquist plot from the impedance testing of an EDLC CNT-GF/F capacitor cell, which displays clear supercapacitor behaviour with an ESR of 0.5 ohm, yielding a maximum power density of 28.3 kW/kg for the full cell. Figure 9 presents the AC capacitance of the full EDLC

cell as a function of AC frequency. It is evident that the EDLC CNT-GF/F cells behave as supercapacitors, as far as power and energy densities are concerned, and they have an energy density of 2.3 Wh/kg.

When the Supor filter is used as a separator, the EDLC CNT-Supor cells (each electrode: 1 cm<sup>2</sup> and 2 mg) display much worse performance than the EDLC CNT-GF/F cells, in a similar way as the EDLC carbon woven fabric-based cells (see Table 1).

**4.3. Hybrid Carbon Woven Fabric-Carbon Nanotube- (CWF-CNT-) Based Capacitors.** Figure 10 presents cyclic voltammetry results for the CFW-CNT-GF/F cell, which clearly exhibits very low power and a maximum potential of 1.8 V. The low performance of the cell is repeated also in the Nyquist plot in Figure 11, where it is evident that the cell has several interface resistances, because of multiple types of interfaces of carbon fabric and CNTs, due to the poor penetration of CNTs in CFW. Furthermore, even in the low frequency region, there is very high loss and consequently current loss.

The EDLC CWF-CNT-Supor cells also showed a maximum operating potential of only 1.8 V and exhibited an ESR of 118 ohm, yielding  $P_{max} = 0.014$  W/cm<sup>2</sup> and  $P_{max, sp} = 0.60$  kW/kg. The addition of MWNTs to the carbon fibre electrode did not yield any considerable improvements with the Supor filter as separator (CWF-CNT-Supor) in the fabricated EDLC cells. The cells exhibited capacitance similar to that of the CNT-Supor cells but with a lower maximum potential of 1.8 V which would decrease both power and energy. Furthermore, the mass of electrodes includes the large mass of the carbon fibre fabric without it contributing really to the capacitance; as a result, the specific properties and energy density are reduced. However, the addition of MWNTs reduces the ESR, increasing  $P_{max}$  (even with lower maximum working potential) and the power density.

## 5. Conclusions

EDLC cells were fabricated with carbon-based fibrous electrodes. Two types of separator membranes were tried: a Supor poly(estere)sulphone) microporous membrane and

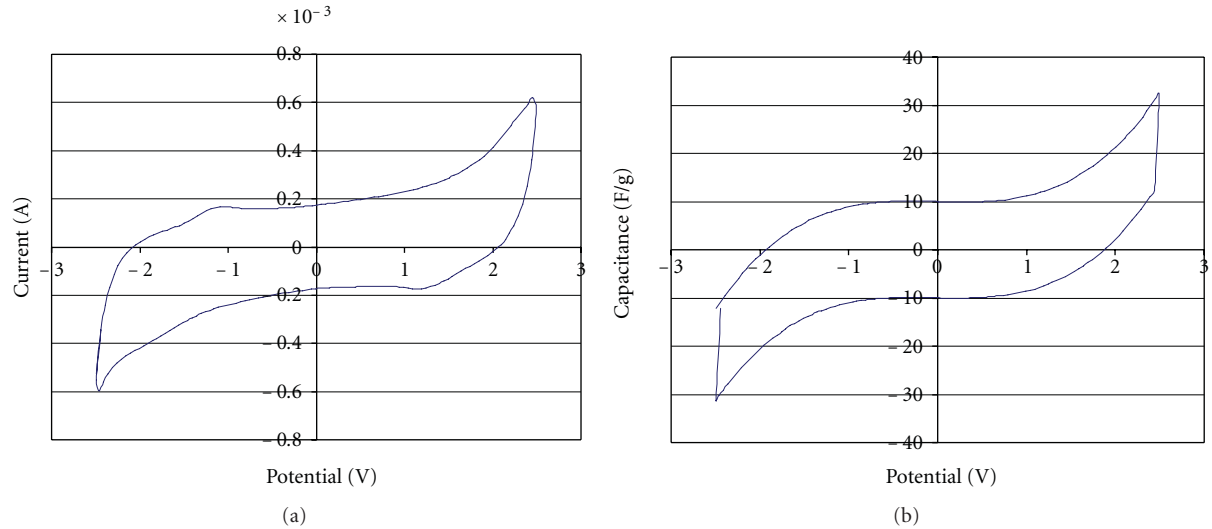


FIGURE 6: Cyclic voltammetry of EDLC CNT-GF/F capacitor from 0 to 2.5 V at a rate of 0.2 V/s and specific capacitance of electrode; each CNT electrode has an area of  $1 \text{ cm}^2$  and mass of 0.2 mg.

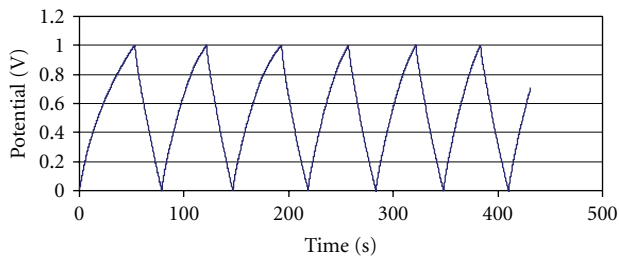


FIGURE 7: Charge-discharge testing of EDLC CNT-GF/F capacitor at constant current steps of  $-20 \mu\text{A}$  and  $+20 \mu\text{A}$ ; each carbon electrode has an area of  $1 \text{ cm}^2$  and mass of 0.2 mg.

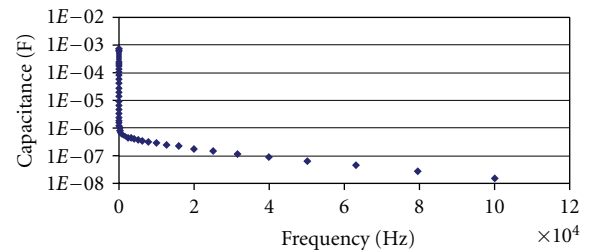


FIGURE 9: Capacitance as a function of frequency from impedance testing of EDLC CNT-GF/F capacitor cell between 100 kHz and 0.02 Hz; each carbon electrode has an area of  $1 \text{ cm}^2$  and mass of 0.2 mg.

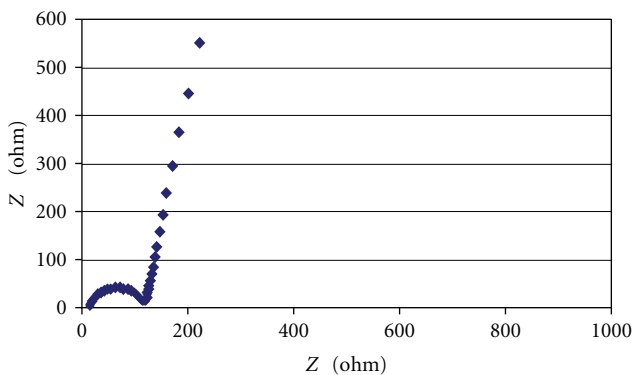


FIGURE 8: Nyquist plot from impedance testing of EDLC CNT-GF/F capacitor between 100 kHz and 0.1 Hz; each carbon electrode has an area of  $1 \text{ cm}^2$  and mass of 0.2 mg.

a GF/F glass microfibre filter. The GF/F separator proved most successful, and its high performance in the EDLC cells could be attributed to the large surface area of its microfibrinous material. A PEO-LiClO<sub>4</sub>-EC-THF gel electrolyte was used that exhibited high maximum voltage of  $\pm 2.3 \text{ V}$  for the

CWF and CNT electrodes, although some small bumps were present in the cyclic voltammetry tests of the CNT electrodes at  $\pm 1.1 \text{ V}$  indicating redox reactions. The best types of EDLC cells were the CWF-GF/F cells which demonstrated superior capacitance, energy, and power per unit area (per  $\text{cm}^2$ ) and the CNT-GF/F cells which demonstrated excellent specific capacitance, power density, and energy density. Data for these two best cells were assembled into the Ragone plots presented in Figure 12. The MWNT electrode has excellent specific properties but, due to its low density, a large area of electrode needs to be coated to achieve the same area-based performance of a carbon fabric EDLC. On the other hand, a carbon fibre fabric can be readily used as electrode, or part of it can be used for a wearable capacitor in wearable or fitted capacitor devices.

Another idea to add a very small amount of MWNTs to increase the surface area of the fabric did not yield fruitful results due to the poor penetration of CNTs into the microfibre fabric. In this case, the area properties of the hybrid electrode were the same as or better than those of the CNT electrode but the maximum voltage fell to 1.8 V.

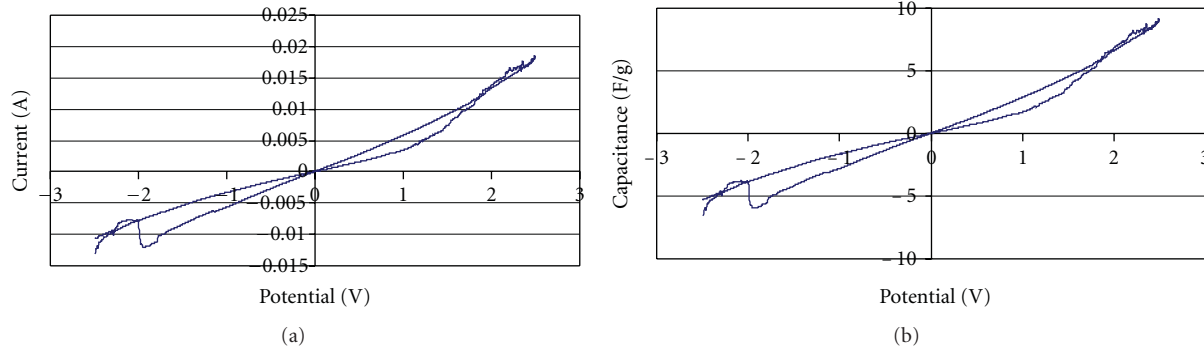


FIGURE 10: Cyclic voltammetry of EDLC CWF-CNT-GF/F capacitor from  $-2.5$  to  $2.5$  V at a rate of  $0.2$  V/s and specific capacitance of electrode; each carbon electrode has an area of  $1$  cm<sup>2</sup> and mass of  $20.2$  mg ( $20$  mg CWF and  $0.2$  mg CNTs).

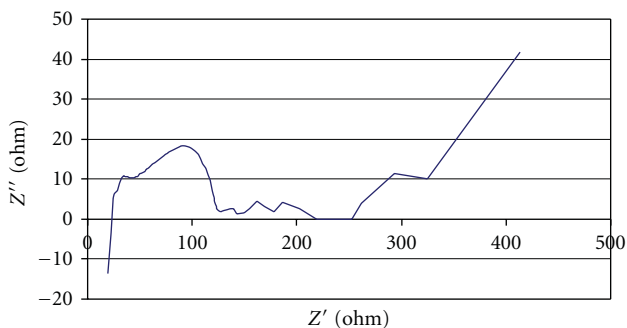


FIGURE 11: Nyquist plot from impedance testing of EDLC CWF-CNT-GF/F capacitor between  $1$  MHz and  $0.03$  Hz; each carbon electrode has an area of  $1$  cm<sup>2</sup> and mass of  $20.2$  mg.

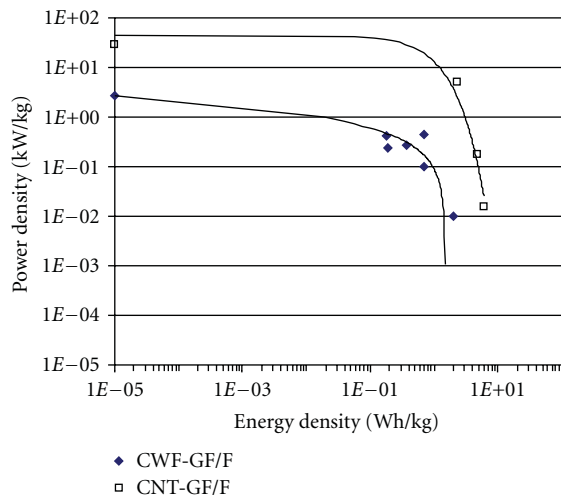


FIGURE 12: Ragone plots of two types of EDLC supercapacitors (full cells): the CWF-GF/F supercapacitor cell and the CNT-GF/F supercapacitor cell.

## Acknowledgment

The authors would like to gratefully acknowledge the funding of this project by IeMRC/EPSC UK, in the form of a research grant for which Dr. O. Moudam was employed as a research fellow.

## References

- [1] C. Arbizzani, M. Mastragostino, and F. Soavi, "New trends in electrochemical supercapacitors," *Journal of Power Sources*, vol. 100, no. 1-2, pp. 164–170, 2001.
- [2] M. Kodama, J. Yamashita, Y. Soneda, H. Hatori, S. Nishimura, and K. Kamegawa, "Structural characterization and electric double layer capacitance of template carbons," *Materials Science and Engineering B*, vol. 108, no. 1-2, pp. 156–161, 2004.
- [3] D. Hulicova, M. Kodama, and H. Hatori, "Electrochemical performance of nitrogen-enriched carbons in aqueous and non-aqueous supercapacitors," *Chemistry of Materials*, vol. 18, no. 9, pp. 2318–2326, 2006.
- [4] D. Tashima, K. Kurosawatsu, M. Otsubo, and C. Honda, "Surface modification of carbon electrode for electric double layer capacitor," *Plasma Processes and Polymers*, vol. 4, no. 1, supplement, pp. S502–S506, 2007.
- [5] E. G. Bushueva, P. S. Galkin, A. V. Okotrub et al., "Double layer supercapacitor properties of onion-like carbon materials," *Physica Status Solidi B*, vol. 245, no. 10, pp. 2296–2299, 2008.
- [6] A. Nishino, "Capacitors: operating principles, current market and technical trends," *Journal of Power Sources*, vol. 60, no. 2, pp. 137–147, 1996.
- [7] E. Heardman, C. Lekakou, and M. G. Bader, "Flow monitoring and permeability measurement under constant and transient flow conditions," *Composites Science and Technology*, vol. 64, no. 9, pp. 1239–1249, 2004.
- [8] S. Amico and C. Lekakou, "An experimental study of the permeability and capillary pressure in resin-transfer moulding," *Composites Science and Technology*, vol. 61, no. 13, pp. 1945–1959, 2001.
- [9] E. Heardman, C. Lekakou, and M. G. Bader, "In-plane permeability of sheared fabrics," *Composites—Part A*, vol. 32, no. 7, pp. 933–940, 2001.
- [10] N. Shirshova, E. Greenhalgh, M. Shaffer, J. H. G. Steinke, P. Curtis, and A. Bismarck, "Structural polymer composites for energy storage devices," in *Proceedings of the 17th International Conference on Composite Materials (ICCM '09)*, Edinburgh, UK, 2009.
- [11] E. Frackowiak and F. Béguin, "Carbon materials for the electrochemical storage of energy in capacitors," *Carbon*, vol. 39, no. 6, pp. 937–950, 2001.
- [12] V. L. Pushparaj, M. M. Shaijumon, A. Kumar et al., "Flexible energy storage devices based on nanocomposite paper," *Proceedings of the National Academy of Sciences of the United States of America*, vol. 104, no. 34, pp. 13574–13577, 2007.

- [13] R. Shi, L. Jiang, and C. Pan, "A single-step process for preparing supercapacitor electrodes from carbon nanotubes," *Soft Nanoscience Letters*, vol. 1, no. 1, pp. 11–15, 2011.
- [14] R. Z. Ma, J. Liang, B. Q. Wei, B. Zhang, C. L. Xu, and D. H. Wu, "Study of electrochemical capacitors utilizing carbon nanotube electrodes," *Journal of Power Sources*, vol. 84, no. 1, pp. 126–129, 1999.
- [15] T. Bordjiba, M. Mohamedi, and L. H. Dao, "Synthesis and electrochemical capacitance of binderless nanocomposite electrodes formed by dispersion of carbon nanotubes and carbon aerogels," *Journal of Power Sources*, vol. 172, no. 2, pp. 991–998, 2007.
- [16] Q. Guo, X. Zhou, X. Li et al., "Supercapacitors based on hybrid carbon nanofibers containing multiwalled carbon nanotubes," *Journal of Materials Chemistry*, vol. 19, no. 18, pp. 2810–2816, 2009.
- [17] R. Kötz and M. Carlen, "Principles and applications of electrochemical capacitors," *Electrochimica Acta*, vol. 45, no. 15–16, pp. 2483–2498, 2000.
- [18] A. K. Shukla, S. Sampath, and K. Vijayamohan, "Electrochemical supercapacitors: energy storage beyond batteries," *Current Science*, vol. 79, no. 12, pp. 1656–1661, 2000.
- [19] S. A. Hashmi, S. Suematsu, and K. Naoi, "All solid-state redox supercapacitors based on supramolecular 1,5-diaminoanthraquinone oligomeric electrode and polymeric electrolytes," *Journal of Power Sources*, vol. 137, no. 1, pp. 145–151, 2004.
- [20] J. Huang, B. G. Sumpter, and V. Meunier, "A universal model for nanoporous carbon supercapacitors applicable to diverse pore regimes, carbon materials, and electrolytes," *Chemistry—A*, vol. 14, no. 22, pp. 6614–6626, 2008.
- [21] K. Hung, C. Masarapu, T. Ko, and B. Wei, "Wide-temperature range operation supercapacitors from nanostructured activated carbon fabric," *Journal of Power Sources*, vol. 193, no. 2, pp. 944–949, 2009.
- [22] C. Lei, P. Wilson, and C. Lekakou, "Effect of PEDOT in carbon-based composite electrodes for electrochemical supercapacitors," *Journal of Power Sources*. In press.
- [23] Z. Algharaibeh and P. G. Pickup, "An asymmetric supercapacitor with anthraquinone and dihydroxybenzene modified carbon fabric electrodes," *Electrochemistry Communications*, vol. 13, no. 2, pp. 147–149, 2011.
- [24] S. Amico and C. Lekakou, "Flow through a two-scale porosity, oriented fibre porous medium," *Transport in Porous Media*, vol. 54, no. 1, pp. 35–53, 2004.
- [25] S. Amico and C. Lekakou, "Mathematical modelling of capillary micro-flow through woven fabrics," *Composites Part A*, vol. 31, no. 12, pp. 1331–1344, 2000.
- [26] A. K. Murugesu, A. Uthayanan, and C. Lekakou, "Electrophoresis and orientation of multiple wall carbon nanotubes in polymer solution," *Applied Physics A*, vol. 100, no. 1, pp. 135–144, 2010.
- [27] R. J. Latham, S. E. Rowlands, and W. S. Schlindwein, "Supercapacitors using polymer electrolytes based on poly(urethane)," *Solid State Ionics*, vol. 147, no. 3–4, pp. 243–248, 2002.
- [28] P. Staiti, M. Minutoli, and F. Lufano, "All solid electric double layer capacitors based on Nafion ionomer," *Electrochimica Acta*, vol. 47, no. 17, pp. 2795–2800, 2002.

## Research Article

# Microwave-Assisted Preparation of Biodegradable Water Absorbent Polyacrylonitrile/Montmorillonite Clay Nanocomposite

**Prafulla K. Sahoo, Trinath Biswal, and Ramakanta Samal**

*Department of Chemistry, Utkal University, Vani Vihar, Bhubaneswar 751004, India*

Correspondence should be addressed to Prafulla K. Sahoo, psahoochemuu@satyam.net.in

Received 3 December 2010; Revised 25 March 2011; Accepted 28 March 2011

Academic Editor: Baoquan Sun

Copyright © 2011 Prafulla K. Sahoo et al. This is an open access article distributed under the Creative Commons Attribution License, which permits unrestricted use, distribution, and reproduction in any medium, provided the original work is properly cited.

Polyacrylonitrile (PAN)/Montmorillonite (MMT) clay nanocomposite was prepared in a microwave oven using a transition metal Co(III) complex taking ammonium persulfate (APS) as initiator with a motive of converting hydrophobic PAN into hydrophilic nanocomposite material via nanotechnology by the inclusion of MMT to the virgin polymer. UV-visible spectral analysis revealed various interactions between the developed complex with other reaction components. The formation of the PAN/MMT nanocomposites was characterized by FTIR. Furthermore, as evidenced by X-ray diffraction (XRD), transmission electron microscopy (TEM), the composite so obtained was found to have nano-order. XRD and TEM were suggesting that montmorillonite layers were exfoliated during the polymerization process. An increasing in the thermal stability for the developed nanocomposite was recorded by thermogravimetric analysis (TGA). The water absorption and biodegradation properties were carried out for its ecofriendly nature and better commercialization.

## 1. Introduction

A great deal of research on organic polymer-layered silicate nanocomposites have been carried out over the past decade due to their substantial enhanced physical properties over virgin polymers, even when prepared with a very small amount of layered silicate [1, 2]. These nanocomposites, especially polymer-layered silicate nanocomposites (PLSNs), are emerging as the most significant and new breed of composite materials due to their extensively enhanced mechanical [3], thermal [4] flammability [5, 6] properties. These unique properties of nanocomposites arise from the maximized contact between the organic and inorganic phase, so fillers with high surface-to-volume ratio are commonly used. Layered silicates such as MMT, which are composed of stacks of parallel lamellae with a 1nm thickness and a high aspect ratio, are typically used.

Unlike to a virgin polymer or conventional micro and macro composites, the improvement in properties of PLSNs is remarkable, including high moduli [7], increased strength

and heat resistance [8], decreased gas permeability [9] and flammability [10], and increased biodegradability [11]. Following to this, there has been considerable interest in theory and simulations addressing the preparation, characterization, and properties of these materials [12], and they are also considered to be the structure and dynamics of polymers in confined environments [13].

Microwave heating is rapidly developing as an alternative to conventional heating techniques used in thermally initiated polymerization. The interaction between the microwave energy and molecular dipole moments of the starting materials provides an effective, selective, clean, and fast synthetic method [14]. However, although many benefits of microwave radiation have been recognized, the use of this radiation in polymer chemistry is still rather unexplored. Microwave radiation may be used as an alternative to thermal polymerization processes [15]. The advantages of microwaves are increased rate of production, improved product characteristics, uniform processing, less processes [16]. There are reports [17–19] that show similar kinetics

under both microwave and thermal methods, indicating that microwave does not alter the reaction products observed in conventional heating, but up to three fold increase in magnitude.

Further, study on green polymeric materials which avoid the use of any toxic or noxious components in their manufacture and could be naturally biodegradable, are in demand, as they reduce the hazardous effect of plastics and other polymeric compounds on environment. So far, biodegradable polymers, such as polylactide (PLA) [20, 21], polyhydroxy butyrate [22], aliphatic polyester [23, 24], and so forth, are mostly used for the preparation of nanocomposites; however, no report has been published regarding biodegradability and water absorbency of PLSNs. So in the present study, an attempt has been taken to highlight these aspects and to prepare PAN/MMT nanocomposites via a nonconventional microwave irradiation method in the absence of surfactant or emulsifier under the catalytic effect of transition metal complex  $[\text{Co(III)en}_2(\text{NO}_2)_2]\text{NO}_3$ . Nonconventional method of synthesis of various polymers under the catalytic effect of complex of transition metals have already been reported [12, 25] in our earlier publications. Thus the most significant outcome of the paper is the preparation of the nonbiodegradable hydrophobic PAN into the biodegradable hydrophilic material by microwave irradiation via the application of nanotechnology. PAN/MMT nanocomposites so obtained were found to be biodegradable and exhibited significant water absorbency.

## 2. Experimental

**2.1. Materials.** Monomer, AN E merck India, was purified as reported earlier [26]. The initiator, APS, and all other reagents like Cobalt (II) Chloride, ethylene diamine (en) and so forth, were from E merck India (AR grade) and were used after purification by standard techniques. Na-MMT clay with cation exchange capacity (CEC) of 90-mequiv/100 g was from Himedia India Ltd.

**2.2. Preparation of  $[\text{Co(III)en}_2(\text{NO}_2)_2]\text{NO}_3$  Complex.** A mixture of 6.85 g of 70% ethylene diamine (en) (0.08 mol) and 10 ml of water was partially neutralized by the addition of 3 ml of concentrated nitric acid (0.048 mol). The resulting solution was added to a solution of 11.5 g of  $\text{Co}(\text{NO}_3)_2 \cdot 6\text{H}_2\text{O}$  (0.04 mol) and 6 g of sodium nitrite (0.087 mol) in 20 ml water. A vigorous stream of air was passed through the solution. The yellow trans- $[\text{Co(III)en}_2(\text{NO}_2)_2]\text{NO}_3$  began to precipitate after 20 minutes. The mixture was cooled in an ice bath and filtered. The yellow crystalline solid was recrystallised from boiling water, washed with alcohol and ether and air dried. The formation of the complex trans- $[\text{Co(III)en}_2(\text{NO}_2)_2]\text{NO}_3$  was confirmed by UV-visible spectral analysis (Scheme 1).

**2.3. Synthesis of PAN Nanocomposites by Microwave Oven.** The polymerization experiments were carried out in a Kenstar (Model No. MOW 9811, 1200 W) domestic MW oven. The average bulk temperature at end of the reaction

was measured by inserting a thermometer in the reaction mixture. All the experiments were done with water and benzene as solvent, and the temperature is less than  $100^\circ\text{C}$ . The polymerization experiment was carried out first in two parts. The first part was carried out in reaction vessel containing the requisite amount (0.1 M) of each trans- $[\text{Co(III)en}_2(\text{NO}_2)_2]\text{NO}_3$  with a known amount of AN in 4/5th part deionized water. At the same time, desired amount of MMT was dispersed in rest 1/5th part of water at same condition. The MMT suspension was added to the reaction vessel and stirred with constant velocity at  $\text{N}_2$  atmospheric pressure. Then requisite amount of initiator solution was carefully injected to the reaction mixture. For all the MW power studies, the exposure time was varied from 30 to 180 sec. After completing reaction, the polymerization was terminated by the addition of a 0.1 M solution of ferrous ammonium sulfate solution. The coagulated products were purified. The variations of different components along with conversions were tabulated in Table 1.

### 2.4. Characterization

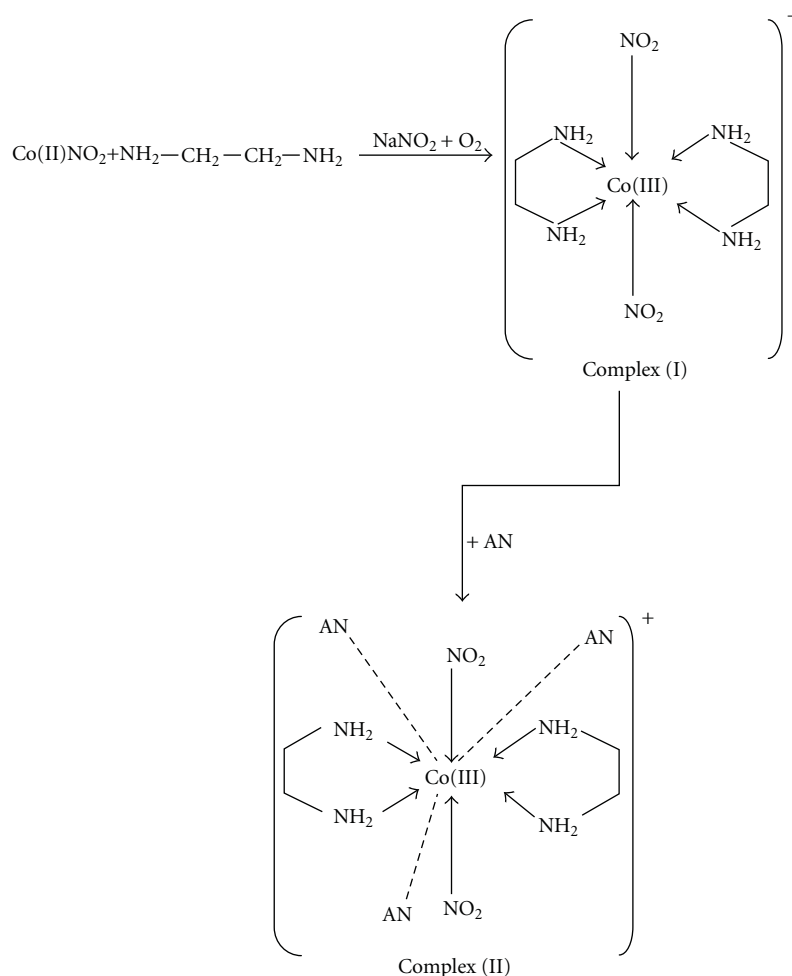
**2.4.1. Infrared Spectra (FTIR).** The IR spectra of PAN and PAN/MMT nanocomposite, in the form of KBr pellets, were recorded with a Perkin-Elmer model Paragon-500 FTIR spectrophotometer.

**2.4.2. X-Ray Diffraction (XRD).** The incorporation of Na-MMT into the matrix was confirmed by using an XRD monitoring diffraction angle  $2\theta$  from  $1.5^\circ$  to  $10^\circ$  on a Philips PW-1847 X-ray crystallographic unit equipped with Guinier focusing camera with Cuk radiation ( $+0.1505\text{ nm}$ ) with a 0.02 s step size and a 2.5 count time.

**2.4.3. Transmission Electron Microscopy (TEM).** Nanoscale structure of PAN/MMT was investigated by means of TEM (H-700, Hitachi Co.), operated at an accelerating voltage of 100 kV. The ultrathin section (the edge of the sample sheet perpendicular to the compression mold) by diamond knife with a thickness of 100 nm was microtomed at  $-80^\circ\text{C}$ .

**2.4.4. Scanning Electron Microscopy (SEM).** The surface morphology of PAN/MMT nanocomposite before and after biodegradation was studied by scanning electron microscopy (SEM) using Jeol Ltd, Japan and Model 5200 scanning electron microscope.

**2.4.5. Mechanical Properties.** Tensile bars were obtained on a Van Dorn 55 HPS 2.8F mini injection molding machine under the following processing conditions: a melt temperature of  $150^\circ\text{C}$ , a mold temperature of  $25^\circ\text{C}$ , an injection speed of 40 mm/s, an injection pressure of 10 MPa, and a holding time of 2 s, with a total cycle time of 30 s. Tensile measurements on injection molded samples of nanocomposites were performed according to ASTM D-638-00 using an Instron test machine Model 5567. Tests were carried out at a crosshead speed of 50 mm/min and a 1 kN load cell without the use of an extensometer. All tests were



SCHEME 1: Schematic representation of  $[\text{Co(III)(en)}_2(\text{NO}_2)_2]\text{NO}_3$  complex (I), (b) coordination of monomer AN with  $[\text{Co(III)(en)}_2(\text{NO}_2)_2]\text{NO}_3$  complex (II).

performed at room temperature and the results were the average of five measurements. The highest value of standard deviation was 15%.

**2.4.6. Thermogravimetric Analysis (TGA).** Thermal properties were measured by using Shimadzu DTA-500 system in air, from room temperature to  $600^\circ\text{C}$  at a heating rate of  $10^\circ\text{C}$  per min.

**2.4.7. UV-Visible Spectral Analysis.** The UV-visible spectra of  $[\text{Co(III)en}_2(\text{NO}_2)_2]\text{NO}_3$  complex vis-à-vis those of the monomer and the initiator were studied using a Perkin Elmer UV-visible spectrophotometer model Lambda-20.

**2.4.8. Water Absorbency.** One gram each of the powdered sample (PAN, PAN/MMT) was palatalized by using 10 tons of pressure of around 0.05 cm of thickness and 1.5 cm of diameter. The pellet was then immersed in water at room temperature until equilibrium was reached. The water absorption was determined by weighing the swollen pellet

after it had been wrapped between the folds of filter paper. The water absorbency [27]  $Q(\text{g H}_2\text{O/g sample})$  was calculated by using the equation:  $Q(\text{g H}_2\text{O/g sample}) = (m - m_0)/m_0$ , where  $m$  and  $m_0$  were denoted by weight of the samples swollen by water and dried weight of the sample, respectively.

## 2.5. Biodegradation

**2.5.1. By Activated Sludge.** In the present work, the activated sludge water was collected [28] in a polypropylene container from a tank area receiving toilet and domestic waste water. The container was filled completely and fully closed. The waste water was then brought to the laboratory immediately. After settling for 1 h, the total solid concentration was increased to 5000 mg/L. The activated sludge water and a polymer sample (0.2 g) were incubated together in a sterilized vessel at room temperature ( $28 \pm 2^\circ\text{C}$ ). Duplicate samples were removed at time intervals for biodegradation study via weight loss. Vessels containing polymer samples without sludge water were treated as controls.

TABLE 1: Effect of variation of concentration of AN, APS, Co(III) complex, MMT, and time on the % of conversion and water absorbency.

Sample code	(AN) $\text{mol} \cdot \text{dm}^{-3}$	(APS) $\times 10^2$ $\text{MoL} \cdot \text{dm}^{-3}$	(Complex) $\times$ $10^2 \text{ mol} \times$ $\text{dm}^{-3}$	(MMT) $\text{mol} \times \text{dm}^{-3}$	Time in Sec	% conversion	Water absorbency Q
S <sub>0</sub>	7.0	2.0	2.0	0.0	180	55.45	09
S <sub>1</sub>	0.38	2.0	2.0	5.0	180	57.19	39
S <sub>2</sub>	0.76	2.0	2.0	5.0	180	64.08	42
S <sub>3</sub>	1.51	2.0	2.0	5.0	180	68.85	74
S <sub>4</sub>	<b>2.27</b>	<b>2.0</b>	<b>2.0</b>	<b>5.0</b>	<b>180</b>	<b>79.06</b>	<b>87</b>
S <sub>5</sub>	3.03	2.0	2.0	5.0	180	64.45	68
S <sub>6</sub>	3.79	2.0	2.0	5.0	180	58.43	59
S <sub>7</sub>	4.55	2.0	2.0	5.0	180	54.57	56
S <sub>8</sub>	2.27	0.5	2.0	5.0	180	25.05	56
S <sub>9</sub>	2.27	1.0	2.0	5.0	180	58.18	69
S <sub>10</sub>	2.27	1.5	2.0	5.0	180	72.65	75
S <sub>11</sub>	2.27	2.0	2.0	5.0	180	79.06	87
S <sub>12</sub>	2.27	2.5	2.0	5.0	180	68.06	79
S <sub>13</sub>	2.27	3.0	2.0	5.0	180	54.49	72
S <sub>14</sub>	2.27	3.5	2.0	5.0	180	48.56	64
S <sub>15</sub>	2.27	2.0	0.5	5.0	180	35.09	69
S <sub>16</sub>	2.27	2.0	1.0	5.0	180	54.54	77
S <sub>17</sub>	2.27	2.0	1.5	5.0	180	68.89	83
S <sub>18</sub>	2.27	2.0	2.0	5.0	180	79.06	87
S <sub>19</sub>	2.27	2.0	2.5	5.0	180	64.00	76
S <sub>20</sub>	2.27	2.0	3.0	5.0	180	56.75	69
S <sub>21</sub>	2.27	2.0	3.5	5.0	180	48.95	62
S <sub>22</sub>	2.27	2.0	2.0	1.25	180	53.41	65
S <sub>23</sub>	2.27	2.0	2.0	2.5	180	62.31	76
S <sub>24</sub>	2.27	2.0	2.0	5.0	180	79.06	87
S <sub>25</sub>	2.27	2.0	2.0	10	180	72.55	84
S <sub>26</sub>	2.27	2.0	2.0	15	180	69.06	80
S <sub>27</sub>	2.27	2.0	2.0	20	180	63.07	76
S <sub>28</sub>	2.27	2.0	2.0	25	180	56.08	73
S <sub>29</sub>	2.27	2.0	2.0	5.0	60	57.09	
S <sub>30</sub>	2.27	2.0	2.0	5.0	90	65.59	
S <sub>31</sub>	2.27	2.0	2.0	5.0	120	69.49	
S <sub>32</sub>	2.27	2.0	2.0	5.0	150	74.55	
S <sub>33</sub>	2.27	2.0	2.0	5.0	180	79.06	
S <sub>34</sub>	2.27	2.0	2.0	5.0	210	79.57	
S <sub>35</sub>	2.27	2.0	2.0	5.0	240	79.65	
S <sub>36</sub>	2.27	2.0	2.0	5.0	300	79.75	

2.5.2. *In Cultured Medium.* A cultured medium was prepared by taking nutrient broth. In that medium, *Bacillus cereus* (gram-positive stain) was inoculated separately. The pure cultures were maintained separately in the incubator. The nutrient broth so prepared was sterilized for 45 m at a pressure of 15 lb/in<sup>2</sup> at 80°C. Then to 10 ml of sterilized broth 0.1 g, each of the samples, that is, PAN, PAN/MMT nanocomposites were added aseptically in separate test tubes,

and each tube of samples were supplemented with inoculum of different bacterial stains separately.

The degradation of samples by *B. cereus* was monitored in time intervals of 1, 7, 15, and 30 days. After the required time period, the samples were washed repeatedly with deionised water, oven dried at  $40 \pm 1^\circ\text{C}$  for 24 h. Then the samples were weighed to determine the weight loss. Biodegradation through *B. cereus* was studied by the amount of CO<sub>2</sub> evolved

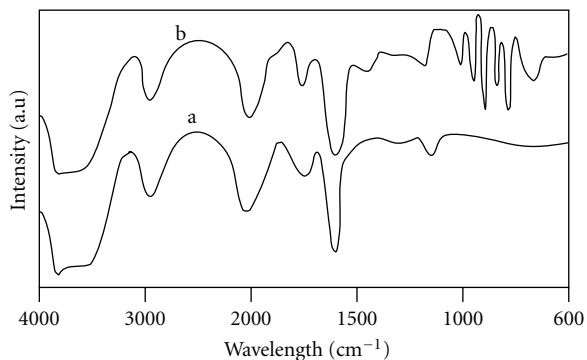


FIGURE 1: FTIR spectra of (a) PAN and (b) PAN/MMT (5 %w/v) nanocomposite.

[29] during the incubation periods of 1, 7, 15, and 30 days.

### 2.5.3. Quantitative Estimation of Free CO<sub>2</sub>

**Chemicals Requirement.** Na<sub>2</sub>CO<sub>3</sub>, phenolphthalein indicator.

**Procedure 1.** The cultured sample (“X” ml) and blank tube were titrated against Na<sub>2</sub>CO<sub>3</sub> (N/50)- (“Y” ml) using phenolphthalein indicator until the pink color persists for at least 30 s. This was continued till getting a concordant reading.

#### Calculation

$$\begin{aligned}
 N_1 V_1 &= N_2 V_2 \\
 (\text{CO}_2) & \quad (\text{Na}_2\text{CO}_3) \\
 \Rightarrow N_1 \times X &= \left(\frac{1}{50}\right) \times Y \\
 \Rightarrow \text{Strength} &= \frac{(Y \times 22)}{(50 \times X)} \quad (1) \\
 \Rightarrow \text{Free CO}_2 &= \left(\frac{Y \times 22 \times 1000}{(50 \times X)}\right) \text{mg/l} \\
 \Rightarrow \text{Free CO}_2 &= \left(\frac{(440 \times Y)}{X}\right) \text{ppm.}
 \end{aligned}$$

## 3. Results and Discussion

From the series of experiments, it was found that the PAN was intercalated into gallery structure of silicate by the catalytic action of [Co(III)(en)<sub>2</sub>(NO<sub>2</sub>)<sub>2</sub>]NO<sub>3</sub> complex. The complex initiating system helps to stabilize the emulsion latex to a high conversion level in the absence of added emulsifier (Table 1). The initiation is a surface catalysis with adequate energy transfer from the complex to the initiator (APS), resulting in a complex initiation mechanism deviating from a simple path of decomposition. The concerted

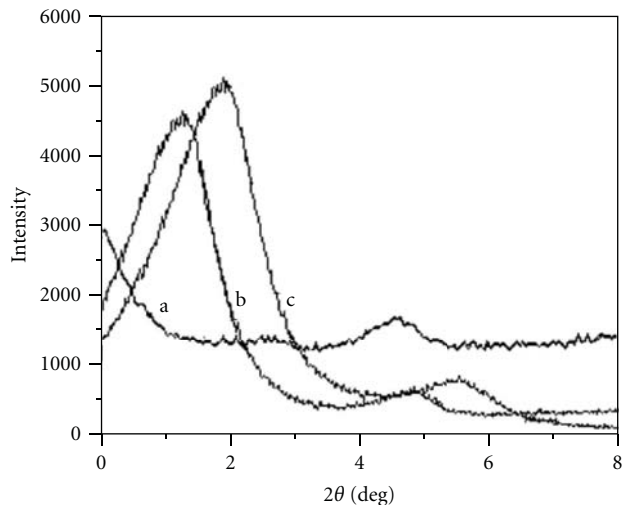


FIGURE 2: XRD of PAN/MMT nanocomposites (a) 5%, (b) 10 %w/v, and (c) pure MMT clay.

generation-consumption criterion is the driving force in the complex-catalyzed peroxide and vinyl polymerization [30].

**3.1. FTIR.** Absorption peaks for PAN, PAN/MMT nanocomposite are shown in Figures 1(a) and (b). The absorption peak at 1079 cm<sup>-1</sup> is due to the Si–O–Si linkage (Figure 1(b)). The peak at 1360 cm<sup>-1</sup> is due to =CH<sub>2</sub> bending, and 1453 cm<sup>-1</sup> is due to the scissoring vibration of terminal methylene group. The stretching vibration of –C≡N and vinyl C–H of the composite showed peak at 2245 cm<sup>-1</sup> and 2935 cm<sup>-1</sup>, respectively. The peak at 2956 cm<sup>-1</sup> is due to antisymmetric >CH<sub>2</sub> stretching. The IR spectra of PAN/MMT (Figure 1(b)) contain all the peaks of both silicate and PAN. Thus, the comparative spectral peaks revealed the formation of PAN/MMT nanocomposite as confirmed further by subsequent studies, XRD, TEM.

**3.2. XRD Analysis.** XRD has been used to evaluate the degree of interaction of the layered silicates with the polymer matrix. The systematic arrangement of the silicate layers of the intercalated composites has been elucidated by XRD in calculating interlayer spacing with the help of Bragg’s equation. Figure 2 shows the XRD diffraction pattern of MMT and PAN/MMT nanocomposite. The MMT layers are exfoliated when MMT ≤ 5% as indicated by the disappearance of any peak Figure 2(a), but when MMT ≥ 10%, it gives intercalated nanocomposites as shown in Figure 2(b) which were further conformed from TEM (Figure 3). Further, the XRD patterns suggest that the hydrophobic PAN is inserted into the galleries of the hydrophilic silicate through emulsion polymerization, and that the disordered insertion of the polymer into hydrophilic silicate layers made the nanocomposite partially hydrophilic in nature.

**3.3. TEM Analysis.** The internal structure of PAN/MMT nanocomposite was further conformed by TEM Figure 3, which directly visualized the expanded layering structure in

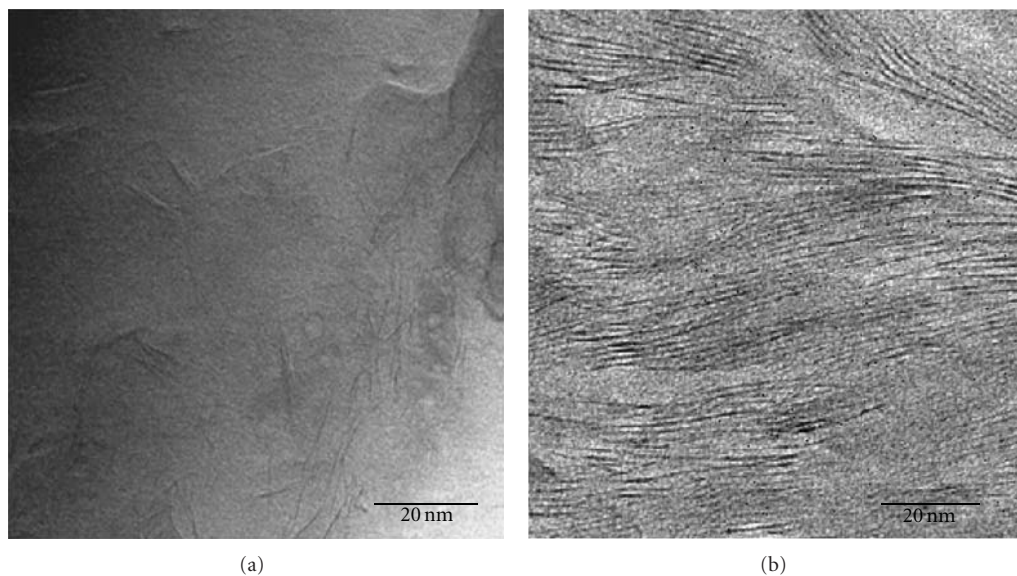


FIGURE 3: TEM micrographs of PAN/MMT nanocomposites (a) 5% and (b) 10%w/v.

the nanocomposites and partial dispersion of silicate layers in polymer matrix [31]. Figure 3(a) demonstrated a mixed nanostructure with well-dispersed layers of polymer blend nanocomposites showing compatibility between PAN and silicate. The interlayer spacing in the figure reveals the intercalation of PAN matrix with silicate layers [32] as evidenced by XRD. Figure 3(b) gives the TEM of nanocomposite after combustion which is in agreement with the result obtained in XRD study.

**3.4. Thermal Analysis.** The thermal properties of the nanocomposite materials have been evaluated by TGA as shown in Figure 4. In contrast to PAN, the onset of decomposition for PAN/MMT nanocomposite is shifted towards a higher temperature with inclusion of MMT, indicating an enhancement of the thermal stability upon intercalation. The PNA/MMT nanocomposite exhibited higher thermal stability due to the higher decomposition onset temperature than that of PAN, which can be attributed to the nanoscale silicate layers preventing outdiffusion of the volatile decomposition product. On the other hand, since the inorganic part (silicate) of the nanocomposite film almost did not lose its weight during the heating period, the shift of weight loss to higher-temperature region might be simply due to that the nanocomposite films possessed relatively small amount (about 4 wt%) of organic polymer that contributed to the weight loss. The higher thermal stability of PAN/MMT nanocomposite suggests that the generated silica-rich char is protecting the polymer from ambient oxygen, and reducing the rate of oxidative degradation in the nanocomposite materials [33] than that of PAN, which can be attributed to the nanoscale clay layers preventing outdiffusion of the volatile decomposition product. On the other hand, the inorganic part of the nanocomposite film almost did not lose its weight during the heating period.

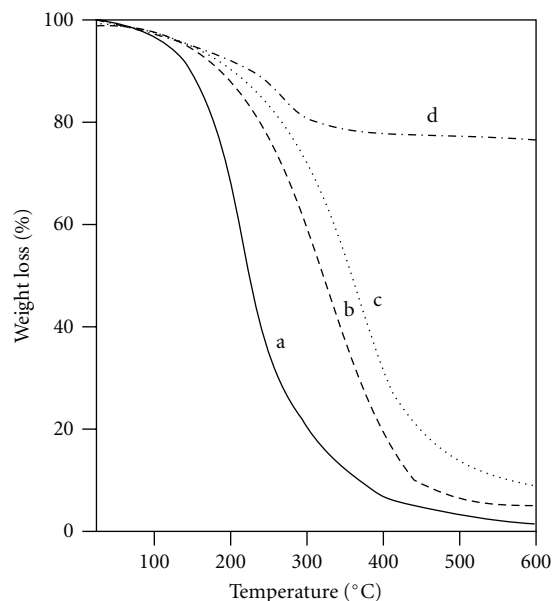


FIGURE 4: TGA of (a) PAN, (b) PAN/MMT (5%w/v) nanocomposite, (c) PAN/MMT (10%w/v) nanocomposite, and (d) MMT Clay.

**3.5. Mechanical Properties.** The mechanical properties, including Young's modulus, elongation at break, toughness, yield stress, and yield strain of all the nanocomposites prepared in this study, together with the corresponding values of the virgin polymer, are given in Table 2. The significant increase in the Young's modulus of nanocomposites with increase of silicate concentration is due to the slight possibility of hydrogen bonding between the nitrile groups of AN and large number of hydroxyl (OH) groups present on the surface of the clay layers [34], where as the yield

TABLE 2: Comparative data of mechanical properties ( $\pm$ error point) of PAN and PAN/MMT nanocomposites.

Sample code	Young's model. (MPa)	Elong. at break (%)	Toughness, (MPa)	Yield strain (%)	Yield stress (MPa)
S <sub>0</sub>	218 $\pm$ 11	708 $\pm$ 40	142.6 $\pm$ 17	24.8 $\pm$ 1.9	18.1 $\pm$ 1.6
S <sub>22</sub>	264 $\pm$ 13	659 $\pm$ 29	84.5 $\pm$ 34	23.6 $\pm$ 2.0	17.6 $\pm$ 1.2
S <sub>24</sub>	365 $\pm$ 12	578 $\pm$ 32	52.1 $\pm$ 29	22.1 $\pm$ 1.6	17.4 $\pm$ 1.6
S <sub>25</sub>	382 $\pm$ 17	493 $\pm$ 28	33.5 $\pm$ 15	21.8 $\pm$ 1.5	16.6 $\pm$ 1.8
S <sub>27</sub>	413 $\pm$ 23	367 $\pm$ 19	20.4 $\pm$ 12	20.2 $\pm$ 0.9	15.8 $\pm$ 1.4

stress and strain decreased monotonically with increase of MMT content. Due to their rigidity, MMT particles cannot be deformed by external stress in the specimen but act only as stress concentrators during deformation process [35]. Elongation at break and toughness of nanocomposites decreased tremendously with increasing MMT content which is in accordance with the results obtained earlier [36]. Therefore, emulsion process played a vital role in the dispersion of MMT in PAN, creating a strong interfacial adhesion with the matrix.

The results of the study on the polymerization of AN initiated by APS catalyzed by,  $[\text{Co(III)(en)}_2(\text{NO}_2)_2]\text{NO}_3$  were tabulated in Table 1. From the results, it is evident that the maximum rate of polymerization and the order of  $R_p$  for various systems are as follows:

$$R_p(\text{APS} + [\text{Co(III)(en)}_2(\text{NO}_2)_2]\text{NO}_3) > R_p(\text{APS}) \quad (2)$$

**3.6. UV-Visible.** The UV-visible spectra of various mixtures like  $[\text{Co(III)(en)}_2(\text{NO}_2)_2]\text{NO}_3$ ,  $[\text{Co(III)(en)}_2(\text{NO}_2)_2] \cdot \text{NO}_3/\text{APS}$ , and  $[\text{Co(III)(en)}_2(\text{NO}_2)_2]\text{NO}_3/\text{AN}/\text{APS}$  before reaction and after reaction were measured in an aqueous solution to obtain a complete picture of the interaction between the reacting species and their relationship with the rate data (Figure 5). The bidentate ligand character of en with colored cations like Co(II) to form chelate complex is well recognized [37], where the Co(III)-en ratio in complex Scheme 1(a) is 1:2 as evidenced by the proportionality found in the rate expression. Further, the central metal ion, Co(III) is coordinated to three molecules of monomer (AN), (Complex-II, Scheme 1(b)) as revealed from the sharp change in absorbance from 1.3 (b) to 1.2 (c) in Figure 5 which is also accorded from the rate expression. On addition of the initiator (APS), to the above mixture (Complex-II), the absorbance reduces from 1.2 (c) to 1.1 (d) showing the initiation of polymerization, thus establishing the mechanism of complex initiation. The polymerization through complex medium is evident by sharp change in absorbance from 1.3 (b) to 0.5 (e) in Figure 5. In addition, the complex formation and initiation of polymerization are also evidenced from the change in  $\text{Co}(\text{NO}_3)_2$  pink color to deep pink with en and the gradual fading of the pink color with reaction time by the addition of monomer and initiator. The high-conversion values with  $[\text{Co(III)(en)}_2(\text{NO}_2)_2]\text{NO}_3$  complex may be due to the high rate production of initiating radicals generated by the heterolysis of the initiator bound by a complex of  $[\text{Co(III)(en)}_2(\text{NO}_2)_2]\text{NO}_3$  where the internal

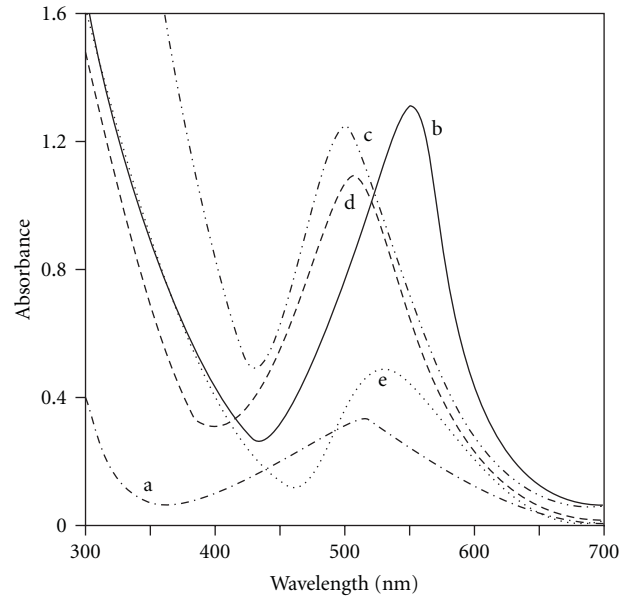


FIGURE 5: UV-visible spectra of (a)  $\text{Co(II)(NO}_2)_2$ , (b)  $[\text{Co(III)(en)}_2(\text{NO}_2)_2]\text{NO}_3$ , (c)  $[\text{Co(III)(en)}_2(\text{NO}_2)_2]\text{NO}_3 + \text{AN}$ , (d)  $[\text{Co(III)(en)}_2(\text{NO}_2)_2]\text{NO}_3 + \text{AN} + \text{APS}$  before reaction, and (e)  $[\text{Co(III)(en)}_2(\text{NO}_2)_2]\text{NO}_3 + \text{AN} + \text{APS}$  after reaction.

energy is transferred to the monomer. The new nonconventional complex initiated system leads to stabilizing the emulsion latex to a high conversion in the absence of an added emulsifier.

It was found that the conversion and the  $R_p$  were strongly affected by the monomer, initiator, and complex concentration and also by the reaction time. The detailed kinetics is discussed as per our previous article [38] and is expressed in rate law.

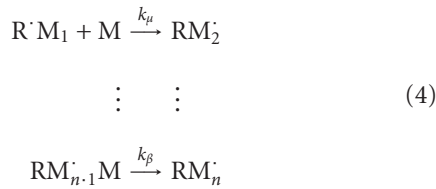
**3.7. Variation of Time.** From Table 1, the variation of conversion with reaction is keeping the concentrations of AN, APS, and  $[\text{Co(III)(en)}_2(\text{NO}_2)_2]\text{NO}_3$  constant at 2,  $10 \times 10^{-3}$  and  $10 \times 10^{-3} \text{ mol dm}^{-3}$ , respectively. It was found that the reaction showed a dead-end polymerization tendency, that is, the initiation activity of the initiator is high at initial period and, hence, after 240 sec, it increases at a comparatively slow rate, where in case of traditional heating more time was required, that is, 3 h for production with less conversion % as compared with microwave irradiation.

### 3.7.1. Chain Initiation by Co Complex

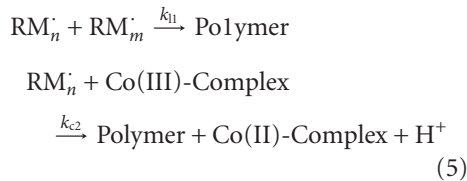


The above complexation mechanism is explained earlier on the basis of the spectral data and Scheme 1(a) and (b).

### 3.7.2. Propagation



### 3.7.3. Termination



From Table 1, applying steady state principle and assuming mutual termination, the rate of expression is observed as follows:

$$R_p \propto [\text{Co(III)}]^{0.43} [\text{APS}]^{0.33} [\text{AN}]^{0.77} \quad (6)$$

## 3.8. Water Absorbency

**3.8.1. Effect of (Monomer).** The effect of variation in monomer concentration on water absorbency of the nanocomposite showed very interesting results (Table 1). It was observed that for an increase in monomer concentration up to  $2.27 \text{ mol}\cdot\text{dm}^{-3}$ , the water absorbency was increased from 38–87, and, thereafter, it decreased. This might be attributed to the fact that, on increasing the monomer concentration beyond a certain value, the hydrophobic character of PAN prevails over the induction of hydrophilic character to the polymer matrix by the exfoliated clay in it. To explain more clearly, within the above specified limits of (monomer), the water absorbency was increased following a better exfoliation of clay because the available

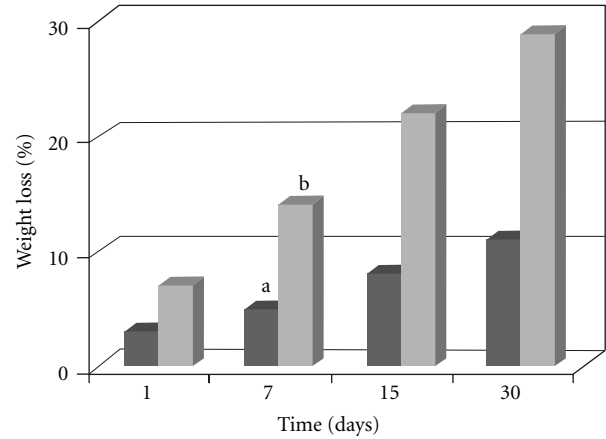


FIGURE 6: Biodegradation by activated sludge of (a) PAN, (b) PAN/MMT (5%w/v) on time versus weight loss.

area in PAN matrix within these limits is just sufficient as required for a better exfoliation. However, with a further increase in the (monomer) up to 4.55, although the available area required for exfoliation of clay was increased but the hydrophobicity of PAN matrix predominated any further increase in the water absorbency due to its comparatively high concentration in comparison to (MMT).

**3.8.2. Effect of (Initiator).** The effect of initiator concentration was studied and presented in Table 1. The swelling amount was found to increase with an increase in APS concentration from  $0.5 \times 10^{-2}$  to  $2 \times 10^{-2} \text{ mol}\cdot\text{dm}^{-3}$  and then decreased slowly due to increase in number of radicals produced as the concentration of APS increased. The increase in the production of radicals at higher initiator concentration increased the rate of polymerization, thereby lessening the crosslinking density or net-like structure of the MMT inside the PAN matrix, and this factor is responsible for the decrease in the swelling capacity of the polymer.

**3.8.3. Effect of  $[[\text{Co(III)}(\text{en})_2(\text{NO}_2)_2]\text{NO}_3]$ .** As reported in our earlier publications, here also the synthesis of the nanocomposite was carried out in the presence of a new complex to catalyze the reaction as well as to avoid the use of any added emulsifier. Accordingly, the synthesis of the nanocomposite was carried out under different  $[\text{Co(III)}(\text{en})_2(\text{NO}_2)_2]\text{NO}_3$  concentrations; however, for concentration  $2 \times 10^{-2} \text{ mol}\cdot\text{dm}^{-3}$ , the resulting nanocomposite sample recorded highest water absorbency, because, at this concentration, the complex was effective in catalyzing the polymerization reaction as well as in decreasing the particle size to nano order. Thereafter, the high concentration of the complex retarded the rate of polymerization and also decreased the % conversion following which the exfoliation of clay inside the PAN matrix was less due to less available area of the polymer matrix thereby decreasing the porous nature of the matrix and hence water absorbency. To add with, on the reduction of the particle size, the porous nature

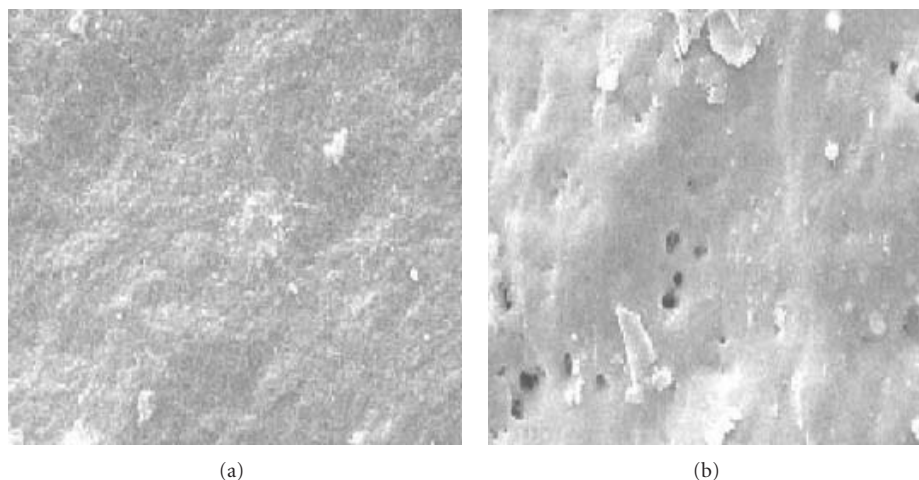


FIGURE 7: SEM of PAN/MMT nanocomposites (a) before and (b) after 30 days biodegradation.

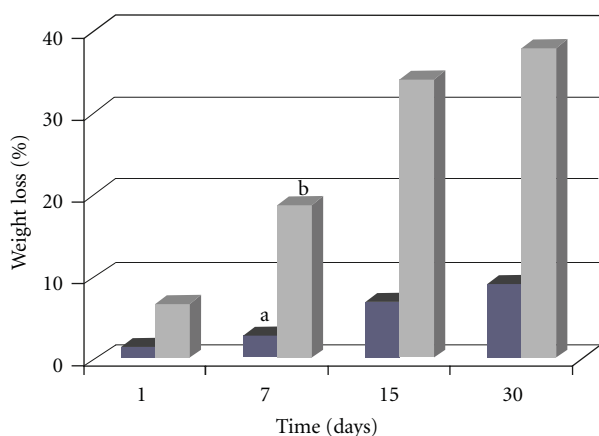


FIGURE 8: Biodegradation by bacteria (*B. cereus*) of (a) PAN, (b) PAN/MMT (5 %w/v) on time versus weight loss.

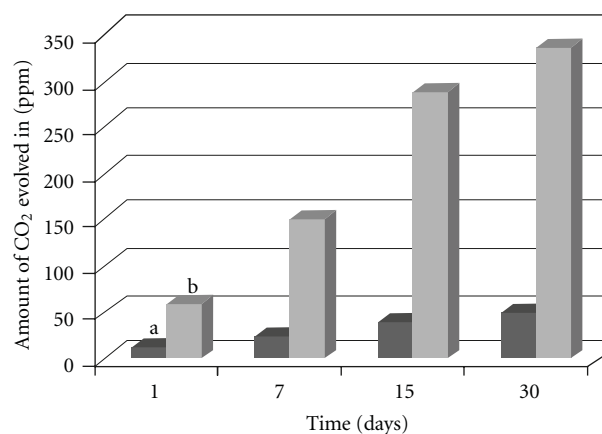


FIGURE 9: Biodegradation by bacteria (*B. cereus*) of (a) PAN, (b) PAN/MMT (5 %w/v) on time versus amount of CO<sub>2</sub> evolved.

of the matrix was increased to an extent of having constant water absorbency.

**3.8.4. Effect of (MMT).** The water absorbency was found to increase with MMT concentrations 1.25 to 5 mol·dm<sup>-3</sup> and then decreased as shown in Table 1. This can be explained on the basis of exfoliation of hydrophilic silicate layers inside hydrophobic PAN matrix making more room for water molecules. With higher silicate concentration, the arrangement of silicate layers inside the matrix increased the hydrophobicity of the polymer nanocomposite since the degree of exfoliation of clay layers inside PAN matrix might be suppressed due to a comparatively less available area of the PAN matrix as required by a higher concentration of clay for a better exfoliation. As a result, the porous nature of the matrix was decreased thereby increasing hydrophobicity of the nanocomposite or decreasing its water absorbency

**3.9. Biodegradation in Activated Sludge and Culture Media.** From the comparative biodegradation study of PAN,

PAN/MMT, it was found that PAN showed low accelerated rate of degradation by weight loss initially, but after 21 days, it was slowed down. The PAN/MMT nanocomposite showed tremendous rate of degradation in activated sludge as shown in Figure 6 since it contains different varieties of microorganisms which can rapidly degrade the sample as confirmed by SEM Figure 7.

The weight loss data in Figure 8 revealed that PAN/MMT nanocomposite degraded under the influence of *B. cereus* at a faster rate than PAN. The degradation value was least in case of PAN due to its hydrophobic nature. Due to the hydrophilic nature of MMT, the water absorbency and the growth of microorganisms have been increased in the PAN/MMT nanocomposite. The rate of water absorbency of PAN and PAN/MMT nanocomposites was given in Table 1 to justify the biodegradability data.

Again, the rate of degradation was also measured by calculating the amount of CO<sub>2</sub> evolved from the cultured medium at interval period of times. The results in Figure 9 showed similar trend of degradation exhibiting

more biodegradability of the nanocomposite than the other samples. On comparison of both weight-loss method and the CO<sub>2</sub> release method for the study of degradation of the nanocomposite, it was inferred that the rate of degradation of PAN/MMT nanocomposite was equivalent in both methods, and it was further concluded that the nanocomposite was biodegradable in nature. Thus the deviation in the degrading behavior of *B. cereus* might be due to the difference in the carbon sources used by the bacteria for their growth.

#### 4. Conclusion

PAN/MMT nanocomposites are prepared by using a Co(III) complex in a domestic microwave oven. In microwave oven, the polymerization took place very fast and consumed very less time. The fast polymerization reactions occurred by fast decomposition of initiator due to the complex. The formation of nanocomposites was characterized by FTIR, further confirmed from XRD and TEM. Due to the bond between PAN and MMT, the thermal stability of PAN/MMT nanocomposite is increased. The mechanical properties of PAN/MMT nanocomposites, UV-visible spectra of complex and the mechanism of polymerization were studied. The biodegradation of the samples was also studied for their better commercialization.

#### References

- [1] H. M. Jeong, B. C. Kim, and E. H. Kim, "Structure and properties of EVOH/organoclay nanocomposites," *Journal of Materials Science*, vol. 40, no. 14, pp. 3783–3787, 2005.
- [2] H. Ishida, S. Campbell, and J. Blackwell, "General approach to nanocomposite preparation," *Chemistry of Materials*, vol. 12, no. 5, pp. 1260–1267, 2000.
- [3] Z. Wang and T. J. Pinnavaia, "Hybrid organic-inorganic nanocomposites: exfoliation of magadiite nanolayers in an elastomeric epoxy polymer," *Chemistry of Materials*, vol. 10, no. 7, pp. 1820–1826, 1998.
- [4] S. Wang, Y. Hu, L. Song, Z. Wang, Z. Chen, and W. Fan, "Preparation and thermal properties of ABS/montmorillonite nanocomposite," *Polymer Degradation and Stability*, vol. 77, no. 3, pp. 423–426, 2002.
- [5] J. W. Gilman, "Flammability and thermal stability studies of polymer layered-silicate (clay) nanocomposites," *Applied Clay Science*, vol. 15, no. 1-2, pp. 31–49, 1999.
- [6] P. K. Sahoo and R. Samal, "Fire retardancy and biodegradability of poly(methyl methacrylate)/montmorillonite nanocomposite," *Polymer Degradation and Stability*, vol. 92, no. 9, pp. 1700–1707, 2007.
- [7] M. Biswas and S. S. Ray, "Recent progress in synthesis and evaluation of polymer-montmorillonite nanocomposites," *Advances in Polymer Science*, vol. 155, pp. 167–221, 2001.
- [8] E. P. Giannelis, "Polymer-layered silicate nanocomposites: synthesis, properties and applications," *Applied Organometallic Chemistry*, vol. 12, no. 10-11, pp. 675–680, 1998.
- [9] R. Xu, E. Manias, A. J. Snyder, and J. Runt, "New biomedical poly(urethane urea)-layered silicate nanocomposites," *Macromolecules*, vol. 34, no. 2, pp. 337–339, 2001.
- [10] S. Bourbigot, M. Le Bras, F. Dabrowski, J. W. Gilman, and T. Kashiwagi, "PA-6 clay nanocomposite hybrid as char forming agent in intumescent formulations," *Fire and Materials*, vol. 24, no. 4, pp. 201–208, 2000.
- [11] S. S. Ray, K. Yamada, M. Okamoto, and K. Ueda, "Polylactide-layered silicate nanocomposite: a novel biodegradable material," *Nano Letters*, vol. 2, no. 10, pp. 1093–1096, 2002.
- [12] P. K. Sahoo and R. Mohapatra, "Synthesis and kinetic studies of PMMA nanoparticles by non-conventionally initiated emulsion polymerization," *European Polymer Journal*, vol. 39, no. 9, pp. 1839–1846, 2003.
- [13] V. Kuppa and E. Manias, "Computer simulation of PEO/layered-silicate nanocomposites: 2. Lithium dynamics in PEO/Li montmorillonite intercalates," *Chemistry of Materials*, vol. 14, no. 5, pp. 2171–2175, 2002.
- [14] X. Fang, C. D. Simone, E. Vaccaro, S. J. Huang, and D. A. Scola, "Ring-opening polymerization of  $\epsilon$ -caprolactam and  $\epsilon$ -caprolactone via microwave irradiation," *Journal of Polymer Science A*, vol. 40, no. 14, pp. 2264–2275, 2002.
- [15] J. Jacob, L. H. L. Chia, and F. Y. C. Boey, "Microwave polymerization of poly(methyl acrylate): conversion studies at variable power," *Journal of Applied Polymer Science*, vol. 63, no. 6, pp. 787–797, 1997.
- [16] M. A. Stuchly and S. S. Stuchly, "Industrial, scientific, medical and domestic applications of microwaves," *IEEE Proceedings A*, vol. 130, no. 8, pp. 467–503, 1983.
- [17] R. Correa, G. Gonzalez, and V. Dougar, "Emulsion polymerization in a microwave reactor," *Polymer*, vol. 39, no. 6-7, pp. 1471–1474, 1998.
- [18] L. H. L. Chia, J. Jacob, and F. Boey, "Radiation curing of poly-methyl-methacrylate using a variable power microwave source," *The Journal of Materials Processing Technology*, vol. 48, no. 1–4, pp. 445–449, 1995.
- [19] J. Jacob, L. H. L. Chia, and F. Y. C. Boey, "Comparative study of methyl methacrylate cure by microwave radiation versus thermal energy," *Polymer Testing*, vol. 14, no. 4, pp. 343–354, 1995.
- [20] M. A. Paul, M. Alexandre, P. Degee, C. Henrist, A. Rulmont, and P. Dubois, "New nanocomposite materials based on plasticized poly(L-lactide) and organo-modified montmorillonites: thermal and morphological study," *Polymer*, vol. 44, pp. 443–450, 2003.
- [21] S. S. Ray, K. Yamada, M. Okamoto, and K. Ueda, "Crystallization behaviour and morphology of biodegradable polylactide/layered silicate nanocomposite," *Polymer*, vol. 44, pp. 857–866, 2003.
- [22] S. H. Park, S. T. Lim, T. K. Shin, H. J. Choi, and M. S. Jhon, "Viscoelasticity of biodegradable polymer blends of poly(3-hydroxybutyrate) and poly(ethylene oxide)," *Polymer*, vol. 42, no. 13, pp. 5737–5742, 2001.
- [23] B. Lepoittevin, N. Pantoustier, M. Alexandre, C. Calberg, R. Jérôme, and P. Dubois, "Polyester layered silicate nanohybrids by controlled grafting polymerization," *Journal of Materials Chemistry*, vol. 12, no. 12, pp. 3528–3532, 2002.
- [24] R. K. Bharadwaj, A. R. Mehrabi, C. Hamilton et al., "Structure-property relationships in cross-linked polyester-clay nanocomposites," *Polymer*, vol. 43, no. 13, pp. 3699–3705, 2002.
- [25] P. K. Sahoo, R. Samal, S. K. Swain, and P. K. Rana, "Synthesis of poly(butyl acrylate)/sodium silicate nanocomposite fire retardant," *European Polymer Journal*, vol. 44, no. 11, pp. 3522–3528, 2008.
- [26] P. K. Sahoo, S. P. Bhattacharjee, and R. K. Samal, "Influence of Cu(II)/salicylaldehyde couple on potassium monopersulphate

- decomposition and acrylonitrile polymerization in solution,” *European Polymer Journal*, vol. 21, no. 5, pp. 499–503, 1985.
- [27] K. Mohana Raju and M. Padmanabha Raju, “Synthesis of novel superabsorbing copolymers for agricultural and horticultural applications,” *Polymer International*, vol. 50, no. 8, pp. 946–951, 2001.
- [28] T. W. Federle, M. A. Barlaz, C. A. Pettigrew et al., “Anaerobic biodegradation of aliphatic polyesters: poly(3-hydroxybutyrate-co-3-hydroxyoctanoate) and poly( $\epsilon$ -caprolactone),” *Biomacromolecules*, vol. 3, no. 4, pp. 813–822, 2002.
- [29] O. P. Vermani and A. K. Narula, *Applied Chemistry (Theory and Practice)*, Wiley Eastern, 1989.
- [30] P. K. Sahoo, M. Dey, and S. K. Swain, “Emulsifier-free emulsion polymerization of acrylonitrile: effect of in situ developed Cu(II)/glycine chelate complex initiated by monopersulfate,” *Journal of Applied Polymer Science*, vol. 74, no. 12, pp. 2785–2790, 1999.
- [31] P. Maiti, P. H. Nam, M. Okamoto, N. Hasegawa, and A. Usuki, “Influence of crystallization on intercalation, morphology, and mechanical properties of polypropylene/clay nanocomposites,” *Macromolecules*, vol. 35, no. 6, pp. 2042–2049, 2002.
- [32] O. Becker, Y.-B. Cheng, R. J. Varley, and G. P. Simon, “Layered silicate nanocomposites based on various high-functionality epoxy resins: the influence of cure temperature on morphology, mechanical properties, and free volume,” *Macromolecules*, vol. 36, no. 5, pp. 1616–1625, 2003.
- [33] C. M. L. Preston, G. Amarasinghe, J. L. Hopewell, R. A. Shanks, and Z. Mathys, “Evaluation of polar ethylene copolymers as fire retardant nanocomposite matrices,” *Polymer Degradation and Stability*, vol. 84, no. 3, pp. 533–544, 2004.
- [34] A. Ambre, R. Jagtap, and B. Dewangan, “ABS nanocomposites containing modified clay,” *Journal of Reinforced Plastics and Composites*, vol. 28, no. 3, pp. 343–352, 2009.
- [35] K. H. Wang, M. H. Choi, C. M. Koo et al., “Morphology and physical properties of polyethylene/silicate nanocomposite prepared by melt intercalation,” *Journal of Polymer Science B*, vol. 40, no. 14, pp. 1454–1463, 2002.
- [36] S. K. Swain and A. I. Isayev, “Effect of ultrasound on HDPE/clay nanocomposites: rheology, structure and properties,” *Polymer*, vol. 48, no. 1, pp. 281–289, 2007.
- [37] *Vogel’s Textbook of Quantitative Inorganic Analysis*, ELBS and Longman, 4th edition, 1978.
- [38] T. Biswal, R. Samal, and P. K. Sahoo, “Complex-mediated microwave-assisted synthesis of polyacrylonitrile nanoparticles,” *Nanotechnology, Science and Applications*, vol. 3, no. 1, pp. 77–83, 2010.

## Research Article

# Enhancing the Mechanical Properties of Cross-Linked Rubber-Toughened Nanocomposites via Electron Beam Irradiation

N. A. Jamal,<sup>1</sup> H. Anuar,<sup>1</sup> and A. R. Shamsul Bahri<sup>2</sup>

<sup>1</sup>Department of Manufacturing and Materials Engineering, Faculty of Engineering, International Islamic University Malaysia, P.O. Box 10, Kuala Lumpur 50728, Malaysia

<sup>2</sup>Crop Improvement and Protection Unit, Production Development Division, Rubber Research Institute Malaysia (RRIM), Sungai Buloh, Selangor Darul Ehsan 47000, Malaysia

Correspondence should be addressed to N. A. Jamal, ayuni\_jamal@yahoo.com

Received 7 November 2010; Revised 13 March 2011; Accepted 14 March 2011

Academic Editor: Guifu Zou

Copyright © 2011 N. A. Jamal et al. This is an open access article distributed under the Creative Commons Attribution License, which permits unrestricted use, distribution, and reproduction in any medium, provided the original work is properly cited.

Improving the mechanical properties of a pristine system is the main target of developing nanocomposites. The nanocomposites systems were first prepared via intercalation technique with different organophilic montmorillonite (OMMT) loading. Two types of cross-linking techniques were applied, namely, as maleic anhydride polyethylene (MAPE) and electron beam (EB) irradiated system. The effectiveness of these systems was then compared with the control one and analyzed based on the mechanical tests and morphological examination. The mechanical tests revealed that control, MAPE, and EB irradiated systems had attained the optimum mechanical properties at 4 vol% OMMT content. EB irradiated unit of a dose of 100 kGy showed excellent mechanical properties with higher crosslinking degree which were proved by gel content analysis. X-ray diffraction (XRD) analysis confirmed the existence of delamination structure with MAPE and EB irradiation techniques based on the disappearance of characteristic peak. The degree of delamination was further investigated by transmission electron microscope (TEM).

## 1. Introduction

Compatibilizer or cross-linking agent is commonly introduced in a nanocomposite purposely to reduce the surface tension between immiscible polymers and filler as well as to improve the surface adhesion of filler. This is done to obtain the optimum filler dispersion which will improve properties of nanocomposite. The compatibilizer is a functionalized nanocomposite which prevents segregation of the polymer components in the polymer. Moreover, cross-linking agent is proved to enhance the rigidity of the polymer [1, 2]. Compatibilizing agents are typically a molecule having one hydrophilic and one organophilic functional group. Compatibilizers containing maleic anhydride functionalities are commonly used and are effective in improving physical properties of composites. A few studies claimed that the miscibility of polymer matrix with clay can be enhanced by introducing compatibilizers containing polar groups, such

as maleated polyethylene (MAPE), carboxylated PE, and so on [3, 4]. In this study, maleated polyethylene, MAPE, has been applied as a compatibilizer agent for the nanocomposite system.

Irradiation processing has been used for many years to modify the properties of formed polymer parts. The property enhancements achieved include increased operating temperature, improved mechanical properties, and increased chemical and solvent resistance. It should be noted that polymer structure influences the cross-linking ability of polymer. Chain cross-linking and scission are the two reactions that occur during EB processing of polymers. Polymers typically undergo simultaneous scission and cross-linking, but, in most cases, with one or the other clearly predominating [5, 6]. Cross-linking is the intermolecular bond formation of polymer chain. The degree of cross-linking is proportional to the radiation dose [7]. Much works have been done on radiation cross-linking of uncross-linked

polymers and cross-linking of various rubbers and plastics by electron beam irradiation [7–9].

In contrast, scission is the opposite process of cross-linking in which the rupturing of C–C bond occurs. Scission reduces cross-linking efficiency and degrades the properties of polymers (chemical resistance, mechanical, and thermal properties). The current study aims to vary and highlight the interest of EB irradiation technique for HDPE/EPDM, where pristine composites and nanocomposites were prepared with different irradiation doses rate and different OMMT loadings. The results obtained for the EB irradiated system were then compared with control and MAPE systems for the determination of the optimum system.

## 2. Experimental Design

**2.1. Materials.** Homopolymer high-density polyethylene (HDPE); (melt index: 3–6 g/10 min, density: 900 kg/cm<sup>3</sup>) supplied by Cementai Chemicals Group, Thailand and ethylene propylene diene monomer (EPDM) supplied by Centre West Sdn Bhd, Malaysia were used as the base polymer matrix. MAPE-Polybond<sup>®</sup> 3009, obtained from Uniroyal Chemical Company, was used as a coupling agent to improve surface adhesion. Commercially available organophilic montmorillonite (OMMT) surface modified with 15–35 wt% octadecylamine and 0.5 wt% amino-propyltriethoxysilane obtained from Sigma-Aldrich Group, Malaysia was used as reinforcing agent to prepare nanocomposites.

**2.2. Compounding.** Melt blending of HDPE (70 vol%) and EPDM rubber (30 vol%) as polymer matrix was carried out first in an internal mixer (Thermo Haake Rheomix 600P). Then, HDPE/EPDM blend was mixed with MAPE and OMMT. The content of MAPE agent was fixed at 3 vol% whereas the contents of OMMT were varied between 2, 4, 6, and 8 vol%. The melt mixing conditions were 150°C and at a rotor speed of 100 rpm. Prior to mixing, the polymer matrix and the nano clays were dehumidified in a dry oven at 110°C for a period of 1 hr. Details on the preparation of HDPE/EPDM and HDPE/EPDM filled OMMT are summarized in Tables 1 and 2.

**2.3. Specimen Preparation.** Subsequently, the blended samples were compression molded as per ASTM-F-412 using a compression molding machine at a temperature range of 135–155°C, 8 tone metric pressures for 14 min.

**2.4. High-Energy EB Irradiation.** The melt compounding samples were exposed under high-energy EB irradiation at different unit of dose of 50, 100, 150, and 200 kGy at room temperature using a 3 MeV electron beam accelerator. The acceleration energy, beam current, and dose rate were set to 2 MeV, 2 mA, and 50 kGy/pass, respectively.

## 3. Characterization Techniques

**3.1. Mechanical Properties.** Test specimens for analyzing mechanical properties were initially conditioned at 23 ± 1°C and 55 ± 2% RH for 24 hr prior to testing. These conditioned specimens were subjected to mechanical testing, and an average from the five testing measurements was reported. The corresponding standard deviation along with the measurement uncertainty value for the experimental data showing maximum deviation was also included.

**3.2. Tensile Test.** Specimens with dimensions of 125 × 1 × 1 mm<sup>3</sup> were subjected to a tensile test as per ASTM F412, using Instron 5567 machine with 5 kN load. Crosshead speed and gauge lengths were set to 50 mm/min and 60 mm.

**3.3. Flexural Test.** Specimens with 125 × 15 × 3 mm dimension were tested in accordance with ASTM D790 by using Instron 5567 machine. A span of 100 mm was used in a 5 kN load cell with crosshead speed of 50 mm/min.

**3.4. Impact Test.** Notched Izod impact test as specified by ASTM D256 standard test method was applied by using Ceast 6545/000 model. Specimens with 62 × 15 × 3 mm<sup>3</sup> dimension were subjected to an impact test with 2.54 mm depth of notch. Before the testing takes place, each sample is immersed into liquid nitrogen for about 30 seconds. The energy absorbed by the specimen in the breaking process is known as the breaking energy (J/m).

**3.5. Gel Content Analysis.** The gel content of the samples was determined by boiling the samples with xylene for 24 hours in accordance with ASTM D2765 procedure. The extracted samples were vacuum dried to constant weight for 16 hours at 75°C. The gel content was calculated as the ratio of weight of dried sample after extraction to the initial weight of the sample before extraction. The results reported were the average of three specimens. The gel content percentage of cross-linked samples was calculated using the formula below:

$$(\%) \text{ Gel content} = \frac{\text{weight after extraction}}{\text{weight before extraction}} \times 100. \quad (1)$$

**3.6. X-Ray Diffraction Analysis (XRD).** X-ray diffractograms of OMMT and the nanocomposites were recorded using Shimadzu 6000 (Japan), X-ray crystallographic unit equipped with nickel filtered Cu K $\alpha$  radiation source operated at 40 kV and 40 mA. The basal spacing or d<sub>001</sub> reflection of the samples was calculated from Bragg's equation by monitoring the diffraction angle 2 $\theta$  from 2 to 10°.

**3.7. Morphological Examination**

**3.8. Transmission Electron Microscope (TEM).** The morphology of the nanocomposites was observed using a JEOL JEM electron microscope with an accelerating voltage of 100 kV. Ultrathin specimens of 100 nm thickness were cut from the middle section of the compression molded bar using a Leica

TABLE 1: Preparation of HDPE/EPDM blend (polymer matrix) via melt blending method.

Polymers	Polymers content (vol%)	Ratio of HDPE to EPDM blend	Total composition
High density polyethylene (HDPE)	70	70 : 30	100
Ethylene propylene diene monomer (EPDM)	30	70 : 30	100

TABLE 2: Composition, parameters, and modification of nanocomposites prepared.

Systems	Polymer matrix	Polymer matrix content (vol%)	OMMT content (vol%)	Surface modification	Total composition
Control	HDPE/EPDM	100	—	—	100
MAPE	HDPE/EPDM	97	—	3 vol% MAPE	100
Control-50 kGy	HDPE/EPDM	100	—	Electron beam irradiation at 50 kGy	100
Control-100 kGy	HDPE/EPDM	100	—	Electron beam irradiation at 50 kGy	100
Control-150 kGy	HDPE/EPDM	100	—	Electron beam irradiation at 50 kGy	100
Control-200 kGy	HDPE/EPDM	100	—	Electron beam irradiation at 50 kGy	100
Control/OMMT	HDPE/EPDM	98, 96, 94, 92	2, 4, 6, and 8	—	100
MAPE/OMMT	HDPE/EPDM	95, 93, 91, 88	2, 4, 6, and 8	3 vol% MAPE	100
50 kGy/OMMT	HDPE/EPDM	98, 96, 94, 92	2, 4, 6, and 8	Electron beam irradiation at 50 kGy	100
100 kGy/OMMT	HDPE/EPDM	98, 96, 94, 92	2, 4, 6, and 8	Electron beam irradiation at 50 kGy	100
150 kGy/OMMT	HDPE/EPDM	98, 96, 94, 92	2, 4, 6, and 8	Electron beam irradiation at 50 kGy	100
200 kGy/OMMT	HDPE/EPDM	98, 96, 94, 92	2, 4, 6, and 8	Electron beam irradiation at 50 kGy	100

Control system = untreated or nonirradiated system; OMMT = organophilic montmorillonite; HDPE = high-density polyethylene; EPDM = ethylene propylene diene monomer; MAPE = maleic anhydride polyethylene.

ultra microtome. The specimens were collected on a trough filled with water and placed on a 200-mesh grid.

## 4. Results and Discussion

**4.1. Tensile Strength and Modulus.** The effect of different clay loading on control, MAPE, and EB irradiated systems is demonstrated in Figures 1 and 2. It is observed that the tensile strength and modulus for all the nanocomposite system began to increase up to 4 vol% of OMMT. As clay loading exceeded 4 vol%, the tensile strength and modulus of all the system were found to decrease. Similar improvement in tensile strength and modulus were also reported by previous researchers in their work on any polymer/organoclay nanocomposites [10, 11]. The primary cause for such improvement was attributed to the presence of immobilized or partially mobilized polymer phases. This is

due to the better interaction of polymer chains with clays and large number of interacting molecules due to the dispersed phase volume ratio characteristic of largely intercalated and exfoliated clay platelets as evidenced by TEM micrograph.

Tensile strength and modulus of both pristine composite and nanocomposite were further improved with MAPE agent, as evidenced in Figures 1 and 2. An increase of 33.79% and 21.52% in tensile strength and modulus were observed for MAPE system as compared to the control one where only 30.66% and 19.52% increment with 4 vol% OMMT were elucidated. This slight increase was believed due to accomplish a larger interlayer distance as the molecular structure of MAPE contains anhydride group highly attracted to OMMT sheets and a longer nonpolar fragment attracted to the HDPE/EPDM matrix.

An increment of 47.14%, 40.24%, 39.84%, and 35.74% in tensile strength were observed for EB irradiated system

TABLE 3: Interplanar spacing and diffraction angle values for control, MAPE, and EB irradiated systems.

Systems	$2\theta$ ( $^{\circ}$ )	Interplanar spacing, $d$ ( $\text{\AA}$ )
Control/4 vol% OMMT	3.570	24.73
MAPE/4 vol% OMMT	3.218	28.72
EB irradiated-100 kGy/4 vol% OMMT	2.845	31.03

with doses rate of 100, 50, 150, and 200 kGy. On the other hand, 49.54%, 31.43%, 23.56%, and 22.33% improvement in modulus were observed at unit of doses of 100, 50, 150, and 200 kGy. The tensile strength and modulus maximized at 18.51 MPa and 701.39 MPa at 4 vol% of OMMT and EB irradiation unit of a dose of 100 kGy. This indicates the formation of radiation induced cross-linking in the rubber and plastic phases as confirmed by the gel content analysis. At higher doses rate, the tensile strength decreased due to the breakdown of the network structure. Evidently, as revealed by XRD and TEM examinations, clay aggregates were broken up and acceptable uniform dispersion of clay particles can be achieved with the aid of EB irradiation.

**4.2. Elongation at Break.** A moderate increment of the elongation at break with initial incorporation of 2 vol% organoclay loading and followed by a sudden dropping of elongation at break upon 6 vol% loading of organoclay is obtained as in Figure 3. Similar results were reported before [12, 13]. The improvement in elasticity may be attributed to the plasticizing effect of the OMMT gallery and to their contribution to the formation of dangling chains but also probably to conformational effects at the clay and matrix interface [14, 15].

Further 9.8% reduction in elongation at break at optimum clay loading of 4 vol% was observed for MAPE system. This is believed to be due to the MAPE reduced chain slippage on the surface of the fillers by the reaction both of filler and matrix. As a result, the elongation at break of the MAPE nanocomposite decreased.

EB irradiated system experienced a continuous decrease in elongation at break with increased unit of dose. Reductions of 10.44%, 11.23%, 15.68%, and 21.19% at optimum clay loading of 4 vol% are obtained with unit of dose of 100, 50, 150, and 200 kGy. Generally, increasing radiation dose resulted in reduction of elongation at break of nanocomposite. Therefore, the reduction in elongation at break at higher filler loading could be attributed to the reduced segmental mobility of polymer chains, which resulted from chain degradation. Also, increasing irradiation dose led to increased cross-linked density and hence hindered the extension of chains which resulted in lower value of elongation at break. The enhanced cross-linking density may not necessarily increase the tensile properties of the polymer matrix as in the case of elongation break due to the EB irradiation-induced scission of polymer chain as well as brittleness character.

**4.3. Flexural Strength and Modulus.** The effect of organoclay loading on the flexural strength and modulus for

control, MAPE, and EB irradiated systems is illustrated in Figures 4 and 5. The same trend in flexural strength and modulus were obtained as in tensile properties. A moderate increase in flexural strength and modulus was observed for MAPE system. This indicates that this functionalization lowered the hydrophobicity of polymer matrix, imparting polarity which makes it more compatible with hydrophilic clay.

A significant increase in flexural strength and modulus were observed with EB irradiated system. An improvement of 39.27% and 39.94% was achieved at 100 kGy unit of dose. As expected, the flexural strength and modulus increased with radiation dose and continued to decrease at doses rate of 150 kGy and above. Such an increase may be attributed to the transfer of electron energy to the polymer. According to Park et al., [15], during irradiation, the electron loses kinetic energy and momentum due to interactions with the polymer. This process will lead to bond cross-linking rather than scission depending on the structure of the polymer particularly breakage of chemical bonding. In contrast, the decrease in strength and modulus at higher doses rate has been attributed to the fact that already formed cross-linked network had become smaller. This is due to the continuing of cross-linking process between the nanocomposites molecules.

**4.4. Impact Strength.** The effect of clay loading on control, MAPE, and EB irradiated system of notched Izod impact strength is depicted in Figure 6. It can be seen that a moderate increment on the impact strength for all pristine and nanocomposite system with initial incorporation of 2 vol% OMMT followed by a sudden dropping at 6 vol% of OMMT loading. This is possible due to the presence of acceptable amount of rubber compound as impact modifier along with OMMT due to the dispersion of rubber phase as spherical domains in polymer matrix, and, it contributes to improve the toughness. Similar pattern behavior was also reported in previous studies [16–18].

The presence of MAPE significantly modified the impact strength value by 19.43% as compared to control system at the optimum level of 4 vol% OMMT loading. This is believed to be due to the higher diffusion of the lower molecular weight MAPE chains through the polymer matrix and its easier penetration into the octadecylamine group formed at the OMMT surface.

EB irradiated system had obtained the highest value of impact strength as compared to control and MAPE systems. The impact strength of EB irradiated increased with clay loading but decreased as clay loading reached 6 vol% and above. For unfilled composites, an increase

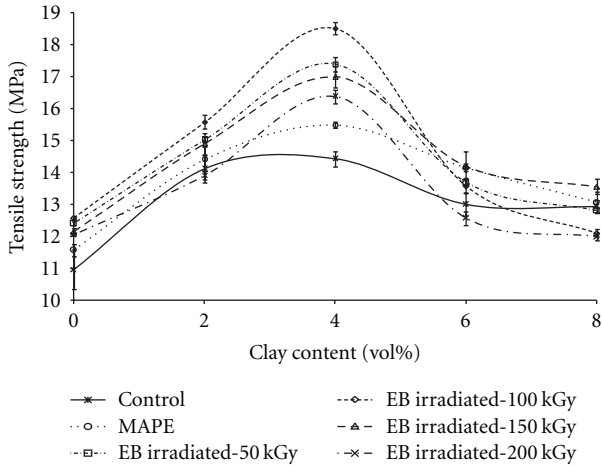


FIGURE 1: Effect of OMMT content and surface modification on tensile strength for control, MAPE, and EB irradiated systems.

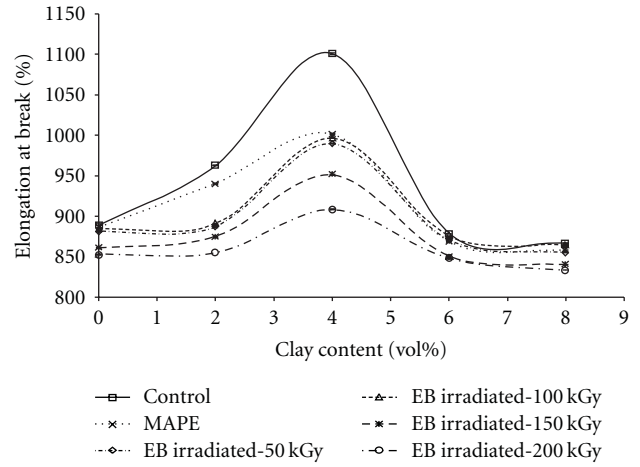


FIGURE 3: Effect of OMMT content and surface modification on elongation at break for control, MAPE, and EB irradiated systems.

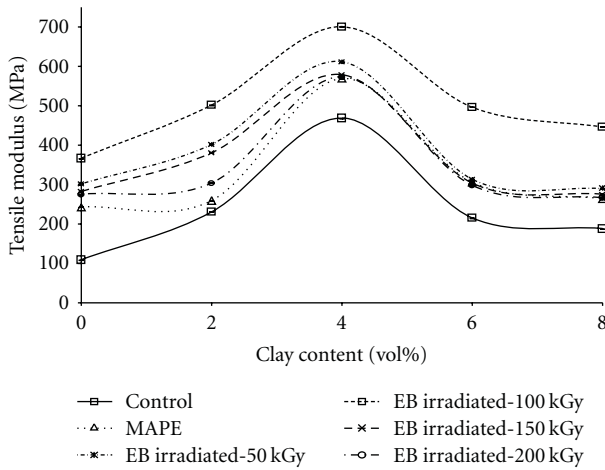


FIGURE 2: Effect of OMMT content and surface modification on tensile modulus for control, MAPE, and EB irradiated systems.

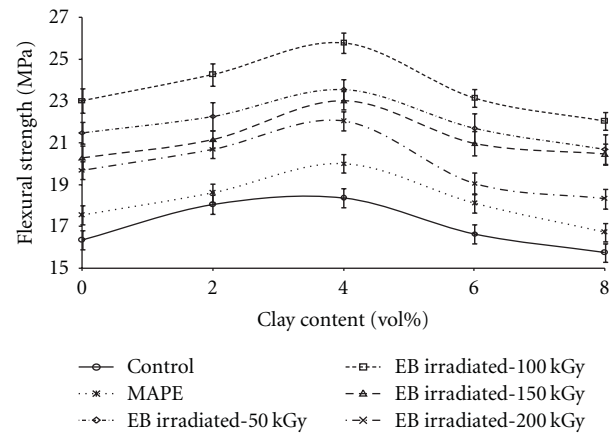


FIGURE 4: Effect of OMMT content and surface modification on flexural strength for control, MAPE, and EB irradiated systems.

of 29.51% is achieved at optimum 100 kGy unit of dose followed by 22.96%, 21.63%, and 20.01% improvement at 50, 150, and 200 kGy. Moreover, the introduction of 4 vol% OMMT loading enhanced the impact strength by 25.34%, 20.22%, 17.54%, and 14.61% at 100, 50, 150, and 200 kGy. This is might be due to the cross-linking effect in pristine composite and nanocomposite systems which resulted in three-dimensional and gel-like structures. In contrast, the reduction in impact strength has contributed to the radiation-induced scission which caused the break age of carbon-carbon bond.

**4.5. Gel Content Analysis.** The susceptibility of control composites as well as nanocomposites to cross-linking process was estimated from the gel fraction determination. The gel content of control, MAPE-treated, and irradiated samples increased with the presence of OMMT at optimum loading of 4 vol%. As shown in Figure 7, there was no gel

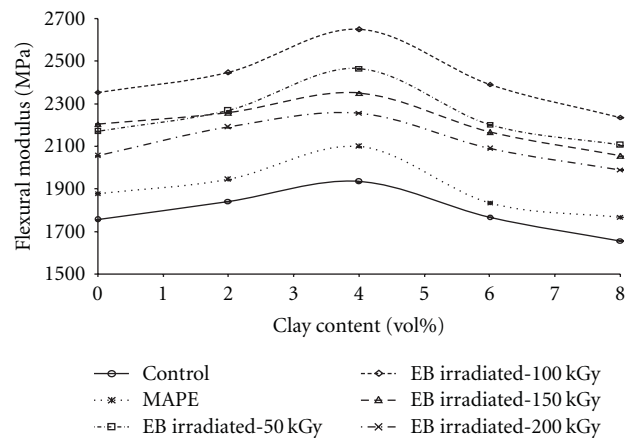


FIGURE 5: Effect of OMMT content and surface modification on flexural modulus for control, MAPE, and EB irradiated systems.

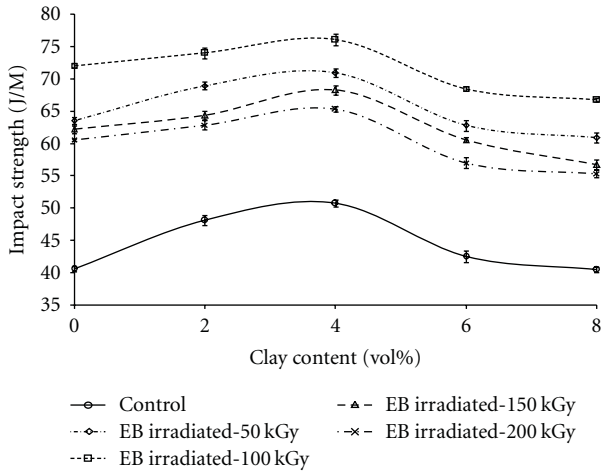


FIGURE 6: Effect of OMMT content and surface modification on impact strength for control, MAPE, and EB irradiated systems.

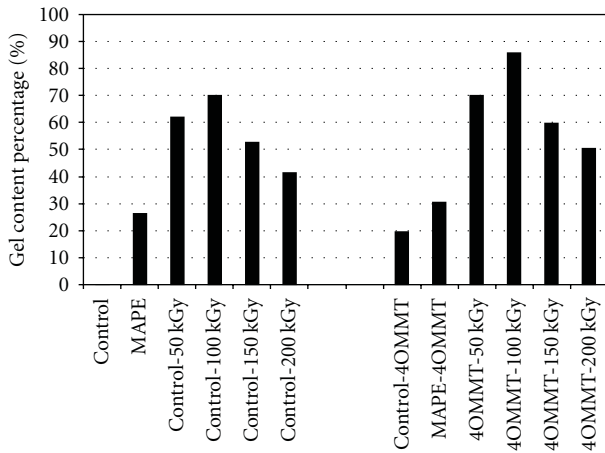
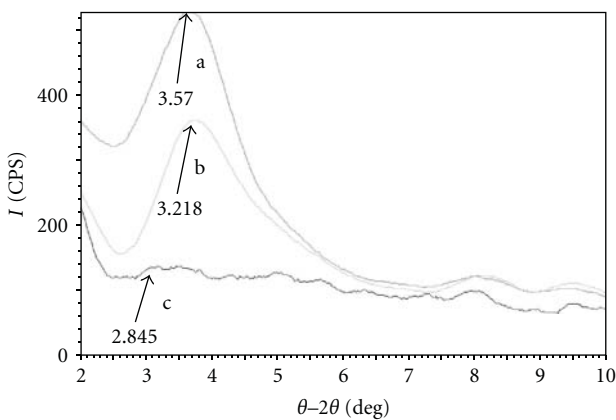


FIGURE 7: Effect of OMMT content and surface modification on gel content.



- (a) Control/4 vol% OMMT
- (b) MAPE/4 vol% OMMT
- (c) EB irradiated-100 kGy/4 vol% OMMT

FIGURE 8: XRD analysis for control, MAPE, and EB irradiated systems.

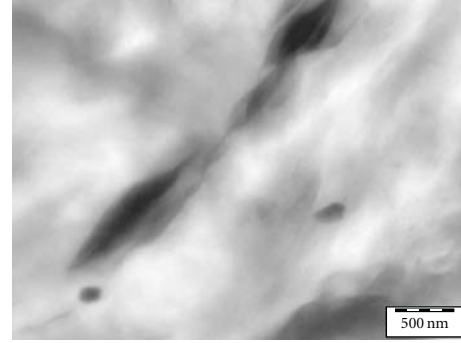


FIGURE 9: TEM micrograph of control system (untreated).

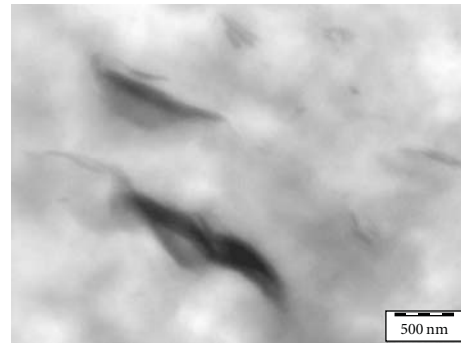


FIGURE 10: TEM micrograph of MAPE system.

formation observed for control system without the addition of OMMT. Only 20% of gel formation was obtained at 4 vol% OMMT loading. The gel percentage of pristine composite increased with OMMT loading for both untreated and treated nanocomposites. This may be attributed to a better dispersion (either partial or fully exfoliated of nano particles) in the nanocomposites. The better dispersion of nano clay resulted in a more uniform distribution of water molecules in the polymer matrix, which leads to higher gel content.

In this study, the tensile strength property was identified to affect the extent of cross-linking via gel formation. A linear relationship is obtained between the tensile strength and gel formation percentage where higher tensile strength will result in higher gel percentage. An improvement of 26.77% and 30.85%, is achieved for both unfilled composite and nanocomposites with MAPE. This shows that MAPE agent can act as plasticizer and decrease the interfacial energy between the two phases. Thus, the wetting of the OMMT with polymer matrix material has been improved. As a result, the percentage of gel content increased.

For EB irradiated system, the gel content increased rapidly by increasing the radiation unit of dose up to 100 kGy, beyond which it slowly decreased. An enhancement of 62.49%, 70.38%, 53.17%, and 41.81% was observed for pristine composite. Moreover, for nanocomposites system, an improvement of 70.44%, 86.02%, 60.25%, and 50.71% was obtained in gel formation. As EPDM and HDPE are organic polymers which are categorized radiation cross-linkable materials then such formation of cross-links upon

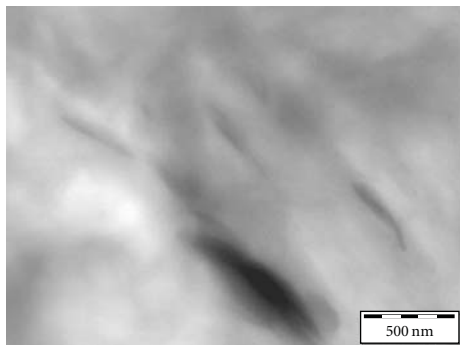


FIGURE 11: TEM micrograph of EB irradiated system.

irradiation are to be expected in them. Kim and Nho [18] mentioned that the degree of cross-linking increases with irradiation dose rate due to the increase in the concentration of the free radicals. As the cross-linking and the chain scission during irradiation occur simultaneously, the decrease in gel formation beyond unit of dose of 100 kGy might be attributed to the loosening of the network upon irradiation.

**4.6. X-Ray Diffraction Analysis (XRD).** Judging from the above results, the optimum OMMT content and EB irradiation unit of dose were taken as 4 vol% and 100 kGy. Therefore, from Section 4.6 until 4.7, the discussions were based on these optimum parameters. The changes in the interlayer distance of clay can generally be elucidated using XRD. The peak for control system (untreated or unirradiated) visibly appeared with highest intensity, indicating that most of the clay is still in the original stacking condition. This is evidenced by the highest diffraction peak which was about 24.73 Å. As discussed by Olalekan et al., 2010 [19], such a characteristic implies that nano particles were not well dispersed in the composite and thus lead to the formation of agglomerates (characteristics of nanomaterials) in the system. The diffraction angle and interplanar spacing values are summarized in Table 3.

As MAPE was added, the (001) peak still appeared, but its intensity was obviously lowered. This suggests that the diffraction peak of MAPE system has shifted toward lower angle and higher diffraction peak which were about 0.36° and 3.9 Å. This shows that the polymer matrix is ready to enter the galleries of OMMT layers resulting in broadening of XRD peak. As a result, the interlayer spacing of the clay increased, and the interaction of the layers should be weakened. However, in the current study, some clay still kept the original stacking condition with MAPE as revealed by TEM micrograph.

On the other hand, nanocomposites with exposure to EB irradiation revealed intercalated structure based on the absence of any basal reflections in the XRD patterns as evidenced by TEM image. It can be seen from Figure 8 and Table 3 that the diffraction peak was significantly shifted towards lower angle and higher diffraction peak which were about 0.83° and 6.30 Å. This suggested that the face-to-face interaction between the OMMT particles layers was

decreased at the benefit of improving the surface interaction between OMMT particles and polymer matrix. Moreover, this might also imply that the interlayer distance between the OMMT particles have become shrunk due to the formation of cross-linking structure [20]. However, the shift in the diffraction peak to lower  $2\theta$  value may not necessarily offer evidence for complete exfoliation, it may also indicate the intercalated structure, which has been confirmed by TEM examination.

**4.7. Transmission Electron Microscope (TEM).** The nanometer scale dispersion of the treated clays OMMT within the polymer matrix is further corroborated with TEM images as depicted in Figures 9, 10, and 11, respectively. The lighter region represents HDPE part and the dark region represents EPDM part whereas the dark lines corresponding to silicate layers (OMMT).

Silicate layers with bulky stacks were found to be intercalated in the polymer matrix for control and MAPE systems as evidenced in Figures 9 and 10, respectively. In the case of control system, the nonuniform of OMMT agglomerates was easily detected. Moreover, it can be seen that the dispersion of the clay particles was poor with large aggregates observed.

However, in the case of EB irradiated system as shown in Figure 11, the large aggregates of clay layers had broken down between three and four aggregates corresponding to the intercalation structure which resulted in being slightly smoother and finer as compared to control and MAPE systems. This indicates that the surface interaction between OMMT particles and HDPE/EPDM matrix had slightly improved. On the other hand, modification of clay with high-energy EB irradiation lowered the electrostatic interactions between the clay layers and enlarged their intragallery spacing thus facilitating intercalation and exfoliation with efficient dispersion of the clay [20–22]. It also demonstrated superior nanocomposites performance as discussed in the Mechanical Properties section.

**4.8. Conclusion.** The effects of MAPE and EB irradiation as cross-linking agents on the mechanical properties and gel content formation of nanocomposites were investigated in the current study. The findings are then summarized as follows.

- (1) A good balance of properties in terms of stiffness and strength was achieved at 4 vol% OMMT content.
- (2) Surface modification through electron beam (EB) radiation has induced high cross-linking as evidenced by gel content analysis, thus enhancing the mechanical properties of unfilled and filled nanocomposites systems.
- (3) A linear relationship between mechanical properties and gel content has been achieved, where the higher the mechanical properties, the greater the gel formation.

- (4) High-energy EB irradiation can be an alternative as better impact and surface modification of nanocomposites system in which it can replace the role of chemical cross-linking which has been applied in many studies for decades.

## Acknowledgments

The authors wish to express their gratitude to University Malaysia Perlis, Ministry of Higher Education (MOHE), and International Islamic Malaysia University for the financial assistance and all the staff in MRB, MINT, SIRIM, and IIUM for their help.

## References

- [1] L. Song, M. Li, Y. Hu, and H. Lu, "Study on preparation and properties of silane-crosslinked polyethylene/ magnesium hydroxide/ montmorillonite nanocomposites," *Journal of Fire Sciences*, vol. 26, no. 6, p. 498, 2008.
- [2] M. N. Satheesh Kumar and Siddaramaiah, "Studies on melamine formaldehyde (MF) loaded polyvinyl acetate—polyester nonwoven fabric composites," *Journal of Thermoplastic Composite Materials*, vol. 20, no. 3, pp. 305–322, 2007.
- [3] J. I. Choi, J. H. Kim, K. W. Lee et al., "Comparison of gamma ray and electron beam irradiations on the degradation of carboxymethylcellulose," *Korean Journal of Chemical Engineering*, vol. 26, no. 6, pp. 1825–1828, 2009.
- [4] M. Kato, H. Okamoto, N. Hasegawa, A. Tsukigase, and A. Usuki, "Preparation and properties of polyethylene-clay hybrids," *Polymer Engineering and Science*, vol. 43, no. 6, pp. 1312–1316, 2003.
- [5] J. Sharif, K. Z. Mohd Dahlan, and W. M. Z. Wan Yunus, "Radiation crosslinked natural rubber/ethylene vinyl acetate/clay nanocomposites—effect of organoclay concentration," *Journal of Nuclear and Related Technologies*, vol. 5, no. 1, pp. 65–80, 2008.
- [6] M. Zenkiewicz and J. Dzwonkowski, "Effects of electron radiation and compatibilizers on impact strength of composites of recycled polymers," *Polymer Testing*, vol. 26, no. 7, pp. 903–907, 2007.
- [7] A. Bhattacharya, "Radiation and industrial polymers," *Progress in Polymer Science*, vol. 25, no. 3, pp. 371–401, 2000.
- [8] I. Banik and A. K. Bhowmick, "Influence of electron beam irradiation on the mechanical properties and crosslinking of fluorocarbon elastomer," *Radiation Physics and Chemistry*, vol. 54, no. 2, pp. 135–142, 1999.
- [9] I. Banik, A. K. Bhowmick, V. K. Tikku, I. A. B. Majali, and R. S. Deshpande, "Effects of electron beam on the structural modification of the copolymeric and the terpolymeric fluorocarbon rubbers," *Radiation Physics and Chemistry*, vol. 51, pp. 195–204, 1998.
- [10] Q. T. Nguyen and D. G. Baird, "Preparation of polymer-clay nanocomposites and their properties," *Advances in Polymer Technology*, vol. 25, no. 4, pp. 270–285, 2006.
- [11] S. Pavlidou and C. D. Papaspyrides, "A review on polymer-layered silicate nanocomposites," *Progress in Polymer Science*, vol. 33, no. 12, pp. 1119–1198, 2008.
- [12] K. Premphet and W. Paecharoenchai, "Quantitative characterization of dispersed particle size, size distribution, and matrix ligament thickness in polypropylene blended with metallocene ethylene-octene copolymers," *Journal of Applied Polymer Science*, vol. 82, no. 9, pp. 2140–2149, 2001.
- [13] M. Pramanik and S. K. Srivastava, "EVA/Clay nanocomposite by solution blending: effect of aluminosilicate layers on mechanical and thermal properties," *Macromolecular Research*, vol. 11, no. 4, pp. 260–266, 2003.
- [14] I. Aravinda, P. Alberta, C. Ranganathaiah, J. V. Kurianb, and S. Thomas, "Compatibilizing effect of EPM-g-MA in EPDM/poly(trimethylene-terephthalate) incompatible blends," *Polymer*, vol. 45, pp. 4925–4937, 2004.
- [15] S. Park, J. Krotine, S. A. B. Allen, and P. A. Kohl, "Electron-beam hardening of thin films of functionalized polynorbornene copolymer," *Journal of Electronic Materials*, vol. 35, no. 5, pp. 1112–1121, 2006.
- [16] M. Hetzer, J. Naiki, H. Zhou, T. Poloso, and D. De Kee, "Thermal dependence of young's modulus of wood/polymer/clay nanocomposites," *Journal of Composite Materials*, vol. 43, no. 20, pp. 2285–2301, 2009.
- [17] M. Mateev and S. Karageorgiev, "The effect of electron beam irradiation and content of EVA upon the gel-forming processes in LDPE-EVA films," *Radiation Physics and Chemistry*, vol. 51, no. 2, pp. 205–206, 1997.
- [18] S. Kim and Y. C. Nho, "Effect of radiation on ultra high molecular weight polyethylene (UHMWPE)," *International Energy Atomic Agency*, vol. 1617, pp. 92–94, 2009.
- [19] S. T. Olalekan, S. A. Muyibi, Q. H. Shah, M. F. Alkhatib, and F. Yusof, "Improving the polypropylene-clay composite using carbon nanotubes as secondary filler," *Energy Research Journal*, vol. 1, pp. 68–72, 2010.
- [20] M. Bousmina, S. S. Ray, and J. Bandyopadhyay, "Thermal and thermo-mechanical properties of poly(ethylene terephthalate) nanocomposites," *Journal of Industrial and Engineering Chemistry*, vol. 13, no. 4, pp. 614–623, 2007.
- [21] M. N. Bureau, F. Perrin-Sarazin, and M. T. Ton-That, "Polyolefin nanocomposites: essential work of fracture analysis," *Polymer Engineering and Science*, vol. 44, pp. 1142–1151, 2004.
- [22] H. J. Bray, S. A. T. Redfern, and S. M. Clark, "The kinetics of dehydration in Ca-montmorillonite: an in situ X-ray diffraction study," *Mineralogical Magazine*, vol. 62, pp. 647–656, 1998.

## Research Article

# The Influence of EB-Irradiated Treatment on Enhancing Barrier Property and Crystallization Behavior of Rubber-Toughened Nanocomposites

N. A. Jamal,<sup>1</sup> H. Anuar,<sup>1</sup> and A. R. Shamsul Bahri<sup>2</sup>

<sup>1</sup> Department of Manufacturing and Materials Engineering, Faculty of Engineering, International Islamic University Malaysia, P.O. Box 10, 50728 Kuala Lumpur, Malaysia

<sup>2</sup> Crop Improvement and Protection Unit, Production Development Division, Rubber Research Institute of Malaysia (RRIM), 47000 Sungai Buloh, Selangor Darul Ehsan, Malaysia

Correspondence should be addressed to N. A. Jamal, ayuni\_jamal@yahoo.com

Received 7 November 2010; Accepted 12 March 2011

Academic Editor: Guifu Zou

Copyright © 2011 N. A. Jamal et al. This is an open access article distributed under the Creative Commons Attribution License, which permits unrestricted use, distribution, and reproduction in any medium, provided the original work is properly cited.

Electron beam (EB) irradiation technique was introduced to modify the crystallization and oxygen (O<sub>2</sub>) barrier properties of high density-polyethylene (HDPE)/ethylene propylene diene monomer (EPDM) matrix and HDPE/EPDM filled with organophilic montmorillonite (OMMT). The absorbed dose for EB-irradiation was fixed at 100 kGy. HDPE/EPDM matrix and HDPE/EPDM filled with OMMT at 4 vol% loading were prepared via melt intercalation method. It was found that the barrier resistance of HDPE/EPDM filled with OMMT against oxygen (O<sub>2</sub>) transmission was significantly enhanced by EB-irradiation absorbed dose of 100 kGy as compared to the control system. The crystallization temperature,  $T_c$ , and melting temperature,  $T_m$ , were also improved with the addition of OMMT along with the aids of EB-irradiation technique. Field emission scanning electron microscope (FESEM) revealed that the stacking condition of OMMT particles was greatly reduced by EB-irradiation treatment as evidenced by finer surface and less formation of voids.

## 1. Introduction

For many years, increasing interest has been devoted to polymeric alloys because blending is an important route for the preparation of materials with synergistic and modified properties [1, 2]. Polymer blends play an important role in achieving the required and desired properties that cannot be gained from a polymer alone. However, such a generalized concept should be more clearly defined to include the scale of the reinforcements since systems can be reinforced chemically at both microscopic and nanoscopic levels. Because of this reason, nanosized filler is introduced in order to develop nanocomposite with desired properties. The nanosized filler is based on the use of a low concentration of expandable smectite clays, such as organomontmorillonite (OMMT), in the matrix. Multifunctional benefits such as mechanical performance, oxygen permeability resistance and flame-retardant characteristics are obtained simultaneously.

Different types of filler or reinforcement can be incorporated into polymer blending system, but the selection of the silicate layer is more preferable. This is due to the fact that use of traditional filler such as talc and mica increases the mechanical properties and yet additionally increases weight which is typically considered a negative factor in designing a material. Because of this reason, clay silicate as an emerging class of filler which requires less content to achieve similar or improved mechanical and thermal properties as well as barrier property has been used in this research work [3, 4]. Small amounts of well-dispersed natural clay can lead to environmentally friendly and inexpensive plastic composites with improved specialized properties and thus produce a new class of lightweight materials. However, immiscibility or incompatibility of most polymers is a serious barrier to processing blends of polymer matrix and nanofiller. A common approach to alleviate this problem involves the addition (or the in situ formation) of an interfacially active

agent, or the so-called compatibilizer, to the blend [5]. Crosslinking agents or the so-called compatibilizer agents have been studied and applied for years due to their ability to improve both physical and chemical interactions between polymer matrix and filler and thus leads to better mechanical and thermal properties.

On the other hand, EB irradiation as one type of high-energy radiation technique has been a popular method of crosslinking instead of chemical crosslinking as it is a fast, pollution free, and simple process. Although there are other high-energy methods like gamma irradiation claimed by Croonenborghs et al. [6] to give similar effects in the investigated polymer properties, gamma irradiation is time consuming as compared to EB irradiation [7, 8]. The importance of doing research work is to make use of time and at the same time reduce the processing cost. Dubey et al. [7] stated that EB irradiation is an excellent irradiation processing compared to other electromagnetic irradiations as it induces the chemical changes in irradiated system radiation by the use of high-energy ionizing radiation. Understanding how and to what extent the characteristics of polymer blend can be altered as a function of the level of radiation exposure is crucial to predicting the performance and utility of irradiated plastics.

Although a lot of work has been done on elastomer blends, studies on the blends of EPDM and HDPE with the addition of OMMT as filler as well as its ability in gas barrier resistance are meager. Therefore, this research initiates to explore the possibilities for making engineered thermoplastic and rubber compound nanocomposite by the treatment of EB irradiation technique. The development of this nanocomposite system is aimed to vary the existing research done in this area as well as being a future and important reference particularly in enhancing the barrier property of nanocomposite.

*1.1. Overview of the Current Stage of Packaging Industry in Malaysia.* For decades, the flexible packaging consumption has grown rapidly within the global community in the United States (USA) in addition to Europe and Japan. In contrast to Malaysia, the fabrication of individual or composite material with superior barrier property is still at a critical stage. This is due to the little effort and interest implemented in the area of study and research in enhancing barrier property for commercial packaging applications as compared to other countries such as USA, Europe, and Japan. An innovation to enhance barrier property of material produced is by developing polymer nanocomposite technology which holds the key to future advances in flexible packaging.

A majority of consumer products use polymeric material or composite material in packaging areas which are commonly applied in the plastic industry. Many different types of commercial plastics, flexible and rigid, are commonly used including polypropylene (PP), nylon, polyethylene terephthalate (PET), and polyethylene (PE). Polymer matrix (HDPE/EPDM) used in this study is known to

possess good water vapor barrier properties. However, it is easily permeated by oxygen, carbon dioxide, and hydrocarbons. Thus the necessity of developing more effective barrier polymers has given rise to different strategies to incorporate and optimize the features from several components. Most schemes to improve gas barrier properties involve either the addition of higher barrier plastics via a multilayer structure (processing techniques) or by introducing filler with high aspect ratio in the polymer matrix.

Polymer nanocomposites which are constructed by dispersing a filler material into nanoparticles that form flat platelets are an ideal system for barrier property construction. These platelets are then distributed into a polymer matrix creating multiple parallel layers which force gases to flow through the polymer in a torturous path, forming complex barriers to gases and water vapor [9]. As more tortuosity is present in a polymer structure, higher barrier properties can be obtained. Once these tiny flat platelets are dispersed into the plastic, they create a path that gases must follow to move through the material, thus greatly slowing their transmission [10]. Therefore, nanocomposites would ease the transition from current packaging with metal layers and glass containers to flexible pouches or rigid plastic structures. The advantages that nanocomposites offer far outweigh the costs and concerns, and with time the technology will be further refined and processes more developed.

## 2. Experimental

*2.1. Materials.* Homopolymer high-density polyethylene (HDPE) (melt index 3–6 g/10 min, density 900 kg/cm<sup>3</sup>) supplied by Cementhai Chemicals Group, Thailand and ethylene propylene diene monomer (EPDM) supplied by Centre West Sdn Bhd, Malaysia were used as the base polymer matrix. Commercially available organophilic montmorillonite (OMMT) surface modified with 15–35 wt.% octadecylamine and 0.5 wt.% aminopropyltriethoxysilane obtained from Sigma-Aldrich Group, Malaysia was used as reinforcing agent to prepare HDPE/EPDM filled with OMMT.

*2.2. Compounding.* Melt blending of HDPE (70 vol%) and EPDM rubber (30 vol%) as polymer matrix was carried out first in an internal mixer (Thermo Haake Rheomix 600P). Then, the HDPE/EPDM blend was mixed with OMMT at HDPE/EPDM : OMMT ratio of 96 : 4 vol%. The melt mixing conditions were 150°C and at a rotor speed of 100 rpm. Prior to mixing, the polymer matrix and the nanoclays were dehumidified in a dry oven at 110°C for a period of 1 hr. Details on the preparation of HDPE/EPDM and HDPE/EPDM filled with OMMT are summarized in Tables 1 and 2.

*2.3. Specimen Preparation.* Subsequently, the blended samples were compression-molded as per ASTM-F-412 using a compression molding machine at a temperature range of 135–155°C and 8 tone metric pressures for 14 min.

TABLE 1: Preparation of HDPE/EPDM blend (polymer matrix) via melt blending method.

Polymers	Polymer content (vol%)	Ratio of HDPE to EPDM blend	Total composition
High-density polyethylene (HDPE)	70	70 : 30	100
Ethylene propylene diene monomer (EPDM)	30	70 : 30	100

TABLE 2: Preparation of HDPE/EPDM and HDPE/EPDM filled with OMMT via melt blending method.

Systems	Polymer matrix	Polymer matrix content (vol%)	Filler content, OMMT (vol%)	Total composition	Surface modification
Control	HDPE/EPDM	96	—	100	—
100 kGy	HDPE/EPDM	96	—	100	Electron beam irradiation at 100 kGy
Control	HDPE/EPDM	96	4	100	—
100 kGy/OMMT	HDPE/EPDM	96	4	100	Electron beam irradiation at 100 kGy

OMMT = organophilic montmorillonite.

TABLE 3: DSC Results for unfilled composites and nanocomposite systems.

Systems	Composite	$T_m$ (°C)	$T_c$ (°C)	$\Delta H$ (J/g)	$X_c$ (%)
Control	HDPE/EPDM	122.5	113.8	110.9	40.04
EB irradiated-100 kGy	HDPE/EPDM	130.8	118.9	132.7	47.91
Control	HDPE/EPDM/OMMT	131.8	115.7	120.5	43.5
EB irradiated-100 kGy	HDPE/EPDM/OMMT	134.1	120.7	146.2	52.78

OMMT = organophilic montmorillonite;  $T_m$  = melting temperature;  $T_c$  = crystallization temperature;  $\Delta H$  = melting enthalpy;  $X_c$  = crystallization percentage.

**2.4. High-Energy EB Irradiation.** The melt compounded samples were exposed to high-energy EB irradiation absorbed dose of 100 kGy at room temperature using a 3 MeV electron beam accelerator. The acceleration energy, beam current, and dose rate were set to 2 MeV, 2 mA, and 50 kGy/pass, respectively.

### 3. Characterization

**3.1. DSC Analysis.** DSC of each sample was performed using Perkin Elmer DSC 7. Samples with weight from 7 to 9 mg were used for the analysis. Measurements of the glass transition temperature,  $T_g$  and crystallization temperature,  $T_c$  were recorded as a function of temperature in the range of  $-80^\circ\text{C}$  to  $200^\circ\text{C}$  with heating rate of  $10^\circ\text{C}/\text{min}$ . The crystallinity % of nanocomposites was determined using the following relationship:

$$(\% \text{ crystallinity}) \quad X_c = \frac{\Delta H_f}{\Delta H_f^0} \times 100, \quad (1)$$

where  $\Delta H_f$  and  $\Delta H_f^0$  are the enthalpy of fusion of the system and the enthalpy of fusion of perfectly (100%) crystalline HDPE, respectively. For  $\Delta H_f^0$  (HDPE), a value of 277 J/g was used for 100% crystalline HDPE homopolymer [11].

### 3.2. Morphology

**3.3. Field Emission Scanning Electron Microscope (FESEM).** Examination of cryogenic fractures surface etched with nitric acid has been performed using JEOL JSM 6700F scanning electron microscope. All samples have been measured after sputter coating with carbon to avoid electrostatic charging and poor image resolution.

**3.4. Gas Barrier Test: Oxygen Transmission Rate ( $O_2TR$ ).**  $O_2TR$  of nanocomposites was analyzed in MOCON OX-TRAN 2/20 devices in accordance to the ASTM D3985 standard method. Specimens having circular shape with thickness of 1 mm and diameter of 130 mm were conditioned in a desiccator at room temperature for a minimum of 48 hours. The test conditions used in determining the  $O_2TR$  of nanocomposites were  $23^\circ\text{C}$  and 0% RH with nitrogen flow rate of 20 mL/min. The resulting permeability was recorded as  $\text{cm}^3/\text{m}^2/\text{day}$ .

## 4. Results and Discussion

**4.1. Differential Scanning Calorimeter Analysis (DSC).** The effect of OMMT loading and EB-irradiated system on the crystallization temperature,  $T_c$ , melting temperature,  $T_m$ , and crystallinity content,  $X_c$  of nanocomposite systems was analyzed by DSC thermograms. The  $T_c$ ,  $X_c$ ,  $T_m$ , and heat

of fusion,  $\Delta H$ , values for both systems are outlined in Table 3. The DSC thermograms of heating scan ( $T_m$ ,  $X_c$ , and  $\Delta H$ ) for unfilled polymer matrix and nanocomposite at 4 vol% clay loading are presented in Figures 1 and 2, respectively. Moreover, the DSC thermograms of cooling scan ( $T_c$ ) for unfilled polymer matrix and nanocomposites at 4 vol% clay loading are demonstrated in Figures 3 and 4. All the heating and cooling scans show only one endothermic as well as exothermic peak, but some differences in the peak temperatures can be revealed. Durmuş et al. [12] mentioned that a single crystallization peak observed for the nanocomposite system could be attributed to the compatibility of the polymer matrix and nanoclay. This indicates that the presence of multiple peaks (possibly attributed to  $\beta$  and  $\gamma$  phases) in the nanocomposite system may be due to the presence of either imperfect or small-sized crystallites [13].

According to Figures 2 and 4, the values of  $T_m$  and  $T_c$  for control and EB-irradiated systems at 4 vol% OMMT were shifted toward the higher temperature range. The  $\Delta H$  values were also increased as compared to the unfilled polymer matrix (refer to Table 3). Similar observations were also reported by previous researchers [12–14]. The addition of OMMT at optimum level of 4 vol% increased the  $T_m$  values for the whole nanocomposite system. The increasing in  $T_m$  values signifies that the crystal thickness in nanocomposites is more perfect than in polymer matrix [14]. Similar improvement pattern was observed for  $T_c$  and  $X_c$  values suggesting that the crystallization mechanism of neat polymer matrix was enhanced. The nucleation mechanism is responsible for the growth of crystals in nanocomposites as OMMT silicates acting as a heterogeneous nucleating agent have increased the overall crystallization rate and the crystalline fraction [15].

The presence of OMMT is identified to narrow the width of the crystalline peak which also indicates an increase in the crystallization rate of the polymer matrix chains. However, such observation is not significant for the current study. Mingliang and Demin [16] stated that the strong interaction existing between polymer matrix molecules and the layers of organoclay has resulted in immobilizing of some polymer matrix as organoclay easily absorbs the polymer molecule segments. These immobilized molecules of polymer matrix contribute to the crystallization process of nanocomposite; therefore, the crystallization of polymer matrix molecules has occurred at higher temperature thus increasing the  $T_c$  values of nanocomposite systems.

The improvement in the values of  $T_m$ ,  $T_c$ ,  $\Delta H$ , and  $X_c$  was obtained with the presence of 4 vol% OMMT by EB irradiation 100 kGy absorbed dose. Such increase can be referred to in Table 3. The increase in crystallinity percentage is believed to be due to the rearrangement of more mobile polymer chains associated with chain scission. Oxidation inhibits crosslinking of nanocomposites and leads to chain scission in the amorphous regions. As a result, the shortened segments can arrange to form new crystals and enhance the degree of crystallinity in irradiated polymer. Moreover, the increase in crystallinity percentage is also caused by fine rearrangements by radiation-induced backbone chain

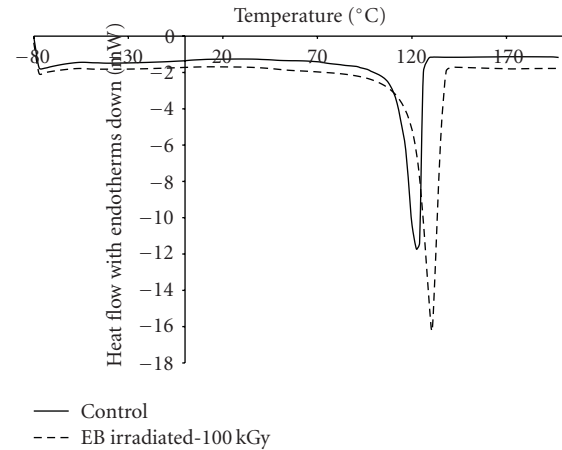


FIGURE 1: Melting endotherms of unfilled polymer matrix for control and EB-irradiated systems.

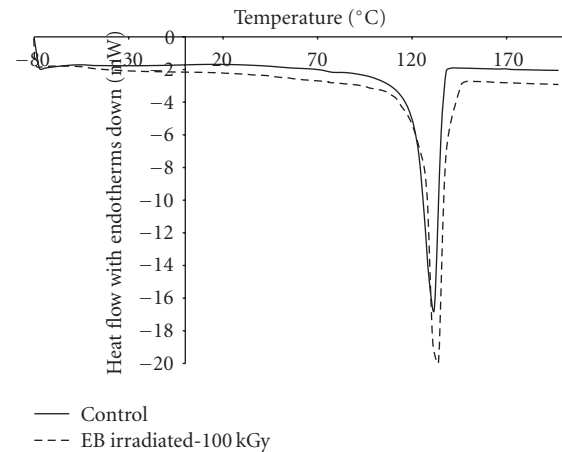


FIGURE 2: Melting endotherms of nanocomposites at 4 vol% clay loading for control and EB-irradiated systems.

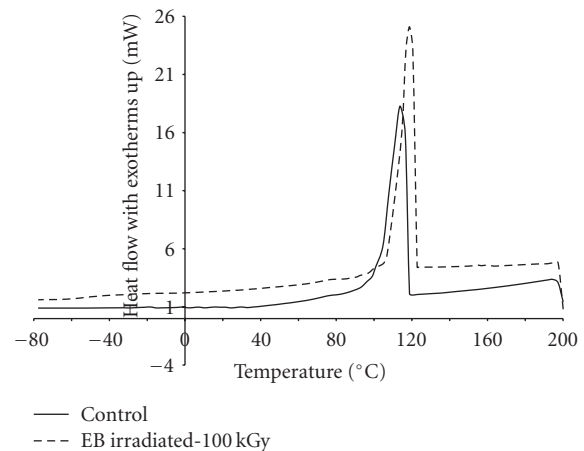


FIGURE 3: Crystallization exotherms of unfilled polymer matrix for control and EB-irradiated systems.

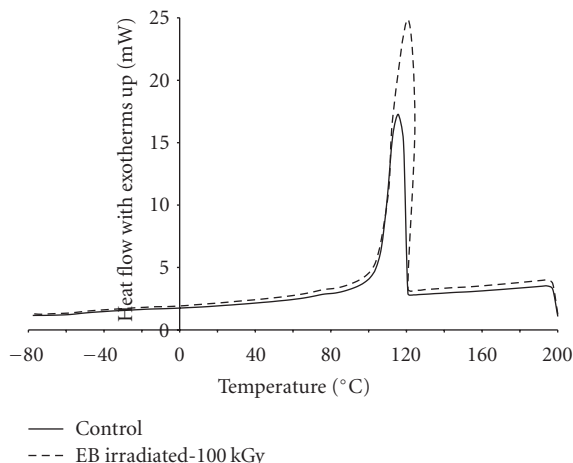


FIGURE 4: Crystallization exotherms of nanocomposites at 4 vol% clay loading for control and EB-irradiated systems.

scission in the lamellae or at the crystal-amorphous interface. Furthermore, the chain freed by scission can move easily and recrystallize [17, 18].

The melting temperatures of the irradiated samples at 100 kGy for both unfilled and 4 vol% filled composites are plotted in Figures 1 and 2. The initial high increase can be attributed to the increase of crystal domains as discussed earlier. The high peak of melting temperatures also suggest that the melting process is being kinetically arrested by the crosslinking, thus producing higher melting temperatures at the relatively fast heating rate of 10°C/min [17, 18]. It can be suggested that crosslinks in the crystal domains may play some role in enhancing the melting temperature of irradiated HDPE/EPDM filled with OMMT. Nho et al. [19] added that the penetration of electron beam shall be more effective in the loosely packed amorphous area because of the amount of oxygen required for the chain scission is higher in the amorphous region as well.

The chain scission and crosslink, therefore, take place predominantly in the amorphous area first. As the polymer chains undergo chain scission in the amorphous region, the increased chain ends provide the mobilities of the entangled chains, leading to the recrystallization of the less-ordered crystals [16, 19]. As the irradiation dose increases and reaches a certain energy level, the electron beam is now able to penetrate into the crystalline domains. The crosslinking points in the crystal domains would hold the chains, reducing the mobility gain from the thermal energy, thus enhancing the thermal stability and requiring higher thermal energy to be melted [19]. Consequently,  $T_m$  values of EB-irradiated system for both unfilled and 4 vol% OMMT-filled composites increased as depicted in Table 3 as well as in Figures 1 and 2.

**4.2. Gas Barrier Testing: Oxygen Transmission Rate ( $O_2TR$ ).** A protection of samples produced against the gas permeation is measured by using the oxygen transmission rate technique ( $O_2TR$ ). The effect of clay loading at 4 vol% as well as

crosslinking techniques on the oxygen ( $O_2$ ) permeability is summarized in Figure 7. As evidenced from Figure 7, the  $O_2$  permeability decreased with the addition of clay loading whereas the introduction of EB irradiation techniques further reduced the value of  $O_2$  permeability. It should be noted that the lower the permeation, the better the barrier. For the control system without any crosslinking treatment, no enhancement in  $O_2$  permeability was observed. Such result is in parallel with the result obtained in Section 4.1 where the higher the crystallinity percentage, the lower the value of  $O_2$  transmission. This is because the crystal regions are impervious to water and oxygen transmission while in the amorphous regions, the water and oxygen molecules are diffused easily. This concept readily accounts for the general observations that gas permeability is reduced by increasing the crystallinity and by decreasing the amorphous phase density.

In the context of gas transport, the nanocomposite is considered to consist of a permeable phase (polymer matrix) in which nonpermeable nanoplatelets are dispersed [20]. In general, there are three main factors that influence the permeability of a nanocomposite which are the volume fraction of the nanoplatelets, the orientation of nanoplatelets relative to the diffusion direction and the aspect ratio [20]. Low fractions of clays which affected in the reduction of the polymer matrix volume are required to achieve equivalent properties in comparison with the traditional composites. Therefore, a decrease of the solubility is expected in the nanocomposite due to the reduced polymer matrix volume, as well as a decrease in diffusion due to a more tortuous path for the diffusing molecules. In addition, the nanoclay layers are believed to be able to act as a trap to preserve the active oxygen foragers in the polymer while reducing the rate of oxygen transmission.

A little enhancement of 11.4% was obtained by EB irradiation absorbed dose of 100 kGy for unfilled composite whereas a significant improvement of 32% was observed with the incorporation of 4 vol% OMMT loading. This indicates that the introduction of EB-irradiation technique significantly modified the barrier property of the system with the aid of OMMT filler. The radiation-induced crosslinking could serve as oxygen scavenger by binding oxygen molecules and thus contribute to the reduction in the oxygen permeability. Moreover, the improvement in barrier property could be related to the enhanced interfacial region between the polymer matrix and OMMT particles which resulted in more homogenous structure (intercalated and exfoliated) as the hydrophobic nature of OMMT was reduced and thus providing more tortuous path. In other words, the reduction of the permeability in the platelet-reinforced nanocomposite was attributed to the lowering of the diffusion coefficient due to a more tortuous path for diffusing molecules as a result of crosslinking formation. Upon irradiation, dense network is always desired as at this stage crosslinking is more prominent than chain scission and thus resulted in improving the thermal properties. This is believed due to the decrease of the free volume that facilitates the diffusion process as the easier pathways has been created for the  $O_2$  transmission.

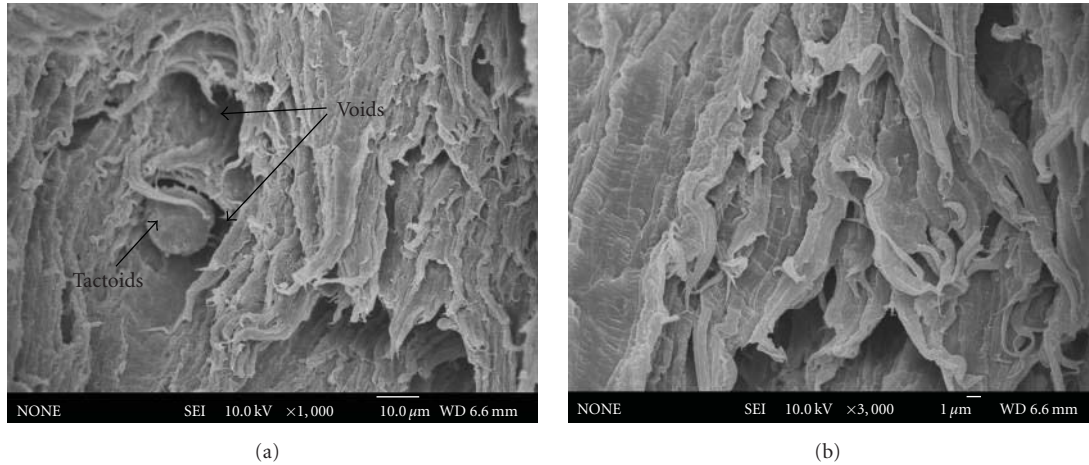


FIGURE 5: FESEM micrographs of control sample.

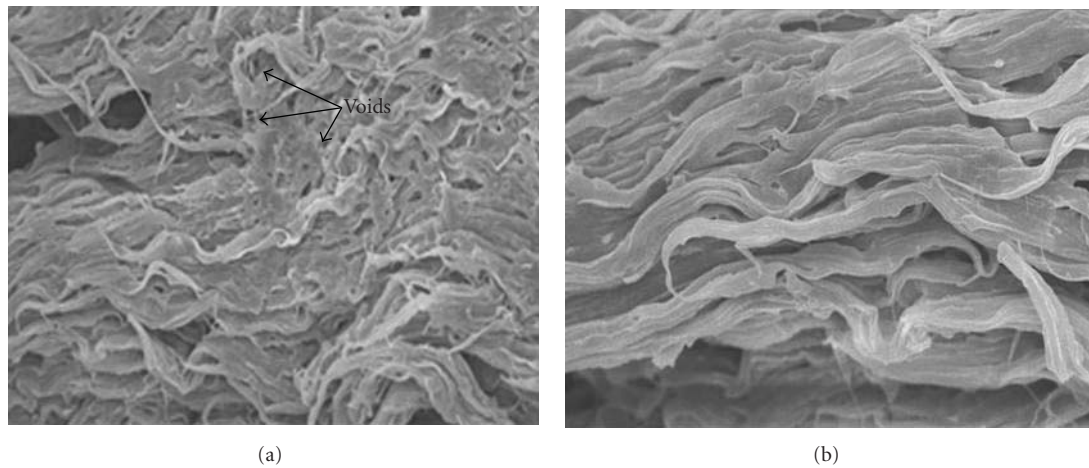


FIGURE 6: FESEM micrographs of EB-irradiated sample.

**4.3. Field Emission Scanning Electron Microscope (FESEM).** FESEM micrographs of HDPE/EPDM and HDPE/EPDM filled with OMMT for control and EB irradiated samples are presented in Figures 5 and 6, respectively. It can be seen that the formation of clay agglomerates known as tactoids could be identified in Figure 5. This is expected as polymer matrix and OMMT particles are immiscible; thus, the clay particles tend to agglomerate as a result of strong interaction existing among these particles rather than interaction with polymer matrix. This resulted in the formation of void which is bigger when compared to EB-irradiated sample as evidenced in Figure 6. The voids being observed earlier are almost covered up after treatment with EB-irradiation absorbed dose of 100 kGy. As a result, there is no presence of tactoids was observed and the clay particles seemed to move freely apart from each other. The formation of fibrils was also visible as a result of the EB irradiated treatment indicating the morphological properties of the strongly enhanced interactions [21]. This resulted in enhancement in

both crystallization as well as barrier properties as discussed in Sections 4.1 and 4.2.

## 5. Conclusion

The findings of the current study demonstrated that EB irradiation is an effective technique to enhance the crystallization and gas barrier properties of HDPE/EPDM and HDPE/EPDM filled with OMMT. Such increase indicated that crosslinking network was successfully created in this system. The addition of 4 vol% OMMT was found to further enhance the thermal and gas barrier properties of HDPE/EPDM as clay particles were able to create more tortuous path due to its impermeable nature towards gases. FESEM micrographs revealed that the formation of bigger voids and tactoids for control system was greatly improved by EB irradiation treatment as voids and tactoids became less visible which resulted in finer and smoother structure.

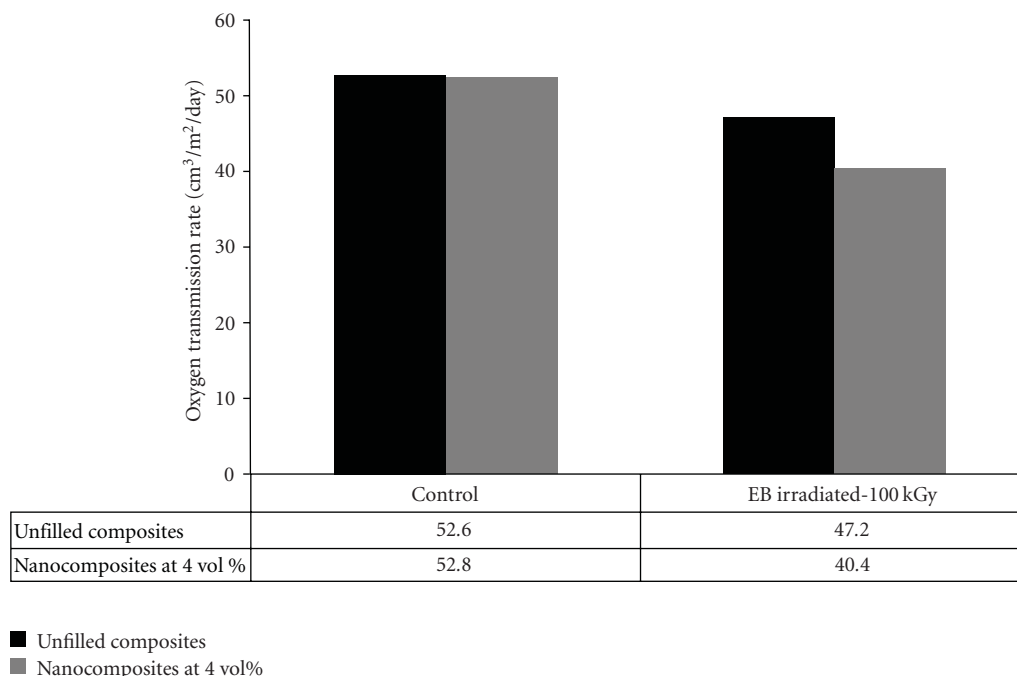


FIGURE 7: Oxygen transmission rate ( $O_2TR$ ) of unfilled composites and nanocomposites for control and EB-irradiated systems.

## Acknowledgments

The authors wish to express their gratitude to the University of Malaysia, Perlis, Ministry of Higher Education (MOHE) and International Islamic University Malaysia for the financial assistance and all the staffs in MRB, MINT, SIRIM, and IIUM for their help in making this study succeed.

## References

- [1] Li. H. Lin, H. J. Liu, and N. K. Yu, "Morphology and thermal properties of poly(L-lactic acid)/ organoclay nanocomposites," *Journal of Applied Polymer Science*, vol. 106, no. 1, pp. 260–266, 2007.
- [2] C. Li and T. W. Chou, "Multiscale modeling of compressive behavior of carbon nanotube/polymer composites," *Composites Science and Technology*, vol. 66, no. 14, pp. 2409–2414, 2006.
- [3] H. R. Dennis, D. L. Hunter, D. Chang et al., "Effect of melt processing conditions on the extent of exfoliation in organoclay-based nanocomposites," *Polymer*, vol. 42, no. 23, pp. 9513–9522, 2001.
- [4] D. F. Eckel, M. P. Balogh, P. D. Fasulo, and W. R. Rodgers, "Assessing organo-clay dispersion in polymer nanocomposites," *Journal of Applied Polymer Science*, vol. 93, no. 3, pp. 1110–1117, 2004.
- [5] H. F. Guo, S. Packirisamy, N. V. Gvozdic, and D. J. Meier, "Prediction and manipulation of the phase morphologies of multiphase polymer blends: 1. Ternary systems," *Polymer*, vol. 38, no. 4, pp. 785–794, 1997.
- [6] B. Croonenborghs, M. A. Smith, and P. Strain, "X-ray versus gamma irradiation effects on polymers," *Radiation Physics and Chemistry*, vol. 76, no. 11-12, pp. 1676–1678, 2007.
- [7] K. A. Dubey, Y. K. Bhardwaj, C. V. Chaudri, and S. Sabharwal, "Role of blend morphology in the radiation processing of SBR-EPDM blends," *BARC Newsletter*, vol. 273, pp. 92–93, 2005.
- [8] M. F. Vallat, S. Marouani, S. Perraud, and N. M. Patlan, "Crosslinked blends and coextruded films by electron beam," *Nuclear Instruments and Methods in Physics Research B*, vol. 236, no. 1-4, pp. 141–144, 2005.
- [9] T. D. Matthew, "Innovative barrier technologies boost viability of pet beer bottles," *Modern Plastics*, pp. 26–27, 2000.
- [10] P. Demetrakakes, "Nanocomposites raise barriers, but also face them: clay-based additives increase the barrier qualities of plastics, but obstacles to commercialization must be overcome," *Nanocomposite Materials*. In press.
- [11] Y. Lei, Q. Wu, and C. M. Clemons, "Preparation and properties of recycled HDPE/clay hybrids," *Journal of Applied Polymer Science*, vol. 103, no. 5, pp. 3056–3063, 2007.
- [12] A. Durmuş, M. Woo, A. Kaşgöz, C. W. Macosko, and M. Tsapatsis, "Intercalated linear low density polyethylene (LLDPE)/clay nanocomposites prepared with oxidized polyethylene as a new type compatibilizer: structural, mechanical and barrier properties," *European Polymer Journal*, vol. 43, no. 9, pp. 3737–3749, 2007.
- [13] J. Bandyopadhyay, S. S. Ray, and M. Bousmina, "Thermal and thermo-mechanical properties of poly(ethylene terephthalate) nanocomposites," *Journal of Industrial and Engineering Chemistry*, vol. 13, no. 4, pp. 614–623, 2007.
- [14] J. W. Lim, A. Hassan, A. R. Rahmat, and M. U. Wahit, "Mechanical behaviour and fracture toughness evaluation of rubber toughened polypropylene nanocomposites," *Plastics, Rubber and Composites*, vol. 35, no. 1, pp. 37–46, 2006.
- [15] T. Y. Tsai, "Templated synthesis of nanoparticles, nanoporous materials and nanowires," *Chemical Information Monthly*, vol. 14, no. 10, pp. 59–69, 2000.
- [16] G. E. Mingliang and J. Demin, "Preparation and properties of polypropylene/clay nanocomposites using an organoclay

- modified through solid state method," *Journal of Reinforced Plastics and Composites*, vol. 28, no. 5, pp. 228–230, 2009.
- [17] S. Kim and Y. C. Nho, "Effect of radiation on ultra high molecular weight polyethylene (UHMWPE)," *International Energy Atomic Agency*, vol. 1617, pp. 93–94, 2009.
- [18] S. Barus, M. Zanetti, P. Bracco, S. Musso, A. Chiodoni, and A. Tagliaferro, "Influence of MWCNT morphology on dispersion and thermal properties of polyethylene nanocomposites," *Polymer Degradation and Stability*, vol. 95, no. 5, pp. 756–762, 2010.
- [19] Y. C. Nho, S. M. Lee, and H. H. Song, "Modification of microstructures and physical properties of ultra high molecular weight polyethylene by electron beam irradiation," *International Energy Atomic Agency*, vol. 1617, pp. 101–103, 2009.
- [20] G. Choudalakis and A. D. Gotsis, "Permeability of polymer/clay nanocomposites: a review," *European Polymer Journal*, vol. 45, no. 4, pp. 972–980, 2009.
- [21] H. M. Dahlan, M. D. K. Zaman, and A. Ibrahim, "Liquid natural rubber (LNR) as a compatibiliser in NR/LLDPE blends—II: the effects of electron-beam (EB) irradiation," *Radiation Physics and Chemistry*, vol. 64, no. 5-6, pp. 429–436, 2002.

## Research Article

# A New Ultra Fast Conduction Mechanism in Insulating Polymer Nanocomposites

M. Xu,<sup>1</sup> G. C. Montanari,<sup>2</sup> D. Fabiani,<sup>2</sup> L. A. Dissado,<sup>3</sup> and A. Krivda<sup>4</sup>

<sup>1</sup> State Key Laboratory of Electrical Insulation and Power Equipment, Xi'an Jiaotong University, West Xianning Road 28, Xi'an 710049, China

<sup>2</sup> Department of Electrical Engineering, University of Bologna, Viale Risorgimento, 2-40136, Bologna, Italy

<sup>3</sup> Department of Engineering, University of Leicester, University Road, Leicester LE17RH, UK

<sup>4</sup> ABB Switzerland Ltd, Corporate Research, CH-5405 Baden-Daettwil, Switzerland

Correspondence should be addressed to M. Xu, xumman@mail.xjtu.edu.cn

Received 8 February 2011; Accepted 13 March 2011

Academic Editor: Guifu Zou

Copyright © 2011 M. Xu et al. This is an open access article distributed under the Creative Commons Attribution License, which permits unrestricted use, distribution, and reproduction in any medium, provided the original work is properly cited.

A brand new phenomenon, namely, electrical conduction via soliton-like ultra fast space charge pulses, recently identified in unfilled cross-linked polyethylene, is shown for the first time to occur in insulating polymer nanocomposites and its characteristics correlated with the electromechanical properties of nanostructured materials. These charge pulses are observed to cross the insulation under low electrical field in epoxy-based nanocomposites containing nanosilica particles with relative weights of 1%, 5%, 10%, and 20% at speeds orders of magnitude higher than those expected for carriers in insulating polymers. The characteristics of mobility, magnitude and repetition rate for both positive and negative charge pulses are studied in relation to nanofiller concentration. The results show that the ultra fast charge pulses (packets) are affected significantly by the concentration of nanoparticles. An explanation is presented in terms of a new conduction mechanism where the mechanical properties of the polymer and movement of polymer chains play an important role in the injection and transport of charge in the form of pulses. Here, the charge transport is not controlled by traps. Instead, it is driven by the contribution of polarization and the resultant electromechanical compression, which is substantially affected by the introduction of nanoparticles into the base polymer.

## 1. Introduction

Insulating polymers are a category of organic materials widely used in electrical apparatus, exhibiting low charge carrier concentration and mobility (usually  $10^{-16}$ – $10^{-14}$   $\text{m}^2 \text{V}^{-1} \text{s}^{-1}$ ), thus low electrical conductivity, even at high fields [1]. Carriers in insulating polymers are introduced by impurities and contaminants, as well as by charges injected from the electrode-insulation interface. When the electrical field applied to the polymer is higher than the threshold for space charge accumulation, charge would be injected into the bulk material from the interface of polymer-electrode and accumulate [2–4], forming homocharge or heterocharge. Based on this traditional conduction mechanism, the current is a continuous flow of carriers, which gradually approaches a steady state value at a given time after the onset of voltage application.

Recently, a brand new phenomenon of charge transport was discovered in some insulating polymers (e.g., minicable with polyethylene insulation [5, 6] and nanostructured epoxy-based material [7]) at relatively low electrical fields, through the use of an ultra fast space charge acquisition system and a conduction current measurement apparatus endowed of low-pass filter [8]. Charge pulses (packets) are observed to travel very rapidly through the insulation bulk with mobility 4 to 5 orders of magnitude higher than that for conventional conduction. These repetitive charge packets have magnitudes that are almost independent of field and temperature and do not show appreciable pulse distortion and attenuation during transit, thus behaving as solitons. Such a mechanism should be, therefore, different from that responsible for traditional charge transportation by hopping through localized states (traps). Previous research work has indicated that this new conduction mechanism could

TABLE 1: Specimen description.

Specimen	Weight percentage of Nano-SiO <sub>2</sub> in epoxy resin
No. 0	0%
No. 1	1%
No. 5	5%
No. 10	10%
No. 20	20%

be associated with the electromechanical compression of the polymer and polarization mode. It is known that the morphology of a polymer can be modified by nanofillers (e.g., nanoparticles, nanowires, and nanolayers), due to the large interface interaction (surface to volume ratio) [9], so that the mechanical, thermal, and electrical properties of the polymer could be affected significantly by the introduction of nanofillers [10, 11].

Here, we report evidence for the presence of such soliton-like ultra fast space charge packets in epoxy-based nanocomposites. The relationship between polymer structure and mechanical property is discussed, and the influence of nanoparticles on the characteristics of the ultra fast charge pulses is investigated in order to determine whether the relationship expected of a mechanism based on electromechanical compression is viable. The experimental results show that the mechanical properties of the nanocomposite material do indeed affect the ultra fast charge packet conduction to a great extent.

## 2. Experiments

**2.1. Materials.** Flat specimens of pure epoxy resin and nano-filled composites were prepared. The base epoxy resin (bisphenol A) and the nanocomposites were cured by anhydride hardener with flexibilizer (20 wt%). The specimens were 1 mm in thickness. The diameter of the filling particles, nanosilica (SiO<sub>2</sub>), was about 25 nm with a density of  $2.1 \times 10^3 \text{ kg m}^{-3}$ . The description of the specimens is reported in Table 1.

Epoxy resin and nano-SiO<sub>2</sub> (Nanopox masterbatch) were mixed for 5 to 10 minutes at 65°C with four blades stainless steel propeller at the speed of 240 r/min. The hardener was added and mixed under the same conditions for another 15 minutes. In the end, the cure accelerator was added into the mixture. The mixture was degassed at about 200 Pa pressure at 65°C. Casting was performed into preheated stainless steel moulds. After casting, degassing was performed once again to remove any air bubbles created during the casting process. Curing was carried out at 80°C for 4 hours and postcuring was performed at 120°C for 10. The casting parameters used in sample preparation follow procedures recommended by epoxy manufacturers within the permitted range.

**2.2. Test Device.** Structure of the specimen (nanoparticle dispersion) was observed by Scanning Electron Microscope (SEM) EL20 produced by FEI corporation. The specimen was broken in liquid nitrogen and metallized on the fracture

section for observation. Space charge accumulation was investigated through the Pulsed Electro Acoustic (PEA) technique. The measurements were performed under the electrical field of  $10 \text{ kV mm}^{-1}$  and a temperature of 70°C. The ultra fast charge packets were recorded by means of Digital Signal Averager, which can acquire, average, and store PEA signals at a very high rate (up to several MHz). Therefore, the space charge profiles were recorded every 0.02 s, each profile being an average of 100 acquired PEA signals.

## 3. Results and Discussion

The dimension and dispersion of nanoparticles in epoxy resin are shown in Figure 1. The observed specimen is no. 10 (10% of nanoparticles). It could be seen that nanoparticles are dispersed evenly in the base polymer with the average diameter less than 80 nm. The interface of nanoparticles and base polymer is not very clear which indicates the particles are coated well by the polymer chains. The abundant microtopography in the fracture section presents the ductile rupture of the specimen. This kind of structure is beneficial to the improvement of mechanical property.

The space charge patterns of pure and nanofilled composites during the first 30 seconds of polarization are shown in Figure 2. The polarity of charge is indicated by different colors, that is, cold colors for negative charge (e.g., black, blue, purple) and warm colors for positive charge (e.g., red, yellow, green). Hence, the distribution, density, and dynamic of the charge can be found in the figure reporting the charge pattern. Heterocharge was accumulated at the electrodes of opposite polarity in all the specimens within the first few seconds of polarization (4~10 s). This phenomenon is associated with the injection of charge pulses at one electrode, which then cross the bulk insulation at high speed and accumulate at the counterelectrode interface due to a delay in charge extraction.

The existence of ultra fast space charge pulses is evidenced in specimen no. 0 (the pure Epoxy resin) by the evolution of charge profiles, shown in Figure 3, Figures 3(a)–3(c) for the positive charge and Figures 3(d)–3(f) for the negative charge. The charge pulse (packet) is labeled by a circle. At time  $t = 0 \text{ s}$ , the charge pulse appears near one electrode and begins to move towards the counterelectrode. The relative time is indicated on the top of each profile to highlight the transport velocity of each charge packet. It can be seen that positive charge pulses move slower than negative pulses. In pure epoxy resin it takes about 0.08 s and 0.06 s to cross through the bulk insulation (1 mm thick) for positive and negative fast charge packet respectively. It can be seen also that the shape of the charge pulse does not change appreciable, as a function of traveling time. Ultra fast space charge profiles obtained under the same measurement conditions for specimens nos. 1, 5, 10, and 20 containing nanoparticles are depicted in Figures 4 to 7. All the fast charge pulses have similar features to those detected in pure epoxy resin, that is, the shape of the charge profile does not change and the pulse mobility remains constant during transit of the bulk insulation. However, the transit

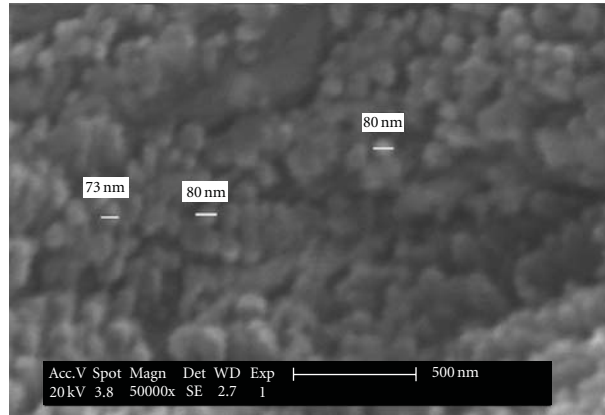


FIGURE 1: SEM image of nanocomposite (specimen no. 10,  $\times 50000$ ).

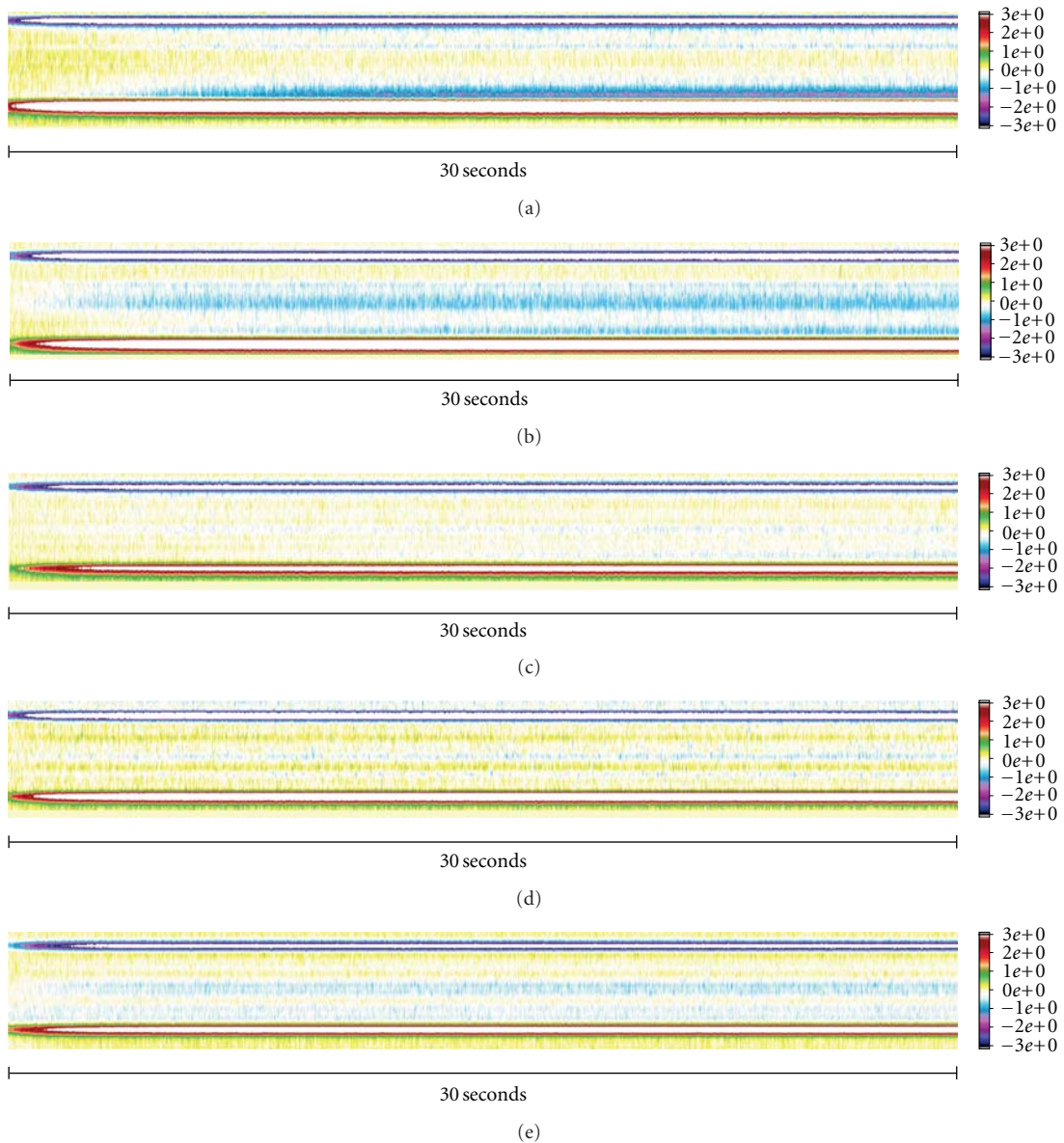


FIGURE 2: Charge patterns of specimens in the first 30 seconds of polarization. (a) No. 0, (b) no. 1, (c) no. 5, (d) no. 10, and (e) no. 20.

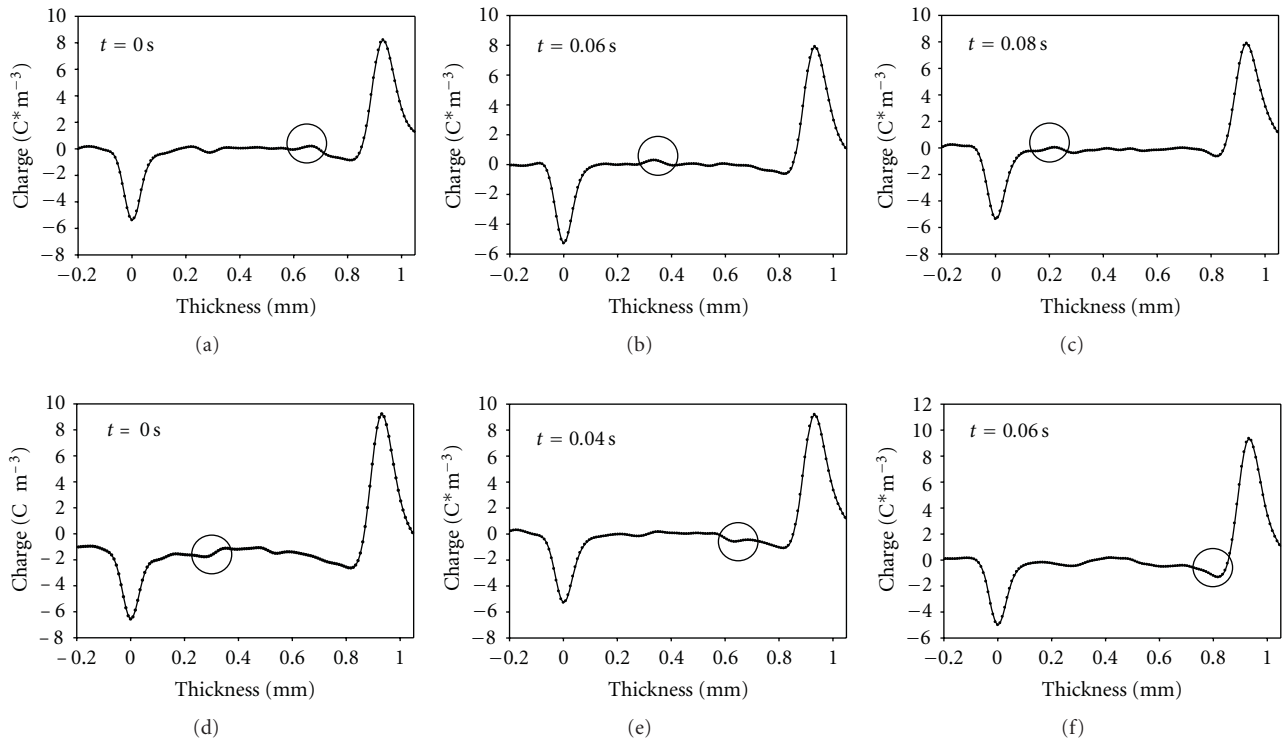


FIGURE 3: Evolution of charge profiles in specimen no. 0 under an electrical field of 10 kV/mm and temperature of 70°C for a positive charge pulse (a)–(c) and negative charge pulse (d)–(f).

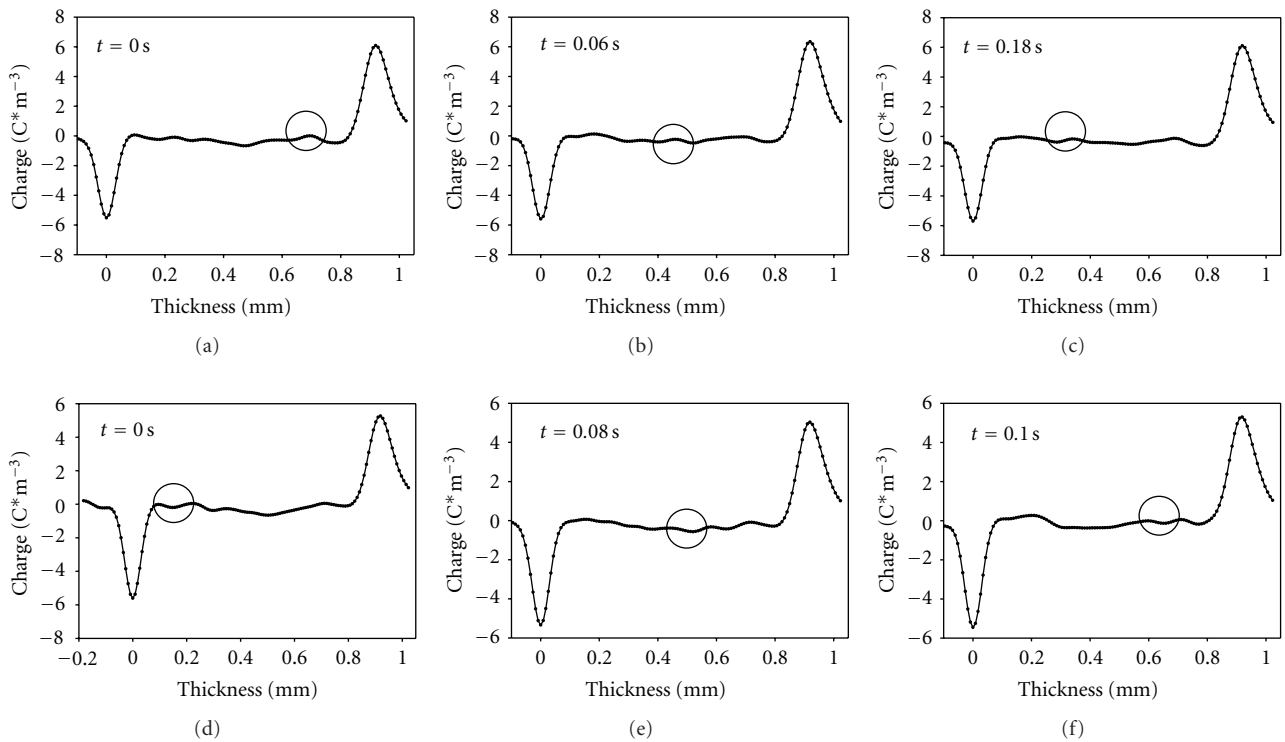


FIGURE 4: Evolution of charge profiles in specimen no. 1 under an electrical field of 10 kV/mm and temperature of 70°C for a positive charge pulse (a)–(c) and a negative charge pulse (d)–(f).

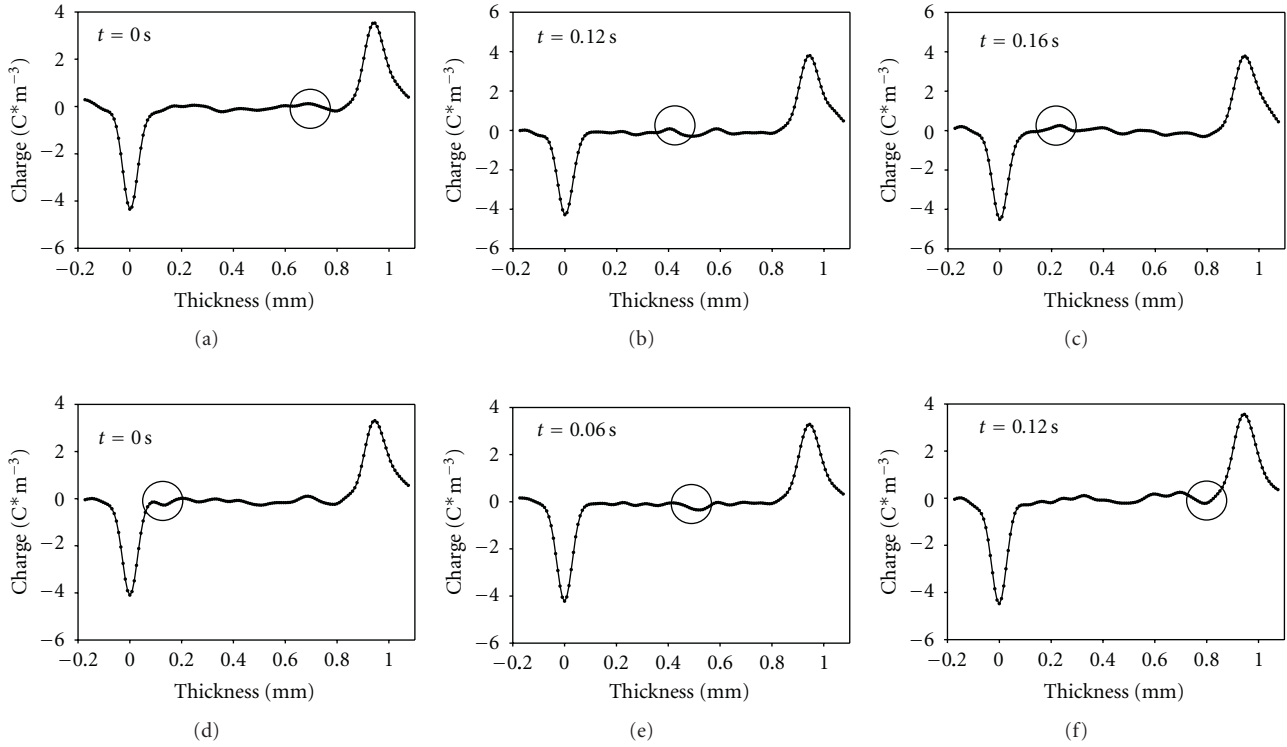


FIGURE 5: Evolution of charge profiles in specimen no. 5 under an electrical field of 10 kV/mm and temperature of 70°C for a positive charge pulse (a)–(c) and a negative charge pulse (d)–(f).

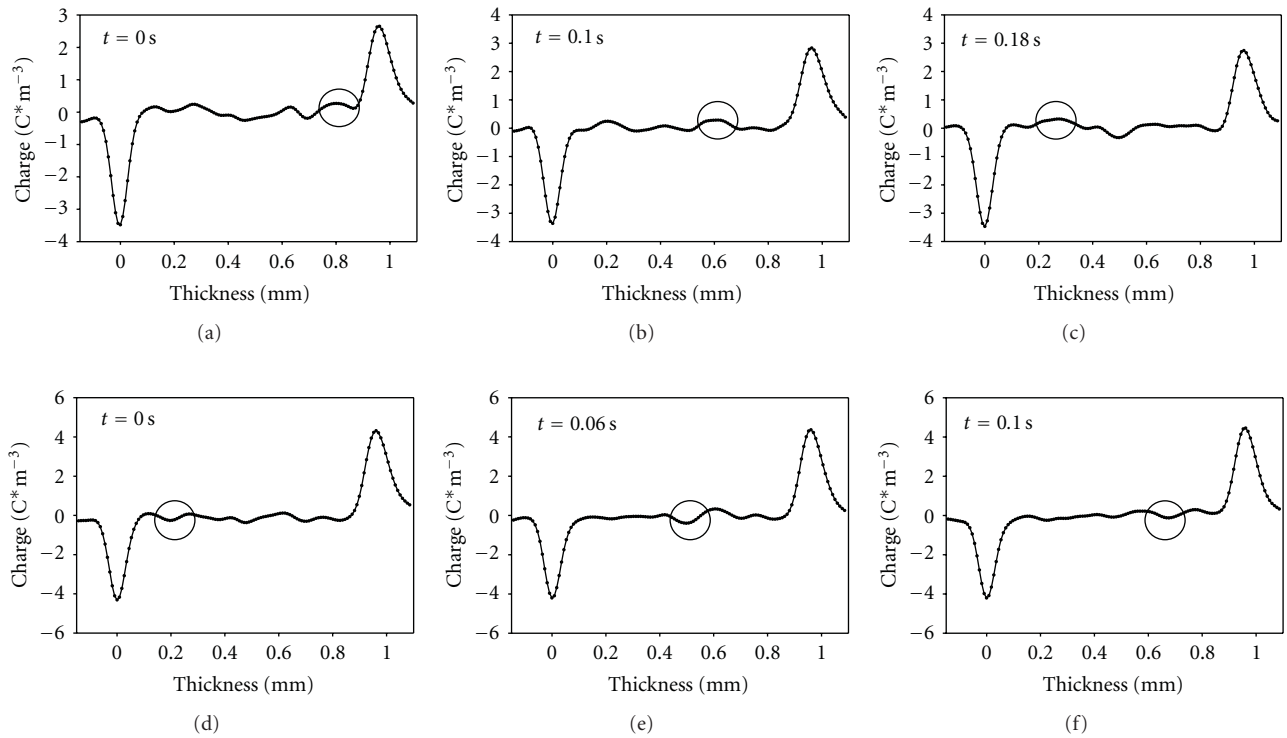


FIGURE 6: Evolution of charge profiles in specimen no. 10 under an electrical field of 10 kV/mm and temperature of 70°C for a positive charge pulse (a)–(c) and a negative charge pulse (d)–(f).

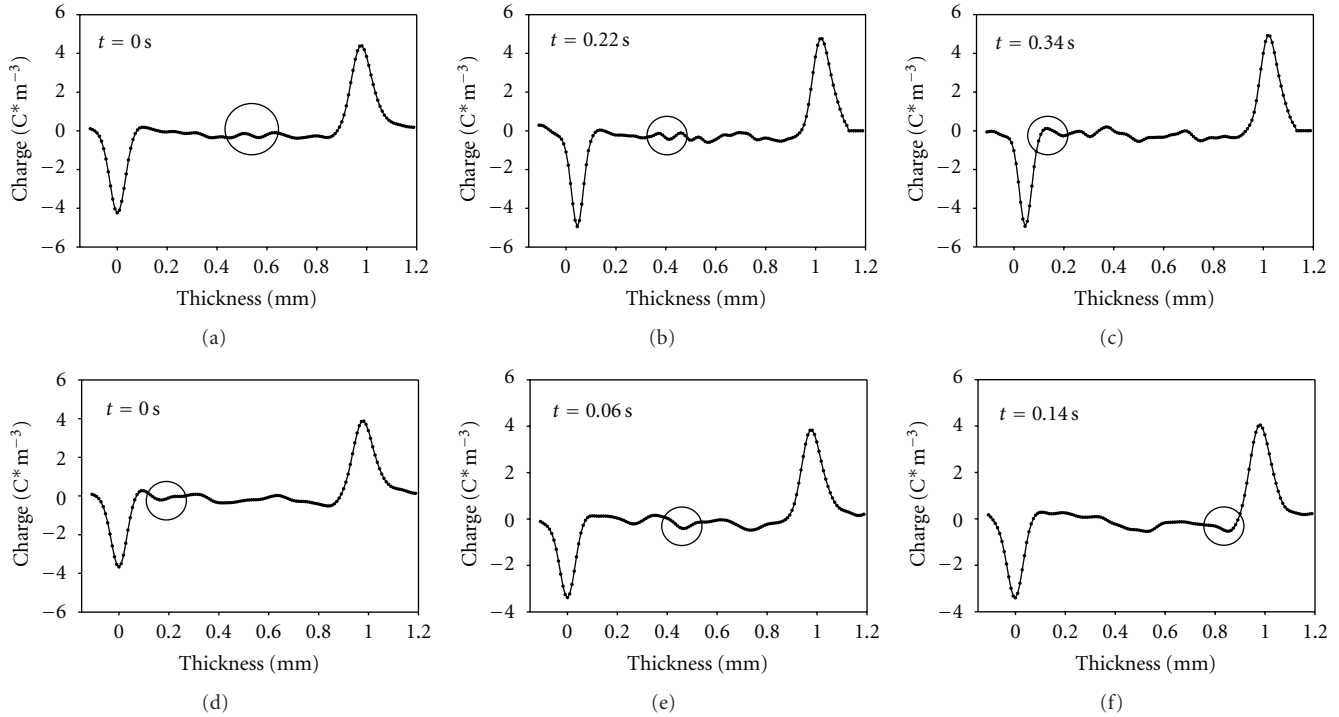
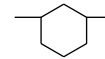


FIGURE 7: Evolution of charge profiles in specimen no. 20 under an electrical field of 10 kV/mm and temperature of 70°C for a positive charge pulse (a)–(c) and a negative charge pulse (d)–(f).

time in nanocomposites is longer than that in pure epoxy resin. In particular, it takes 0.34 s and 0.14 s for positive and negative charge pulses to cross the material containing 20% nanoparticles compared to the 0.08 s and 0.06 s of the pure epoxy. These figures show clearly that the transport of positive and negative charge pulses is affected significantly by the presence of nanofillers.

The injection and transport of soliton-like charge pulses in pure epoxy resin can be explained by considering the effect of the electromechanical compression at the electrode-insulation interface. Figure 8 shows a sketch explaining such charge injection mechanism. According to Lewis et al. [12], the applied electric field produces a precompression at the electrode-polymer interface. A critical amount of charge,  $\Delta Q$ , needs to be available at the electrode-insulation interface in order to create an extracompression of the polymer chains against the electrode suitable for the charge  $\Delta Q$  to tunnel into the chain in the form of a charge layer. After charge injection, the electric field decreases by  $\Delta E$ , leading the polymer chain to release, thus stopping further charge injection while simultaneously carrying the layer of charge into the polymer. Charge pulse transport occurs through the polymer chain displacements produced by electromechanical compression and electrical polarization at the charged boundary  $\Delta Q$ ,  $\Delta E$ , which bring polymer chains close enough to allow for charge tunneling or the opening up of free space [13], thereby allowing the coherent advance of the charge layer. This mechanism allows the charge to be injected as pulses of magnitude  $\Delta Q$  and transported in the bulk insulation [7, 8, 13] as a coherent unit that is, a charge soliton.

The results obtained here for the pure epoxy resin are different to those reported previously dealing with ultra fast space charge transport in nanostructured epoxy-based materials [7]. In [7], ultra fast charge pulses could not be found in the pure epoxy material unless an external compression was applied. To understand the difference in behavior, two aspects about the materials must be highlighted. On one hand, the main chemical structures (shown in Figure 8) of the two kinds of base epoxy resin are different. The epoxy studied in the former paper is Aldrich cycloaliphatic-epoxy. The typical chemical structure is summarized in Figure 9(a). This is a kind of epoxy resin with short molecular chain and rigid groups in the main chain, such as the ring structure



and ester bond ( $-\text{COO}-$ ). The glass transition temperature  $T_g$  is very high (usually higher than 200°C [14]). Hence, molecular chains cannot move easily for lack of flexibility, that is, it is difficult to compress the polymer as required for the charge soliton mechanism. In contrast, the epoxy resin studied here is a bisphenol A epoxy, see Figure 9(b), which has longer polymer chains. There are several different kinds of flexible bonds in the main chain, such as carbon-carbon bonds (C–C) and ether bonds ( $-\text{O}-$ ), which will provide more flexibility to the molecular chain. In addition, the curing procedures of the two epoxy-based materials are different. The epoxy resin studied previously is solidified by means of radiation without hardener, according to which,

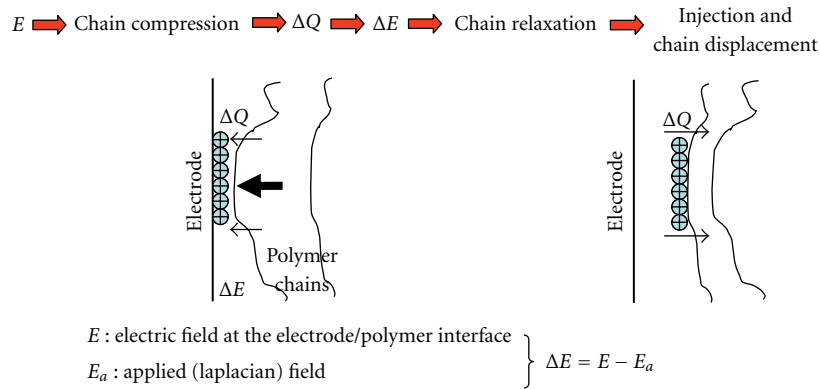


FIGURE 8: Soliton injection mechanism due to electromechanical compression of the electrode-insulation interface.

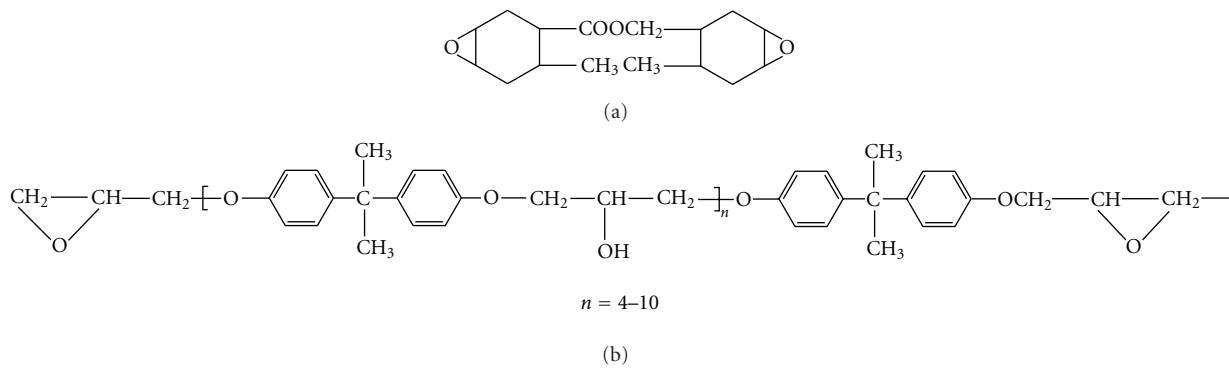


FIGURE 9: Chemical structures of two kinds of epoxy resin (a) cycloaliphatic-epoxy, (b) bisphenol A epoxy.

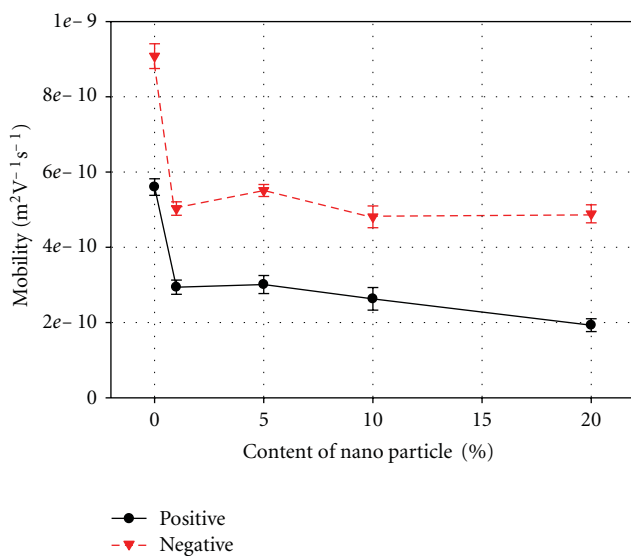
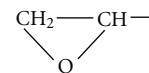


FIGURE 10: Charge mobility of positive and negative charge pulses in pure epoxy resin and epoxy-based nanocomposites (90% confidence interval).

the solidification of epoxy resin involved the ring-opening reaction at the epoxide groups



of chains, cross-linked with each other. Therefore, the structure of the epoxy is tight and polymer chains are close to each other. In the specimen investigated here, the epoxy hardening system consists of hardener (Anhydride) and 20 wt% flexibilizer. The epoxy chains are connected by small molecules. It is because of the presence of so many small molecules dispersed in the polymer chains that there is enough free volume for chains to move and change position, so that the  $T_g$  of this kind of epoxy resin is rather low (about 20°C). As mentioned above [13], it has been proposed that the generation and transport of ultra fast charge pulses in polymers is related to electromechanical compression and movement of polymer chains undergoing the corresponding relaxation process (e.g.,  $\beta$  and  $\gamma$  relaxation in polyethylene [5, 6, 8]). Hence, the more flexible the molecular chain is, the easier ultra fast charge pulses are generated.

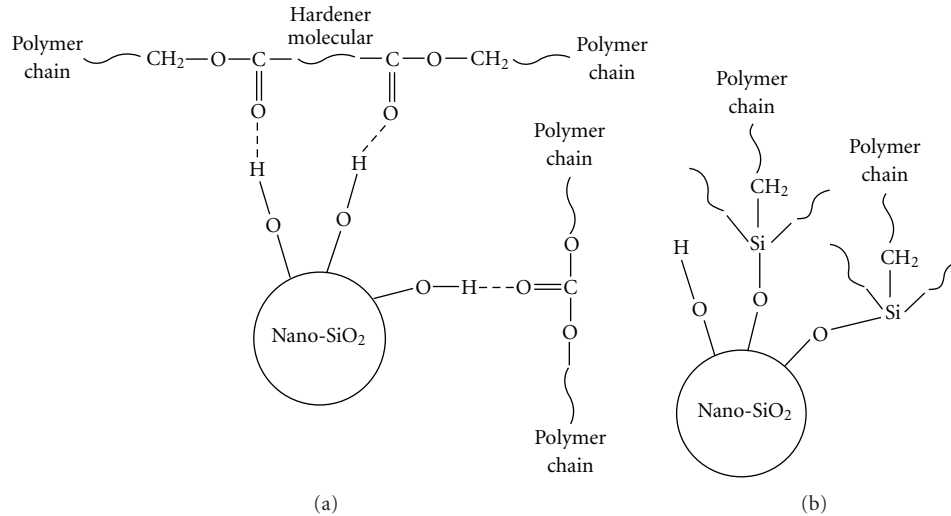


FIGURE 11: Cross-link structure built by nanoparticle in polymer chain (a) crosslinked by physical absorption (H-bond) (b) crosslinked by chemical bond (Coupling agent).

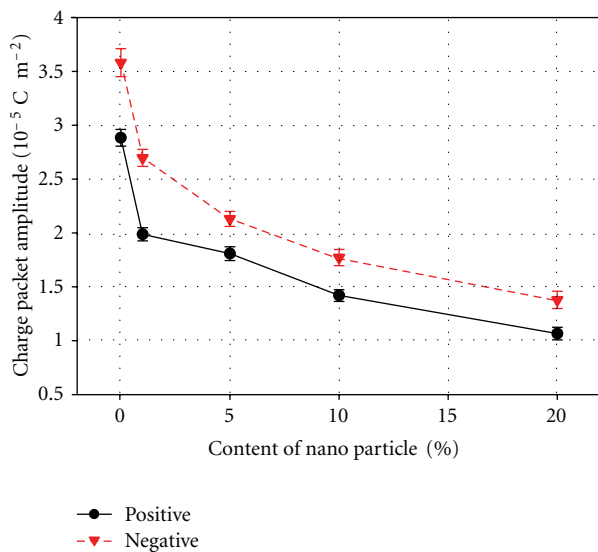


FIGURE 12: Charge pulse amplitude for pure epoxy resin and epoxy-based nanocomposites (90% confidence interval).

The different behavior of the two pure epoxy specimens, that is, cycloaliphatic and bisphenol, the former in its glassy state and the latter in its flexible state, lend support to the proposed conduction mechanism in which electromechanical compression, which may be influenced by the structure of polymer, controls the ultra fast charge pulse conduction.

The mobility ( $\mu$ ) of charge packet can be calculated from

$$\mu = \frac{v}{E}, \quad (1)$$

where  $v$  is charge velocity (ms<sup>-1</sup>) and  $E$  is the average electrical field (Vm<sup>-1</sup>).

An estimate of the velocity of a charge packet,  $v$ , can be obtained from the charge profiles (e.g., Figures 3–7) and

used to calculate the mobility of both positive and negative charge pulses in specimens acquired under the condition of 10 kV mm<sup>-1</sup> and 70°C, see Figure 10. It can be seen that the mobility of the ultra fast charge pulses is in the range of 10<sup>-9</sup>–10<sup>-10</sup> m<sup>2</sup> V<sup>-1</sup> s<sup>-1</sup>, which is much higher than conventional charge mobility. In particular, the mobility is 5.6 × 10<sup>-10</sup> m<sup>2</sup> V<sup>-1</sup> s<sup>-1</sup> for positive charge pulses and 9.1 × 10<sup>-10</sup> m<sup>2</sup> V<sup>-1</sup> s<sup>-1</sup> for negative charge pulses, respectively, in the pure epoxy resin. The introduction of nanoparticles into the base polymer causes the charge pulse mobility and amplitude to decrease, the latter to 1/3–1/4 of its value in the pure resin. It should also be noticed that the positive charge pulse mobility decreases much more than that of negative charge pulses when increasing the nanoparticle content in the composite.

In [13] it was speculated that the positive solitons (charge pulses) move by means of the single bond rotation (e.g.,  $\gamma$ -mode in PE), which allows hole transfer to a neighboring chain by reverse tunneling of electrons, which then travel a distance by the subsequent chain displacement. In the case of negative soliton (charge pulse) motion, it was suggested that electron packets injected and trapped in free volume move into neighboring free volume through an easy path produced when the hindering chains are opened up by chain relaxation (e.g.,  $\beta$ -mode in PE). The different modes of motion of positive and negative charge pulses result in a different charge mobility and lack of superposition of positive and negative pulses. When nanoparticles are added to the base polymer, their large specific surface area and surface energy allows each particle to act as a cross-link point in the polymer by means of the physical absorption effect (H-bond) or chemical bond (e.g., silane coupling agent) created between particle surface and polymer chains. The chemical structure of cross-linking in the polymer through nanoparticles is sketched in Figure 11. Therefore, the cross-link degree of epoxy resin is increased by the presence of nanoparticles. In other words, the molecular chain movement and bond rotation in the

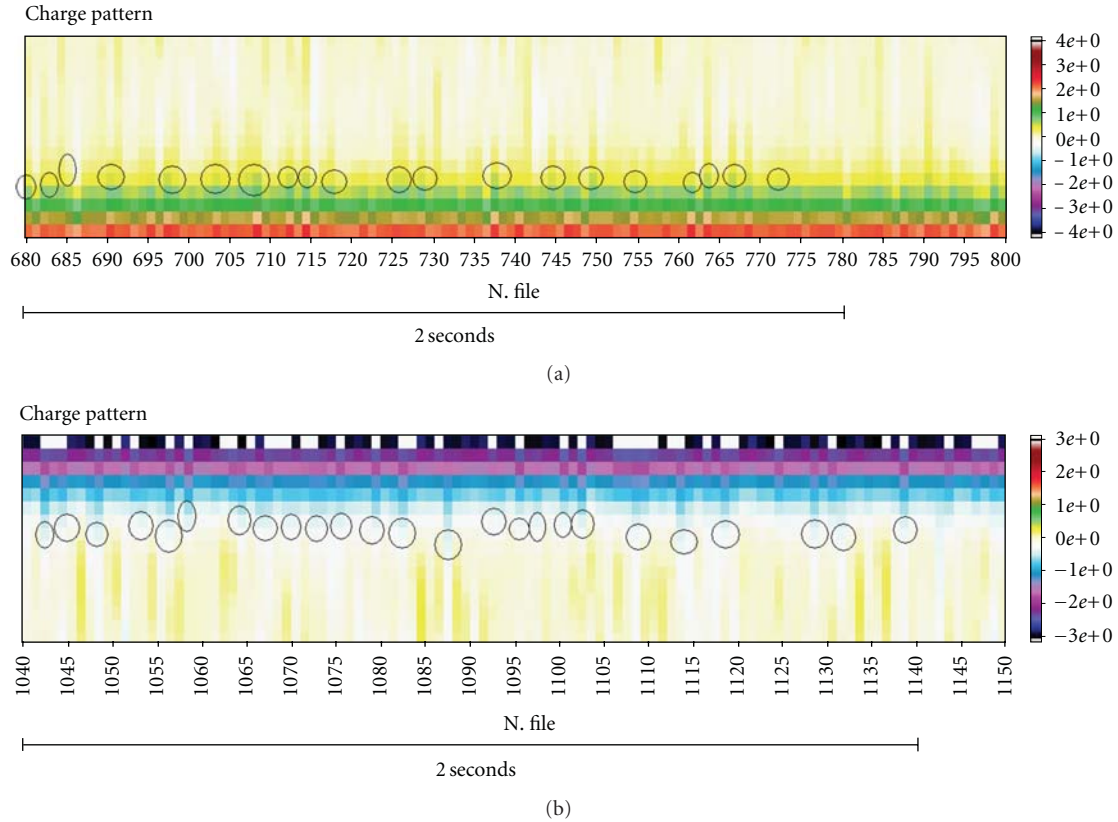


FIGURE 13: Enlargement of the charge pattern in specimen no. 0 (Figure 1(a)) positive (a) and negative (b) charge pulses are labeled by circles.

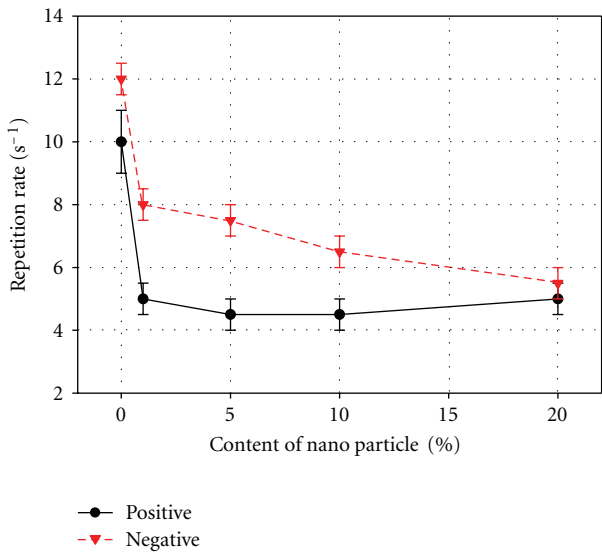


FIGURE 14: Charge pulse repetition rate of pure epoxy resin and epoxy-based nanocomposites (90% confidence interval).

polymer are all restricted by the presence of nanoparticles. In this circumstance, it is more difficult, for example, for positive charge pulses to tunnel into other chains or negative charge pulses to move into neighboring free volume. Consequently the mobility of both positive and negative charge pulses should decrease as observed.

The charge pulse amplitude ( $\text{Cm}^{-2}$ ) is obtained as the area of the pulse shown in Figure 3 to Figure 7, that is, it is calculated as the integral of the charge volume density over the pulse width. The result at  $T = 70^\circ\text{C}$  and  $E = 10\text{ kV mm}^{-1}$  is plotted in Figure 12. Here it can be seen that the absolute amplitudes of positive and negative charge pulses in pure Epoxy resin are  $2.88 \times 10^{-5}\text{ Cm}^{-2}$  and  $3.58 \times 10^{-5}\text{ Cm}^{-2}$ , respectively, and that both positive and negative pulse amplitudes decrease with rising nanoparticle concentration. In particular, the amplitude in the nanocomposite with 20% nanoparticles is only 37.0% and 38.5% of that relevant to the pure material for positive and negative charge pulses respectively.

Interestingly, the influence of nanoparticles on amplitude and mobility of ultra fast charge shows a similar trend to that found for conventional (slow) high-field space charge packets. It is reported that both the amount of charge and mobility in MgO/LDPE nanocomposite decrease with nanofiller content, which is considered that the trapping effect of the injected charge by MgO nanofiller may hinder the space charge injection and charge transport in polymer [15].

The number of electronic charges contained in one fast charge pulse can be calculated by multiplying the pulse charge amplitude ( $\text{Cm}^{-2}$ ) by the area of the PEA electrode and dividing by the charge quantity of an electron ( $1.6 \times 10^{-19}\text{ C}$ ). The results are listed in Table 2, which shows that there are more than  $10^{15}$  charges in one pulse injected from the electrodes in the case of the pure polymer with

TABLE 2: Number of electronic charges per fast packet.

Specimen	Number of charge/( $\times 10^{14}$ )	
	Positive charge	Negative charge
No. 0	14.1	17.6
No. 1	9.8	13.2
No. 5	8.9	10.5
No. 10	7.0	8.7
No. 20	5.2	6.8

the amount decreasing monotonically with the increase in concentration of nanoparticles in the composite. This shows that the number of electronic charges per pulse injected into insulating polymer is reduced by the presence of nanoparticles.

The charge repetition rate (RR) was estimated from the space charge patterns (Figure 2). As an example, Figure 13 shows an enlargement of the regions near the anode (a) and near the cathode (b) in Figure 2(a) in order to estimate the charge repetition rate (the charge pulses are labeled by circles). It can be seen clearly from Figure 13(a) that several positive and negative charge packets are injected into the insulating bulk. There are 20 positive and 24 negative charge packets injected into the material in 100 acquisition files, respectively, that is, about 2 s (the acquisition time is set to be 0.02 s for obtaining one charge profile). Hence, the charge packet repetition rate for positive ( $RR^+$ ) and negative charge ( $RR^-$ ) could be calculated as

$$\begin{aligned} RR^+ &= \frac{20}{100 \times 0.02} = 10 \text{ (s}^{-1}\text{)}, \\ RR^- &= \frac{24}{100 \times 0.02} = 12 \text{ (s}^{-1}\text{)}. \end{aligned} \quad (2)$$

Therefore, 10 positive and 12 negative fast charge packets are injected into pure polymer in one second, which is a higher rate than that observed in XLPE [6]. Figure 14 shows the repetition rates of the nanofilled composites counted in the same way as for specimen no. 0. As can be seen the repetition rate reduces when nanoparticles are added into the material. In [13], it was suggested that the repetition rate was governed by the replenishment of the charge reservoir at the electrode-polymer interface to the level  $\Delta Q$  at which it is capable of initiating pulse injection. The reduction of RR with increasing nanofiller content may, therefore, be due to the modification of the electrode-polymer interface caused by the presence of nanofiller.

It must be emphasized again that this new conduction phenomena occurs under relatively low electrical fields, that is, close to the operating field for electrical equipment, and has a fundamental interaction with the electromechanical property of the insulating polymer, thus with its structural characteristics. Therefore, it might be possible to apply it to the online diagnosis of insulation ageing in electrical equipment, as well as an indication of the proper nanofiller concentration to achieve specific electromechanical characteristics.

## 4. Conclusions

Ultra fast space charge pulses have been observed in flexible pure epoxy resin and epoxy-based nanocomposites. The characteristics of these ultra fast charge pulses, that is, mobility, amplitude, and repetition rate, are affected significantly by the concentration of nanoparticles, for both positive and negative charge pulses. Such phenomena can be explained by a new conduction mechanism associated with the chemical structure and electrical/mechanical properties of an insulating polymer, which can be modified by nanoparticles. The effects of the nanoparticles are regarded as changing the mechanical properties by increasing cross-link degree and chain stiffness. This gives further support to the contention that the mechanism of the ultra fast soliton transport is governed by the electromechanical compression of an insulating material.

## References

- [1] D. A. Seanor, *Electrical Properties of Polymers*, Academic Press, London, UK, 1982.
- [2] L. A. Dissado and G. C. Fothergill, *Electrical Degradation and Breakdown in Polymers*, Peregrinus Press, Stevenage, UK, 1992.
- [3] G. C. Montanari, "The electrical degradation threshold of polyethylene investigated by space charge and conduction current measurements," *IEEE Transactions on Dielectrics and Electrical Insulation*, vol. 7, no. 3, pp. 309–315, 2000.
- [4] G. C. Montanari, "Dielectric material properties investigated through space charge measurements," *IEEE Transactions on Dielectrics and Electrical Insulation*, vol. 11, no. 1, pp. 56–64, 2004.
- [5] D. Fabiani, G. C. Montanari, L. A. Dissado, C. Laurent, and G. Teyssedre, "Fast and slow charge packets in polymeric materials under DC stress," *IEEE Transactions on Dielectrics and Electrical Insulation*, vol. 16, no. 1, Article ID 4784573, pp. 241–250, 2009.
- [6] D. Fabiani, G. C. Montanari, and L. A. Dissado, "Space charge accumulation due to ultra fast charge packets in XLPE insulated cables: the effect of temperature and field," in *Proceedings of the 9th IEEE International Conference on Properties and Applications of Dielectric Materials (ICPADM '09)*, pp. 337–340, Harbin, China, 2009.
- [7] D. Fabiani, G. C. Montanari, E. Siracusano, and L. A. Dissado, "Ultra fast space charge packets in nanostructured epoxy-based materials," in *Proceedings of the Annual Report Conference on Electrical Insulation and Dielectric Phenomena (CEIDP '09)*, pp. 31–34, West Lafayette, Ind, USA, October 2009.
- [8] D. Fabiani, G. C. Montanari, and L. A. Dissado, "Fast pulse-like conduction in XLPE based materials detected through charging current measurements," in *Proceedings of the IEEE International Conference on Solid Dielectrics (ICSD '10)*, pp. 1–4, Postan, Germany, 2010.
- [9] G. Polizos, V. Tomer, E. Manias, and C. A. Randall, "Epoxy-based nanocomposites for electrical energy storage. II: nanocomposites with nanofillers of reactive montmorillonite covalently-bonded with barium titanate," *Journal of Applied Physics*, vol. 108, no. 7, Article ID 074117, 10 pages, 2010.
- [10] T. J. Lewis, "Nanomeric dielectrics," *IEEE Transactions on Dielectrics and Electrical Insulation*, vol. 1, no. 5, pp. 812–825, 1994.

- [11] S. Li, G. Yin, G. Chen et al., "Short-term breakdown and long-term failure in nanodielectrics: a review," *IEEE Transactions on Dielectrics and Electrical Insulation*, vol. 17, no. 5, pp. 1523–1535, 2010.
- [12] T. J. Lewis, J. P. Llewellyn, and M. J. van der Sluijs, "Electrokinetic properties of metal-dielectric interfaces," *IEEE Transactions on Dielectrics and Electrical Insulation*, vol. 140, no. 5, pp. 385–392, 1993.
- [13] D. Fabiani, G. C. Montanari, and L. A. Dissado, "High mobility conduction in insulating polymers through fast soliton-like charge pulses," *Journal of Physics: Conference Series*, vol. 183, Article ID 012010, pp. 1–6, 2009.
- [14] X. Huang, Y. Zheng, P. Jiang, and YI. Yin, "Influence of nanoparticle surface treatment on the electrical properties of cycloaliphatic epoxy nanocomposites," *IEEE Transactions on Dielectrics and Electrical Insulation*, vol. 17, no. 2, Article ID 5448121, pp. 635–643, 2010.
- [15] Y. Murakami, M. Nemoto, S. Okuzumi et al., "DC conduction and electrical breakdown of MgO/LDPE nanocomposite," *IEEE Transactions on Dielectrics and Electrical Insulation*, vol. 15, no. 1, pp. 33–39, 2008.